UNIVERSIDAD DE GRANADA

TESIS DOCTORAL

Para la obtención del

Grado de Doctor por la Universidad de Granada

MODELOS ESTRUCTURALES DE VELOCIDAD Y ATENUACIÓN SÍSMICA EN ZONAS VOLCÁNICAS ACTIVAS

AUTOR

Ignacio Castro Melgar

DIRECTORES

Jesús Miguel Ibáñez Godoy y Janire Prudencio Sóñora

Departamento de Física Teórica y del Cosmos

Programa de Doctorado en Ciencias de la Tierra

Mayo 2022

Un Talgo mañanero parte de Zaragoza por San José

Desde el puente del Camino Miraflores

Un abuelo y su nieto lo despiden

¡Cuántas ilusiones!

A mi yayo Luis

AGRADECIMIENTOS

buenos y sobre todo en los malos momentos, pero con respecto a está tesis, por confiar en mi determinación y en mis elecciones incluso cuando no lo veíais claro, ese es el apoyo más difícil, pero sin duda el más necesario. Habéis demostrado el mayor amor hacia un hijo, no el de las palabras sino el de los actos, y por ello os estaré siempre agradecido A mi hermana, qué puedo decir de ella, tanto empeño tengo en escribir estas palabras que no me salen, así que las resumiré: te quiero y te necesito junto a mí siempre, independientemente de la distancia física que haya. Ya sea para charlas banales sobre baloncesto o para contarnos confesiones y pedirnos consejo. Qué orgullo y qué felicidad ser tu tato.

Un apartado distinto es el de aquellos que no me han aportado específicamente a mi tesis, porque han tenido una tarea mucho mayor, la de ayudarme a formarme como persona, a ser quien soy, a pensar como lo hago y que, sin duda, sin esa formación, sin esos valores, jamás podría haberme enfrentado a este arduo camino. Hablo sin duda de mi Yayo Luis, un faro de luz incombustible que, aunque ya no esté con nosotros, sigue guiándome día a día y no dudo que lo seguirá haciendo; mi Yaya Dolores, pura pasión, la mayor de las energías combinada con el amor incondicional por sus nietos, me has enseñado a no achantarme ante nada ni ante nadie; Pepe, un filósofo sin pretenderlo, un hombre tranquilo que transmite enseñanzas de vida a cada momento y del que he aprendido a valorar lo importante y mi Yaya Aurita, por darme el amor y la devoción más completa y generosa , y eso es algo que ninguna enfermedad puede borrar.

Por último, quiero agradecer a la persona que más ha estado presente en esta tesis, Juana, has sabido ser la mejor pareja, amiga y compañera de fatigas. La importancia que tienes aquí es vital, hemos celebrado los éxitos y los malos momentos juntos, siempre has tenido palabras de aliento y he tenido tu ayuda cuando la he necesitado. Cuesta decir en pocas líneas tantísimo, pero gracias por impulsarme y apoyarme en este arduo camino, y qué ganas de que sigamos descubriendo nuevas etapas juntos, gracias por todo.

DOCTORADO INTERNACIONAL

En cumplimiento de los requisitos de la normativa de la Escuela Internacional de Posgrado de la Universidad de Granada (UGR) para obtener el Título de Doctor/a con mención europea/internacional, Don Ignacio Castro Melgar ha incluido un idioma extranjero en la redacción de la tesis doctoral y ha realizado tres estancias de investigación internacionales, junto con los requerimientos pertinentes en relación a la composición del tribunal y la obtención de informes firmados por expertos doctores pertenecientes a instituciones no españolas.

Idioma de presentación de la tesis doctoral

Con el objetivo de cumplir con el requisito de redactar una parte de la tesis en una lengua distinta a las oficiales de España, se ha escrito el resumen y las conclusiones tanto en inglés como en español. De esta manera, se facilita el entendimiento de la tesis a los lectores no hispanohablantes.

Estancias de investigación

Con respecto al requisito mínimo de realizar una estancia de investigación de 3 meses en una Universidad o Centro de Investigación extranjero, se ha cumplido holgadamente realizando 3 estancias de 3 meses cada una.

La primera estancia se ha desarrollado en el *Dipartimento di Scienze Biologiche, Geologiche e Ambientali* en la *Università Degli Studi di Catania* (Catania, Italia), del 15 de diciembre del 2020 al 15 de marzo del 2021 bajo la tutorización del Dr. Andrea Cannata. Esta estancia ha contribuido al estudio de las Islas Eolias y a la publicación del artículo *Small-Scale Volcanic Structures of the Aeolian Volcanic Arc Revealed by Seismic Attenuation* en la revista *Frontiers in Earth Science* (JCR: Q2 / SJR: Q1).

La segunda estancia se ha realizado en la *School of Environmental Sciences* en la *University of Liverpool* (Liverpool, Reino Unido) del 6 de abril del 2021 al 6 de julio del

2021 siendo supervisado por el Dr. Silvio De Angelis. Esta estancia ha contribuido al estudio de la isla volcánica de Montserrat y actualmente se está redactando el artículo científico para la publicación en una revista de alto impacto.

La tercera estancia se ha desarrollado en el *Deparment of Geography* en la *Harokopio University of Athens* (Kallithea, Grecia) del 1 de septiembre del 2021 al 1 de diciembre del 2021, tutorizado por el Dr. Issaak Parcharidis. Ha sido financiada por la convocatoria de plazas de movilidad internacional de estudiantes de doctorado Cursos Académicos 2020/2021 y 2021/2020, modalidad 3: estancias de movilidad internacional en el marco del Programa 1.2 del Plan Propio de Internalización de la Universidad de Granada. Esta estancia ha permitido los estudios de la isla de La Palma y del Complejo Volcánico de Santorini. Estas investigaciones se han traducido en la redacción de dos artículos científicos, el primero se encuentra actualmente bajo revisión en la revista *Natural Hazards* (JCR: Q2 / SJR: Q1) y el segundo en fase final de preparación y será enviado próximamente a una revista indexada en la *Web of Science*. Además de contribuciones a congresos internacionales como *Safe Greece 2021* o *Living Planet Symposium 2022*.

Índice

RESUMEN EXTENDIDO

La relación entre la humanidad y los volcanes siempre ha resultado de gran complejidad, debido a que es indudable el riesgo que entraña vivir en un entorno volcánico, no obstante, los beneficios que estas zonas fértiles aportan a sus poblaciones son numerosos. A pesar de la peligrosidad de las erupciones, los avances científicos están permitiendo conocer mejor el fenómeno volcánico, tanto a nivel estructural como de vigilancia volcánica. La sismología volcánica nos permite conocer el estado actual del volcán mediante el estudio de los eventos sismo-volcánicos. Un análisis que no se limita al estudio del estado del volcán, si no que permite avanzar en el conocimiento de la dinámica volcánica y su estructura interna. En la actualidad, la tomografía sísmica es la técnica más potente y que aporta mayor fiabilidad para el estudio de la estructura interna de los volcanes.

Un parámetro de gran utilidad para estudiar los medios volcánicos a través de tomografías sísmicas es la velocidad, sin embargo, este parámetro tiene menor sensibilidad a la detección de las heterogeneidades presentes en los volcanes que otros como la atenuación sísmica. Así, el estudio de las propiedades de atenuación de un área concreta nos permite identificar distintos cuerpos existentes en el medio; debido a su mayor sensibilidad a la estructura interna y a la presencia de fluidos. De esta manera, los estudios de atenuación suponen un gran avance en el conocimiento de la estructura interna de los volcanes, incorporando modelos más precisos y fiables.

Los primeros estudios de atenuación sísmica se basaban en la obtención de valores medios para una región de estudio. Posteriormente, los avances en la potencia de cálculo y/o el desarrollo de nuevos modelos teóricos de atenuación sísmica, permitieron la separación fiable de los fenómenos de la atenuación intrínseca y *scattering*. En la actualidad, las investigaciones de atenuación sísmica se están centrando en determinar la estructura de atenuación en una zona de estudio. Cuando esta estructura de atenuación se representa bidimensionalmente o tridimensionalmente toma el nombre de tomografía de atenuación sísmica.

Esta tesis tiene como objetivo la obtención de modelos estructurales de volcanes activos, como las Islas Eolias y el Monte Etna, a partir de tomografías sísmicas de atenuación, con el objetivo de contribuir a avanzar en el conocimiento estructural de las

áreas bajo estudio en esta tesis. Por tanto, los objetivos específicos para las Islas Eolias, la primera región bajo estudio, son: obtener un modelo de atenuación bidimensional y separación de las contribuciones de atenuación intrínseca y *scattering* mediante el modelo de difusión. Para la segunda región estudiada, el Monte Etna, los objetivos específicos son: alcanzar dos modelos tomográficos, una representación bidimensional con separación de efectos de *scattering* y de absorción anelástica, utilizando el modelo difusión, y un segundo modelo, en este caso tridimensional, de la distribución de los valores de atenuación, a partir del método de normalización de la coda. Además, para el Monte Etna, se pretende realizar una interpretación conjunta de diferentes modelos tomográficos, tanto en velocidad como en atenuación, para avanzar en el conocimiento de su estructura interna.

Partiendo de la idea de que la propagación de las ondas sísmicas se ve afectada por el medio que atraviesan, dado que la Tierra es heterogénea y anelástica, esta afectación se traduce en una pérdida de energía: en primer lugar, por la falta de elasticidad y, en segundo, por la presencia de diferentes cuerpos heterogéneos que pueden producir refracciones, reflexiones o una nueva distribución de energía por procesos de *scattering*. A estos habría que añadirle un tercer grupo, el referido a la expansión geométrica.

El fenómeno de la expansión geométrica o *geometrical spreading* es un proceso geométrico por el cual la energía de las ondas sísmicas transmitidas desde una fuente debe mantenerse, al atravesar un medio elástico, homogéneo e isótropo. La absorción anelástica o atenuación intrínseca es un fenómeno por el cual la amplitud de las ondas sísmicas es atenuada en función de la distancia a causa de efectos no elásticos. De esta manera, el medio absorbe la energía elástica en forma de calor a causa de la fricción. Es una propiedad intrínseca del medio de propagación y depende de sus características tectónicas y geológicas. El fenómeno atenuativo que sufre una onda sísmica es el que produce la anisotropía y la falta de homogeneidad de la Tierra, y recibe el nombre de *scattering*. Las heterogeneidades en el medio de propagación originan una redistribución de la energía tanto en tiempo como en el espacio, al cambiar la propagación de las ondas y/o cambios de fase. Conocer la aportación de *scattering* supone conocer la mayor o menor heterogeneidad del medio de propagación.

El parámetro más utilizado para el estudio de la atenuación sísmica es el factor de calidad (Q). Este indica la relación existente entre la energía total almacenada y la energía disipada para un mismo volumen de material sometido cíclicamente a un esfuerzo elástico

en un ciclo de excitación armónica. En el término de atenuación sísmica, representado por el factor de calidad (*Q*), se incluyen los efectos de la atenuación intrínseca (*Qi*) y los de la atenuación por *scattering* (*Qs*). Este último, aunque es una redistribución de la energía, también contribuye a la pérdida de energía del factor de calidad.

Las regiones de estudio en esta tesis son el Monte Etna y las Islas Eolias, que se encuadran en un marco geodinámico complejo. Los datos utilizados para llevar a cabo esta tesis han sido obtenidos por el experimento de sísmica activa TOMO-ETNA, llevado cabo en el verano de 2014, un experimento que implicó una gran cantidad de recursos humanos y materiales. El área del experimento alcanzó los 300 x 300 km. El conjunto final de la base de datos del experimento TOMO-ETNA consistió en 26364 disparos de aire comprimido, siendo 9705 disparos de refracción y 16659 disparos de reflexión, registrados en más de 200 estaciones sísmicas. En total la base de datos se compuso de 5140980 señales.

Los métodos utilizados para realizar los estudios que se integran han sido, por un lado, el modelo de difusión, que permite diferenciar la contribución por atenuación intrínseca y *scattering*. Para ello, se lleva a cabo una aproximación de la teoría de transferencia de energía en la que se asume fenómenos de *scattering* fuerte. Debido al carácter heterogéneo de las regiones volcánicas, el modelo de difusión es el más adecuado para estudiar la atenuación sísmica. Por otro lado, también se utiliza el método de normalización de la coda, el cual determina el factor de calidad de una región mediante la razón de la amplitud espectral de las ondas directas y las ondas coda. Este método, no permite la separación de la atenuación intrínseca y de *scattering*, ya que se obtiene un factor de calidad total, pero sí permite conocer la distribución tridimensional del mismo.

La segunda parte de esta tesis doctoral recoge los trabajos científicos realizados y publicados. En primer lugar, se presenta la primera tomografía sísmica de atenuación bidimensional realizada con separación de la atenuación intrínseca y por *scattering* de las Islas Eolias. Este archipiélago representa uno de los mejores ejemplos de un arco insular volcánico de pequeña dimensión, caracterizado por la alternancia de diferentes dominios estructurales. Usando el modelo de difusión como base para el análisis, y con datos del experimento de sísmica activa TOMO-ETNA, se analizan más de 76700 trayectorias sísmicas fuente-estación. Utilizando frecuencias de 4 a 24 Hz, se identifica una atenuación regional alta, comparable con otras áreas volcánicas del mundo. Como en la mayoría de las regiones volcánicas, la atenuación por *scattering* predomina sobre la

atenuación intrínseca, pero algunas características son específicas del área. Las estructuras volcánicas presentan la mayor contribución de *scattering,* especialmente en el rango de bajas frecuencias. Se interpreta que este comportamiento refleja el tamaño pequeño de las islas y el tamaño relativamente pequeño de los sistemas de alimentación magmáticos individuales. Además, el fuerte *scattering* observado en la zona más septentrional se asocia al sistema de fallas Eolias-Tindari-Letojanni. En contraste, lejos de las islas volcánicas, la atenuación intrínseca domina sobre la atenuación por *scattering*. Interpretamos este cambio en el comportamiento atenuante como un reflejo del gran volumen de material sedimentario depositado en el lecho marino. Debido a su naturaleza poco consolidada, los sedimentos facilitan la atenuación intrínseca por disipación de energía, pero en general presentan una alta homogeneidad estructural que se refleja en bajos niveles de *scattering*. Los resultados muestran que esta región no está sustentada por un gran complejo estructural volcánico como el que se encuentra debajo del cercano volcán Monte Etna. En cambio, se observan estructuras volcánicas subterráneas aisladas y dimensionalmente más pequeñas. La identificación de tales características facilita una mejor interpretación geológica; separando las estructuras marinas consolidadas de los elementos volcánicos subterráneos independientes. Los resultados de este estudio proporcionan un modelo para nuevas investigaciones en regiones similares de todo el mundo.

En segundo lugar, el trabajo presentado es una tomografía sísmica de atenuación bidimensional de la región volcánica del Monte Etna con separación de la atenuación intrínseca y *scattering*. El análisis realizado utiliza la base de datos del experimento de sísmica activa TOMO-ETNA llevado a cabo en 2014, que cubre completamente el área bajo estudio. A partir del modelo de difusión se observa que los efectos de *scattering* dominan sobre la atenuación intrínseca, lo que sugiere que la región es muy heterogénea. La comparación con los análisis realizados en otros volcanes revela que la región del Monte Etna se caracteriza por una alta atenuación intrínseca, como resultado de la presencia de grandes depósitos volcanoclásticos a poca profundidad. La distribución bidimensional de anomalías de atenuación intrínseca y por *scattering* muestra la presencia de regiones caracterizadas por efectos de atenuación alta y baja, correspondientes a varias características tectónicas y volcánicas. En particular, se identifica una región de alta atenuación en el sector SO del complejo volcánico del Monte Etna, que se correlaciona con altas tasas de sismicidad y actividad eruptiva. Este trabajo apoya la hipótesis de un

vínculo entre la dinámica del flanco SO y la recarga del volcán en las últimas décadas, ocurriendo bajo el cráter de la cumbre y, secundariamente, en la zona superior del rift sur.

El tercer trabajo presentado consiste en la realización de una nueva imagen tridimensional de atenuación del volcán Etna a través de una tomografía sísmica basada en el método de normalización de la coda. El Monte Etna es un laboratorio natural ideal para la aplicación de técnicas de tomografía, debido a los altos niveles de sismicidad que abarcan una amplia gama de distancias y profundidades epicentrales. Utilizando las *waveforms* de la base de datos generada en el experimento de sísmica activa TOMO-ETNA, se realiza una interpretación conjunta de los modelos de inversión tomográfica y geofísica para limitar mejor las interpretaciones de la estructura volcánica. Se realiza una comparación de los resultados de la tomografía de atenuación con modelos de inversión sísmica (dos modelos sísmicos de onda P y un modelo de atenuación sísmica de onda coda 3D) y la literatura, para resaltar e interpretar los elementos estructurales y su impacto en la dinámica del volcán. De esta manera, se crea una nueva imagen de la estructura interna del Monte Etna que ayuda a limitar el comportamiento volcánico presente y futuro. En particular, este estudio se enfoca en el almacenamiento de magma debajo del área de la cumbre, que se identifica con un gran volumen de alta atenuación, que se caracteriza por propiedades físicas compatibles con la presencia de magma y otros fluidos. La existencia de un volumen tan grande de magma en la corteza poco profunda debajo del monte Etna tiene implicaciones para el potencial eruptivo del volcán.

La última parte de la tesis recoge las principales conclusiones a las que llega esta investigación:

- Para las Islas Eolias se han obtenido los primeros mapas bidimensionales de las contribuciones de atenuación intrínseca y de *scattering*. Es una región fuertemente atenuada, con una mayor contribución de atenuación por *scattering*. Las islas que integran el archipiélago no son un gran complejo volcánico, si no que son estructuras pequeñas y numerosas, aisladas entre sí.

- En el Monte Etna se han utilizado métodos pioneros en el área de estudio, comprobándose muy eficaces en su aplicación para la región, así como una interpretación conjunta de diferentes tomografías sísmicas de velocidad y atenuación que se revelan como una de las herramientas más útiles y potentes para estudiar los complejos volcánicos. El Monte Etna es una región muy heterogénea y con gran presencia de

depósitos volcanoclásticos superficiales. Se ha identificado en la tomografía sísmica 2D una región que se interpreta como la zona de recarga del volcán en las últimas décadas. En la tomografía sísmica 3D se ha identificado un gran cuerpo de material parcialmente fundido que se ha interpretado como el reservorio magmático superficial que nutría a los episodios eruptivos que tuvieron lugar durante el verano de 2014.

Esta tesis propone como líneas futuras aplicar las metodologías de esta tesis a la región de El Hierro (España). Además, se han obtenido tomografías sísmicas de atenuación 2D y 3D para la obtención de la estructura tridimensional del volcán Soufrière Hills, en la isla de Montserrat (Reino Unido) y de la región geotermal "The Geysers" en California (EUA), estudios pendientes de ser publicados en revistas de alto impacto.

EXTENDED ABSTRACT

The relationship between humanity and volcanoes has always been highly complex, due to the undoubted risk of living in a volcanic environment, however, the benefits that these fertile areas bring to their populations are numerous. Despite the danger of eruptions, scientific advances are allowing a better understanding of the volcanic phenomenon, both at a structural level and a volcano monitoring. An analysis that is not limited to the study of the state of the volcano, but that allows us to advance in the knowledge of the volcanic dynamics and its internal structure. At present, seismic tomography is the most powerful technique and the one that provides the greatest reliability for the study of the internal structure of volcanoes.

A very useful parameter to study volcanic environments through seismic tomography is velocity, however, this parameter has less sensitivity to the detection of heterogeneities present in volcanoes than others such as seismic attenuation. Thus, the study of the attenuation properties of a specific area allows us to identify different bodies existing in the environment; due to its greater sensitivity to the internal structure and to the presence of fluids. In this way, attenuation studies represent a great advance in understanding the internal structure of volcanoes, incorporating more precise and reliable models.

The first seismic attenuation studies were based on obtaining mean values for a study region. Then, advances in computing power and/or the development of new theoretical models of seismic attenuation allowed the reliable separation of intrinsic attenuation and scattering phenomena. Currently, seismic attenuation investigations are focusing on determining the attenuation structure in a study area. When this attenuation structure is represented in two or three dimensions, it is called seismic attenuation tomography.

This thesis aims to obtain structural models of active volcanoes, such as the Aeolian Islands and Mount Etna, from seismic attenuation tomography, with the aim of contributing to advance the structural knowledge of the areas under study in this thesis. Therefore, the specific objectives for the Aeolian Islands, the first region under study, are: to obtain a two-dimensional attenuation model and separation of the intrinsic attenuation and scattering contributions using the diffusion model. For the second region studied,

Mount Etna, the specific objectives are: to achieve two tomographic models, a two-dimensional representation with separation of scattering and anelastic absorption effects using the diffusion model, and a three-dimensional model of the distribution of the values of attenuation, using the coda normalization method. In addition, for Mount Etna, a joint interpretation of different tomographic models is to be carried out, both in velocity and in attenuation, to advance in the knowledge of its internal structure.

Starting from the idea that the propagation of seismic waves is affected by the medium they pass through, given that the Earth is heterogeneous and inelastic, this affectation translates into a loss of energy: firstly, due to the lack of elasticity and, secondly, due to the presence of different heterogeneous bodies that can produce refractions, reflections or a new distribution of energy by scattering processes. To these should be added a third group, that referred to geometric expansion.

The phenomenon of geometrical spreading is a geometric process by which the energy of seismic waves transmitted from a source must be maintained when passing through an elastic, homogeneous and isotropic medium. Anelastic absorption or intrinsic attenuation is a phenomenon by which the amplitude of seismic waves is attenuated as a function of distance due to non-elastic effects. In this way, the medium absorbs elastic energy in the form of heat due to friction. It is an intrinsic property of the propagation medium and depends on its tectonic and geological characteristics. The attenuating phenomenon suffered by a seismic wave is what produces the anisotropy and lack of homogeneity of the Earth, and is called scattering. The heterogeneities in the propagation medium cause a redistribution of energy both in time and in space by changing the propagation of the waves and/or phase changes. To know the contribution of scattering means to know the greater or lesser heterogeneity of the propagation medium.

The most used parameter for the study of seismic attenuation is the quality factor (Q). This indicates the relationship between the total energy stored and the energy dissipated for the same volume of material cyclically subjected to elastic stress in a harmonic excitation cycle. The seismic attenuation term, represented by the quality factor (Q), includes the effects of intrinsic attenuation (Q_i) and those of scattering attenuation (Q_s). The latter, although it is a redistribution of energy, also contributes to the energy loss of the quality factor.

The study regions in this thesis are Mount Etna and the Aeolian Islands, which are located in a complex geodynamic framework. The data used to carry out this thesis have been obtained by the TOMO-ETNA active seismic experiment carried out in the summer of 2014, an experiment that involved a large amount of human and material resources. The area of the experiment reached 300 x 300 km. The final set of the TOMO-ETNA experiment database consisted of 26364 compressed air shots, of which 9705 were refraction shots and 16659 reflection shots, recorded at more than 200 seismic stations. In total, the database was made up of 5140980 signals.

The methods used to carry out the studies that are integrated have been, on the one hand, the diffusion model, which allows differentiating the contribution by intrinsic attenuation and scattering. For this, an approximation of the energy transfer theory is carried out in which strong scattering phenomena are assumed. Due to the heterogeneous nature of volcanic regions, the diffusion model is the most suitable to study seismic attenuation. On the other hand, the coda normalization method is also used, which determines the quality factor of a region by the ratio of the spectral amplitude of the direct waves and the coda waves. This method does not allow the separation of intrinsic attenuation and scattering, since a total quality factor is obtained, but it does allow to know its three-dimensional distribution.

The second part of this PhD thesis collects the scientific works carried out and published. First, the first two-dimensional attenuation seismic tomography performed with separation of intrinsic and scattering attenuation of the Aeolian Islands is presented. This archipelago represents one of the best examples of a small volcanic insular arc, characterized by the alternation of different structural domains. Using the diffusion model for the analysis, and with data from the TOMO-ETNA active seismic experiment, more than 76700 source-station seismic trajectories are analyzed. Using frequencies from 4 to 24 Hz, a high regional attenuation is identified, comparable to other volcanic areas of the world. As in most volcanic regions, scattering attenuation predominates over intrinsic attenuation, but some features are area-specific. Volcanic structures present the greatest contribution of scattering, especially in the low frequency range. This behavior is interpreted to reflect the small size of the islands and the relatively small size of the individual magmatic feed systems. In addition, the strong scattering observed in the northernmost area is associated with the Aeolian-Tindari-Letojanni fault system. In contrast, away from volcanic islands, intrinsic attenuation dominates over scattering

attenuation. We interpret this change in attenuating behavior as a reflection of the large volume of sedimentary material deposited on the seafloor. Due to their unconsolidated nature, sediments facilitate intrinsic attenuation due to energy dissipation, but in general they present a high structural homogeneity that is reflected in low levels of scattering. The results show that this region is not a large volcanic structural complex like the Mount Etna volcano. Instead, isolated and dimensionally smaller subterranean volcanic structures are observed. The identification of these characteristics facilitates a better geological interpretation; separating the consolidated marine structures from the independent subterranean volcanic elements. The results of this study provide a model for further research in similar regions around the world.

Second, the work presented is a two-dimensional attenuation seismic tomography of the Mount Etna volcanic region with separation of intrinsic attenuation and scattering. The analysis performed uses the database of the active seismic experiment TOMO-ETNA carried out in 2014, which completely covers the area under study. Using the diffusion model, it is observed that the scattering effects dominate over the intrinsic attenuation, which suggests that the region is very heterogeneous. Comparison with analyzes performed on other volcanoes reveals that the Mount Etna region is characterized by high intrinsic attenuation, as a result of the presence of large volcanoclastic deposits at shallow depths. The two-dimensional distribution of intrinsic and scattering attenuation anomalies shows the presence of regions characterized by high and low attenuation effects, corresponding to various tectonic and volcanic features. In particular, a region of high attenuation is identified in the SW sector of the Mount Etna volcanic complex, which correlates with high rates of seismicity and eruptive activity. This work supports the hypothesis of a link between the dynamics of the SW flank and the recharge of the volcano in recent decades, occurring under the summit crater and, secondarily, in the upper zone of the southern rift.

The third work presented consists of the realization of a new three-dimensional image of attenuation of the Etna volcano through a seismic tomography based on the coda normalization method. Mount Etna is an ideal natural laboratory for the application of tomography techniques, due to the high levels of seismicity that cover a wide range of distances and epicentral depths. Using the waveforms of the database generated in the TOMO-ETNA active seismic experiment, a joint interpretation of the tomographic and geophysical inversion models is carried out to better limit the interpretations of the

volcanic structure. A comparison of attenuation tomography results with seismic inversion models (two P-wave seismic models and one 3D coda-wave seismic attenuation model) and the literature is performed to highlight and interpret structural elements and their impact on the dynamics of the volcano. In this way, a new image of the internal structure of Mount Etna is created that helps to limit present and future volcanic behavior. In particular, this study focuses on magma storage below the summit area, which is identified as a large volume of high attenuation, characterized by physical properties compatible with the presence of magma and other fluids. The existence of such a large volume of magma in the shallow crust below Mount Etna has implications for the volcano's eruptive potential.

The last part of the thesis contains the main conclusions reached by this research:

- For the Aeolian Islands, the first two-dimensional maps of the intrinsic attenuation and scattering contributions have been obtained. It is a strongly attenuated region, with a higher contribution of scattering attenuation. The islands that make up the archipelago are not a large volcanic complex, but rather small and numerous structures, isolated from each other.

- On Mount Etna, pioneering methods have been used in the study area, proving to be very effective in their application to the region, as well as a joint interpretation of different velocity and attenuation seismic tomographies, which are revealed as one of the most useful tools and powerful for studying volcanic complexes. Mount Etna is a very heterogeneous region with a large presence of superficial volcanoclastic deposits. A region has been identified in the 2D seismic tomography that is interpreted as the recharge zone of the volcano in recent decades. The 3D seismic tomography has identified a large body of partially molten material that has been interpreted as the surface magmatic reservoir that fed the eruptive episodes that took place during the summer of 2014.

This thesis proposes as future lines to apply the methodologies of this thesis to the region of El Hierro (Spain). In addition, 2D and 3D attenuation seismic tomography has been obtained to obtain the three-dimensional structure of the Soufrière Hills volcano, on the island of Montserrat (United Kingdom) and of the geothermal region "The Geysers" in California (USA), studies pending publication in high-impact journals.

ÍNDICE DE FIGURAS

LISTADO DE PUBLICACIONES

Los artículos de investigación que forman parte del trabajo de esta tesis doctoral son los siguientes.

I.   **Castro-Melgar, I.**, Prudencio, J., Cannata, A., Del Pezzo, E. and Ibáñez, JM. (2021) Small-Scale Volcanic Structures of the Aeolian Volcanic Arc Revealed by Seismic Attenuation. *Frontiers in Earth Science.* 9:725402. https://doi.org/10.3389/feart.2021.725402

II. Ibáñez, J.M., **Castro-Melgar, I.**, Cocina, O., Zuccarello, Z., Branca, S., Del Pezzo, E. and Prudencio, J. (2020). First 2-D intrinsic and scattering attenuation images of Mt Etna volcano and surrounding region from active seismic data, *Geophysical Journal International*, *220*(1), 267–277, https://doi.org/10.1093/gji/ggz450

III. **Castro-Melgar, I.**, Prudencio, J., Del Pezzo, E., Giampiccolo, E., and Ibáñez, J. M. (2021). Shallow magma storage beneath Mt. Etna: Evidence from new attenuation tomography and existing velocity models. *Journal of Geophysical Research: Solid Earth*, *126*(7), e2021JB022094. https://doi.org/10.1029/2021JB022094

Además, se han realizado otras publicaciones relacionadas de manera directa o indirecta con el trabajo de la presente tesis.

IV. Cocina, O., Ibanez, J., Zuccarello, L., Del Pezzo, E., **Castro-Melgar, I**. and Prudencio, J. (2019). 2D and 3D attenuation tomographies at Mt. Etna (Italy). *Geophysical Research Abstracts*, *21*, EGU21019-1426.

V.   Prudencio, J., **Castro-Melgar, I.**, Taira, T., Gritto, R. and Ibáñez, J.M. (2020). Seismic Attenuation Imaging of The Geysers Geothermal Field, USA. *AGU Fall Meeting Abstracts 2020*, S061-0015

VI.   Lekkas, E., Meletlidis, S., Kyriakopoulos, K., Manousaki, M., Mavroulis, S., Kostaki, E., Michailidis, A., Gogou, M., Mavrouli, M., **Castro-Melgar, I.**, Gatsios, T. and Parcharidis, I. (2021). The 2021 Cumbre Vieja volcano eruption in La Palma (Canary Islands). *Newsletter of Environmental, Disaster and Crises Management Strategies*, *26*, ISSN 2653-9454.

VII.   **Castro-Melgar, I.**, Prudencio, J., Ibáñez, J., Gatsios, T. and Parcharidis, I. (2021). Operational Monitoring of a Volcano Before Entering in Unrest Phase Using Sentinel 1 DINSAR and MTINSAR: The Case of La Palma Volcanic Islands. *SafeGreece Conference Proceedings 2021,* pp. 117-120, ISSN 2654-1823.

VIII.   **Castro-Melgar, I.,** Gatsios, T., Prudencio, J., Ibáñez, J. and Parcharidis, I. (2022). Operational use of Sentinel 1 data and interferometric methods to detect precursors for volcanic hazard warning system: the case of La Palma volcanic complex last eruption. *Living Planet Symposium 2022*.

IX.   **Castro-Melgar, I.**, Gatsios, T., Prudencio, J., Ibáñez, J. and Parcharidis, I. (2022). INSAR techniques monitoring La Palma island to reveal deformation before unrest period to mitigate impact, *Natural Hazards (under review)*

PREFACIO

La presente tesis está dividida en tres partes.

La primera de ellas incluye una introducción que recoge la importancia del estudio de los volcanes, el fenómeno de atenuación sísmica y las tomografías sísmicas, para acabar con la exposición de motivaciones y objetivos. A continuación, aborda el marco geodinámico y las regiones de estudio, el contexto volcánico y los estudios previos de tomografías sísmicas que se han realizado. El capítulo 4 presenta los datos y la metodología que se han utilizado en la tesis. Este capítulo a su vez se divide en tres partes, primero se tratan los datos, su origen y el experimento *TOMO-ETNA*, seguidamente se explica el modelo de difusión y la distribución bidimensional, para acabar con el método de normalización de la coda y la distribución tridimensional. La primera parte finaliza con las referecias bibliografía utilizadas.

En la segunda parte de la memoria se exponen los principales hallazgos a partir de los artículos científicos que componen esta tesis, y se divide en 2 capítulos: el primero de ellos recoge la publicación relativa a las Islas Eolias, "Small-Scale Volcanic Structures Of The Aeolian Volcanic Arc Revealed By Seismic Attenuation". En el segundo capítulo se encuentran las publicaciones relativas al Monte Etna: "First 2-D Intrinsic and Scattering Attenuation Images of Mt Etna Volcano and Surrounding Region from Active Seismic Data" y "Shallow Magma Storage Beneath Mt. Etna: Evidence from New Attenuation Tomography and Existing Velocity Models"

En la tercera parte se establecen las conclusiones principales y se proporcionan las líneas futuras de la investigación llevada a cabo en esta tesis, tanto en inglés como en español.

Por último, se incluye la bibliografía general consultada para esta investigación, así como los anexos, donde se recogen todas aquellas publicaciones que no forman parte del compendio de artículos pero que están relacionadas de manera directa o indirecta con la tesis.

PRIMERA PARTE

1. INTRODUCCIÓN

El origen de la palabra volcán proviene de Vulcano, que en la mitología romana es el dios del fuego. Para la mitología griega su nombre era Hefestos (Ἥφαιστος), de ahí que volcán en griego se conozca como Ηφαίστειο. En estos ejemplos se deja constancia de que la humanidad ha entendido los volcanes desde siempre como algo cercano a los dioses, a lo sobrenatural, a una naturaleza poderosa y destructiva, pero también fascinante, admirable y beneficiosa. La relación entre la humanidad y los volcanes siempre ha sido complicada, pero los beneficios de estos a las poblaciones que se asentaban en sus tierras han sido numerosos: fértiles tierras sobre las que cultivar, acceso a agua dulce o minería como cobre, plomo y cinc, entre otros. Sin embargo, es indudable la amenaza que supone vivir en las cercanías de un volcán.

Existen muchos ejemplos de catástrofes volcánicas: la erupción de Toba (Indonesia) hace unos 75000 años, por ejemplo, es considerada un cataclismo mundial. Según Ambrose (1998), la población humana se pudo ver comprometida como especie, reduciéndose a unos 10000 individuos, debido al descenso en la temperatura media de la Tierra de 10º durante varios años. En la edad de bronce se sitúa la erupción minoica de la Isla de Thera (Grecia), datada entre el 1500 y el 1600 a.C. Se estima que se emitieron más de 60 km^3 de material y formó un cráter de 6 x 11 km; y, probablemente, tuvo un efecto catastrófico en las poblaciones del Egeo meridional. Otro ejemplo, también mediterráneo, es la erupción del monte Vesubio (Italia) del año 79. Está considerada la primera erupción documentada a través de las cartas de Plinio el Joven y es hoy conocida porque sepultó en su totalidad a las localidades de Pompeya y Herculano en la bahía de Nápoles. Avanzando hasta el siglo XIX, se puede mencionar la erupción del volcán Tambora (Indonesia) en 1815, que alcanzó un valor 7 sobre 8 en el Índice de explosividad volcánica (VEI) (Briffa et al., 1998). Las consecuencias de la erupción fueron más de 71000 muertos según Oppenheimer (2003) y un descenso en las temperaturas que se conoce como "el año sin verano" en 1816. En el siglo XX podemos resaltar las erupciones del monte Pelée (Martinica) en 1902, con 30000 víctimas, la erupción de Monte Saint Helens (EUA) en 1980, erupción catalogada de VEI 5 o la erupción del Nevado del Ruiz (Colombia) en 1985, que destruyó el pueblo de Armero y originó decenas de miles de muertos a causa de los lahares. En el siglo XXI, y dentro del contexto europeo, destaca la erupción del Eyjafjallajökull (Islandia) de 2010, que provocó el cierre parcial del tráfico aéreo en

Europa durante varias semanas, afectando al menos a 10 millones de pasajeros. Recientemente, en septiembre de 2021 el volcán de Cumbre Vieja entró en erupción en la isla de La Palma (España). Esta erupción, que fue precedida por un aumento de la sismicidad y deformación en la zona oeste de la isla (Lekkas et al., 2021), tuvo una afectación muy importante a los habitantes de la región, con alrededor de 2000 edificios destruidos y 1218 hectáreas cubiertas de lava.

A pesar de la peligrosidad de las erupciones, los avances científicos están permitiendo conocer mejor el fenómeno volcánico, tanto a nivel estructural como a nivel de vigilancia volcánica. En la actualidad, diferentes disciplinas permiten realizar un seguimiento volcánico: la geodesia, a través de la medición de la deformación del terreno mediante diferentes técnicas como la Interferometría radar de apertura sintética (InSAR) o el Sistema de Posicionamiento Global (GPS); la geoquímica, que mediante el estudio de los gases que se emiten a través de las fumarolas, pozos u otros entornos cercanos al volcán, nos permite analizar cambios en su composición o las razones entre gases de origen magmático; o la gravimetría y el magnetismo, que nos permiten identificar intrusiones magmáticas o de diques (Battaglia et al., 2008). Entre todas ellas, la sismología es la disciplina con mayor tradición y confianza para conocer el estado actual del volcán mediante el estudio de las señales sísmicas. Un sistema de vigilancia volcánica robusto, junto con una adecuada respuesta entre las autoridades y la población, permite implementar protocolos de alerta temprana eficaces para ayudar a mitigar los daños.

Como se ha mencionado anteriormente, la sismología volcánica nos permite conocer el estado actual del volcán mediante el estudio de los eventos sismo-volcánicos (eventos volcano-tectónicos (VT), largo periodo (LP), tremor, etc.). Sin embargo, el análisis de estos eventos no se limita al estudio del estado del volcán, si no que permiten avanzar en el conocimiento de la dinámica volcánica y su estructura interna. En la actualidad, la tomografía sísmica es la técnica más potente y que aporta mayor fiabilidad para el estudio de la estructura interna de los volcanes. La primera imagen de tomografía sísmica se obtuvo en California (EUA), a mediados de los años 70, donde se empleó para estudios regionales usando telesismos. Sin embargo, la resolución que ofrecían estas primeras investigaciones era muy limitada (Aki et al., 1974). A mediados de la década de los 80 se empezaron a desarrollar nuevos algoritmos que permitieron aplicar la técnica a los volcanes. De esta manera, Thurber (1984), obtuvo la primera tomografía sísmica en velocidad a partir de la inversión de las ondas P del volcán Kilauea (Hawaii, EUA).

Existen muchas características físico-químicas que pueden contribuir al conocimiento de la estructura volcánica. Esto supone que la elección de un parámetro para su estudio suponga un verdadero desafío. Como se ha observado, en las primeras tomografías sísmicas el parámetro que se invertía era la velocidad de propagación de las ondas sísmicas. La velocidad es un parámetro de gran utilidad a la hora de estudiar los medios volcánicos. Así, existen multitud de ejemplos de modelos tomográficos obtenidos a partir de las primeras llegadas de P y S: Zollo et al. (1998) para el volcán Vesubio, Aloisi et al. (2002) para el volcán Etna, Zandomeneghi et al. (2008) para las Islas Azores, Zandomeneghi et al. (2009) para la Isla Decepción, García-Yeguas et al., (2012) para la isla de Tenerife o Díaz-Moreno et al. (2018) para el Monte Etna, entre otros muchos. Sin embargo, el parámetro de la velocidad tiene menor sensibilidad a la detección de las heterogeneidades presentes en los volcanes que otros parámetros como es la atenuación sísmica.

Así, el estudio de las propiedades de atenuación de un área concreta nos permite identificar distintos cuerpos existentes en el medio, debido a su mayor sensibilidad a la estructura interna y a la presencia de fluidos. Es por ello, que el desarrollo de los estudios de atenuación está suponiendo un gran avance en el conocimiento de la estructura interna de los volcanes, incorporando modelos más precisos y fiables.

Los primeros estudios de atenuación sísmica se basaban en la obtención de valores medios para una región de estudio. Una de las aplicaciones de un valor medio en atenuación era la diferenciación mediante este parámetro de áreas volcánicas y tectónicas (Mayeda et al., 1992; Del Pezzo et al., 1995; Sato and Fehler, 1998). Por otro lado, la obtención del valor medio también sirvió para analizar como variaba la atenuación con el tiempo para una misma región, con el objetivo de identificar precursores para terremotos significativos (Jin and Aki, 1991).

En las primeras décadas de estudio de este parámetro queda patente la utilidad de esta herramienta para caracterizar un determinado medio. Continuando con la línea evolutiva de los estudios de atenuación sísmica, los avances en la potencia de cálculo y/o el desarrollo de nuevos modelos teóricos de atenuación sísmica permitieron la separación fiable de los fenómenos de la atenuación intrínseca y *scattering* (Akinci et al., 1995; Del Pezzo et al., 2001; Hoshiba et al., 2001; Martinez-Arevalo et al., 2003; Del Pezzo et al., 2006; Giampiccolo et al., 2006; Prudencio et al., 2013a; 2013b; 2015a; 2017a; 2017b; 2018; Ibáñez et al., 2020).

En la actualidad, las investigaciones de atenuación sísmica se están centrando en determinar la estructura de atenuación en una zona de estudio. Cuando esta estructura de atenuación se representa bidimensionalmente o tridimensionalmente toma el nombre de tomografía de atenuación sísmica. En un principio, la obtención de las tomografías sísmicas en atenuación suponía un gran reto debido a la falta de modelos que explicasen adecuadamente el fenómeno atenuativo, las bases de datos incompletas en espacio y tiempo, y la falta de potencia computacional para el cálculo. Sin embargo, existen muchos ejemplos de cómo se han ido solventando estos problemas y se han obtenido modelos de tomografía atenuativa utilizando distintas técnicas. El estudio, por ejemplo, del ensanchamiento del primer pulso (Stacey et al., 1975) fue aplicado por Wu y Lees (1996) para obtener la estructura atenuativa de California, el de Bianco et al. (1999) para conocer la estructura del Vesubio o el trabajo de Martinez-Arevalo et al. (2003) para la Isla Decepción; la técnica del decaimiento de la amplitud espectral de Scherbaum (1990) fue aplicada por Martinez-Arevalo et al. (2005) para el Mt. Etna o el método de normalización de la coda desarrollado por Aki (1980; 1982), que ha sido aplicado por Del Pezzo (1995) en Granada, De Siena et al. (2009) en el Vesubio o, más recientemente, aplicado por Prudencio y Manga (2020) en Long Valley (California, EUA).

1.1.   Motivación y objetivos

Esta tesis nace de la necesidad de conocer en profundidad la estructura interna de una de las regiones de mayor interés volcanológico: Sicilia; donde encontramos el Monte Etna y las Islas Eolias. Si bien se han realizado tomografías sísmicas en las regiones de estudio en el pasado, estas han sido incompletas o no han sido resueltas con la resolución deseada. Mediante la aplicación de una metodología fiable y robusta como son el modelo de difusión y el método de normalización de la coda, se pretende avanzar en el conocimiento de la estructura interna de las Islas Eolias y el Monte Etna con un nivel de detalle no alcanzado hasta el momento.

Así, el objetivo principal de este trabajo es la obtención de modelos estructurales de volcanes activos, como las Islas Eolias y el Etna, a partir de tomografías sísmicas de

atenuación con el objetivo de contribuir a avanzar en el conocimiento estructural de las áreas bajo estudio en esta tesis.

Por tanto, los objetivos específicos para las Islas Eolias, la primera región bajo estudio, son: obtener un modelo de atenuación bidimensional y separación de las contribuciones de atenuación intrínseca y *scattering* mediante el modelo de difusión. Para la segunda región estudiada, el Monte Etna, los objetivos específicos son: alcanzar dos modelos tomográficos, una representación bidimensional con separación de efectos de *scattering* y de absorción anelástica utilizando el modelo difusión, y un segundo modelo, en este caso tridimensional, de la distribución de los valores de atenuación, a partir del método de normalización de la coda. Además, para el Monte Etna, se pretende realizar una interpretación conjunta de diferentes modelos tomográficos, tanto en velocidad como en atenuación, para avanzar en el conocimiento de su estructura interna.

2. ATENUACIÓN SÍSMICA

Como se ha mencionado anteriormente, esta tesis centra su estudio en la atenuación sísmica. La atenuación resulta un fenómeno intuitivo, es decir, cualquier persona entiende que cuanto más nos alejemos del foco emisor de un sonido determinado, este tenderá a escucharse con menor intensidad de forma general. Si incorporamos este fenómeno al campo de las ondas sísmicas, tenemos la misma situación: por regla general, cuanto más nos alejemos del epicentro de un terremoto, menor serán los efectos que sufrimos. Este fenómeno es un proceso de atenuación de las ondas elásticas y recibe el nombre de atenuación sísmica. La propagación de las ondas sísmicas se ve afectada por el medio que atraviesan, por tanto, dado que la Tierra es heterogénea y anelástica, esta afectación se traduce en una pérdida de energía: en primer lugar, por la falta de elasticidad y, en segundo lugar, por la presencia de diferentes cuerpos heterogéneos que pueden producir refracciones, reflexiones o una nueva distribución de energía por procesos de *scattering*. De esta manera, podemos agrupar todos estos fenómenos en dos tipos distintos de atenuación: los que se deben a la anelasticidad y los que se deben a la heterogeneidad. A estos habría que añadirle un tercer grupo que es el de la expansión geométrica.

2.1.   Expansión geométrica

El fenómeno de la expansión geométrica o *geometrical spreading* es un proceso geométrico por el cual la energía de las ondas sísmicas transmitidas desde una fuente, al atravesar un medio elástico, homogéneo e isótropo, debe mantenerse. Esto supondrá que cuanto mayor es la distancia recorrida por el frente de ondas, la energía por unidad de volumen disminuirá y, consecuentemente, la amplitud del movimiento oscilatorio. Como vemos en la Figura 1, conforme la onda atraviesa un medio, el frente de onda aumenta su superficie y la energía contenida en un punto del frente de onda (P2) es menor que en el frente de onda en un momento de tiempo anterior (P1). En este caso no podemos hablar de pérdida de energía, si no de pérdida aparente de energía, puesto que la energía total de la onda sigue siendo constante.
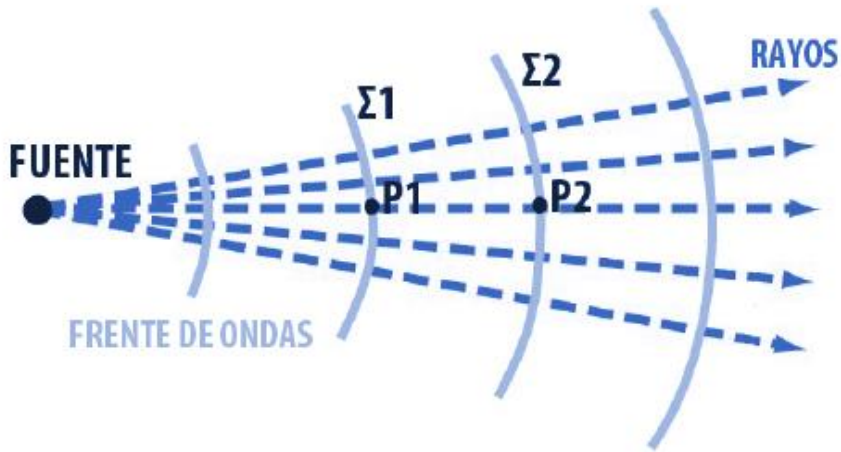
Figura 1. La fuente emite ondas circulares (Σ1 y Σ2), la energía que posee en cada frente de ondas es la misma, sin embargo, la energía contenida en el punto P2 es menor que en el punto P1 (Tipler and Mosca, 2005).

Un ejemplo de expansión geométrica consistiría en soplar a través de un tubo con forma de cono. Podríamos observar que según si soplamos en un extremo u otro el aire saldrá con más o menos fuerza. En este caso, el aire saldrá con mayor fuerza al soplar por el extremo de mayor radio. Esto es debido a que cuando ejecutamos la acción de soplar estamos generando ondas de presión que, si se distribuyen en volúmenes mayores, la onda de presión en un punto determinado contiene menor energía que si esa onda se distribuye en volúmenes más pequeños. Otro ejemplo clásico de expansión geométrica consiste en lanzar una piedra a un volumen de agua en reposo, esto generará ondas y se podrá observar cómo las ondas internas tendrán una mayor altura en la columna de agua que las ondas en las zonas exteriores.

Considerando la Tierra como homogénea e isótropa y que el avance de las ondas sísmicas se realiza en un medio tridimensional, los frentes de ondas son superficies esféricas con un radio igual a la distancia hipocentral: *d=v·t*, siendo *v* y *t,* la velocidad y el tiempo, respectivamente, de la propagación de la onda sísmica. Por consiguiente, la pérdida de energía para ondas superficiales es proporcional a:

$$E(t) \propto t^{-1} \tag{1.1}$$

Y en el caso de las ondas internas, P y S:

$$E(t) \propto t^{-2} \tag{1.2}$$

Para un medio heterogéneo, la energía estará en función del tiempo de propagación:

$$E(t) \propto t^{-n} \tag{1.3}$$

A partir de aquí se han de considerar los efectos que tiene la expansión geométrica $G(t)$ (siendo t el tiempo de propagación del frente de onda) sobre la amplitud de onda y no sobre la energía. Esto es debido a nuestra incapacidad de medir directamente la energía. Si asumimos que la Tierra es un medio homogéneo y que dispone de una relación lineal entre el esfuerzo y la deformación, la energía será proporcional al cuadrado de la amplitud ($A \sim E^{1/2}$) (Martinez-Arevalo, 2015). Por tanto, si definimos la función geométrica para las ondas superficiales:

$$G(t) \propto \frac{1}{t^{0,5}} \tag{1.4}$$

Y para las ondas internas:

$$G(t) \propto \frac{1}{t^1} \tag{1.5}$$

De esta manera, se obtiene una ley de proporcionalidad entre $G(t)$ y el tiempo de propagación en el caso de un medio homogéneo, isótropo y una fuente puntual. Se puede comprobar que utilizando estudios de refracción sísmica en medios no homogéneos el exponente n de la función expansión geométrica es sensible a la estructura de velocidad de la corteza y mayor cuanto más heterogéneo es el medio (Banda et al., 1982). El exponente n para las ondas superficiales e internas es distinto, siendo 0.5 y 1, respectivamente (Frankel et al., 1990; Ibáñez et al., 1993; Akinci et al., 1995). A pesar de esto, cuando no se conoce la estructura de velocidad de la zona de estudio y a causa de la complejidad para distinguir la expansión geométrica de la atenuación, se considera que la Tierra es un medio homogéneo. Así, los índices de expansión geométrica son 0.5 para ondas superficiales y 1 para ondas internas, y se añaden los efectos de la heterogeneidad de la expansión geométrica en el término que describe los efectos de atenuación.

2.2. Absorción anelástica o atenuación intrínseca

La absorción anelástica o atenuación intrínseca es un fenómeno por el cual la amplitud de las ondas sísmicas es atenuada en función de la distancia a causa de efectos no elásticos. De esta manera, el medio absorbe la energía elástica en forma de calor a causa de la fricción (Anderson and Archambeau, 1964). Es una propiedad intrínseca del medio de propagación y depende de sus características tectónicas y geológicas.

Un ejemplo intuitivo de la atenuación intrínseca es el propuesto por Tipler (1999) sobre la disminución de la amplitud de la oscilación con el tiempo de un péndulo simple (Figura 2). La disminución viene acontecida a causa de que una proporción de la energía de oscilación del péndulo es empleada para superar la fuerza de rozamiento con el aire. Es decir, el péndulo simple en su posición A se encuentra en posición de equilibrio, al desplazarlo un ángulo δ lo situamos en su posición B. Si lo soltamos comenzará a oscilar hasta B'. Con el paso del tiempo, la amplitud de la oscilación del péndulo irá disminuyendo hasta alcanzar de nuevo la posición de equilibrio A. El péndulo utiliza su energía cinética y potencial para realizar un trabajo que supere la fuerza de rozamiento del aire y esto hace que pierda energía y se produzca la disminución de la amplitud de la oscilación.
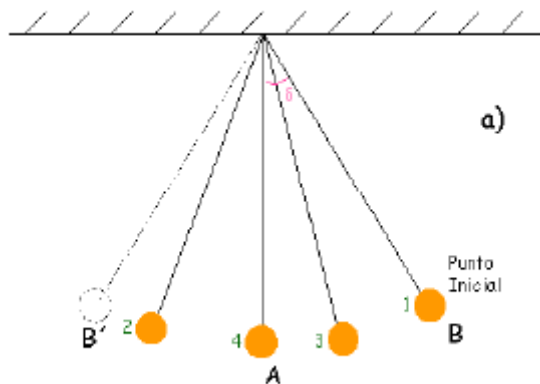
Figura 2: Esquema del movimiento oscilatorio del péndulo simple, el péndulo se encuentra en posición de equilibrio en su posición A, al desplazar un ángulo δ lo situamos en posición B y empieza a oscilar. Si no existiera absorción inelástica el péndulo se movería de manera indefinida entre B y B' (Tipler, 1999)

Otra manera de explicar la absorción de la energía es mediante la propagación de una perturbación. Este fenómeno podemos ilustrarlo con una cuerda que está unida en un extremo a la pared y la agitamos desde el otro. La deformación que habremos creado se moverá a lo largo de toda la cuerda hasta el extremo unido a la pared generando un pulso de onda que se desplazará a través de la cuerda como se aprecia en la Figura 3. Conforme aumente el tiempo desde el origen, irá disminuyendo la amplitud y aumentará la duración de la onda a causa de que parte de la energía se utiliza en superar la inercia de la cuerda a la propagación de la deformación (Tipler, 1999)
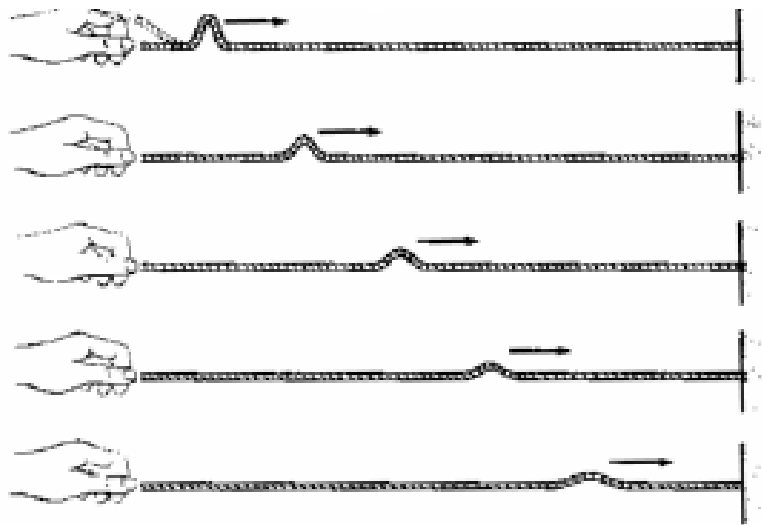
Figura 3. Pulso de onda donde se observa que al aumentar el tiempo desde el origen irá disminuyendo la amplitud y aumentará la duración de la onda (Tipler, 1999)

Aplicado este fenómeno a las ondas sísmica y al medio de propagación, los mecanismos de fricción interna que dan origen a la absorción anelástica todavía no son conocidos en profundidad debido a su elevada complejidad. Sin embargo, en la práctica, la atenuación intrínseca es la principal responsable de que este tipo de ondas tengan una amplitud menor de la que se espera en función de la teoría de la elasticidad, ya que esta solo considera los efectos de frontera (reflexión, refracción, etc.) y la expansión geométrica.

Siguiendo a Prudencio (2013), podemos añadir al tratamiento teórico el efecto de la anelasticidad terrestre mediante dos posibilidades: modificando las ecuaciones de la elastodinámica, como por ej. la ecuación de Navier-Stokes, con el objetivo de introducir un nuevo término empírico o considerando el carácter anelástico de la Tierra. Esta última opción, a pesar de que pueda parecer más apropiada, supone grandes dificultades para su desarrollo teórico, por lo que la primera opción es la más utilizada en la actualidad. De esta manera, consideramos la velocidad de propagación de la onda (v) o el número de onda (k) como un número complejo (Aki and Richards, 1980), esto supone incluir un término exponencial con la distancia hipocentral que representa la atenuación intrínseca conocido como término de atenuación ($e^{-\gamma R}$).

2.3.   Scattering

Otro fenómeno atenuativo que sufre una onda sísmica es el que produce la anisotropía y la falta de homogeneidad de la Tierra, y recibe el nombre de *scattering*. Como Sato y Fehler (1998) indican, la litosfera es un medio altamente heterogéneo y la existencia de heterogeneidades a distintas escalas (de decenas de metros a cientos de kilómetros) produce, por el Principio de Huygens, un efecto en la propagación de las ondas. Este principio establece que cuando una onda interacciona con una heterogeneidad, genera un foco de ondas secundarias con foco en la heterogeneidad y con la misma velocidad de propagación y frecuencia que la onda original. Por tanto, las heterogeneidades en el medio de propagación originan una redistribución de la energía tanto en tiempo como en el espacio al cambiar la propagación de las ondas y/o cambios de fase. Conocer la aportación de *scattering* supone conocer la mayor o menor heterogeneidad del medio de propagación.

Un concepto importante a la hora de hablar de *scattering* es la longitud de onda (λ). La relación de este término con el tamaño de la heterogeneidad (a) determinará distintos fenómenos en función del tipo de interacción, como observamos en la Figura 4:

- $\lambda >> a$: Al ser la longitud de onda mayor que la dimensión de la heterogeneidad esta no es detectada y la probabilidad de *scattering* es muy reducida.
- $\lambda << a$: La longitud de onda es menor que el tamaño de la heterogeneidad por lo que estos se muestran como límites de diferentes capas y el mecanismo fundamental es la reflexión y/o refracción de las ondas.
- $\lambda \sim a$: El *scattering* es el fenómeno que produce la principal pérdida de energía.
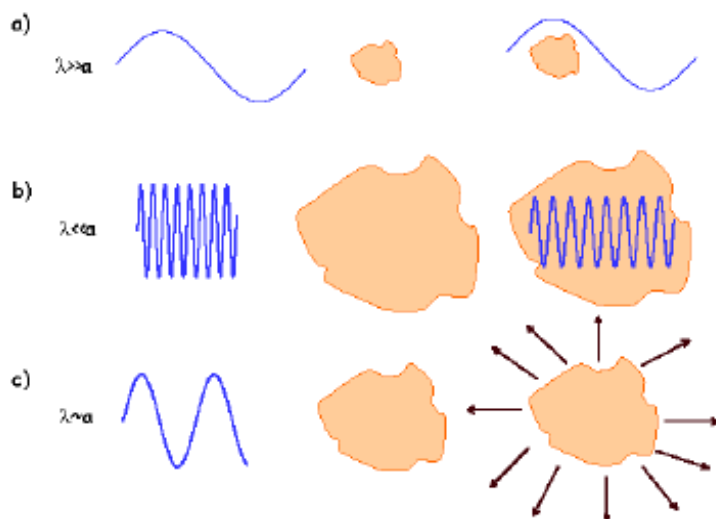
Figura 4. Relación entre la longitud de onda (λ) y el tamaño de la heterogeneidad (a). En a) la longitud de onda es mayor que la dimensión de la heterogeneidad por lo que no es detectada. b) la longitud de onda es menor que el tamaño de la heterogeneidad y esta es considerada como un medio con velocidad de propagación diferente. c) las dimensiones son adecuadas para el proceso de *scattering* (Herraiz y Espinosa, 1987)

En función de la dirección que tome las ondas de scattering con respecto a la onda incidente podemos clasificar el *scattering* en:

- *Forward-scattering*: la mayor parte de la energía de las ondas secundarias mantiene la dirección de la onda incidente.
- *Back-scattering*: la mayor parte de la energía de las ondas de scattering toma la dirección opuesta de la onda incidente.

29

Otra manera de clasificar el scattering es en función de la relación existente entre la pérdida de energía por *scattering* y la energía que incide en la heterogeneidad:

- *Scattering* fuerte: se tiene una alta pérdida de energía en relación a la que posee la onda incipiente.

$$\frac{\Delta E_S}{E_{incid}} \approx 1 \tag{1.6}$$

- *Scattering* débil: ocurre el fenómeno opuesto que en el caso anterior, se produce una pequeña pérdida de energía.

$$\frac{\Delta E_S}{E_{incid}} << 1 \tag{1.7}$$

En los casos prácticos, lo habitual es encontrar un proceso mixto que se sitúe entre los casos extremos y se produzca un proceso de *scattering* múltiple, es decir, cada heterogeneidad interactúa, además de con la onda que incide desde la fuente, con ondas secundarias producidas por otras heterogeneidades.

Por tanto, podemos definir el *scattering,* no como un proceso que disipe energía como sí ocurría en la atenuación intrínseca, si no como un fenómeno de redistribución de la energía.

2.4.   Factor de calidad

El parámetro más utilizado para el estudio de la atenuación sísmica es el factor de calidad (Q). Este indica la relación existente entre la energía total almacenada (*E*) y la energía disipada por fenómenos de absorción anelástica (*ΔE*), para un mismo volumen de material, sometido cíclicamente a un esfuerzo elástico en un ciclo de excitación armónica:

$$\frac{1}{Q(f)} = -\frac{\Delta E}{2\pi E} \qquad (1.8)$$

Una consideración importante que hay que hacer a la hora de determinar Q es que el cálculo depende de la onda con la que trabajamos, no solo del método. Esto se tendrá que tener en cuenta para correlacionar los valores de Q con otros estudios, dependiendo si es un análisis de ondas P (Q_α), ondas S (Q_β), ondas Lg (Q_{Lg}) u ondas de coda (Q_c).

En el término de atenuación sísmica, representado por el factor de calidad (Q) se incluyen los efectos de la atenuación intrínseca (Q_i) y los de la atenuación por *scattering* (Q_s). Este último, aunque es una redistribución de la energía, también contribuye a la pérdida de energía del factor de calidad. Podemos deducir que en el caso de encontrarnos en un medio homogéneo y que el *scattering* no contribuyese o su contribución fuera cercana a 0, el factor de calidad Q solo se debería a la anelasticidad del medio. Esta situación no es la que nos encontraríamos en la práctica; en la Tierra lo más común es que tanto la atenuación intrínseca como la de *scattering* contribuyan de manera simultánea y conjunta a Q. Por tanto, dado que la absorción anelástica está caracterizada por su factor de calidad Q_i y el factor de calidad Q_s caracteriza a la atenuación por *scattering*, la fórmula en la que se relacionan con el factor de calidad Q (Dainty and Toksöz, 1981) incluirá los distintos fenómenos y se podrá determinar de manera experimental:

$$\frac{1}{Q(f)} = \frac{1}{Q_i(f)} + \frac{1}{Q_s(f)} \qquad (1.9)$$

En los entornos volcánicos, debido a que son medios muy heterogéneos, el factor de calidad de atenuación por *scattering* (Q_s) domina con respecto al factor de calidad de atenuación intrínseca (Q_i). La atenuación por scattering domina a la atenuación intrínseca en los entornos volcánicos, esto ha sido corroborado por múltiples estudios como Wegler y Lühr (2001) en el volcán Merapi, Wegler (2003) al obtener que el camino libre medio en el Vesubio ($l_{tr} \approx 200m$) era un orden de magnitud menor que la escala de longitud de atenuación intrínseca ($l_i = 2{,}3 - 10km$) o Prudencio et al. (2017a) en el volcán Asama. En la Figura 5 es posible observar cómo varía el factor de calidad de la absorción anelástica o atenuación intrínseca (Q_i) para diferentes regiones volcánicas y a distintas

frecuencias. Se aprecia un aumento de Q_i al incrementarse la frecuencia de análisis. Por otro lado, en la Figura 6 vemos cómo cambia, pero en este caso con respecto al factor de calidad del *scattering* (Q_s).
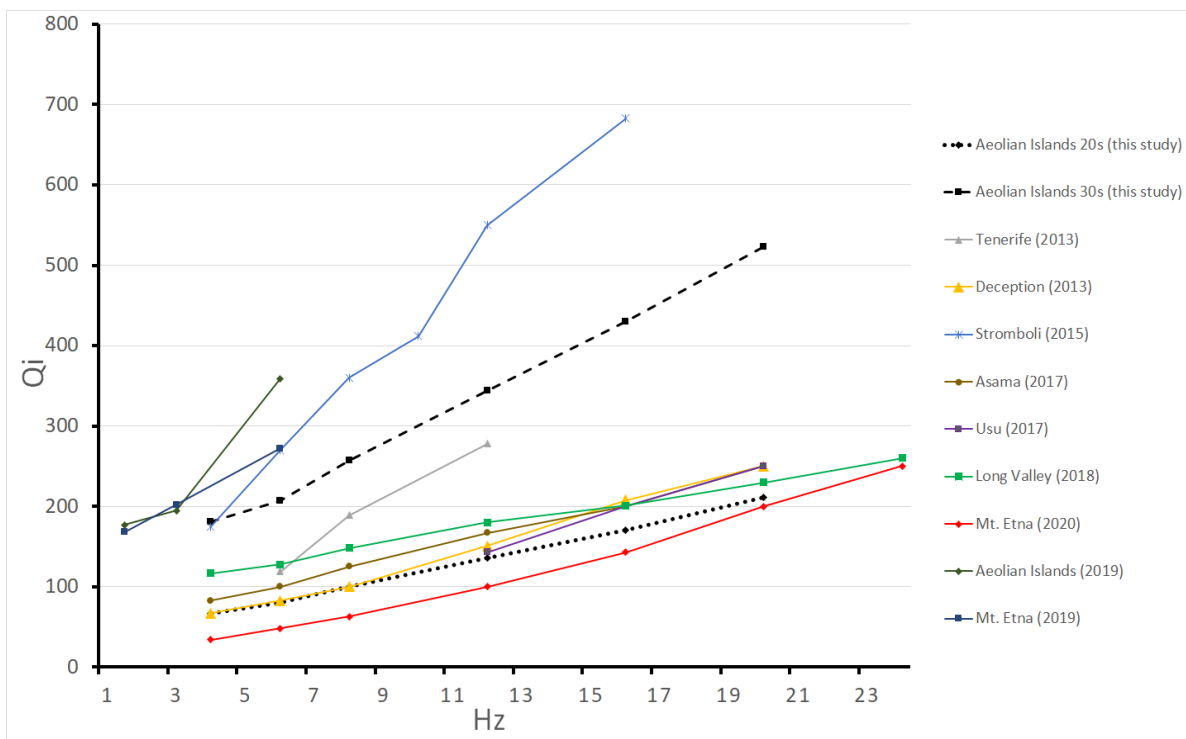
Figura 5. Factor de calidad de la absorción anelástica o atenuación intrínseca (Q_i) para diferentes regiones volcánicas (Castro-Melgar et al., 2021a)
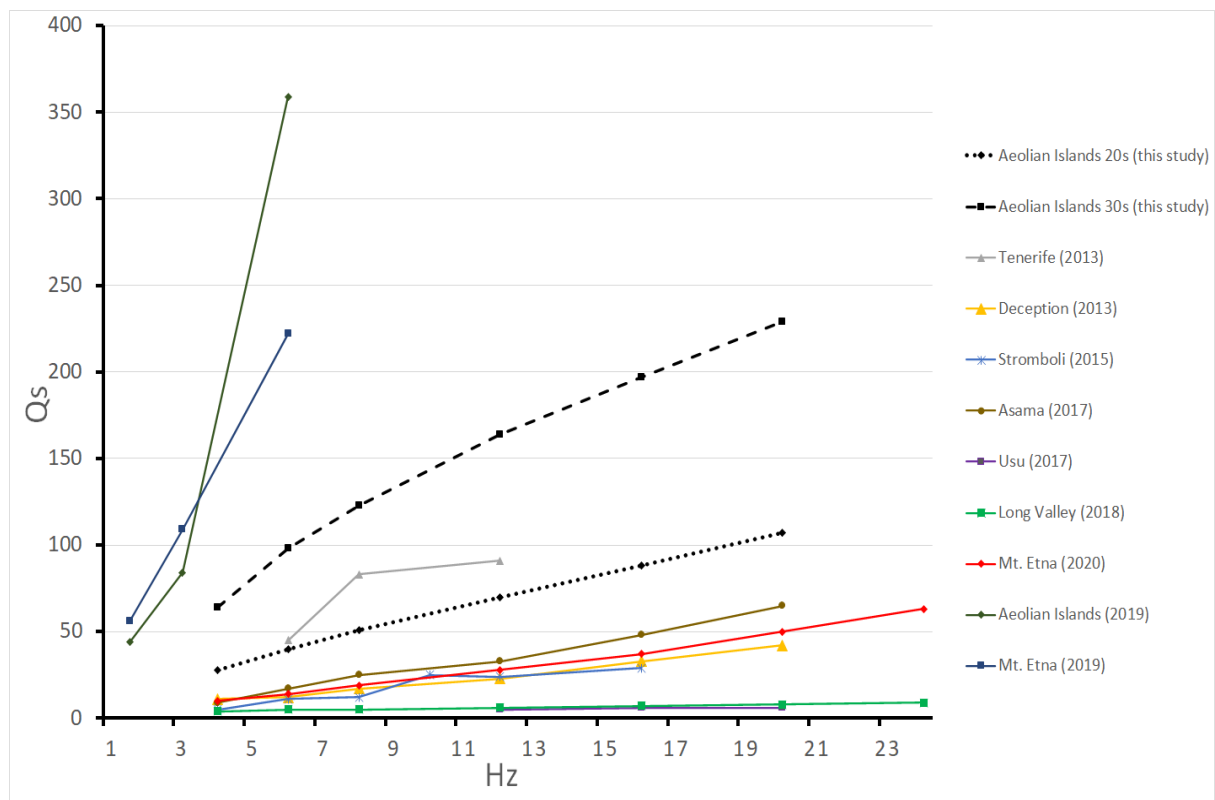
Figura 6. Factor de calidad de la atenuación por *scattering* (Q_s) para diferentes regiones volcánicas (Castro-Melgar et al., 2021a)

3. REGIONES DE ESTUDIO

Como se ha mencionado anteriormente las regiones de estudio de esta tesis son el Mt. Etna y las Islas Eolias y se encuadran en un marco geodinámico complejo, como se puede apreciar en la figura 7. Sicilia es una gran isla mediterránea formada a partir de la colisión de las placas euroasiática y africana durante la subducción de la losa africana con inversión hacia el oeste desde finales del Oligoceno. Está compuesta por cinco unidades tectónicas: 1) la unidad de la cadena Apenino-Magrebí (color amarillo en figura 7), que ocupa la mayor parte de Sicilia, cubriendo toda la zona central de norte a sur; 2) las unidades del sistema de empuje externo están emplazadas en la zona más occidental de la isla (color verde claro en figura 7); 3) las unidades de *foreland* en el sur de la isla (color verde, figura 7); 4) en la zona noreste de la isla conectando con la península itálica dominan las unidades de cadena Kabilo-Calábrita (color morado en figura 7) y, por último, 5) las regiones de estudio de esta tesis que aparecen en color rojo en la figura 7 y han sido identificadas como volcanes cuaternarios y sometidas a esfuerzos por líneas de fallas importantes.

El volcanismo de la región está fuertemente relacionado con el sistema de subducción que se encuentra en Sicilia, dado que el retroceso de la placa africana origina una región de baja presión en el manto, debajo de la zona de Calabria. Esto origina a su vez un ascenso del material astenosférico debajo de la placa africana lateralmente hacia el noreste, originando un gran volumen de magma, que dio lugar al vulcanismo presente en la región (Gvirtzman and Nur, 1999), como se puede apreciar en la figura 8

El Monte Etna es un estratovolcán activo localizado en la región oriental de Sicilia. La formación del volcán comenzó hace aproximadamente 0.5 millones de años, a partir de vulcanismo submarino en las profundidades de Gela, formándose *pillow* lavas de composición toleítica. Estas primeras lavas evolucionaron hace 0.3 Ma hacía una meseta de lava toleítica a partir de erupciones fisurales en una antigua llanura aluvial. Posteriormente, el vulcanismo evolucionó hasta formar un volcán de escudo hace 0.22 Ma, con una longitud de 15 Km en dirección N-S, esta dinámica se desplazó hacia el oeste, emplazándose hace unos 129 mil años en la localización que actualmente tiene (Branca et al., 2008).
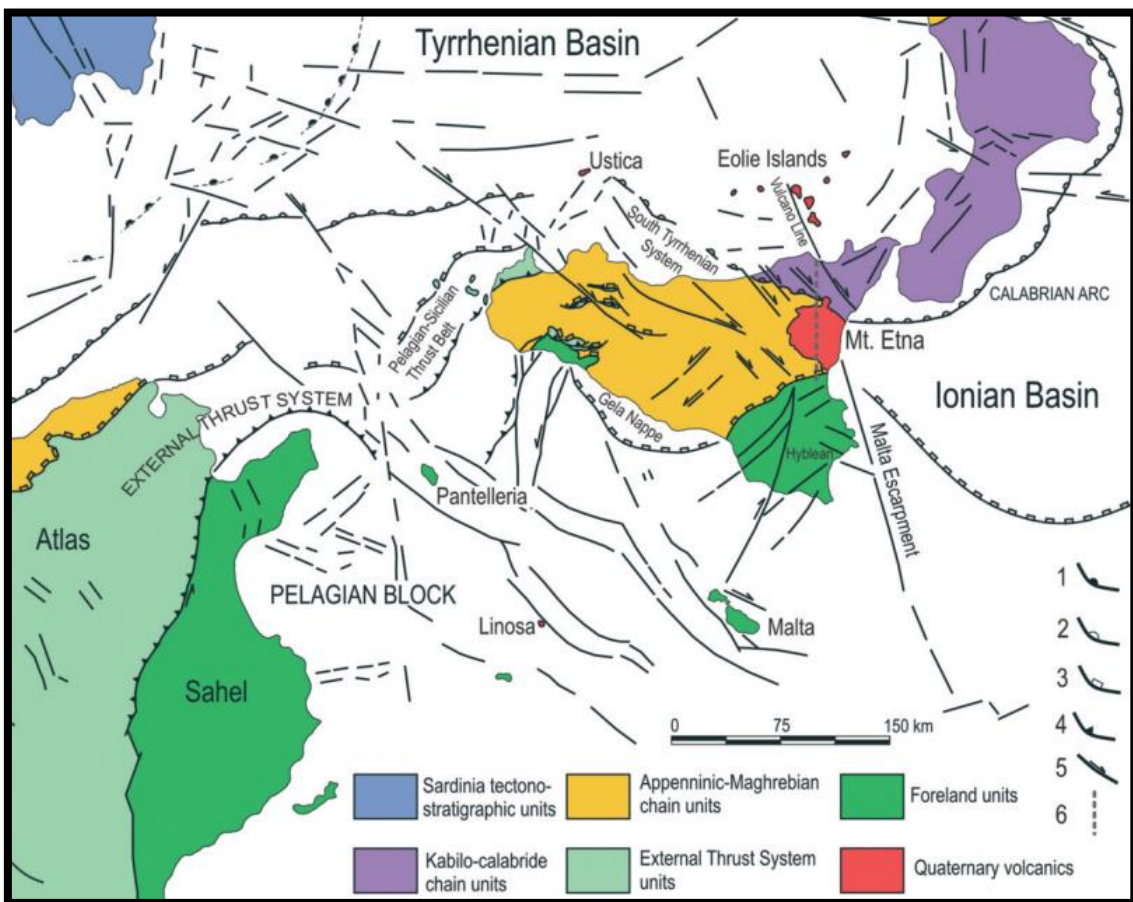
Figura 7. Marco estructural de la isla de Sicilia. (Modificado de Branca et al., 2011)

En las proximidades del Monte Etna se encuentran 3 estructuras regionales que lo rodean: al norte y al oeste se sitúa la cadena apenino-magrebí, en la parte sur se encuentra la meseta de Hyblean, que pertenece a la placa africana (Lentini et al., 2006) y al este se sitúa la cuenca extensional del Jónico del Mesozoico medio-tardío (Catalano et al., 2001). Este límite de colisión induce una compresión regional N-S combinada con una extensión E-W, relacionada con el escarpe de Malta (Bousquet y Lanzafame, 2004). Este régimen extensional se ubica en la parte oriental del volcán. Además, en el sector occidental, nos encontramos con un dominio de compresión regional en relación con la colisión de las placas euroasiática y africana (Monaco et al., 2005). Este complejo marco geodinámico hace que la discontinuidad de la Moho varíe entre una profundidad máxima de 30 kilómetros debajo de la meseta de Hyblean hasta una profundidad más superficial a 18 kilómetros en la cuenca Jónica (Nicolich et al., 2000). Distintos autores apuntan a que la ubicación del Monte Etna, según la descripción regional, no se ajusta al magmatismo

típico de una región de arco o al de una expansión de arco posterior asociada con la subducción de los Apeninos, ya que no posee las características identificativas de una región u otra (Doglioni et al., 2001; Patanè et al., 2011).
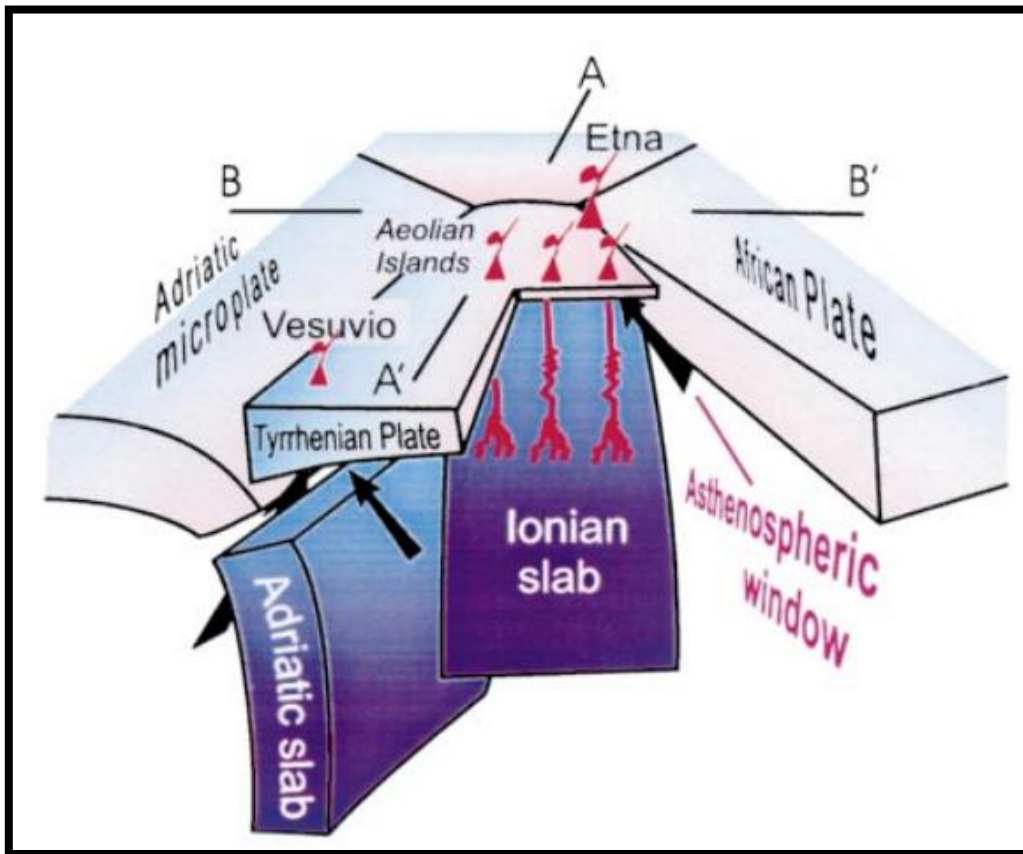
Figura 8. Esquema tridimensional de la zona de subducción del sur del Tirreno. (Modificado de Gvirtzman and Nur, 1999)

Las islas Eolias se sitúan en el Mar Tirreno meridional, donde, desde un punto de vista geodinámico, coexisten dos zonas de alto contraste tectónico. Por una parte, existen zonas extensionales como, por ejemplo, las cuencas de Vavilov y Marsili, y por otra, regiones comprensivas como el arco Calabro-Peloritano. Existe también una migración hacia el este de un campo de tensión extensional desde el margen sardo hasta la cuenca de Marsili (Ferrari and Manetti, 1993). La actividad volcánica está relacionada con la zona de subducción Calabro-Jónica que ha sufrido el mismo proceso de migración hacia el este (Savelli, 1988). El vulcanismo ocurrió durante las principales fases de formación de la cuenca en la parte posterior del arco. La migración del arco y la extensión del arco posterior relacionado es impulsada por el hundimiento gravitacional de la losa

descende que se inició en el sitio de un antiguo cinturón orogénico. (Ferrati and Manetti,1988)

3.1.   Islas Eolias

El archipiélago de las Islas Eolias se encuentra situado al sur de Italia (Figura 9) y es una estructura volcánica de unos 200 kilómetros de longitud. Está situado en el margen interior de un cinturón herciniano (Arco Calabro-Peloritano), afectado en el cuaternario superior por un levantamiento y una tectónica extensional. La estructura del cinturón Calabro-Peloritano consiste en un apilamiento de capas compuestas de rocas metamórficas y rocas graníticas prealpinas, rocas sedimentarias del Mesozoico al Terciario, secuencias ofiolíticas y sedimentos cuaternarios (Díaz-Moreno, 2016). El basamento del arco Calabro-Peloritano se extiende desde el norte por la región de Calabria hasta el este de la isla de Sicilia y conecta el sur de los Apeninos y la cadena siciliano-Magrebí. Es delimitado al norte por la línea tectónica de Sangineto y al sur por el sistema de fallas Tindari-Letojanni-Malta.

Las siete islas que forman el archipiélago de las Islas Eolias (Alicudi, Filicudi, Salina, Lipari, Vulcano, Panarea y Stromboli) son edificios volcánicos que han alcanzado el nivel del mar. Se emplazan sobre una corteza continental de entre 15 a 20 kilómetros de espesor, y sus productos tienen edades comprendidas entre los 1,3 Ma. y el presente, siendo Alicudi y Filicudi las islas más antiguas que se formaron hace aproximadamente 1 Ma. Actualmente la actividad volcánica se encuentra situada en las islas de Stromboli y Vulcano. La peculiaridad del vulcanismo de las Islas Eolias es la superposición espacio-temporal de productos con diferentes afinidades magmáticas a lo largo de todo el arco volcánico (Beccaluva et al.,1985). Para muchos autores el origen del vulcanismo actual en el archipiélago eólico está relacionado con un modelo de subducción pasiva de una laja litosférica (Barberi et al., 1973; Malinverno and Ryan, 1986; Patacca and Scandone, 1989) buzándose a lo largo de un plano de Benioff orientado al ONO, que representan los restos de la subducción del Oligo-Mioceno (Scandone, 1979). La subducción cuasi-vertical de la laja subducida explicaría la producción de magmas con diferentes afinidades magmáticas a diferentes profundidades y su localización en el mismo punto.
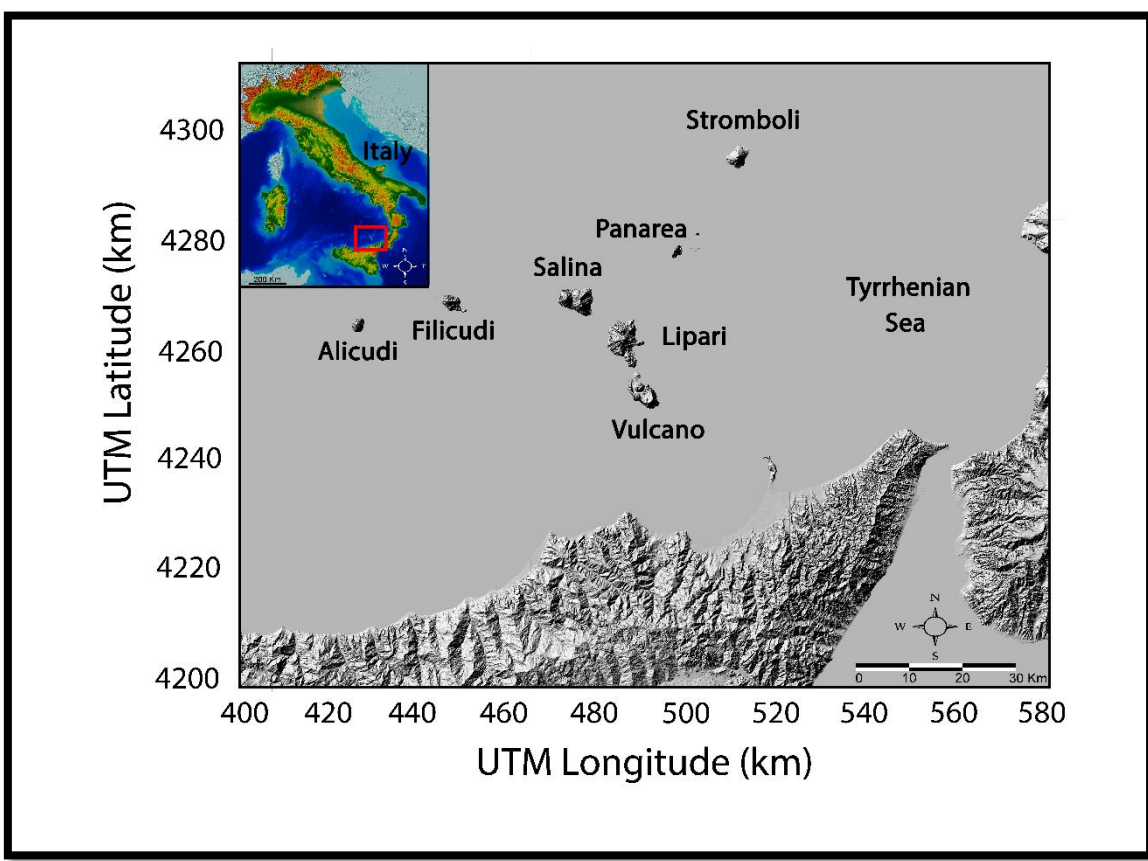
Figura 9. Localización de las Islas Eolias (Modificado de Castro-Melgar et al., 2021a)

La estructura del archipiélago Eólico ha sido investigada en las últimas décadas a través de tomografías sísmicas con datos provenientes de terremotos y sísmica activa de alta resolución. Uno de los primeros artículos sobre estructura interna del volcán de Stromboli fue el trabajo realizado por Chouet et al. (1998) donde presenta un modelo del interior de la isla obtenido a partir del estudio del tremor, donde destacan anomalías de baja velocidad consistentes con cuerpos basálticos solidificados. Chiarabba et al. (2004) realizan un estudio de la estructura interna de la isla de Vulcano mediante una tomografía sísmica de los 2 primeros kilómetros de profundidad con terremotos locales. Como resultados obtienen que los reservorios magmáticos someros están alineados con dirección NO-SE y controlados por fallas normales N-S. Castellano et al. (2008) llevaron a cabo un experimento de sísmica activa alrededor de la isla de Stromboli con el objetivo avanzar en el conocimiento que se tenía hasta el momento de la estructura interna de la isla, que se limitaba a unos pocos cientos de metros.

Ese mismo año, Chiarabba et al. (2008) presentan un modelo tomográfico en velocidad para la zona de subducción del sur del Mar Tirreno, obtenida a partir de la inversión de los tiempos de llegada de las ondas P y S. Para ello, utilizarían una base de datos recopilada durante 15 años. Los autores obtienen distintas estructuras de baja y alta velocidad de ondas P en forma de arco entre los 25 y 100 km de profundidad; mientras que para las profundidades de entre 100 y 300 kilómetros, encontraron dos zonas de alta velocidad que se localizan bajo la región de Nápoles y el Tirreno sur.

La base de datos obtenida durante el experimento llevado a cabo por Castellano et al. (2008) permitió que años más tarde dos investigaciones se llevasen a cabo. En primer lugar, Prudencio et al. (2015a) realizaron una tomografía de atenuación bidimensional para la isla de Stromboli. Para ello, los autores analizaron alrededor de 22.000 formas de onda generadas por disparos de aire comprimido y registrados en 33 estaciones sísmicas y 10 OBS (*Ocean Bottom Seismometer*). Los principales resultados mostraron cómo la atenuación por *scattering* prevalece sobre la atenuación intrínseca, compatible con un área altamente heterogénea y, además, identificaron una anomalía de alta atenuación localizada en la parte de mayor actividad volcánica. Posteriormente, Patanè et al. (2017), utilizando la misma base de datos generada durante el experimento de Castellano et al. (2008) y 269 eventos locales, obtienen nuevas imágenes tomográficas de velocidad V_p, V_s y la razón V_p/V_s de Stromboli. El principal resultado obtenido propuesto por los autores es la localización de una cámara magmática superficial localizada a poca profundidad (2-4 km bajo el nivel del mar) y caracterizada por dos cuerpos anómalos de baja razón V_p/V_s.

Díaz-Moreno et al. (2018) obtuvieron un nuevo modelo tomográfico en velocidad con la base de datos generada durante el experimento TOMO-ETNA (Ibáñez et al., 2016a; 2016b; Coltelli et al., 2016). En sus resultados, destacan una fuerte anomalía de baja velocidad localizada entre Stromboli y Panarea que la literatura previa propone como un volumen significativo de manto parcialmente fundido que nutre la actividad volcánica de las Islas Eolias (Figura 10).
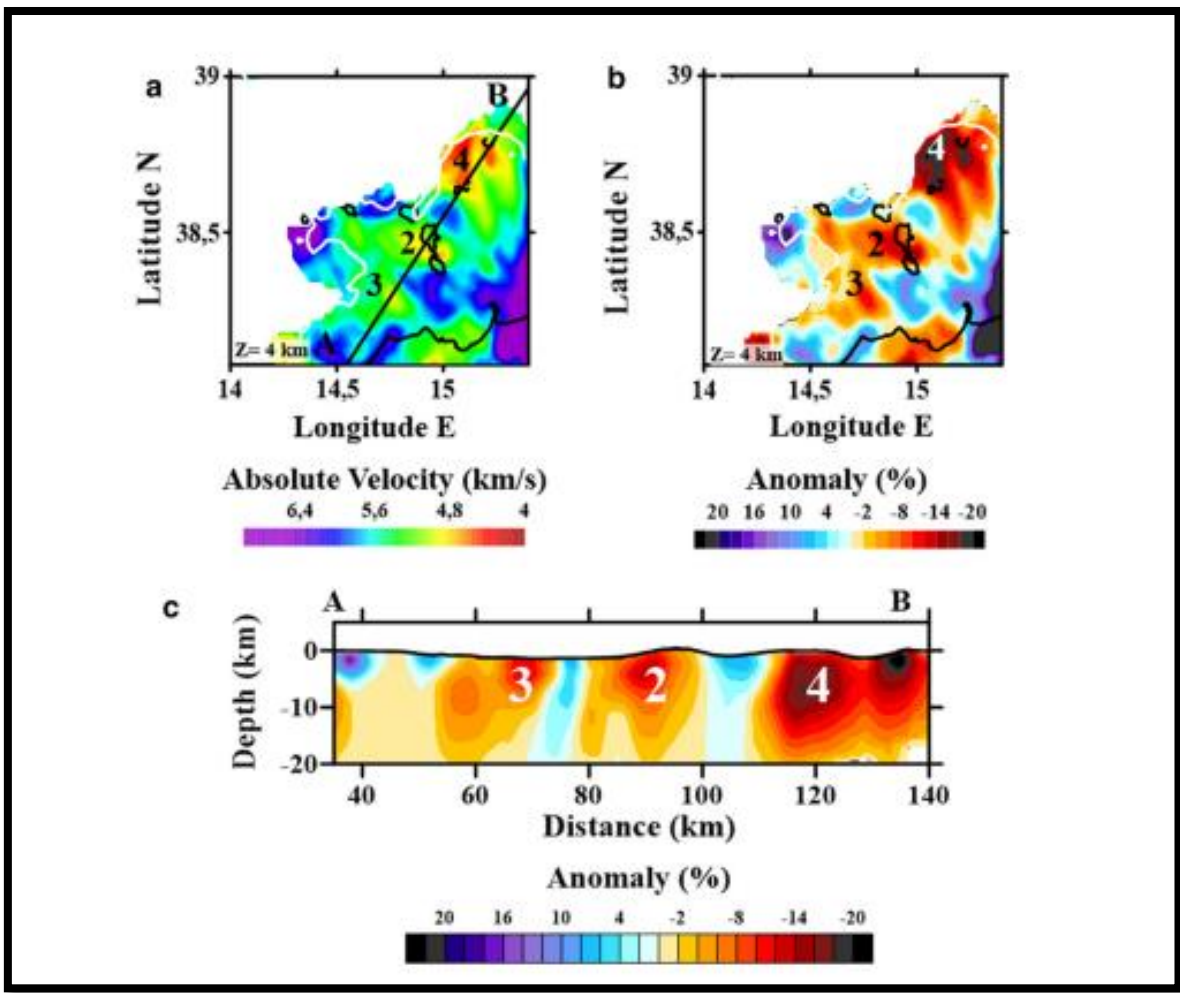
Figura 10. a) Velocidad absoluta de la onda P para el área de las Islas Eolias. b) Anomalías de velocidad de la onda P para la misma región. c) Sección vertical A-B con las anomalías de velocidad de la onda P (Díaz-Moreno et al., 2018)

3.2.   Monte Etna

El volcán Etna, considerado uno de los más activos del mundo, está situado en la costa este de Sicilia (Italia). Alcanza una altura de 3357 metros y tiene un perímetro de aproximadamente 140 kilómetros (Chester et al., 1985). El Monte Etna es un estratovolcán que presenta varios cráteres activos. Actualmente, hay 5 cráteres principales activos que son: Voragine (VOR), Bocca Nuova (BN), North East Crater (NEC), South East Crater (SEC) y New South East Crater (NSEC) (Figura 11). En los últimos 60 años la frecuencia eruptiva del Monte Etna ha sido muy alta. Se han intercalado periodos donde se han dado episodios explosivos intensos, pero de corta duración, junto con otros

40

episodios de duración más prolongada. Desde 1970 y hasta principios del siglo XX Behncke y Neri (2003) individualizaron 200 episodios eruptivos. Por tanto, la actividad eruptiva del volcán es habitual y caracterizada por desgasificaciones de volátiles, explosiones, fuentes de lava y flujos de lava. Estos últimos tienen lugar en el Valle del Bove, una amplia depresión localizada en el flanco este del volcán (Doglioni et al., 2001). De esta manera, la actividad presente puede ser clasificada en dos tipos principales (Díaz-Moreno, 2016):

- Desgasificación prácticamente continua con actividad estromboliana ocasional, que suele producirse en los cráteres de la cumbre. Este tipo de dinámica eruptiva puede ser combinada al mismo tiempo con erupciones hidromagmáticas y estrombolianas, junto a flujos y fuentes de lava.
- Erupciones en los flancos. Erupciones de tipo efusivo a través de la apertura de nuevas fisuras (Cristofilini, et al., 1988).

La primera red sísmica que se instaló en el Monte Etna data de mediados de los años 70, aunque una de las primeras investigaciones se realizó en la década de los 60 cuando Cassinis et al. (1969) estudiaron la estructura interior de la isla de Sicilia y una parte del área de estudio involucraba al Mt. Etna. A partir de la realización de perfiles de refracción, identificaron una anomalía de baja velocidad a 9-24 km de profundidad. Posteriormente, se llevó a cabo un experimento de sísmica pasiva en 1977, en el que se instalaron alrededor del volcán un número elevado de estaciones sísmicas (de 1 y 3 componentes) (Colombi et al., 1979). La base de datos proporcionada por el experimento de sísmica pasiva fue utilizada por Sharp et al., (1980) para crear una base de datos de tiempos de llegada de ondas P y S a partir de terremotos regionales y telesismos, lo que permitió a los investigadores obtener la primera tomografía sísmica de velocidad del volcán (figura 12). Como resultado más relevante cabe destacar la identificación de una gran anomalía de baja velocidad situada a unos 20 km de profundidad que los autores interpretaron como una cámara magmática.
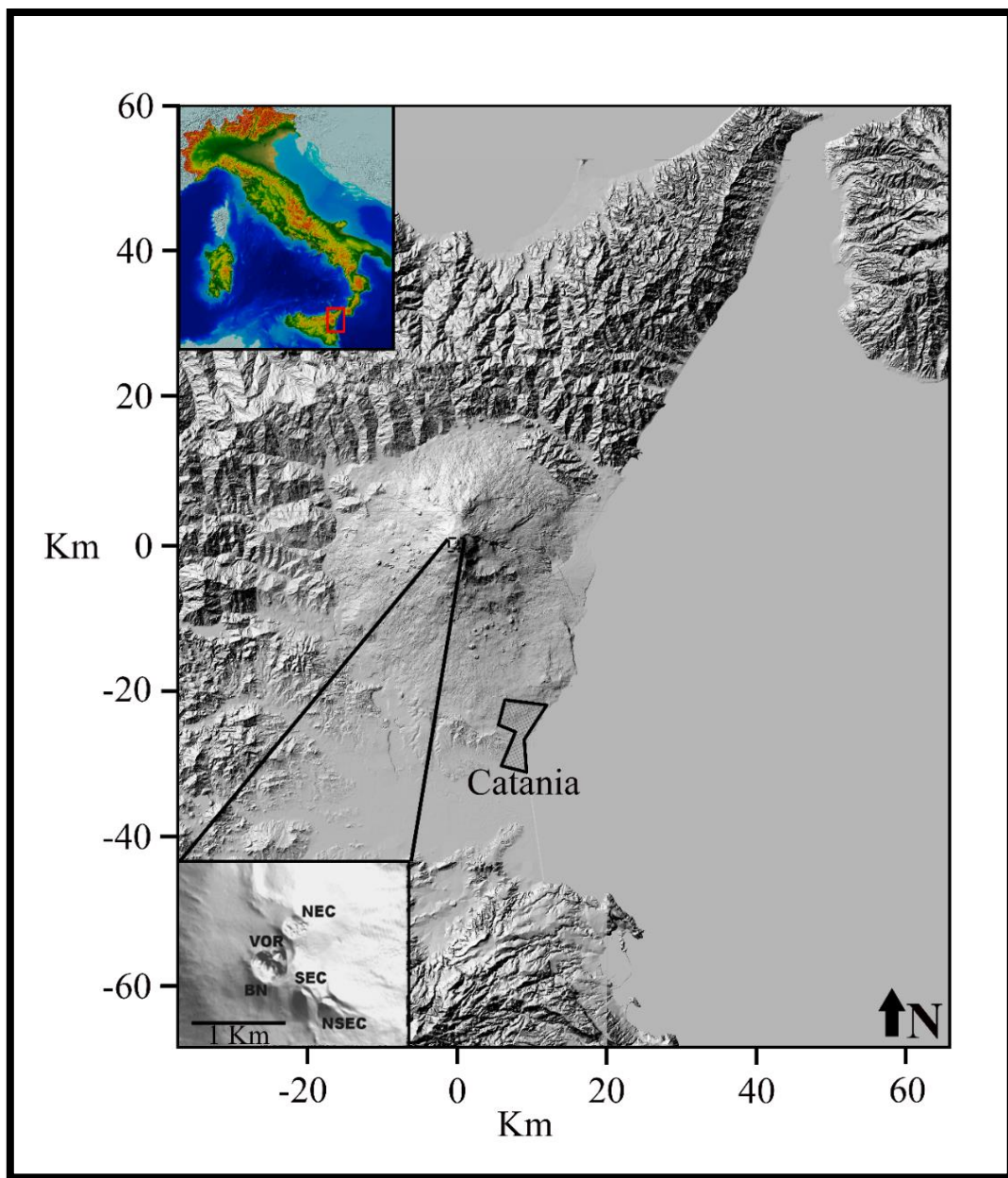
Figura 11. Localización del Mt. Etna y los 5 principales cráteres activos. (Modificado de Castro-Melgar et al., 2021b).

4 años más tarde se llevó a cabo el experimento de sísmica activa *GEOTRAVERSE EUROPEA* mediante la realización de disparos en tierra y mar para la obtención de perfiles sísmicos en toda la isla de Sicilia. Hirn et al. (1991) utilizaron la base de datos obtenida durante el experimento, que consistía en 2200 llegadas de onda P para obtener una estructura en velocidad de los primeros 6 km de profundidad. Los autores identificaron un área de alta velocidad al que llamaron *High Velocity Body* (HVB) situada en el SE del volcán. Este cuerpo de alta velocidad fue confirmado pocos años después

por Cardaci et al. (1993), a través de la inversión de 3000 llegadas de onda P. Además, estos autores situaron la cámara magmática del Etna al SO a una profundidad aproximada de 10 km a partir de la identificación de una anomalía de baja velocidad.
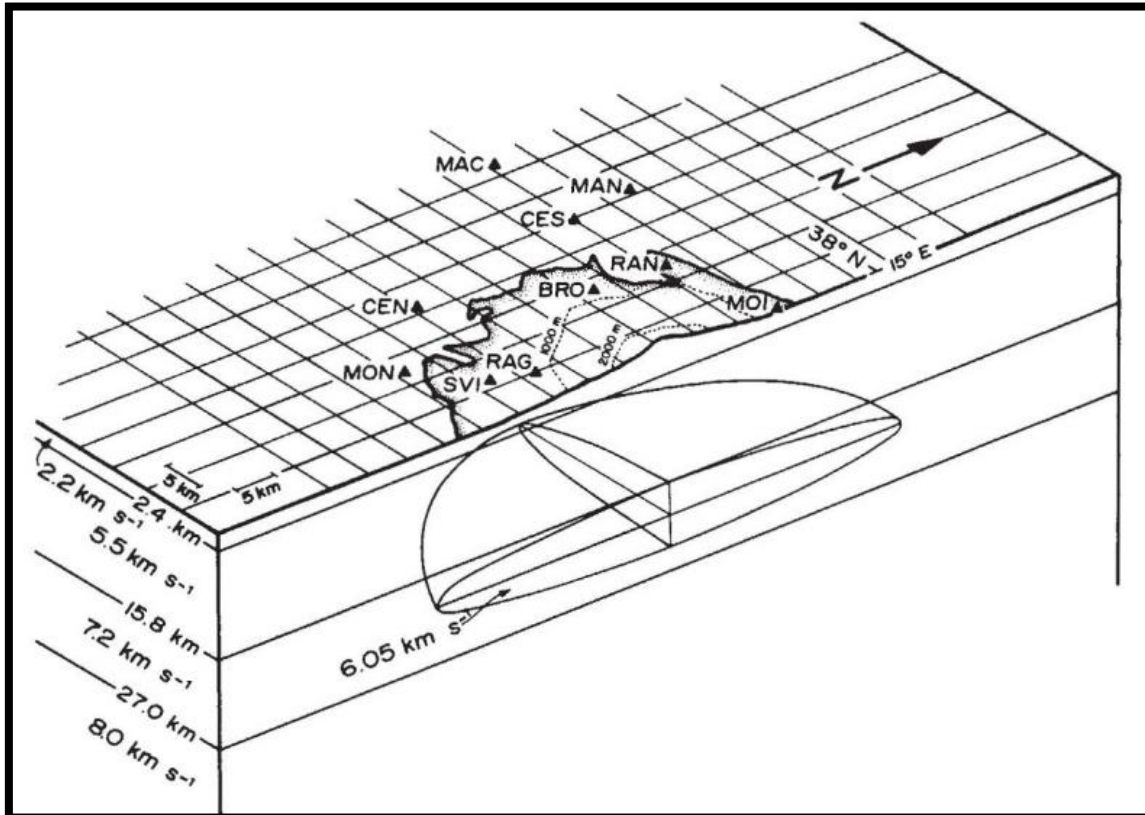
Figura 12. Diagrama del corte del modelo de la corteza y anomalía de baja velocidad debajo del Etna. (Modificado de Sharp et al., 1980).

En 1992 tiene lugar un hito importante en la historia de investigación sísmica del Monte Etna, cuando se desarrolla el primer experimento de sísmica activa (*ETNASEIS)* centrado en el volcán. El experimento se realizó mediante disparos de aire comprimido generados en el mar y registrados en estaciones sísmicas. Este se realizó en dos fases utilizando distintos barcos. En una primera se realizaron 2 perfiles, mientras que en la segunda se hicieron 3. Si bien uno de los objetivos de Hirn et al. (1997) era mejorar la tomografía previa que los autores habían hecho en 1991, la alta atenuación que presentan las estructuras volcánicas unido a otros problemas técnicos, imposibilitó que los datos tuvieran la suficiente calidad para obtener un modelo robusto de la estructura interna. De todas maneras, Hirn et al. (1997) consiguieron profundizar hasta los 15 km, mejorando

en ese sentido la tomografía previa de 1991. Ese mismo año, De Luca et al. (1997) realizan una tomografía sísmica en velocidad en el volcán. Esta tomografía se llevó a cabo a partir de 1249 terremotos y 23.000 y 10.000 llegadas de onda P y S, respectivamente. Los autores identificaron el cuerpo de alta velocidad anteriormente descrito y además obtuvieron como resultado una anomalía de baja V_p/V_s que los autores interpretan como un flujo ascendente de agua caliente localizada al SE del Monte Etna.

Posteriormente, Villaseñor et al. (1998), con una base de datos compuesta por 512 terremotos y 4000 llegadas de onda P registradas en 29 estaciones a lo largo de 12 años, realizan una nueva tomografía que vuelve a identificar un *High Velocity Body (*HVB) y un cuerpo vertical de baja velocidad bajo la zona de cráteres, que interpretan como los conductos magmáticos del volcán.

Posteriormente, las bases de datos se nutren de numerosos terremotos superficiales gracias a la ocurrencia de dos erupciones laterales (2001 y 2003) que son acompañadas por un fuerte incremento en la sismicidad. Patanè et al. (2002) aprovecharon esta nueva base de datos para mejorar la resolución de las tomografías superficiales (hasta 7 km). Los autores realizaron la inversión de las llegadas de P y S de 286 eventos registrados durante la erupción lateral de 2001. Obtienen una alta resolución en los primeros 3 km de profundidad e iluminan una nueva anomalía de baja razón V_p/V_s que identifican como el área de fractura principal de la erupción. Un año más tarde, Patanè et al. (2003), basándose en la tomografía obtenida el año anterior, realizan una interpretación conjunta con datos gravimétricos y geodésicos y proponen la existencia de un área de acumulación de magma situada a 3 km de profundidad (Figura 13).

Un año más tarde, se presentaron dos trabajos de estructura de atenuación sísmica basados en el estudio de las ondas P. Por un lado, Martínez-Arévalo et al. (2005) realizaron una tomografía tridimensional de atenuación de ondas P (Q_p) de alta resolución para los 2 primeros km de profundidad en el volcán Etna, utilizando 291 eventos superficiales registrados en el año 2001. Los autores identificaron una región anómala con bajos valores de Q_p, que se localizó en la región del dique de la erupción del 2001 y que fue interpretada como la intrusión de un magma rico en gas. Ese mismo año, De Gori et al. (2005) presentaron un nuevo modelo de estructura atenuativa hasta una profundidad de 15 km. Estos investigadores identificaron dos anomalías de bajo Q_p localizadas al sur y SO de la cumbre del volcán que interpretaron como cuerpos donde se almacenan fluidos magmáticos.
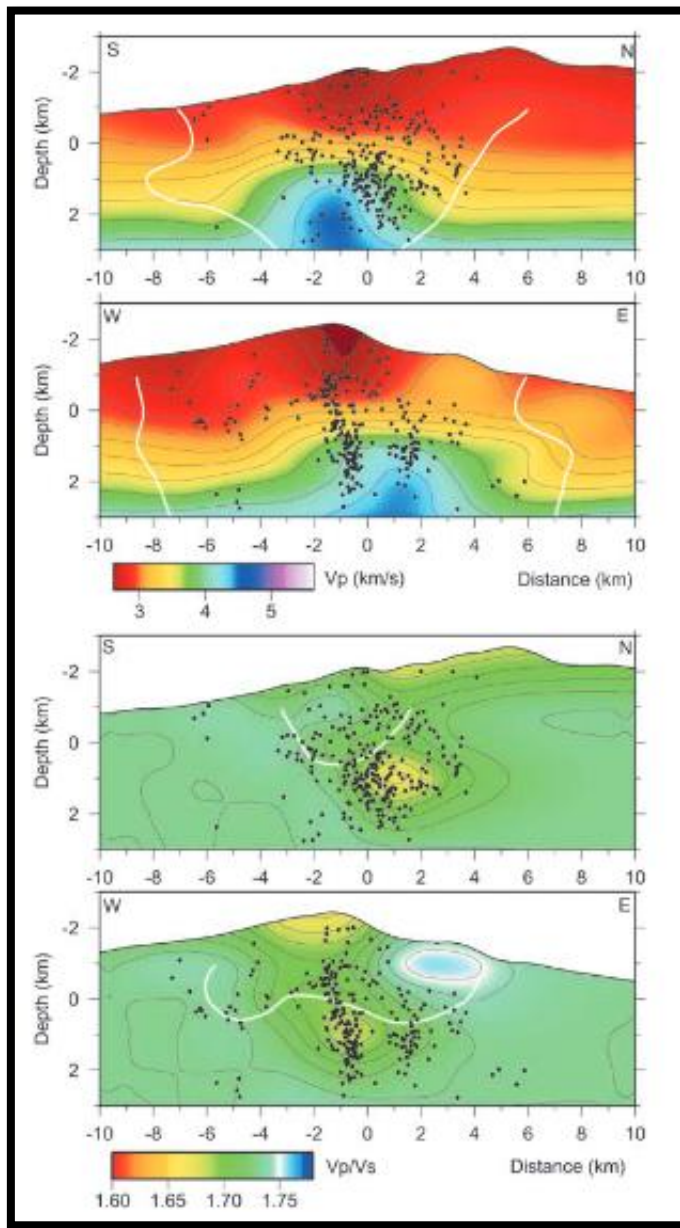
Figura 13. Secciones verticales S-N y O-E del modelo de V_p en la parte superior y V_p/V_s en la parte inferior. Las líneas blancas marcan los límites de las regiones bien resueltas. Los puntos negros representan los terremotos ocurridos a $\pm$ 1 Km de las secciones. (Patanè et al., 2002)

Patanè et al. (2006) vuelven a utilizar la base de datos perteneciente a las erupciones laterales del 2001 y 2003 para estudiar las propiedades elásticas de las ondas sísmicas con el objetivo de identificar la evolución de las intrusiones magmáticas. Para ello, los autores invirtieron las llegadas de las ondas P y S de 700 terremotos y obtuvieron una tomografía 4D, es decir, obtuvieron diferentes modelos tomográficos en el tiempo.

Los resultados mostraron una anomalía de baja razón V_p/V_s que relacionaron con la intrusión del dique.

Monteiller et al. (2009), basándose en el método de dobles diferencias, realizaron una nueva tomografía sísmica del Monte Etna que permitió identificar una zona en forma de aro circundando, el HVB. Esta nueva zona fue interpretada por parte de los autores como presencia de material parcialmente fundido.

Dos años más adelante, De Gori et al. (2011) presentan un nuevo trabajo de tomografía 4D, en este caso de atenuación, donde se mostró por primera vez la existencia de un aumento de la atenuación debido al emplazamiento del magma dentro de la corteza, pronosticando una erupción incipiente del volcán.

Un año después, Alparone et al. (2012) realizaron una nueva tomografía sísmica con datos en velocidad y atenuación para identificar zonas de baja velocidad, baja razón V_p/V_s y con una anomalía negativa de atenuación. Los autores localizaron esta zona sobre el HVB y la interpretaron como un cuerpo de magma rico en gas.

Más recientemente, Díaz-Moreno et al. (2018) realizaron una tomografía conjunta de sismicidad activa y pasiva para las regiones del Monte Etna y las Islas Eolias, siendo el primer trabajo tomográfico que une sísmica activa y pasiva. La tomografía sísmica se realizó con 452 terremotos registrados a lo largo de 4 meses y la base de datos del experimento *TOMO-ETNA* (Ibáñez et al., 2016a; 2016b; Coltelli et al., 2016). En total se invirtieron 184797 y 11802 llegadas de la onda P de sísmica activa y pasiva, respectivamente. Entre sus resultados para el volcán Etna se incluye la identificación de una discontinuidad que corresponde al sistema de fallas Eolias-Tindari-Letojanni y la identificación de una anomalía de alta velocidad al SE del volcán que se interpretó como el sistema de conductos de un antiguo volcán (Figura 14).
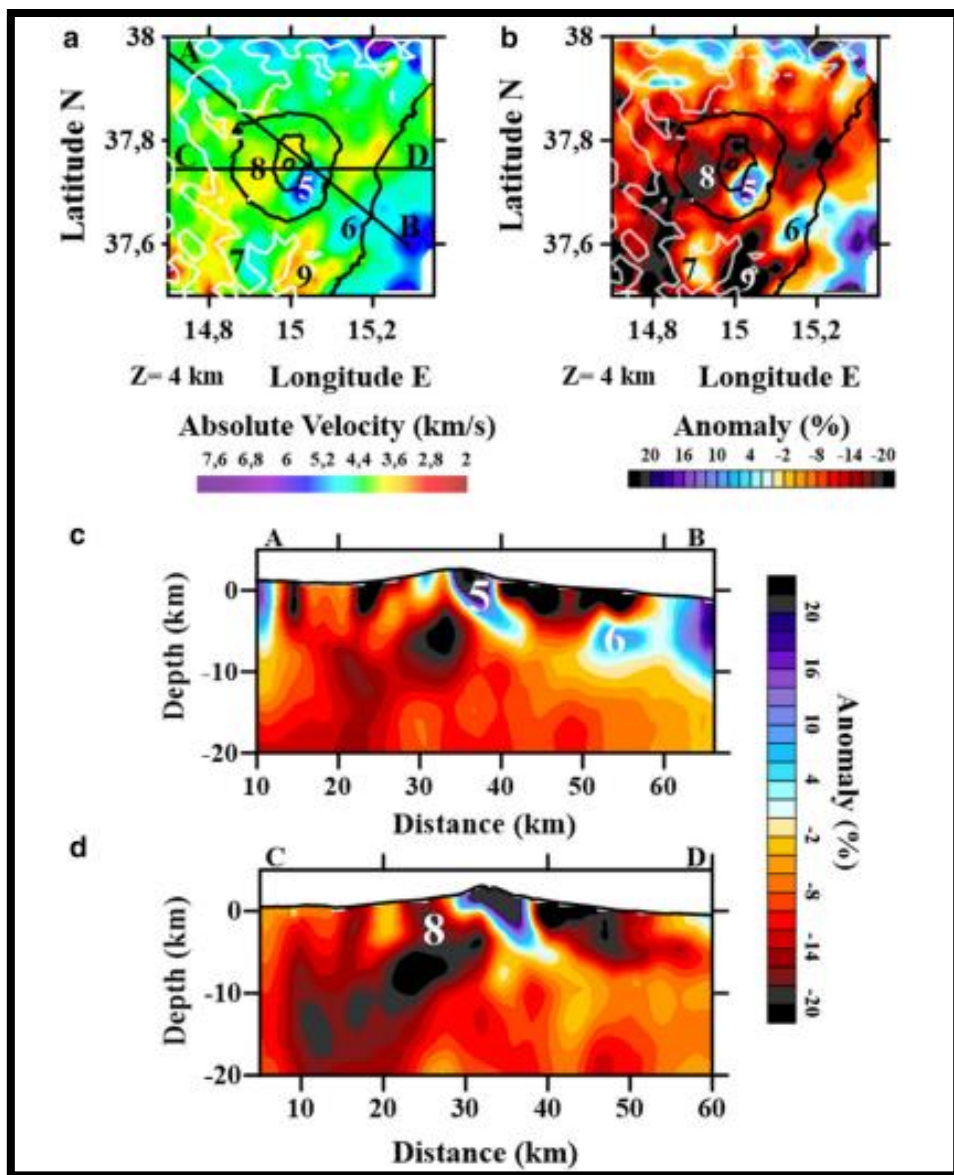
Figura 14. a) Velocidad absoluta de la onda P para el área del Monte Etna. b) Anomalías de velocidad de la onda P para la misma región. c) Sección vertical A-B con las anomalías de velocidad de la onda P. d) Sección vertical C-D con las anomalías de velocidad de la onda P. (Díaz-Moreno et al., 2018)

4. DATOS Y METODOLOGÍA

4.1.   Datos

Para obtener un modelo tomográfico de alta resolución es necesario una distribución uniforme de eventos sísmicos registrados en una red sísmica densificada (Lees, 2007). Debido a que esta situación ideal es complicada de obtener, la estructura interna de muchos volcanes no ha podido ser aún estudiada. Las regiones volcánicas suelen presentar una cobertura de rayos irregular debido a dos razones: 1) la dificultad de instalar estaciones homogéneamente a lo largo de toda la región debido a su terreno abrupto y 2) la distribución heterogénea de los epicentros que normalmente están localizados en una zona concreta. Esto hace que para tener un modelo tomográfico de alta resolución sea necesario el análisis de bases de datos registradas durante largos periodos de tiempo. Por otro lado, este problema puede solucionarse mediante la realización de experimentos de sísmica activa. Las fuentes artificiales pueden ser muy diversas: desde explosiones químicas como Shimizu et al. (1997) en Unzen o Tomatsu et al (2001) en Kirishima a disparos de aire comprimido como TOMOVES en el Vesubio (Gasparini et al., 1998), TOMODEC en la Isla Decepción (Zandomeneghi et al., 2009), TOMTEIDEVS en la isla de Tenerife (Ibáñez et al., 2008) o SEA-CALIPSO en la Isla de Montserrat (Voight et al., 2010). La principal limitación es que se basan en el análisis de los tiempos de llegada de las ondas P, pero se ha comprobado que, para el estudio de la estructura interna de islas volcánicas, los disparos realizados mediante cañones de aire comprimido instalados en buques oceanográficos son los más indicados, ya que nos permiten obtener una cobertura de rayos óptima.

En lo referente a las Islas Eolias y el Monte Etna, uno de los primeros estudios de sísmica activa que se realizaron fue en 1968 con el objetivo de estudiar la estructura de refracción sísmica de Sicilia (Cassinis et al., 1969). En 1977, se realizó el primer sondeo sísmico profundo centrado en el volcán del Monte Etna (Colombi et al., 1979). Más adelante, en 1992, se llevó a cabo el experimento ETNASEIS (Hirn et al., 1997; Nicolich et al., 2000) donde se estudió la estructura del Monte Etna junto a la cuenca marina del Jónico. Años más tarde, Castellano et al. (2008) realizaron un experimento de sísmica activa llevado a cabo entre noviembre y diciembre de 2006 en los alrededores de la isla

de Stromboli. Para tal experimento realizaron disparos de aire en alta mar que fueron registrados por 33 estaciones sísmicas y 10 OBS.

TOMO-ETNA es el experimento de sísmica activa que proporciona la base de datos que se ha analizado en esta tesis doctoral. El experimento se realizó durante los meses de junio y julio de 2014 e implicó el uso de una gran cantidad de recursos humanos y materiales, incluidos buques oceanográficos, hidrográficos y logísticos de Italia, España y Grecia. El área cubierta por el experimento fue de 300 x 300 km (Díaz-Moreno et al., 2018). Durante este experimento se desplegó una red sísmica temporal que permitió densificar y completar la red permanente ya existente. La red sísmica total contó con un total de 267 estaciones sísmicas. El *Geophysical Instrument Pool Postdam* (GIPP) de Alemania aportó las estaciones sísmicas portátiles terrestres de corto periodo (Ibáñez et al., 2016a; 2016b). Estas se componen por un sistema de adquisición DATACUBE3 y sismómetros triaxiales PE-6/B 4.5HZ o Mark L-4C-3D. Con respecto a las estaciones sísmicas portátiles de banda ancha, también aportadas por el GIPP (Ibáñez et al., 2016a; 2016b) cuentan con un sistema de adquisición EarthData PR6-24 y un sismómetro Nanometrics Trillium Compact. En el experimento TOMO-ETNA se desplegaron 80 estaciones de corto periodo y 17 estaciones de banda ancha. Estas estaciones sísmicas no solo registraron las explosiones generadas por los disparos de aire comprimido, sino que además también registraron sismicidad natural (Barbieri et al., 2016).

En adición a las estaciones de tierra, se desplegaron dos conjuntos de *Ocean Bottom Seismometers* (OBS). Uno de ellos consistía en 15 estaciones OBS LC SP 4×4 IGPP-SIOUCSD OBS de la Unidad Tecnológica Marina (CSIC-UTM) de España. El otro conjunto de OBS fue proporcionado por el INGV Osservatorio de Gibilmanna de Italia, y consistieron en un total de 12 OBS de dos tipologías distintas, por un lado, el registro de geófonos SM/6 de período corto con un rango de frecuencia 4.5-140 Hz y por otro, sensores de banda ancha Güralp CMG40TOBS con un registro de entre 60 s y 100 Hz (Díaz-Moreno, 2016).

También fueron utilizadas 133 estaciones sísmicas de la red permanente del INGV, estas estaciones son sismómetros de banda ancha con sensores Nanometrics Trillium de 3 componentes.

La fuente activa fue proporcionada por el buque oceanográfico Sarmiento de Gamboa y consistió en un conjunto de 16 cañones de aire desplegados formando un

conjunto de 2 líneas a 10 metros debajo del nivel del mar. Para el experimento de refracción se dispararon cada 90 s, mientras que para el experimento de reflexión se dispararon cada 30 s (Díaz-Moreno, 2016). En esta tesis se ha comprobado que los disparos más energéticos (Castro-Melgar et al., 2021a) eran equivalentes a terremotos de magnitud 1.4 según la escala de magnitud de Havskov et al. (2003) para regiones volcánicas.

El conjunto final de la base de datos del experimento TOMO-ETNA consistió en 26364 disparos de aires comprimido, siendo 9705 disparos de refracción y 16659 disparos de reflexión, registrados en más de 200 estaciones sísmicas. En total la base de datos se compuso de 5140980 señales (Ibáñez et al., 2016a; 2016b).

Para el estudio de las Islas Eolias se han utilizado los disparos generados en el mar Tirreno. De las estaciones sísmicas que había disponibles, se han seleccionado 37 en base a la calidad de los registros, garantizando que todas las islas tuvieran al menos 1 estación sísmica analizada. En total se obtuvieron 127650 formas de ondas de calidad. De la misma manera, en el estudio del Monte Etna, se utilizaron los disparos de aire comprimido generados en el mar Jónico. Finalmente, se utilizaron 145 estaciones sísmicas y se analizaron un total de 1380473 sismogramas. En la figura 15 se puede observar la distribución de las estaciones y los disparos utilizados para la presente tesis y para cada región de estudio.
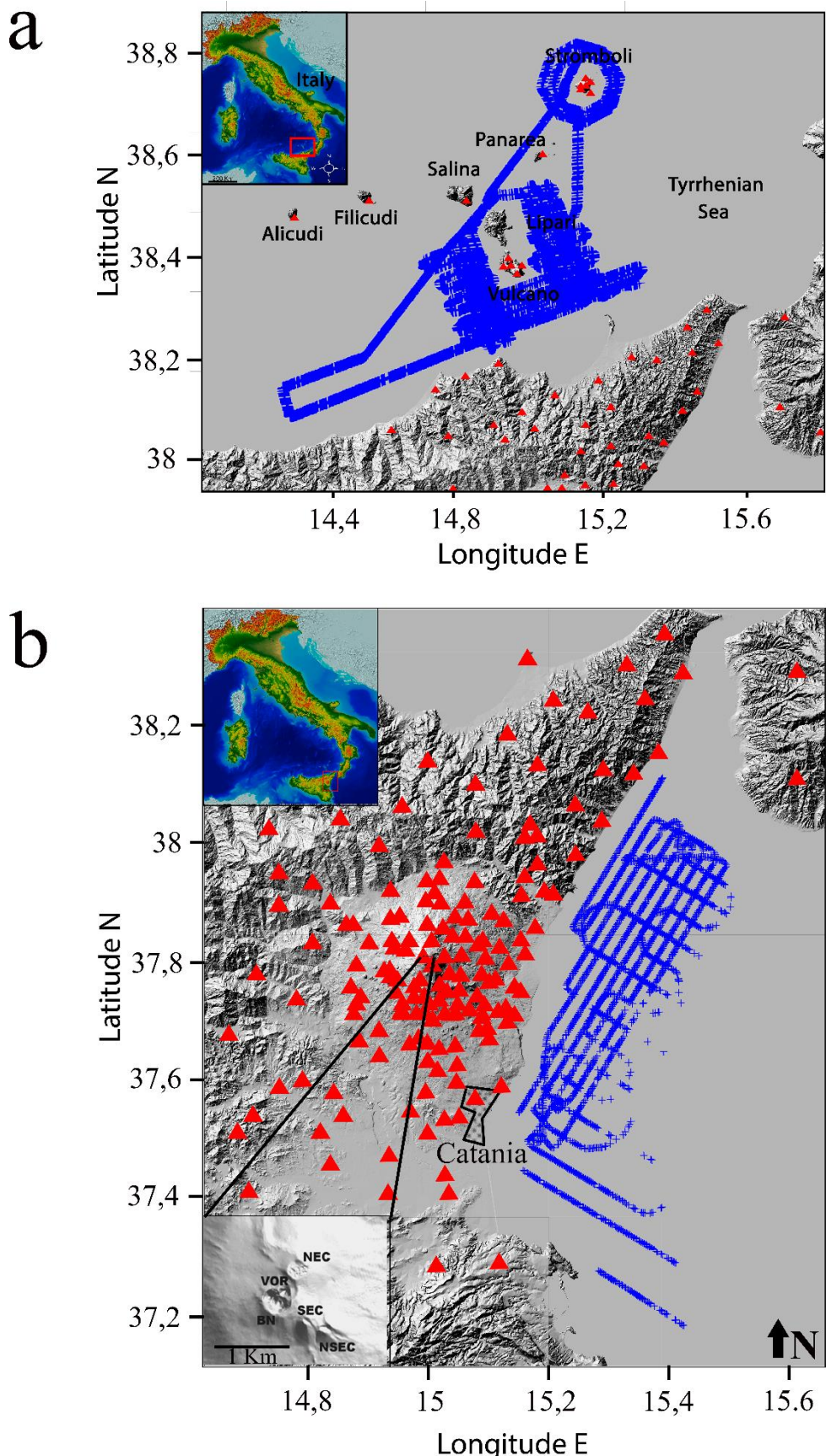
Figura 15: Localización de las regiones de estudio. a) Islas eolias y a) Monte Etna. Los triángulos rojos representan las estaciones sísmicas y las cruces azules los disparos efectuados con cañones de aire. (Figura modificada de Castro-Melgar et al. 2020; 2021a)

4.2.   Modelo de difusión y distribución bidimensional

El modelo de difusión (Wegler, 2004) permite diferenciar la contribución por atenuación intrínseca y *scattering*. Para ello, se basa en una aproximación asintótica de la teoría de transferencia de energía (Wu, 1985; Zeng,1991; Zeng, 1993) en la que se asumen fenómenos de *scattering* fuerte. Debido al carácter heterogéneo de las regiones volcánicas, el modelo de difusión es el más adecuado para estudiar la atenuación sísmica. Debido a la complejidad matemática de la ecuación de la teoría de transferencia de energía, Wegler y Lühr (2001) realización una aproximación más sencilla que permite ajustar linealmente los datos con el modelo de difusión.

$$E(|x|, t) = E_0 (4\pi Dt)^{-p/2} e^{(-bt - \frac{|x|^2}{4dt})} \tag{3.1}$$

Siendo:

$$\mathrm{p} = \frac{v}{\eta_s d} \tag{3.2}$$

y

$$\mathrm{b} = \eta_i v \tag{3.3}$$

El término *d* es el coeficiente de difusividad, para las ondas internas consideraremos *p=3*, mientras que para las ondas superficiales *p=2*. Ajustando la envolvente de energía mediante su cálculo experimental a la ecuación 3.1 nos permite invertir para los parámetros *d* y *b* y esto a su vez nos permite extraer por separado las contribuciones de los factores de calidad para atenuación intrínseca y de *scattering* (Prudencio, 2013).

Como se ha mencionado anteriormente, para obtener los valores de atenuación intrínseca y *scattering* se ha seguido el procedimiento descrito por Wegler y Luhr (2001) y optimizado por Prudencio et al. (2013), para ello se siguen los siguientes pasos:

En primer lugar, se establece los parámetros relacionados con el filtrado y la duración de las señales. Para el filtrado se han seleccionado 6 frecuencias centrales (4, 6, 8, 12, 16 y 20Hz). Con respecto a la duración de las señales se estableció un *lapsetime* de 20 s y otro 30s. *Lapsetime* corresponde al tiempo máximo de la ventana de análisis. Por el contrario, el tiempo de inicio de la ventana de análisis es definido por la llegada de la onda P.

Una vez la señal es filtrada a la frecuencia correspondiente, se calcula la envolvente de la señal entre el tiempo mínimo y máximo. Una vez obtenida, se realiza el ajuste del modelo de difusión, lo que nos permite invertir los parámetros obteniendo los valores relacionados con la contribución de los coeficientes de atenuación intrínseca y de *scattering* por separado y los errores del ajuste.

Wegler y Lühr (2001) para el volcán de Merapi y Wegler (2003) para el volcán Vesubio obtuvieron en sus resultados que la atenuación por *scattering* dominaba en al menos un orden de magnitud sobre la atenuación intrínseca a la frecuencia de análisis. Este resultado se ha observado posteriormente en los trabajos de Prudencio et al. (2015b; 2015c; 2018; 2020) y en los resultados presentados en esta tesis.

4.2.1. Distribución bidimensional

Para poder obtener la distribución espacial de los parámetros obtenidos mediante el modelo de difusión, se ha de ser capaz de representar espacialmente e individualmente los valores de Q_i y Q_s. En la literatura, existen distintas metodologías, por ejemplo, mediante la asignación de Q a la posición de la estación, utilizada por Carcolé y Sato (2010); asignarlo a un punto situado entre la estación y la fuente, como Pujades et al. (1990) o Canas et al. (1995), o una metodología de retroproyección basada en una función de ponderación espacial empírica de los parámetros de atenuación como Prudencio et al. (2013a)

En la presente tesis la representación de los valores de atenuación se ha realizado a partir de funciones de ponderación espacial que describen la sensibilidad bidimensional en el espacio de los datos de atenuación intrínseca y de *scattering*. El método de representación fue desarrollado por Del Pezzo et al. (2016) y se ha aplicado con éxito en diferentes volcanes como por ejemplo Prudencio et al. (2018) en Long Valley (EUA).

Del Pezzo et al. (2016) estimaron las funciones para la representación bidimensional utilizando un enfoque heurístico basado en las soluciones numéricas de Montecarlo de la ecuación del transporte de energía. Las funciones de ponderación calculadas numéricamente para cada par fuente-receptor se aproximaron mediante la expresión:

$$w[x, y, x_r, y_r, x_s, y_s]$$
$$= \frac{1}{4\pi\delta_x D^2 \delta_y} Exp\left[-\frac{\left(x - \frac{x_r + x_s}{2}\right)^2}{2(\delta_x D)^2} + \frac{\left(y - \frac{y_r + y_s}{2}\right)^2}{0.5(\delta_y D)^2}\right]$$
$$+ \frac{1}{2\pi\delta_x D^2 \delta_y} Exp\left[-\frac{(x - x_s)^2}{2(\delta_x D)^2} + \frac{(y - y_s)^2}{2(\delta_y D)^2}\right] \quad\quad (3.4)$$
$$+ \frac{1}{2\pi\delta_x D^2 \delta_y} Exp\left[-\frac{(x - x_r)^2}{2(\delta_x D)^2} + \frac{(y - y_r)^2}{2(\delta_y D)^2}\right]$$

Siendo $w[x, y, x_r, y_r, x_s, y_s]$ proporcionales a la probabilidad de que para un par fuente-receptor con coordenadas x_s, y_s y x_r, y_r, los parámetros estimados Qi[-1] y Qs[-1] (atenuación intrínseca y *scattering* respectivamente) sean efectivamente los valores verdaderos en el punto del espacio bidimensional con las coordenadas x e y. Así, δ_x e δ_y representan la apertura espacial bidimensional. $w[x, y, x_r, y_r, x_s, y_s]$ se ajusta correctamente a las funciones de ponderación numérica con $\delta_x = \delta_y = 0.2$.

Por consiguiente, los resultados obtenidos en los parámetros de atenuación Qi[-1] y Qs[-1] para una trayectoria fuente-receptor, son asignados a todo el volumen del espacio que se pondera por el valor de $w[x, y, x_r, y_r, x_s, y_s]$ de la trayectoria fuente-receptor considerada. Discretizando la región de estudio en celdas, se obtendrá para cada una de

las celdas en las que se ha dividido el volumen un número, N, de medidas ponderadas, este valor representa el número de parejas fuente-receptor.

Finalmente, se estima el valor de Qi^{-1} y Qs^{-1} a través de la estadística gaussiana ponderando la media aritmética con la ecuación:

$$Q^{-1}[x,y] = \frac{\sum_{k=1}^{N} w[x,y,x_{rk},y_{rk},x_{sk},y_{sk}]\, Q_k^{-1}}{\sum_{k=1}^{N} w[x,y,x_{rk},y_{rk},x_{sk},y_{sk}]} \tag{3.5}$$

Siendo $Q^{-1}[x,y]$ la estimación del factor de calidad para un punto bidimensional en su celda central (x,y), k es el índice fuente-receptor que va de 1 a N, Q_k^{-1}, x_{rk}, y_{rk} las coordenadas para el receptor y x_{sk}, y_{sk} las coordenadas de la fuente para cada par fuente-receptor.

4.3. Método de normalización de la coda y distribución tridimensional

El método de normalización de la coda determina mediante la razón de la amplitud espectral de las ondas directas y las ondas coda el factor de calidad de una región. Este método, no permite la separación de la atenuación intrínseca (Qi) y de *scattering* (Qs) ya que se obtiene un factor de calidad total (Qt), pero sí permite conocer la distribución tridimensional del mismo.

Este método parte de la ecuación del espectro de la densidad de la energía sísmica con respecto a la frecuencia y la distancia (Sato, 1977; Aki, 1980; Aki, 1982):

$$E_{ij(f,r)} = S_i(f)\theta_{ij}(\vartheta,\varphi)I_j(f)T_j(f)G_{ij}(r)exp\left(-2\pi f\frac{t_{ij}}{Q_t^{ij}}\right) \tag{3.6}$$

Siendo $E_{ij(f,r)}$ el espectro de la densidad de la energía sísmica, *f* la frecuencia de radiación de las ondas P entre la fuente (*i*) y la estación a lo largo del recorrido del rayo (*j*). El espectro de energía de la fuente es $S_i(f)$ y lo modula el patrón de radiación $\theta_{ij}(\vartheta, \varphi)$, al ser la fuente un disparo de aire comprimido consideraremos $\theta_{ij}(\vartheta, \varphi) = 1$ puesto que es un escenario de un patrón de radiación isótropo. $I_j(f)$ es la función de transferencia instrumental, mientras que $T_j(f)$ es la de sitio y G es el parámetro de expansión geométrica. El tiempo de viaje del rayo es descrito por t_{ij} siendo *r* su coordenada. Por último, Q_t^{ij} es el factor de calidad total a lo largo de todo el recorrido del rayo.

Así, el método de normalización de la coda se fundamenta en que las ondas de coda, son en realidad, ondas que han experimentado el proceso de *scattering* a causa de las heterogeneidades aleatoriamente distribuidas en el medio (Sato, 1977; Aki, 1980, 1982). Este método busca la normalización de la amplitud espectral de la fuente a través de las ondas de coda en un lapso de tiempo determinado, y de esta manera obtener el coeficiente de atenuación sísmica total. Este término, proporcional a Q_t^{-1}, para cada pareja estación-fuente en un lapso de tiempo concreto es representado en la ecuación 3.7.

$$\frac{E_{ij(f,r)}}{E^C(f, t_c)} = \frac{G_{ij}(r)}{P(f, t_c)} exp\left[-2\pi f \int_{ray} \frac{dl}{v(l)Q(l)}\right] \tag{3.7}$$

La fórmula 3.7 se puede transformar siguiendo $G_{ij}(r) = (\frac{r}{r_0})^{2\gamma}$ mediante la transformación de la energía en amplitud, siendo *r* la longitud del rayo, *r₀* la longitud de referencia que se ha establecido en 1 km y *γ* es el término para la expansión geométrica.

$$\ln(\frac{|A_{ij}^S(f)|}{|A_{ij}^C(f, t_c)|}) = \ln\frac{r^{-\gamma}}{P_A(f, t_c)} - \pi f \int_{r_{ij}} \frac{dl}{v(l)Q_s(l)} \tag{3.8}$$

Siendo A_{ij}^S la amplitud espectral para las ondas S, mientras que el término A_{ij}^C es la amplitud espectral para las ondas coda. El término r_{ij} hace referencia a longitud del

rayo en cada una de las parejas *ij*. Posteriormente se reemplaza el término A_{ij} por la media en una banda de frecuencias con centro en f_c:

$$\ln\left(\frac{<A_{ij}^S>f_c}{<A_{ij}^C>f_c,t_c}\right) = -\gamma ln(r) + K(f_c,t_c) - \pi f_c \int_{r_{ij}} \frac{dl}{v(l)Q_s(l)} \qquad (3.9)$$

Siendo *K* el logaritmo de P_A. A continuación, se añade el *slowness* en la ecuación 3.9 y se discretiza la integral:

$$R_{ij} = K(f,t_c) - \pi f \sum_{b=1}^{B} l_{ijb}s_b Q_b^{-1} \qquad (3.10)$$

El término R_{ij} es el logaritmo neperiano para la ratio espectral por *r*. El índice *B* hace referencia al número de bloques y *b* cada uno de los bloques, según se ha dividido el área de estudio. El término l_{ijb} es la longitud del segmento del rayo para un bloque *b*. s_b es el término del slowness. Cumpliendo la condición $Q_b^{-1} \leq Q^{-1} > +\delta Q_b^{-1}$, siendo Q^{-1} el promedio del volumen y δQ_b^{-1} la anomalía en cada bloque *b*, entonces:

$$R_{ij} = K(f,t_c) - \pi f (F_{Q_{ij}} + \sum_{b=1}^{B} l_{ijb}s_b Q_b^{-1}) \qquad (3.11)$$

Donde,

$$F_{Q_{ij}} = \sum_{b=1}^{B} l_{ijb}s_b < Q^{-1} > \qquad (3.12)$$

Al conocer el valor de $< Q^{-1} >$ o es posible obtenerlo de manera independiente y se obtiene la ecuación 3.13:

$$R_{ij} = K(f, t_c) - \pi f F_{Q_{ij}} - \pi f \sum_{b=1}^{B} l_{ijb} s_b \delta Q_b^{-1} \qquad (3.13)$$

Esta expresión se puede invertir de manera lineal para la obtención de δQ_b^{-1} y así, se puede calcular la distribución de anomalías de atenuación en cada uno de los bloques b.

4.3.1. Distribución tridimensional

Como se ha mencionado anteriormente, la expresión 3.13 se puede invertir de manera lineal para obtener δQ_b^{-1}. Por tanto, el procedimiento para obtener la distribución tridimensional corresponde al de una tomografía sísmica.

Como es conocido, la obtención de una tomografía sísmica tridimensional se resume en 4 pasos:

1. En primer lugar, se parametriza el modelo, para ello hay que dividir todo el volumen geométricamente. Esto se realiza debido a que es imposible que la totalidad de la región de estudio sea cubierta por los rayos sísmicos.
2. Posteriormente, se han de calcular los datos experimentales. Para ello, se obtienen las razones espectrales.
3. A continuación, se realiza la inversión, este paso supone calcular Q_p^{-1}.
4. Finalmente, se realiza el control de calidad del modelo, mediante diferentes test de anomalías sintéticas.

Trazado de los rayos sísmicos

Existen distintos métodos de trazado de rayos como es el método de diferencias finitas (Vidale, 1990) o el método de *bending* (doblamiento) (Um and Thurber, 1987). El método de *bending* se basa en satisfacer el principio de Fermat ajustando la geometría de la trayectoria del rayo hasta conseguir el resultado más preciso (Figura 16).
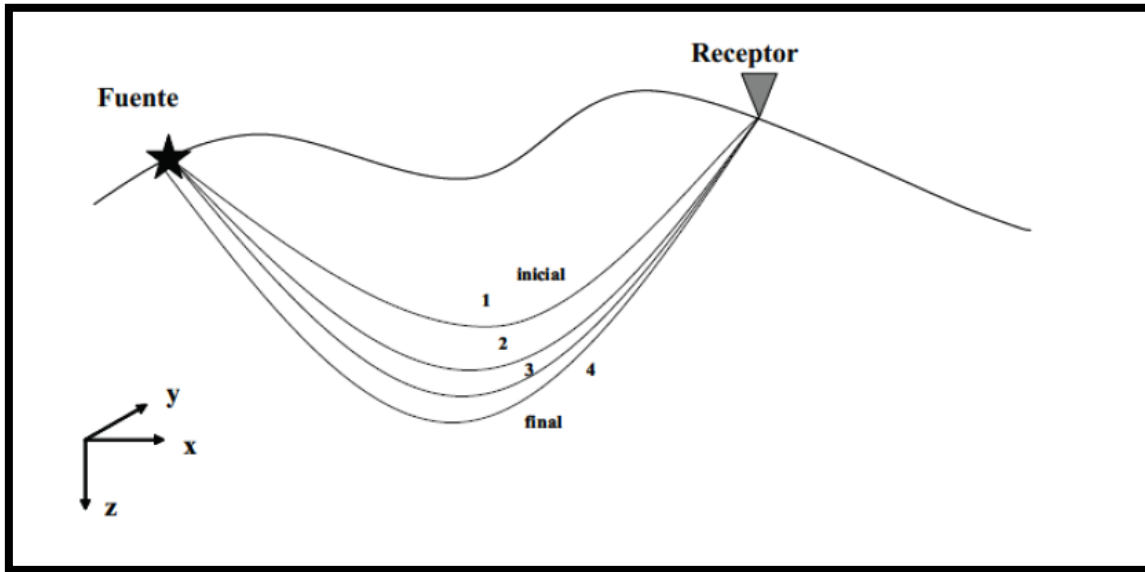
Figura 16: Método de trazado de rayos *bending*, el trazado del rayo sísmico se ajusta progresivamente hasta satisfacer de la manera más adecuada el principio de Fermat. (Imagen modificada de Prudencio, 2013).

Un nuevo método surgido a partir del *bending* es el desarrollado por Um y Thurber (1987), la técnica de *pseudo-bending* se basa en un esquema de perturbación por el cual el tamaño de paso de integración es dividido en dos sucesivamente. El método comienza con una trayectoria inicial definida en tres puntos, que es interpolada a partir del punto central y de manera iterativa a través de una interpretación geométrica de la expresión del rayo sísmico hasta que se cumple con un límite establecido. Los segmentos de la trayectoria del rayo se dividen y el esquema de perturbación se vuelve a iniciar continuando iterativamente hasta que se encuentra una solución satisfactoria de camino más rápido (Figura 17).
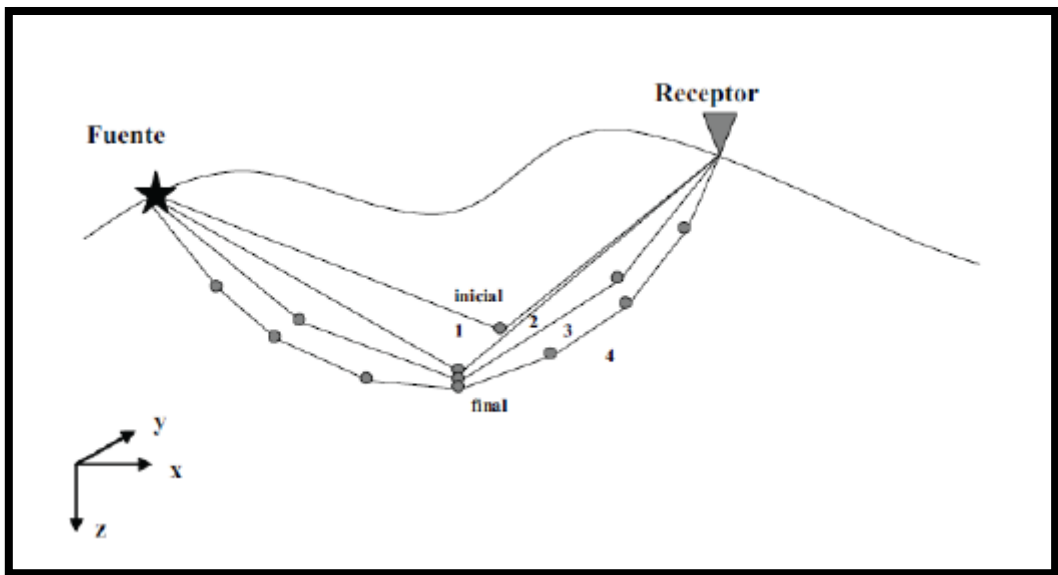
Figura 17: Método de *pseudo-bending* desarrollado por Um and Thurber (1987) basado en un esquema de perturbación definido en tres puntos que se van dividiendo en sucesivas iteraciones. (Imagen modificada de Prudencio, 2013).

Esta tesis debido a las características de la región, utiliza el método de *bending* para realizar el trazado de los rayos sísmicos. La aproximación elegida (Um and Thurber, 1987) funciona muy bien en estructuras volcánicas que se caracterizan por variaciones de velocidad bruscas (De Siena et al., 2009). Este método ha sido aplicado de manera satisfactoria por Prudencio et al. (2015b) en Isla Decepción.

Inversión de ratios espectrales

El propósito de la inversión es calcular los valores del vector correspondientes a los parámetros del modelo. Distinto al caso de las tomografías de velocidad, las de atenuación se realizan mediante una inversión lineal, por lo que se obtienen a partir de un ajuste de mínimos cuadrados.

Un problema que puede aparecer en la inversión y que no permite una solución con la estabilidad requerida es la existencia de componentes nulos dentro de la matriz. Esto puede ocurrir a causa de bloques no resueltos, al no ser traspasados por los rayos. Otro problema que puede aparecer es el exceso de presencia de ruido que conlleve una

indeterminación. Para reducir estos problemas se aplica la el método de Tickhonov de regulación de problemas.

L-Curve

El gráfico de *L-curve* se emplea para visualizar la norma de la solución en función de los residuos. Mediante el método de *L-Curve* se puede obtener el valor del peso, expresado mediante λ, para la mejor solución obtenida. La forma característica del gráfico al utilizar una escala logarítmica es una L, como se puede apreciar en la Figura 18. La intersección de los dos segmentos es el punto de inflexión de la curva para la mejor solución.
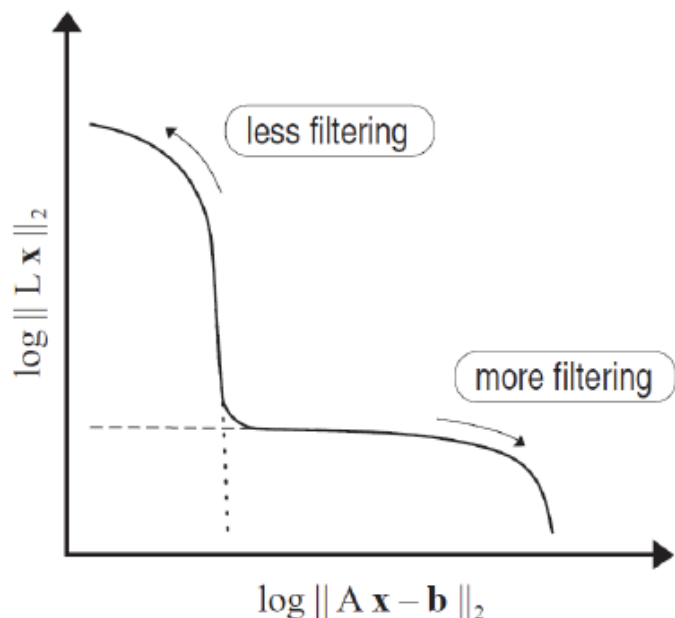
Figura 18: Modelo teórico de L-*Curve.* (Hansen, 1994)

4.4.   Test sintéticos

Para comprobar que el modelo obtenido es robusto se debe estudiar la calidad de la inversión a través de test sintéticos.

Uno de los más utilizado en la literatura científica es el *Checkerboard test*. Este test se basa en dividir el área en distintas áreas alternando anomalías de alta y baja atenuación, utilizando la misma escala de resolución del modelo. En la salida del modelo, aquellas regiones que muestren el patrón del modelo inicial estarán bien resueltas, por lo que son las zonas donde se considera que el modelo tiene buena resolución. Aquellas que no se resuelvan correctamente, no se deberán considerar a la hora de interpretar, ya que no están bien resueltas. Otro de los test más utilizados es el de anomalías libres, que consiste en incorporar una serie de anomalías concretas y ver cómo se reproducen. En la Figura 19 se puede observar la aplicación de estos dos test sintéticos.
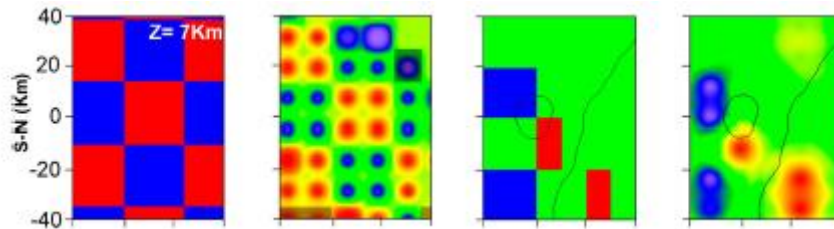
Figura 19: La primera columna representa el modelo inicial del *Checkerboard test*, la segunda el modelo de salida de dicho test, la columna tercera es un modelo inicial donde se han incorporado una serie de anomalías y la cuarta columna, el modelo de salida del test. Se resuelve correctamente toda la región a excepción de la esquina superior derecha y la esquina inferior izquierda. (Figura modificada de Castro-Melgar et al., 2021b)

5. BIBLIOGRAFÍA

Aki, K., Christoffersson, A., Husebye, E. S. and Powell, C. (1974). Three-dimensional seismic velocity anomalies in the crust and upper-mantle under the USGS, California seismic array. *Eos Transactions. American Geophysical Union*, *56*, 1145.

Aki, K. and Richards, P.G. (1980). Quantitative seismology. Theory and methods. *W.H. Freeman, San Francisco*.

Aki, K. (1980). Attenuation of shear-waves in the lithosphere for frequencies from 0.05 to 25 Hz. *Physics of the Earth and Planetary Interiors*, *21*(1), 50-60. https://doi.org/10.1016/0031-9201(80)90019-9

Aki, K. (1982). Scattering and attenuation. *Bulletin of the Seismological Society of America*, *72*(6B), 319-330, https://doi.org/10.1785/BSSA07206B0319

Akinci, A., Del Pezzo, E. and Ibañez, J. (1995). Separation of scattering and intrinsic Attenuation in southern Spain and western Anatolia (Turkey). *Geophysical Journal International*, *121*(2), 337-353. https://doi.org/10.1111/j.1365-246X.1995.tb05715.x

Aloisi, M., Cocina, O., Neri, G., Orecchio, B. and Privitera, E. (2002). Seismic tomography of the crust underneath the Etna volcano, Sicily. *Physics of the Earth and Planetary Interiors*, *134*, 139-155. https://doi.org/10.1016/S0031-9201(02)00153-X

Alparone, S., Barberi, G., Cocina, O., Giampiccolo, E., Musumeci, C. and Patanè, D. (2012). Intrusive mechanism of the 2008–2009 Mt. Etna eruption: Constraints by tomographic images and stress tensor analysis. *Journal of volcanology and geothermal research*, *229*, 50-63. https://doi.org/10.1016/j.jvolgeores.2012.04.001

Ambrose, S. H. (1998). Late Pleistocene human population bottlenecks, volcanic winter, and differentiation of modern humans. *Journal of human evolution*, *34*(6), 623-651. https://doi.org/10.1006/jhev.1998.0219

Anderson, D.L. and Archambeau, C.B. (1964). The anaelasticity of the Earth. *Journal of Geophysical Research*, *69*(10), 2071-2084. https://doi.org/10.1029/JZ069i010p02071

Banda, E., Deichmann, N., Braile, L.W. and Ansorge, J. (1982). Amplitude study of the Pg phase. *Journal of Geophysics*, *51*, 153-154.

Barberi, F., Gasparini, P., Innocenti, F. and Villari, L. (1973). Volcanism of the southern Tyrrhenian Sea and its geodynamic implications. *Journal of Geophysical Research*, *78*(23), 5221-5232. https://doi.org/10.1029/JB078i023p05221

Barberi, G., Giampiccolo, E., Musumeci, C., Scarfì, L., Bruno, V., Cocina, O., Diaz-Moreno, A., Sicali, S., Tusa, G., Tuvè, T., Zuccarello, L., Ibanez, J. M. and Patanè, D. (2016). Seismic and volcanic activity during 2014 in the region involved by TOMO-ETNA seismic active experiment. *Annals of Geophysics*. https://doi.org/10.4401/ag-7082

Battaglia, M., Gottsmann, J., Carbone, D. and Fernández, J. (2008). 4D volcano gravimetry. *Geophysics*, *73*(6), WA3-WA18. https://doi.org/10.1190/1.2977792

Beccaluva, L., Gabbianelli, G., Lucchini, F., Rossi, P. L. and Savelli, C. (1985). Petrology and K/Ar ages of volcanics dredged from the Eolian seamounts: implications for geodynamic evolution of the southern Tyrrhenian basin. *Earth and Planetary Science Letters*, *74*(2-3), 187-208. https://doi.org/10.1016/0012-821X(85)90021-4

Behncke, B. and Neri, M. (2003). The July–August 2001 eruption of Mt. Etna (Sicily). *Bulletin of Volcanology*, *65*(7), 461-476. https://doi.org/10.1007/s00445-003-0274-1

Bianco, F., Castellano, M., Del Pezzo, E. and Ibáñez, J.M. (1999). Attenuation of short-period seismic waves at Mt. Vesuvius, Italy. *Geophysical Journal International*. *138*(1), 67-76. https://doi.org/10.1046/j.1365-246x.1999.00868.x

Bousquet, J. C. and Lanzafame, G. (2001). Nouvelle interpretation des fractures des eruptions laterales de l'Etna; consequences pour son cadre tectonique. *Bulletin de la Société Géologique de France*, *172*(4), 455-467. https://doi.org/10.2113/172.4.455

Branca, S., Coltelli, M., De Beni, E. and Wijbrans, J. (2008). Geological evolution of Mount Etna volcano (Italy) from earliest products until the first central volcanism (between 500 and 100 ka ago) inferred from geochronological and stratigraphic data. *International Journal of Earth Sciences*, *97*(1), 135-152. https://doi.org/10.1007/s00531-006-0152-0

Branca, S., Coltelli, M., Groppelli, G. and Lentini, F. (2011). Geological map of Etna volcano, 1: 50,000 scale. *Italian Journal of Geosciences*, *130*(3), 265-291. https://doi.org/10.3301/IJG.2011.15

Briffa, K., Jones, P., Schweingruber, F.H. and Osborn, T.J. (1998) Influence of volcanic eruptions on Northern Hemisphere summer temperature over the past 600 years. *Nature,* 393**,** 450–455 https://doi.org/10.1038/30943

Canas, J. A., Pujades, L. G., Blanco, M. J., Soler, V. and Carracedo, J. C. (1995). Coda-Q distribution in the Canary Islands. *Tectonophysics*, *246*(4), 245-261. https://doi.org/10.1016/0040-1951(94)00258-B

Carcolé, E. and Sato, H. (2010). Spatial distribution of scattering loss and intrinsic absorption of short-period S waves in the lithosphere of Japan on the basis of the Multiple Lapse Time Window Analysis of Hi-net data. *Geophysical Journal International*, *180*(1), 268-290. https://doi.org/10.1111/j.1365-246X.2009.04394.x

Cardaci, C., Coviello, M., Lombardo, G., Patanè, G. and Scarpa, R. (1993). Seismic tomography of Etna volcano. *Journal of volcanology and geothermal research*, *56*(4), 357-368. https://doi.org/10.1016/0377-0273(93)90002-9

Cassinis, R., Finetti, I., Giese, P., Morelli, C., Steinmetz, L. and Vecchia, O. (1969). Deep seismic refraction research on Sicily. *Bolletino di Geofisica Teorica ed Applicata*, *11*(43/44), 140-160.

Castellano, M., Augusti, V., De Cesare, W., Favali, P., Frugoni, F., Montuori, C., Sgroi, T., De Gori, P., Govoni, A., Moretti, M., Patanè, D., Cocina, O., Zuccarello, L., Marsella, E., Aiello, G., Di Fiore, V., Ligi, M., Bortoluzzi, G., Ferrante, V., Marchetti, E., Lacanna, G. and Ulivieri, G. (2008). Seismic tomography experiment at Italy's Stromboli Volcano. *Eos, Transactions American Geophysical Union*, *89*(30), 269-270. https://doi.org/10.1029/2008EO300001

Castro-Melgar, I., Prudencio, J., Cannata, A., Del Pezzo, E. and Ibanez, J.M. (2021a). Small-scale volcanic structures of the Aeolian volcanic arc revealed by seismic Attenuation. *Frontiers in Earth Science*. 9:725402. https://doi.org/10.3389/feart.2021.725402

Castro-Melgar, I., Prudencio, J., Del Pezzo, E., Giampiccolo, E. and Ibanez, J.M. (2021b). Shallow magma storage beneath Mt. Etna: Evidence from new Attenuation tomography and existing velocity models. *Journal of Geophysical Research: Solid Earth*, *126*(7), e2021JB022094. https://doi.org/10.1029/2021JB022094

Catalano, R., Doglioni, C. and Merlini, S. (2001). On the mesozoic Ionian basin. *Geophysical Journal International*, *144*(1), 49-64. https://doi.org/10.1046/j.0956-540X.2000.01287.x

Chester, D. K. (1985). *Mount Etna: the anatomy of a volcano.* Stanford University Press.

Chiarabba, C., Pino, N. A., Ventura, G. and Vilardo, G. (2004). Structural features of the shallow plumbing system of Vulcano Island Italy. *Bulletin of volcanology*, *66*(6), 477-484. https://doi.org/10.1007/s00445-003-0331-9

Chiarabba, C., De Gori, P. and Speranza, F. (2008). The southern Tyrrhenian subduction zone: deep geometry, magmatism and Plio-Pleistocene evolution. *Earth and Planetary Science Letters*, *268*(3-4), 408-423. https://doi.org/10.1016/j.epsl.2008.01.036

Chouet, B., De Luca, G., Milana, G., Dawson, P., Martini, M. and Scarpa, R. (1998). Shallow velocity structure of Stromboli Volcano, Italy, derived from small-aperture array measurements of Strombolian tremor. *Bulletin of the Seismological Society of America*, *88*(3), 653-666. https://doi.org/10.1785/BSSA0880030653

Colombi, B., Guerra, I., Luongo, G. and Scarascia, S. (1979). Profilo sismico a rifrazione Acireale-Termini Imerese. *Contributti preliminar allá sorveglianza e rischio vulcanico (Etna-Eolie)*, 155-170.

Coltelli, M., Cavallaro, D., Firetto Carlino, M., Cocchi, L., Muccini, F., D'Aessandro, A., Claude, M. E., Monaco, C., Ibáñez, J., Zgur, F., Patanè, D., Carmisciano, C., D'Anna, G., Gonzales, M. T. P., Teixido, T., D'Anna, R., Fertitta, G., Passafiume, G., Speciale, S., Grassa, F., Karageorgis, A., Sormani, L., Facchin, L., Visnovic, G., Cotterle, D., Blanos, R., Mansutti, P., Sulli, A., Cultrera, F., Carrion, F. and Rapisarda, S. (2016). The marine activities performed within the TOMO-ETNA experiment. *Annals of Geophysics*. https://doi.org/10.4401/ag-7081

Cristofolini, R., Gresta, S., Imposa, S. and Patanè, G. (1988). Feeding mechanism of eruptive activity at Mt. Etna based on seismological and petrological data. In *Modeling of Volcanic Processes,* Vieweg+Teubner Verlag, Wiesbaden, 73-93. https://doi.org/10.1007/978-3-322-89414-4_3

Dainty, A.M. and Toksöz, M.N. (1981). Seismic codas on the Earth and the Moon: a comparison. *Physics of the Earth and Planetary Interiors*, *26*(4), 250-260. https://doi.org/10.1016/0031-9201(81)90029-7

De Gori, P., Chiarabba, C. and Patanè, D. (2005). Qp structure of Mount Etna: Constraints for the physics of the plumbing system. *Journal of Geophysical Research: Solid Earth*, *110*(B5). https://doi.org/10.1029/2003JB002875

De Gori, P., Chiarabba, C., Giampiccolo, E., Martinez–Arèvalo, C. and Patanè, D. (2011). Body wave attenuation heralds incoming eruptions at Mount Etna. *Geology*, *39*(5), 503-506. https://doi.org/10.1130/G31993.1

De Luca, G., Filippi, L., Patanè, G., Scarpa, R. and Vinciguerra, S. (1997). Three-dimensional velocity structure and seismicity of Mt. Etna volcano, Italy. *Journal of volcanology and geothermal research*, *79*(1-2), 123-138. https://doi.org/10.1016/S0377-0273(97)00026-7

De Siena, L., Del Pezzo, E., Bianco, F. and Tramelli, A. (2009). Multiple resolution seismic attenuation imaging at Mt. Vesuvius. *Physics of the Earth and Planetary Interiors*, *173*(1-2), 17-32. https://doi.org/10.1016/j.pepi.2008.10.015

Del Pezzo, E., Ibáñez, J., Morales, J., Akinci, A. and Maresca, R. (1995). Measurements of intrinsic and scattering seismic attenuation in the crust. *Bulletin of Seismological Society of America*, *85*(5), 1373-1385. https://doi.org/10.1785/BSSA0850051373

Del Pezzo, E., Bianco, F. and Saccorotti, G. (2001). Separation of intrinsic and scattering Q for volcanic tremor: an application to Etna and Masaya Volcanoes. *Geophysical Research Letters*, *28*(16), 3083-3086. https://doi.org/10.1029/2001GL013372

Del Pezzo, E., Bianco, F., De Siena, L. and Zollo, A. (2006a). Small scale shallow Attenuation structure at Mt. Vesuvius, Italy. *Physics of the Earth and Planetary Interiors, 157*(3-4), 257-268. https://doi.org/10.1016/j.pepi.2006.04.009

Del Pezzo, E., Ibanez, J., Prudencio, J., Bianco, F. and De Siena, L. (2016). Absorption and scattering 2-D volcano images from numerically calculated space-weighting functions. *Geophysical Journal International*, *206*(2), 742-756. https://doi.org/10.1093/gji/ggw171

Díaz-Moreno, A. (2016). Joint active and passive seismic Tomography in active volcanoes: The case of study of Mt. Etna, and further implications in active volcanic regions. *PhD thesis, Universidad de Granada, Spain.*

Díaz-Moreno, A., Barberi, G., Cocina, O., Koulakov, I., Scarfì, L., Zuccarello, L., Prudencio, J., García-Yeguas, A., Álvarez, I., García, L. and Ibáñez, J.M. (2018). New insights on Mt. Etna's crust and relationship with the regional tectonic framework from joint active and passive p-wave seismic tomography. *Surveys in Geophysics*, *39*, 57-97. https://doi.org/10.1007/s10712-017-9425-3

Doglioni, C., Innocenti, F. and Mariotti, G. (2001). Why Mt Etna?. *Terra Nova*, *13*(1), 25-31. https://doi.org/10.1046/j.1365-3121.2001.00301.x

Ferrari, L. and Manetti, P. (1993). Geodynamic framework of the Tyrrhenian volcanism: a review. *Acta Vulcanol*, *3*, 1-10.

Frankel, A., McGarr, A., Bicknell, J., Mori, J., Seeber, L. and Cranswick, E. (1990). Attenuation of high-frequency shear waves in the crust: Measurements from New York State, South Africa and southern California. *Journal of Geophysical Research*, *95*(B11), 17441-17457. https://doi.org/10.1029/JB095iB11p17441

Gasparini, P. and TomoVes Working Group. (1998). Looking inside Mt. Vesuvius. *Eos, Transactions American Geophysical Union*, *79*(19), 229-232. https://doi.org/10.1029/98EO00165

García-Yeguas, A., Koulakov, I., Ibáñez, J. M. and Rietbrock, A. (2012). High resolution 3D P wave velocity structure beneath Tenerife Island (Canary Islands, Spain) based on tomographic inversion of active-source data. *Journal of Geophysical Research: Solid Earth*, *117*(B9). https://doi.org/10.1029/2011JB008970

Giampiccolo, E., Tuvé, T., Gresta, S. and Patane, D. (2006). S-waves attenuation and separation of scattering and intrinsic absorption of seismic energy in southeastern Sicily (Italy). *Geophysical Journal International*, *156*(1), 211-222. https://doi.org/10.1111/j.1365-246X.2006.02881.x

Gvirtzman, Z. and Nur, A. (1999). The formation of Mount Etna as the consequence of slab rollback. *Nature*, *401*(6755), 782-785. https://doi.org/10.1038/44555

Hansen, P. C. (1994). Regularization tools: a Matlab package for analysis and solution of discrete ill-posed problems. *Numerical algorithms*, *6*(1), 1-35. https://doi.org/10.1007/BF02149761

Havskov, J., Peña, J. A., Ibáñez, J. M., Ottemöller, L. and Martínez-Arévalo, C. (2003). Magnitude scales for very local earthquakes. Application for Deception Island Volcano (Antarctica). *Journal of volcanology and geothermal research*, *128*(1-3), 115-133. https://doi.org/10.1016/S0377-0273(03)00250-6

Herraiz, M. and Espinosa, A.F. (1987), Coda waves a review. *Pure and Applied Geophysics*, *125*, 499-577. https://doi.org/10.1007/BF00879572

Hirn, A., Nercessian, A., Sapin, M., Ferrucci, F. and Wittlinger, G. (1991). Seismic heterogeneity of Mt Etna: structure and activity. *Geophysical Journal International*, *105*(1), 139-153. https://doi.org/10.1111/j.1365-246X.1991.tb03450.x

Hirn, A., Nicolich, R., Gallart, J., Laigle, M., Cernobori, L. and ETNASEIS Scientific Group. (1997). Roots of Etna volcano in faults of great earthquakes. *Earth and Planetary Science Letters*, *148*(1-2), 171-191. https://doi.org/10.1016/S0012-821X(97)00023-X

Hoshiba, M., Rietbrick, A., Scherbaum, F., Nakahara, H. and Haberland, C. (2001). Scattering attenuation and intrinsic absorption using uniform and depth-dependent model application to full seismogram envelope recorded in northern Chile. *Journal of Seismology*, *5*, 157-179. https://doi.org/10.1023/A:1011478202750

Ibañez, J., Del Pezzo, E., Alguacil, G., De Miguel, F., Morales, J., De Martino, S., Sabbarese, C. and Posadas, A.M. (1993). Geometrical spreading function for short-period s and coda waves recorded in southern Spain. *Physics of the Earth and Planetary Interiors*, *80*, 25-36. https://doi.org/10.1016/0031-9201(93)90070-P

Ibáñez, J. M., Rietbock, A. and García-Yeguas, A. (2008). Imaging an active volcano edifice at Tenerife Island, Spain. *Eos, Transactions American Geophysical Union*, *89*(32), 289-290. https://doi.org/10.1029/2008EO320001

Ibáñez, J. M., Prudencio, J., Díaz-Moreno, A., Patanè, D., Puglisi, G., Lühr, B. G., Carrión, F., Dañobeitia, J. J., Coltelli, M., Bianco, F., Del Pezzo, E., Dahm, T., Willmott, V. and Mazauric, V. (2016a). The TOMO-ETNA experiment: an imaging active campaign at Mt. Etna volcano. Context, main objectives, working-plans and involved research projects. *Annals of Geophysics*, *59*(4), S0426-S0426. https://doi.org/10.4401/ag-7079

Ibáñez, J. M., Díaz-Moreno, A., Prudencio, J., Patené, D., Zuccarello, L., Cocina, O., Lühr, B. G., Carrión, F., Coltelli, M., Bruno, P. P. G., Bianco, F., Hellweg M., Abreu, R.,

Alguacil, G., Álvarez, I., Aranda, C., Benítez, C., Buontempo L., Feriche, M., García, L., García-Quiroga, D., Martín, J. B. M., Morales, J., Serrano, I., Titos, M., Urbano, L., Aiesi, G., Azzaro, R., Barberi, G., Cantarero, M., Cappuccio, P., Cavallaro, D., Contrafatto, D., Di Prima, S., Falsaperla, S., Carlino, M. F., Giampiccolo, E., Larocca, G., Musumeci, C., Paratore, M., Pellegrino, D., Pulvirenti, N., Rapisarda, S., Sassano, M., Scarfì, L., Scuderi, L., Sicali, A., Tusa, G., Tuvè, T., Del Pezzo, E., Fiore, S., Galluzzo, D., La Rocca, M., Longobardi, M., Nocerino, L., Scognamiglio, S., Bottari, C., Criscuoli, F., De Gori, P., Giovani, L., Messina, A., Silvestri, M., Salimbeni, S., Dahm, T., García-Yeguas, A., Ontiveros, A., Coello, E., Cordero, M., Guillén, C., Romero, M. C., McCann, H., Bretón, M., Boyd, S., Koulakov, I. and Abramenkov, S. (2016b). TOMO-ETNA experiment at Etna volcano: activities on land. *Annals of Geophysics*, *59*(4). https://doi.org/10.4401/ag-7080

Ibáñez, J.M., Castro-Melgar, I., Cocina, O., Zuccarello, L., Branca, S., Del Pezzo, E. and Prudencio, J. (2020). First 2-D intrinsic and scattering Attenuation images of Mt Etna Volcano and surrounding región from active seismic data. *Geophysical Journal International*, *220*(1), 267-277. https://doi.org/10.1093/gji/ggz450

Jin, A. and Aki, K. (1991). Observational and physical basis for coda precursor. *Evaluation of Proposed Earthquake Precursors (Ed. M. Wyss), AGU, Washington D.C.*

Lees, J. M. (2007). Seismic tomography of magmatic systems. *Journal of Volcanology and Geothermal Research*, *167*(1-4), 37-56. https://doi.org/10.1016/j.jvolgeores.2007.06.008

Lekkas, E., Meletlidis, S., Kyriakopoulos, K., Manousaki, M., Mavroulis, S., Kostaki, E., Michailidis, A., Gogou, M., Mavrouli, M., Castro-Melgar, I., Gatsios, T. and Parcharidis, I. (2021). The 2021 Cumbre Vieja volcano eruption in La Palma (Canary Islands). *Newsletter of Environmental, Disaster and Crises Management Strategies*, *26*, ISSN 2653-9454

Lentini, F., Carbone, S. and Guarnieri, P. (2006). Collisional and postcollisional tectonics of the Apenninic-Maghrebian orogen (southern Italy). *Geological Society of America Special Papers, 409*, 57-81. https://doi.org/10.1130/2006.2409(04)

Malinverno, A. and Ryan, W. B. (1986). Extension in the Tyrrhenian Sea and shortening in the Apennines as result of arc migration driven by sinking of the lithosphere. *Tectonics*, *5*(2), 227-245. https://doi.org/10.1029/TC005i002p00227

Martinez-Arevalo, C. (2005). Estructura superficial de atenuación para ondas sísmicas directas, p y s, en ambientes volcánicos. Aplicación al volcán Isla Decepción (Antártida) y al volcán Etna (Italia). *PhD thesis, Universidad de Granada, Spain*.

Martinez-Arevalo, C., Bianco, F., Ibañez, J. and Del Pezzo, E. (2003). Shallow seismic Attenuation and shear-wave splitting in the short-period range of Deception Island volcano (Antarctica). *Journal of Volcanology and Geothermal Research*, *128*(1-3), 89-113. https://doi.org/10.1016/S0377-0273(03)00248-8

Martinez-Arevalo, C., Patane, D., Rietbrock, A. and Ibáñez, J. (2005). The intrusive process leading to the Mt. Etna 2001 flank eruption: Constraints from 3-D attenuation tomography. *Geophysical Research Letters*, *32*(21). https://doi.org/10.1029/2005GL023736

Mayeda, K., Koyanagi, S., Hoshiba, M., Aki, K. and Zeng, Y. (1992). A comparative study of scattering, intrinsic, and coda Q^{-1} for Hawaii, Long Valley, and central California between 1.5 and 15.0 Hz. *Journal of Geophysical Research*, *97*(B5), 6643-6659. https://doi.org/10.1029/91JB03094

Monaco, C., Catalano, S., Cocina, O., De Guidi, G., Ferlito, C., Gresta, S., Musumeci, C. and Tortorici, L. (2005). Tectonic control on the eruptive dynamics at Mt. Etna Volcano (Sicily) during the 2001 and 2002–2003 eruptions. *Journal of Volcanology and Geothermal Research*, *144*(1-4), 211-233. https://doi.org/10.1016/j.jvolgeores.2004.11.024

Monteiller, V., Got, J. L., Patanè, D., Barberi, G. and Cocina, O. (2009). Double-difference tomography at Mt Etna volcano: Preliminary results. In *The VOLUME Project–VOLcanoes: Understanding subsurface mass moveMEnt*. ISBN 978-1-905254-39-2

Nicolich, R., Laigle, M., Hirn, A., Cernobori, L. and Gallart, J. (2000). Crustal structure of the Ionian margin of Sicily: Etna volcano in the frame of regional evolution. *Tectonophysics*, *329*(1-4), 121-139. https://doi.org/10.1016/S0040-1951(00)00192-X

Oppenheimer, C. (2003). Climatic, environmental and human consequences of the largest known historic eruption: Tambora volcano (Indonesia) 1815. *Progress in Physical Geography 27*(2), 230-259. https://doi.org/10.1191/0309133303pp379ra

Patacca, E. and Scandone, P. (1989). *Post-Tortonian mountain building in the Apennines. The role of the passive sinking of a relic lithospheric slab*.

Patane, D., Chiarabba, C., Cocina, O., De Gori, P., Moretti, M. and Boschi, E. (2002). Tomographic images and 3D earthquake locations of the seismic swarm preceding the 2001 Mt. Etna eruption: evidence for a dyke intrusion. *Geophysical Research Letters*, *29*(10), 135-1. https://doi.org/10.1029/2001GL014391

Patanè, D., De Gori, P., Chiarabba, C. and Bonaccorso, A. (2003). Magma ascent and the pressurization of Mount Etna's volcanic system. *Science*, *299*(5615), 2061-2063. https://doi.org/10.1126/science.1080653

Patanè, D., Barberi, G., Cocina, O., De Gori, P. and Chiarabba, C. (2006). Time-resolved seismic tomography detects magma intrusions at Mount Etna. S*cience*, *313*(5788), 821-823. https://doi.org/10.1126/science.1127724

Patanè, D., Aliotta, M., Cannata, A., Cassisi, C., Coltelli, M., Di Grazia, G., Montalto, P. and Zuccarello, L. (2011). Interplay between Tectonics and Mount Etna's volcanism: insights into the geometry of the plumbing system. In *New frontiers in tectonic research-at the midst of plate convergence*. Edited by Uri Schattner, pp. 73-104, ISBN 978-953-307-594-5

Patanè, D., Barberi, G., De Gori, P., Cocina, O., Zuccarello, L., Garcia-Yeguas, A., Castellano, M., D'Alessandro, A. and Sgroi, T. (2017). The shallow magma chamber of Stromboli Volcano (Italy). *Geophysical Research Letters*, *44*(13), 6589-6596. https://doi.org/10.1002/2017GL073008

Prudencio, J. (2013). From 2D to 3D attenuation tomography in volcanoes. The study of Tenerife (Canary Islands) and Deception Island (Antarctica). *PhD thesis, Universidad de Granada, Spain.*

Prudencio, J., Del Pezzo, E., García-Yeguas, A. and Ibáñez, J. (2013a). Spatial distribution of intrinsic and scattering seismic attenuation in active volcanic islands, i: model and the case of Tenerife Island. *Geophysical Journal International*, *195*(3), 1942-1956. https://doi.org/10.1093/gji/ggt361

Prudencio, J., Ibáñez, J., García-Yeguas, A., Del Pezzo, E. and Posadas, A. (2013b). Spatial distribution of intrinsic and scattering seismic attenuation in active volcanic islands, ii: Deception Island images. *Geophysical Journal International, 195*(3), 1957-1969. https://doi.org/10.1093/gji/ggt360

Prudencio, J., Del Pezzo, E., Ibáñez, J.M., Giampiccolo, E. and Patané, D. (2015a). Two-dimensional seismic attenuation images of Stromboli Using active data. *Geophysical Research Letters*, *42*(6), 1717-1724. https://doi.org/10.1002/2015GL063293

Prudencio, J., De Siena, L., Ibáñez, J.M., Del Pezzo, E., García-Yeguas, A. and Díaz-Moreno, A. (2015b). The 3D attenuation structure of Deception Island (Antarctica). *Surveys in Geophysics*, *36*, 371-390. https://doi.org/10.1007/s10712-015-9322-6

Prudencio, J., Ibáñez, J. M., Del Pezzo, E., Martí, J., García-Yeguas, A. and De Siena, L. (2015c). 3D attenuation tomography of the volcanic island of Tenerife (Canary Islands). *Surveys in Geophysics*, *36*(5), 693-716. https://doi.org/10.1007/s10712-015-9322-6

Prudencio, J., Aoki, Y., Takeo, M., Ibáñez, J.M., Del Pezzo, E. and Song, W. (2017a) Separation of scattering and intrinsic attenuation at Asama volcano (Japan): Evidence of high volcanic structural contrasts. *Journal of Volcanology and Geothermal Research, 333*, 96-103. https://doi.org/10.1016/j.jvolgeores.2017.01.014

Prudencio, J., Taira, T., Aoki, Y., Aoyama, H. and Onizawa, S. (2017b) Intrinsic and scattering attenuation images of Usu volcano, Japan. *Bulletin of Volcanology*, *79*(4), 1-12. https://doi.org/10.1007/s00445-017-1117-9

Prudencio, J., Manga, M. and Taira, T. (2018). Subsurface structure of Long Valley caldera imaged with seismic scattering and intrinsic attenuation. *Journal of Geophysical Research: Solid Earth*, *123*(7), 5987-5999. https://doi.org/10.1029/2017JB014986

Prudencio, J. and Manga, M. (2020). 3-D seismic attenuation structure of Long Valley caldera: looking for melt bodies in the shallow crust. *Geophysical Journal International*, *220*(3), 1677-1686. https://doi.org/10.1093/gji/ggz543

Pujades, L.G., Canas, J.A., Egozcue, J.J., Puigví, M.A., Gallart, J., Lana, K., Pous, J. and Casas, A. (1990). Coda-Q distribution in the Iberian Peninsula. *Geophysical Journal International*, *100*(2), 285-301. https://doi.org/10.1111/j.1365-246X.1990.tb02486.x

Sato, H. (1977). Energy propagation including scattering effects sengle isotropic scattering approximation. *Journal of Physics of the Earth*, *25*(1), 27-41. https://doi.org/10.4294/jpe1952.25.27

Sato, H. and Fehler, M. (1998). Seismic wave propagation and scattering in heterogeneous Earth. *1st edition, Springer, New York.*

Savelli, C. (1988). Late Oligocene to Recent episodes of magmatism in and around the Tyrrhenian Sea: implications for the processes of opening in a young inter-arc basin of intra-orogenic (Mediterranean) type. *Tectonophysics*, *146*(1-4), 163-181. https://doi.org/10.1016/0040-1951(88)90089-3

Scandone, P. (1979). Origin of the Tyrrhenian Sea and Calabrian arc. *Bollettino della Società Geologica Italiana*, *98*(1), 27-34.

Scherbaum, F. (1990). Combined inversion for the three-dimensional Q structure and source parameters using microearthquake spectra. *Journal of Geophysical Research*, *95*(B8), 12423-12438. https://doi.org/10.1029/JB095iB08p12423

Sharp, A. D. L., Davis, P. M. and Gray, F. (1980). A low velocity zone beneath Mount Etna and magma storage. *Nature*, *287*(5783), 587-591. https://doi.org/10.1038/287587a0

Shimizu, H. and Explosion Seismic Research Group of Unzen Volcano (1997). Subsurface structure of Unzen volcano derived from the 1995 explosion experiment. *Proceedings DPRI symposium on Magma Exploration, 9-15*.

Stacey, F.D., Gladwin, M.T., McKavanagh, B., Linde, A.T. and Hastie, L.M. (1975). Anelastic damping of acoustic and seismic pulses. *Geophysical Surveys*, *2*, 133-151. https://doi.org/10.1007/BF01447906

Thurber, C. H. (1984). Seismic detection of the summit magma complex of Kilauea volcano, Hawaii. *Science*, *223*(4632), 165-167. https://doi.org/10.1126/science.223.4632.165

Tipler, P.A. (1999). Física. *Ed. Reverté.*

Tipler, P. and Mosca, G. (2005). Física para la ciencia y la tecnología. *Ed. Reverté.*

Tomatsu, T. Kumagai, H. and Dawson, P. B. (2001). Tomographic inversion of P-wave velocity and Q structures beneath the Kirishima volcanic complex, southern Japan, based

on finite difference calculations of complex traveltimes. *Geophysical Journal International*, *146*(3), 781-794. https://doi.org/10.1046/j.1365-246X.2001.00491.x

Um, J. and Thurber, C. (1987). A fast algorithm for two-point seismic ray tracing. *Bulletin of the Seismological Society of America*, *77*(3), 972-986. https://doi.org/10.1785/BSSA0770030972

Vidale, J. E. (1990). Finite-difference calculation of traveltimes in three dimensions. *Geophysics*, *55*(5), 521-526. https://doi.org/10.1190/1.1442863

Villasenor, A., Benz, H. M., Filippi, L., De Luca, G., Scarpa, R., Patanè, G. and Vinciguerra, S. (1998). Three-dimensional P-wave velocity structure of Mt. Etna, Italy. *Geophysical research letters*, *25*(11), 1975-1978. https://doi.org/10.1029/98GL01240

Voight, B. and Sparks, R. S. J. (2010). Introduction to special section on the eruption of Soufrière Hills Volcano, Montserrat, the CALIPSO Project, and the SEA-CALIPSO arc-crust imaging experiment. *Geophysical Research Letters*, *37*. https://doi.org/10.1029/2010GL044254

Wegler, U. and Lühr, B.G. Scattering behaviour at Merapi volcano (Java) revealed from an active seismic experiment. (2001). *Geophysical Journal International*, *145*(3), 579-592. https://doi.org/10.1046/j.1365-246x.2001.01390.x

Wegler, U. (2003). Analysis of multiple scattering at Vesuvius volcano, Italy, using data of the TomoVes active seismic experiment. *Journal of Volcanology and Geothermal Research*, *128*(1-3), 45-63. https://doi.org/10.1016/S0377-0273(03)00246-4

Wegler, U. (2004). Diffusion of seismic waves in a thick layer: Theory and application to Vesuvius volcano. *Journal of Geophysical Research: Solid Earth*, *109*(B7). https://doi.org/10.1029/2004JB003048

Wu, R. S. (1985). Multiple scattering and energy transfer of seismic waves—separation of scattering effect from intrinsic attenuation—I. Theoretical modelling. *Geophysical Journal International*, *82*(1), 57-80. https://doi.org/10.1111/j.1365-246X.1985.tb05128.x

Wu, H. and Lees, J.M. (1996). Attenuation of coso geothermal area, California, from waves pulse width. *Bulletin of Seismological Society of America*, *86*(5), 1574-1590. https://doi.org/10.1785/BSSA0860051574

Zandomeneghi, D., Almendro, J., Ibáñez, J. and Saccorotti., G. (2008). Seismic tomography of cental Sao Miguel, Azores. *Physics of the Earth and Planetary Interiors*, *167*, 8-18. https://doi.org/10.1016/j.pepi.2008.02.005

Zandomeneghi, D., Barclay, A., Almendros, J., Ibáñez, J. and Wilcock., W.S.D. (2009). Crustal structure of Deception island volcano from p wave seismic tomography: tectonic and volcanic implications. *Journal of Geophysical Reseach*, *114*. https://doi.org/10.1029/2008JB006119

Zeng, Y. (1991). Compact solutions for multiple scattered wave energy in time domain. *Bulletin of the Seismological Society of America*, *81*(3), 1022-1029.

Zeng, Y. (1993). Theory of scattered P-and S-wave energy in a random isotropic scattering medium. *Bulletin of the Seismological Society of America*, *83*(4), 1264-1276. https://doi.org/10.1785/BSSA0830041264

Zollo, A., Gasparini, P., Virieux, J., Biella, G., Boschi, E., Capuano, P., De Franco, R., Dell'Aversana, P., De Matteis, R., De Natale, G., Iannaccone, G., Guerra, I., Le Meura, H. and Mirabile, L. (1998). An image of mt. Vesuvius obtained by 2-d seismic tomography. *Journal of Volcanology and Geothermal Research*, *82*, 161-173. https://doi.org/10.1016/S0377-0273(97)00063-2

SEGUNDA PARTE

I.   PUBLICACIONES: ISLAS EOLIAS

i.   SMALL-SCALE VOLCANIC STRUCTURES OF THE AEOLIAN VOLCANIC ARC REVEALED BY SEISMIC ATTENUATION

Publicado en: Frontiers in Earth Science

2020 Journal Impact Factor: 3,498; H-INDEX: 30

JCR: Q2 Geosciences, multidisciplinary

SJR: Q1 Earth and Planetary Sciences (miscellaneous)

Castro-Melgar, I., Prudencio, J., Cannata, A., Del Pezzo, E. and Ibáñez, JM. (2021) Small-Scale Volcanic Structures of the Aeolian Volcanic Arc Revealed by Seismic Attenuation. *Frontiers in Earth Sciences,* 9:725402. https://doi.org/10.3389/feart.2021.725402

SMALL-SCALE VOLCANIC STRUCTURES OF THE AEOLIAN VOLCANIC ARC REVEALED BY SEISMIC ATTENUATION

Ignacio Castro-Melgar[1], Janire Prudencio[1,2], Andrea Cannata[3,4], Edoardo Del Pezzo[2,5] and Jesús M. Ibáñez

[1]*Department of Theoretical Physics and Cosmos, University of Granada, Granada, Spain*

[2]*Andalusian Institute of Geophysics, University of Granada, Granada, Spain*

[3]*Dipartimento di Scienze Biologiche, Geologiche e Ambientali, Università Degli Studi di Catania, Catania, Italy*

[4]*Istituto Nazionale di Geofisica e Vulcanologia, Osservatorio Etneo, Catania, Italy*

[5]*Istituto Nazionale di Geofisica e Vulcanologia, Osservatorio Vesuviano, Napoli, Italy*

Summary

We present the first two-dimensional (2-D) spatial distribution of seismic scattering and intrinsic attenuation beneath the Aeolian Islands arc. The Aeolian Islands archipelago represents one of the best examples of a small dimension volcanic island arc characterized by the alternation of different structural domains. Using the seismic wave diffusion model as the basis for the analysis, and using data from an active seismic experiment (TOMO-ETNA), we analysed more than 76,700 seismic paths marked by epicentre-seismic station pairs. Based on frequencies of 4–24 Hz, we identified high regional attenuation, comparable with other volcanic areas of the world. We used two different seismogram lengths, reflecting two different sampling depths, which allowed us to observe two different attenuative behaviours. As in most volcanic regions, scattering attenuation predominates over intrinsic attenuation, but some characteristics are area-specific. Volcanic structures present the highest contribution to scattering, especially in the low frequency range. This behaviour is interpreted to reflect the small size of the islands and the potentially relatively small size of individual magmatic feeding systems. In addition, strong scattering observed in one zone is associated with the northernmost part of the so-called Aeolian-Tindari-Letojanni fault system. In contrast, away from the volcanic islands, intrinsic attenuation dominates over scattering attenuation. We interpret

this shift in attenuative behaviour as reflecting the large volume of sedimentary material deposited on the seabed. Owing to their poorly consolidated nature, sediments facilitate intrinsic attenuation via energy dissipation, but in general present high structural homogeneity that is reflected by low levels of scattering. Our results show that this region is not underlain by a large volcanic structural complex such as that beneath nearby Mt. Etna volcano. Instead, we observe dimensionally smaller and isolated subsurface volcanic structures. The identification of such features facilitates improved geological interpretation; we can now separate consolidated marine structures from independent subsurface volcanic elements. The results of this study provide a model for new research in similar regions around the world.

Key words: Seismic attenuation, seismic active experiment, Aeolian islands, scattering, intrinsic attenuation scaterring and intrinsic attenuation at Aeolian islands

1. INTRODUCTION

Volcanologists seek to understand the nature and structure of the Earth by inferring the physical properties of volcanic structures, determining degrees of homogeneity or heterogeneity, and trying to understand the dynamic nature volcanic eruptions. Volcanic regions offer an attractive paradigm for the scientific community; observations of volcanic regions reflect the external manifestations of numerous internal dynamic processes (e.g., energy and chemical exchanges, rheological transformations, and the evolution of physical properties) at different depths and under different physical conditions. However, models of subsurface features are based on indirect observations. Imaging volcanic structures remains a challenge for the seismological community, even when similar structures have been identified for multiple volcanoes using different methods (e.g., velocity and attenuation from active and passive seismic sources; Zandomeneghi et al., 2008; Zandomeneghi et al., 2009; Rawlinson et al., 2010; García-Yeguas et al., 2012; García-Yeguas et al., 2014; De Siena et al., 2014; Koulakov and Shapiro, 2015; Prudencio et al., 2015a; Prudencio et al., 2015b; De Siena et al., 2017; Prudencio and Manga, 2020; Gabrielli et al., 2020). In particular, high contrast heterogeneities and the identification of structural changes related to magma transport are challenging for these methods (e.g., Castro-Melgar et al., 2021; Giampiccolo et al., 2021). The quality of tomographic images depends strongly on the spatial distribution of both

sources and receivers. At the same time, volcanoes present complex morphologies that may not be reflected in the distribution of seismic stations, and the deployment of dense temporary seismic networks can greatly improve the resolution of tomographic images (e.g., Ibáñez et al., 2016a; Ibáñez et al., 2016b; Zulfakriza et al., 2020). However, for island archipelagos, installation sites are limited by islands' spatial distributions. The Aeolian Islands volcanic arc represents a particularly complex case.

The Aeolian volcanic province consists of seven main islands and a number of additional seamounts forming a volcanic arc (Lucchi et al., 2013). The islands have represented a fundamental reference for volcanology, with Stromboli and Vulcano giving their names to so-called "Strombolian" and "Vulcanian" eruptions. The latter is also the source of the term "volcano." The region has been a focus of volcanological research, and is of great interest to the general public, partly owing to the paroxysmal activity of Stromboli. For example, during the summer 2019, two powerful paroxysms (July 3 and August 28) produced bombs, lapilli fallout, and small pyroclastic density currents (e.g., Giudicepietro et al., 2020; Giordano and De Astis, 2021; Viccaro et al., 2021) that caused widespread fires and damage across the island, including injuries and one fatality. This eruption, for which there were no apparent observable precursors, challenged the often-accepted paradigm that volcanoes always act in the same way. Subsequently, on May 19, 2021 a new explosive eruption of Stromboli generated another non-typical pyroclastic flow. Stromboli is not the only active volcano in the Aeolian Archipelago; Vulcano, the southernmost island, produced many eruptions in historical times, the most recent of which occurred from 1888 to 1890 (Selva et al., 2020 and references therein). Although permanent residents of the Aeolian Islands are not numerous, the population dramatically increases during the summer season, leading to a sharp increase in the associated volcanic risk (Rosi et al., 2013; Selva et al., 2020; Giordano and De Astis., 2021). Hence, it is crucial to properly assess volcanic hazards in the Aeolian volcanic province and their evolution over time, including the monitoring of activity (e.g., seismic, ground deformation, geochemical) and investigations of magmatic dynamics, plumbing system structures, and regional crustal structures, all of which play a fundamental role.

Various techniques have been proposed for modelling subsurface dynamics, including Deep Learning and Machine Learning (e.g., Titos et al., 2018; Bueno et al., 2019; Bueno et al., 2021; Martínez et al., 2021), satellite remote sensing (e.g., Ganci et al., 2020), among others (e.g., Saccorotti and Lokmer, 2021). However, tomographic

analysis based on seismic velocity and attenuation remains one of the best tools because it can provide direct links between changes in wave-field properties and the physical conditions of the medium (Castro-Melgar et al., 2021). Obtaining tomographic images of the Aeolian Islands is complex, especially owing to the geographical dispersion and small sizes of the islands. For example, Lipari covers an area of 37 km2, Vulcano is just 21 km2, and Stromboli is just 13 km2. These factors preclude a high density of seismic stations, while the installation and maintenance of long-term ocean bottom seismic stations remains difficult. Active seismic experiments of small regions have been performed at Deception Island (Zandomeneghi et al., 2009) and Montserrat (Shalev et al., 2010; Voight et al., 2014). However, the resolution of a similar experiment carried out for the island of Stromboli (Castellano et al., 2008) was limited (Prudencio et al., 2015c; Patanè et al., 2017). The velocity structure of the region has been considered in a number of studies (e.g., Chiarabba et al., 2008; Díaz-Moreno et al., 2018), including those with a focus on Stromboli (e.g., Chouet et al., 1998; Petrosino et al., 1999; La Rocca et al., 2000; Petrosino et al., 2002; Linde et al., 2014). Recently, Del Pezzo et al. (2019) obtained an average value of intrinsic and scattering attenuation, giving the first approximation of the average attenuation behaviour of the region since the work of Del Pezzo et al. (1983). These results show that on average this region has much stronger scattering attenuation behaviour than that around Mt. Etna volcano, suggesting a high degree of heterogeneity. In this study, we used data generated by the TOMO-ETNA experiment to produce a two-dimensional (2-D) attenuation model of the Aeolian Islands region, with a focus on separating intrinsic and scattering attenuation effects. The Aeolian Islands archipelago represents one of the best examples of a small dimension volcanic island arc characterised by the alternation of different structural domains. The identification of such features, which can be detected by lateral small scale attenuation contrasts, facilitates improved geological interpretation, allowing us to separate consolidated marine structures from independent volcanic units. In this paper, we show that kernel-based, separated intrinsic- and scattering-attenuation imaging allows the detection of local lateral contrasts in attenuation; we believe that our findings will open up new research avenues for similar regions around the world. Finally, we directly compare the attenuation features of this region with the nearest volcanic complex, Mt. Etna, about which a number of recent studies have been published (Ibáñez et al., 2020; Castro-Melgar et al., 2021; Giampiccolo et al., 2021).

2. GEOLOGICAL SETTING

The Aeolian volcanic arc is located at the convergent boundary between the African and Eurasian plates (e.g., Ventura, 2013) and has been the focus of geological, geodynamic, and seismic studies. Here, we present a short summary of some of the most relevant results. Several lines of evidence suggest how these volcanoes belong to a subduction-dominated area. The geochemical characteristics of the volcanic rocks, the occurrence of deep earthquakes (down to ∼600 km), and the presence of basins of oceanic nature in the Southern Tyrrhenian Sea (such as the Magnaghi, Vavilov and Marsili basins) all suggest subduction related to the rollback of the Ionian slab below the Calabrian Arc (e.g., Gvirtzman and Nur, 2001; Chiarabba et al., 2008; Ventura, 2013). See Figure 1 of De Astis et al. (2003) and Figure 2.1 of Ventura (2013) for additional details.

The Aeolian volcanic province consists of seven main islands and several seamounts forming a half-ring structure around the Marsili Basin (Lucchi et al., 2013). Among the main islands, Stromboli, Vulcano, Lipari, and Panarea are considered active. On the basis of structural and volcanological features, the Aeolian Islands and associated seamounts can be divided into three main sectors (see Figure 1 of De Astis et al., 2003): 1) the western sector, including some seamounts and the Alicudi and Filicudi Islands; 2) the central sector, with the islands of Salina, Lipari, and Vulcano; and 3) the eastern sector, including Panarea, Stromboli, and some seamounts.

Structurally, the Aeolian archipelago is dominated by three main fault systems (see Figures 2, 4 of De Astis et al., 2003): 1) the "Sisifo-Alicudi" fault system, a WNW–ESE striking system characterising the volcanoes of the western sector; 2) the "Aeolian–Tindari–Letojanni" fault system, a NNW–SSE striking system influencing the volcanoes in the central sector; and 3) a NNE–SSW to NE–SW fault system affecting Stromboli and Panarea. Concerning the seismicity of the Aeolian area, intermediate and deep hypocentres (focal depth >30 km) concentrate along the Ionian slab (e.g., Selvaggi and Chiarabba, 1995). In addition, earthquakes are located in the crust at focal depths of 5–7 km b.s.l., as well as at the crust-mantle transition (15–20 km b.s.l.). The epicentral distribution of the seismicity partially reflects the spatial distribution of the aforementioned main structural features (e.g., De Luca et al., 1997; De Astis et al., 2003). Indeed, two main epicentral alignments can be noted, those striking WNW–ESE,

corresponding to the "Sisifo–Alicudi" fault system, and NNW–SSE, overlapping the "Aeolian–Tindari–Letojanni" fault system.

In terms of crustal structure, tomography, deep seismic sounding, and gravity data suggest a decrease of crust thickness in the Marsili Basin, as well as along the Salina–Lipari–Vulcano NNW–SSE-striking alignment (e.g., De Luca et al., 1997; Ventura et al., 1999; Pepe et al., 2000; Ventura, 2013). In particular, in the Marsili Basin the Moho is at ~10 km depth (e.g., Pontevivo and Panza, 2006).

3. MATERIAL AND METHODS

3.1 Seismic Data

TOMO-ETNA was an active seismic experiment designed to improve understanding of the structure beneath Mt. Etna (Ibáñez et al., 2016a; Ibáñez et al., 2016b). The experiment involved the use of a large number of human and material resources (including seismic stations, and oceanographic, hydrographic, and logistical support vessels from Italy, Spain, and Greece). For this reason, it was decided to maximize the efficiency of the work by extending the shot locations from Ionian Sea to the Tyrrhenian Sea to include the Aeolian Islands (Coltelli et al., 2016).

The experiment, divided into several phases (between June and December 2014), generated active seismic signals using different capacities and powers of the air-guns. Those with the highest capacity (shots carried out in July 2014) were performed using compressors with 5,500 cubic inches of capacity. The aim was to generate two types of signal, one for producing images based on the refraction of seismic waves (using the maximum energy), and the other (based on lower power air-gun shots) to obtain images of marine structures using multi-channel techniques based on seismic reflection. Only shots generated with the maximum energy presented sufficient quality (based on the signal-to-noise ratio) to be used in tomographic structural models (both velocity and attenuation). Castro-Melgar et al. (2021) found that the most energetic shots had an equivalent duration magnitude of up to 1.4, based on the magnitude scale of Havskov et al. (2003) for volcanic regions. To this limitation we add a high content of background noise, which is typical of seismic signals in populated areas or on small islands (due to oceanic noise); as such, not all of the signals generated in the experiment were useful for

this study. For our attenuation model, we only used signals generated in the Tyrrhenian Sea. From the set of all available seismic stations, we selected 37, guaranteeing at least one seismic station on each of the islands plus a number located on the island of Sicily (Figure 1). Seismic stations deployed on the island of Sicily (13 stations) belong to the portable seismic network provided by the Geophysical Instrument Pool Potsdam (GIPP), Germany. They are DATACUBE3 recorders and triaxial PE-6/B 4.5 Hz or Mark L-4C-3D seismometers. Seismic stations in the Aeolian Islands (24 stations) belong to the INGV (Istituto Nazionale di Geofisica e Vulcanologia) permanent network operated by the Osservatorio Etneo (the INGV Etna Observatory). Seismic stations of this network are broadband three-component Nanometrics Trillium seismometers (see Ibáñez et al., 2016a; Ibáñez et al., 2016b, for additional details). This distribution is not ideal for highdefinition analysis, but was the best available. Of all the air- gun shots made in the Tyrrhenian Sea, we initially selected 3,450 (Figure 1). The available shot-station pairs provided an initial number of 127,650 waveforms.
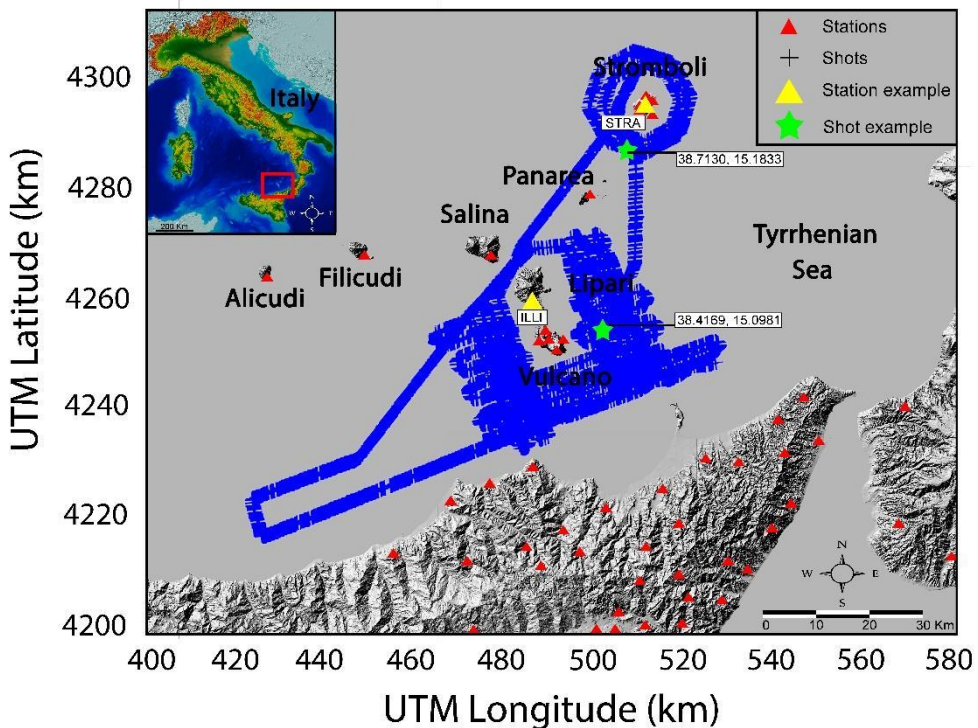
FIGURE 1 | Map of the study region. Red triangles represent the locations of seismic stations used in this study. Blue crosses are the locations of air-gun shots generated during

the TOMO-ETNA experiment. The highlighted stations (yellow triangles) and shots (green stars) are the stations and shots used as examples in Figures 2, 3. The Digital Elevation Model (DEM) used for this figure was obtained using the database of Tarquini et al. (2007).

3.2 METHODOLOGY

The TOMO-ETNA database has previously been used to determine the attenuation structure of the Mt. Etna volcano region. For these studies, two methodologies have been used: 1) the separation of the intrinsic attenuation (Q_i^{-1}) and scattering (Q_s^{-1}) contributions through the diffusion model (Wu, 1985) and its 2-D spatial representation (Ibáñez et al., 2020); and 2) a 3-D attenuation tomographic study (Castro-Melgar et al., 2021) using the coda normalization method (Aki, 1980). Therefore, we tested the resolution of both of these methods in this study. The coda normalization method was ruled out owing to the poor resolution of the results (based on checkerboard and isolated anomaly tests). However, since the theoretical basis for the representation of the separation of Q_i^{-1} and Q_s^{-1} assigns attenuation values to a broader spatial region (e.g., Del Pezzo et al., 2018; Del Pezzo and Ibáñez, 2020), the checkerboard test indicated that a significant part of the region to be studied could be interpreted in a reliable way using this approach.

The diffusion method to obtain Q_i^{-1} and Q_s^{-1} and its spatial representation are explained in detail by numerus authors (e.g., Wegler and Luhr, 2001; Del Pezzo, 2008) and have been widely used (e.g., Prudencio et al., 2013a for Tenerife Island; Prudencio et al., 2013b for Deception Island; Prudencio et al., 2015c for Stromboli volcano; Prudencio et al., 2017a for Asama volcano; Prudencio et al., 2017b for Usu volcano; Prudencio et al., 2018 for Long Valley). This method is based in the assumption that the seismogram energy envelope can be modelled by the so-called radiative transfer equation (also called the transport model; Sato et al., 2012). Wegler and Luhr (2001) demonstrated that when the propagation medium can be assumed as extremely heterogeneous, as in volcanic structures or the shallowest part of the crust, then the diffusion approximation of the transport model is valid. In this approximation, the seismogram energy envelope is developed as a function of lapse time and source–receiver distance in terms of intrinsic and scattering attenuation coefficients. In this approach the seismic energy density as a

86

function of time and source–station distance is linearised with respect to the two attenuation parameters, making it possible to separate the contributions of scattering and intrinsic attenuation effects through simple linear inversion (Prudencio et al., 2013a). Here, we simply highlight that by using the diffusivity (d) and coefficient for intrinsic attenuation (b) to estimate the intrinsic and scattering attenuation Q factors (Q_i and Q_s, respectively) as follows:

$$Q_i = \frac{2\pi f}{b} \tag{1}$$

$$Q_s = \frac{2\pi f p d}{v^2} \tag{2}$$

where f is the frequency and v is the velocity of S waves. In addition, the total attenuation value ($Q_t{}^{-1}$) is represented as:

$$Q_t^{-1} = Q_i^{-1} + Q_s^{-1} \tag{3}$$

As described in the next section, the determination of the coefficients b and d is carried out by fitting the energy of the entire seismogram, after the arrival of the P-wave, according to the equations representing the diffusion model.
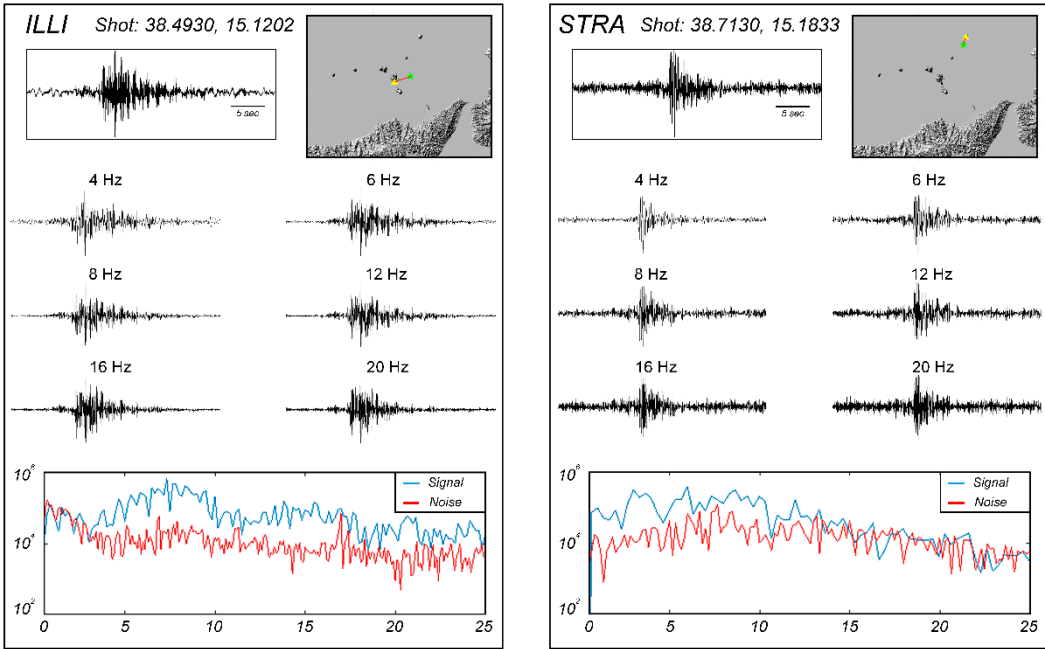
FIGURE 2 | Example seismograms recorded on Lipari and Stromboli islands. Signals were filtered in six selected frequency bands. The bottom plots show the spectra of the signal and pre-event noise, which reflect the quality of the signals. Seismic stations and shots are identified in Figure 1. The shot recorded at station ILLI is that depicted in Figure 3.

3.3 Data Analysis

The data analysis process was systematically structured to ensure the highest quality of data. This process is summarised in the following steps.

3.1.1 Signal-to-Noise Ratio

Each seismogram associated with a shot-station pair was studied according to its signal-to-noise spectral relationship for the selected frequency bands. To determine if a signal was able be analysed, or in which frequency bands the attenuation parameters could be studied, the signal-to-noise ratio should be higher than 2. This study was performed automatically. Each signal used was previously used by Díaz Moreno et al. (2018) for a study of the velocity tomography model. Therefore, each signal already had a determined

arrival time of the P wave. In this way, to determine the noise signal level, a 5 s pre-event window was selected 10 s before the arrival of the P wave. Similarly, from the arrival of the P phase, another 5 s window was taken. Finally, for the coda at the end of each window of the coda (20 or 30 s) another window of 5 s was recalculated. In this way all signals with P/noise and coda/noise ratios lower than 2 were discarded. Figure 2 shows an example of a signal used in this study in all frequency bands, and another example where the signal was used only for the band between 2 and 12 Hz. According to the theoretical active source model described in Coltelli et al. (2016), all the seismic signals could be analysed in the band between 4 and 20 Hz.

3.1.2 Filtering

To determine the different frequency bands for analysis, we followed the procedure described in Ibáñez et al. (2020). In the procedure described above, the quality of the signal was studied without filtering the signal. It is possible that this ratio is not optimal for the analysis of all frequencies. Therefore, we first analysed the spectra of a selected sample of seismograms to identify the frequency range in which the signal-to-noise ratio was suitable for further analysis. These frequency bands were determined according to previous studies and the theoretical spectra of the active source model (Coltelli et al., 2016). On the basis of this additional check we selected six frequency bands centred on 4, 6, 8, 12, 16, and 20 Hz. We filtered the active source seismograms using an eight-pole Butterworth bandpass filter with a bandwidth of fc $\pm$ 0.6 fc.
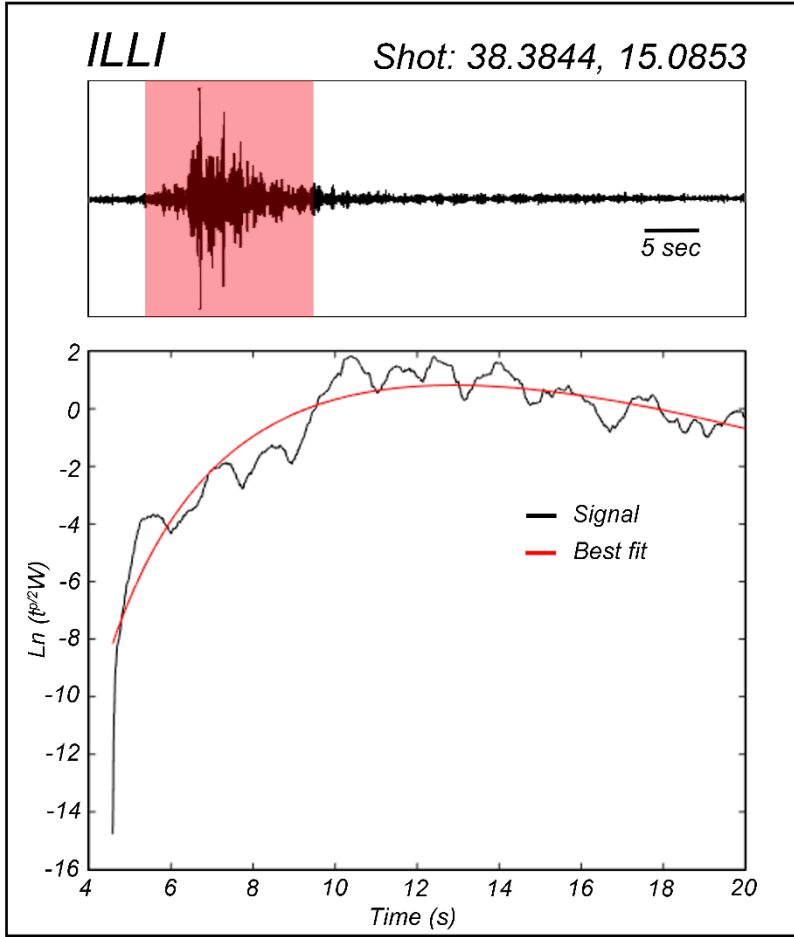
FIGURE 3 | Comparison of best fits between the data and model for an example seismogram recorded on the island of Lipari (see Figure 2).

3.1.3 Signal Extraction

Based on the signal-to-noise ratio, two analysis time windows with fixed lapse-times at 20 and 30 s were selected. The selected lapse times are associated with the duration of the signal but are also in agreement with the diffusion approximation, which means that longer lapse times will not follow the model. The start time of this window, t_{min}, corresponds to the P wave picking time determined by Díaz-Moreno et al., 2018 using an automatic signal processing algorithm described in García et al. (2016). To determine the end time of this window, we distinguished between window duration and lapse time. Lapse time is the time interval between the moment in which the active seismic signal was generated and the time in which the signal arrived at the seismic station. Given the fixed lapse times used here, we have different window analysis

durations. For short epicentral distances, the window length is larger than for large epicentral distances. This is because at short distances the arrival of the P wave is fixed earlier than for longer distances. To determine the lapse time and hence the window length, we assumed an average V_p velocity of 5.3 km/s, which corresponds to the average velocity of the first 4–5 km as determined by Díaz-Moreno et al. (2018); we fixed a V_p/V_s ratio of 1.73. According to the studies cited above, we assumed that our envelope was formed by P to S-converted waves. Following this estimation of start and end times of the window analysis, it was possible to extract the signal windows to be fitted within each selected frequency band.

3.1.4 Signal Envelope

We used the Hilbert transform to obtain the signal envelope of the energy of every extracted and filtered window. As described by Del Pezzo et al. (2016), there are no substantial differences in the attenuation values according to the seismic components; in this study we used the vertical component Z. We used a moving window of 0.7 s and 50% overlap to create the envelope to be fitted.

3.1.5 Water-Wave Extraction

The air-gun shots used for the present study were generated on the surface of the sea. This type of signal produces secondary waves that travel directly from the source to the station through the water volume (so-called water-waves); these have similar characteristics to the well-known T-waves (Carmona et al., 2015). This type of signal and how it could negatively affect in the determination of Q_i^{-1} and Q_s^{-1} were discussed in detail by Ibáñez et al. (2020). These waves must be extracted or removed from the envelope of the energy before proceeding with the estimation of the coefficients of attenuation. According to Eq. 8 of Ibáñez et al. (2020) it is possible to estimate the theoretical arrival of these waves. Once this time was calculated for every shot-station pair it was removed from the envelope of the signal for an interval between 0.5 s before and 2.5 s after the theoretically estimated first onset of water waves. As it is indicated in Figure 3 of Ibáñez et al. (2020) this procedure increases the quality of the fitting procedure.
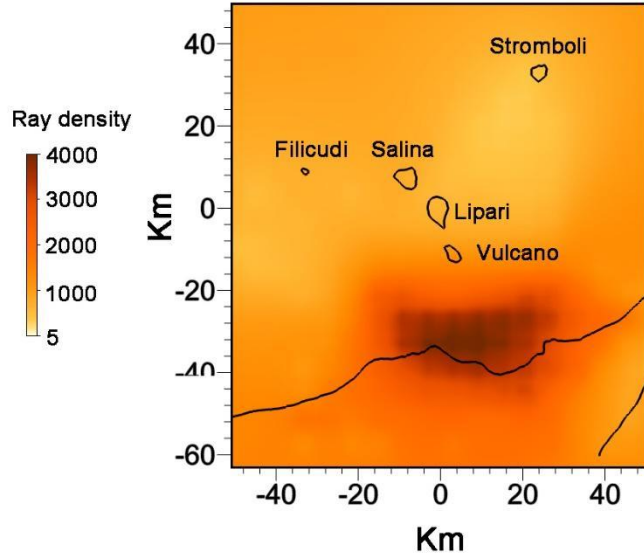
FIGURE 4 | Representation of the set of ray paths used in the present work. Blue triangles represent the positions of seismic stations. Red crosses are the locations of the air-gun shots generated during the TOMO-ETNA experiment.

3.1.6 Coefficient Estimation

After obtaining the envelope—that is, the energy according to Eq. 2 of Prudencio et al. (2013a)—we multiplied each value by $t^{p/2}$, where p is the theoretical geometrical spreading value, assumed to be 3 for S-waves (as applied in our previous studies), and then took the logarithm on the energy envelope. The whole envelope was fitted to Eq. 3 using the mean square fitting as done previously (e.g., Prudencio et al., 2013a). To define the quality of the results for each fit we obtained individual correlation coefficient; all results with correlation coefficients of <0.7 were removed. Using Eqs 5, 6 of Prudencio et al. (2013a), b and d were derived for every single shot-station pair. Using Eqs 1–3 of the present manuscript, we derived single values for the scattering (Q_s), intrinsic (Q_i), and total (Q_t) quality factors. Figure 3 shows the best fit obtained for an example seismogram recorded on the island of Lipari.

Figure 4 shows all of the densities of the ray paths used in the present work. As shown, the edges of the area, which includes the island of Stromboli, have less coverage than the centre region (on and below the islands of Lipari and Vulcano). However, even in the areas with the poorest coverage, more than 100 rays cross each of the cells in which the area under study is divided.

3.4 Data Mapping

To plot the spatial distribution of attenuation parameters, we followed the approach of Del Pezzo et al. (2016), as also described in Del Pezzo and Ibáñez (2020). Ibáñez et al. (2020) provide a detailed description of this procedure for data associated with Mt. Etna volcano. In brief, a back-projection method is used to plot spatial variations of Q_i and Q_s using a space-weighting function. We numerically estimated the energy envelope using the Monte Carlo approach of Yoshimoto (2000), who assumed that energy particles propagate according to Fermat's rule and change direction on meeting randomly distributed scatterers; this distribution depends on the attenuation parameters. At the receivers, the sum of their energies defines the energy envelope; as such, the weighting function can be estimated. We obtained an intrinsic attenuation weighting function from the path density, and a scattering attenuation weighting function from the collision density. For each source-station pair, the Q_i and Q_s distributions were obtained by applying the weighting function described in Del Pezzo et al. (2016). We divided the area into cells, and for each cell we assigned corresponding Q_i and Q_s values. The final spatial distribution corresponds to total, intrinsic, and scattering values obtained by averaging all values assigned to every cell. This method is dependent on the experimental configuration, and is not affected by data quality (Prudencio et al., 2017a; Prudencio et al., 2017b).

3.5 Resolution Test

Following Ibáñez et al. (2020), we performed a series of tests to determine the quality of the spatial representation of the Q_i, Q_s, and Q_t values. In contrast to the ordinary checkerboard-like 2-D test, as described in Prudencio et al. (2013a) and Prudencio et al. (2013b), we used a spatial representation of the uncertainty associated with the estimates

of Q values in each pixel, as described in detail in Del Pezzo and Ibáñez (2020). This method was the most suitable for the present case, in which we did not perform an inversion of parameters as in most seismic tomography studies, but a projection mapping of the estimated parameters in the space through the weighting functions. To complete the uncertainty representation, we also present the density of the spatial ray path coverage (Figure 4), where a higher density of rays indicates better represented areas. In Figure 5 we show the pattern of "'Resolution" quantity (see Del Pezzo and Ibáñez, 2020) and the standard deviation associated with the single Q values in each pixel.

The area with the best ray coverage (Figure 4) presents the best accuracy in our results, and is associated with a region covering the southernmost islands, the portion of the Tyrrhenian Sea between them, and northern Sicily. The entire archipelago of the Aeolian Islands is well resolved; the area located to the northwest of the selected region has the poorest reliability, although the errors do not exceed 25%. As seen in successive figures, the spatial distribution of the attenuation anomaly implies variation of up to 120%; as such, although the values themselves may not be exact, interpretations based on deviations from the mean will be reliable. Therefore, we conclude that the region selected for study is well represented by our seismic attenuation maps.
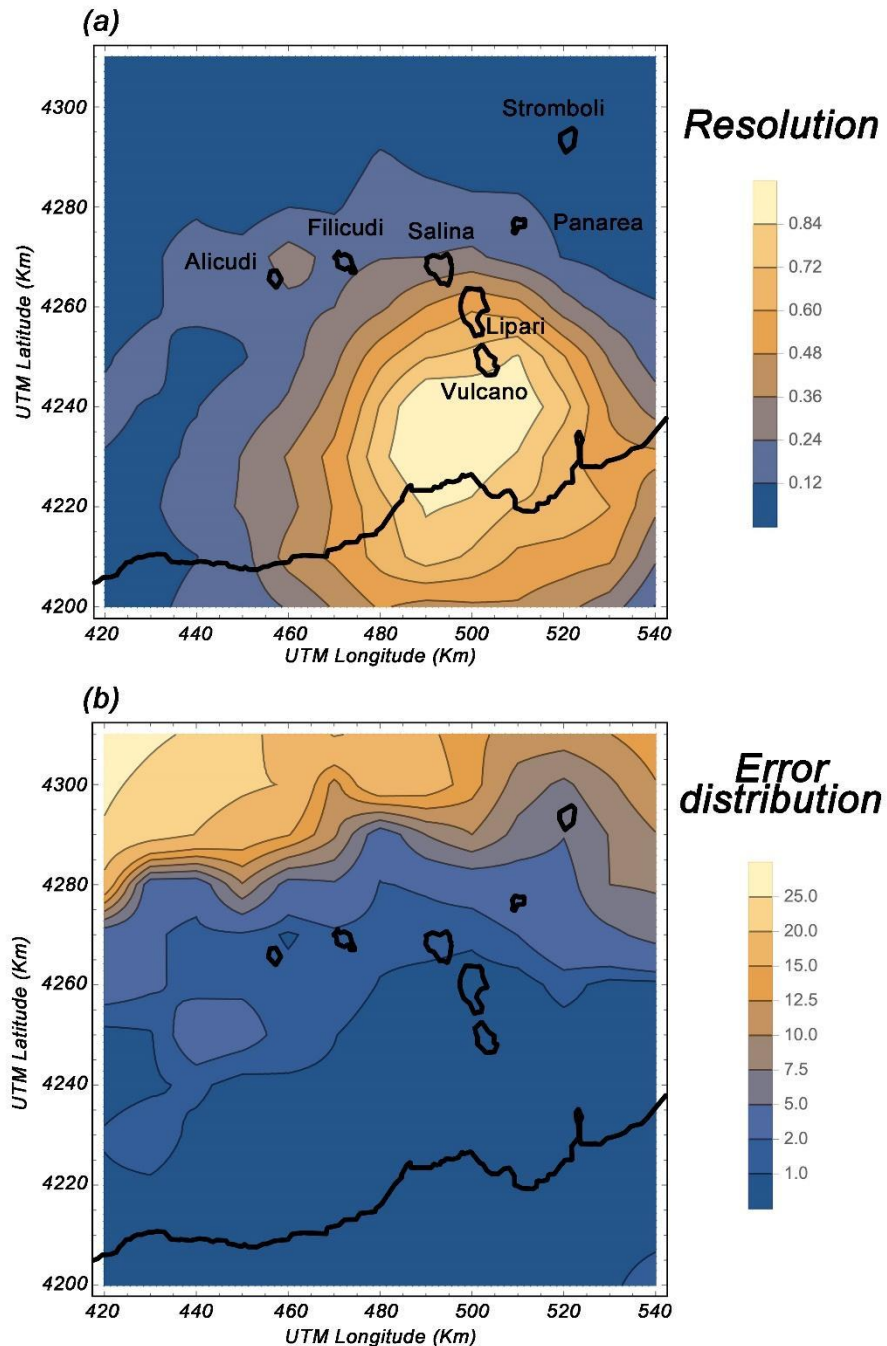
FIGURE 5 | Resolution tests to provide a quality check of the validity of the obtained images. Resolution tests showing the spatial distribution of (A) calculated standard deviation σ and (B) estimated errors. The results for the Aeolian Islands study region confirm that the data are reliable and can be used for interpretation.

95

4. RESULTS AND DISCUSSION

We excluded topographic effects, depth dependence, and energy leakage (Sanborn and Cormier, 2018), which can introduce bias; for example, topography generates surface wave scattering. While Prudencio et al. (2017a) found these effects are minor for the approach taken in this study (and even lower when attenuation is mapped as perturbation), Del Pezzo et al. (2018) showed that for shallow active sources, 3-D images strongly resemble 2-D images, minimising the utility of this approach.

TABLE 1 | Average values of Q_i^{-1}, Q_s^{-1}, Q_t^{-1}, Q_i, Q_s, and Q_t for a lapse time of 20 s for the Aeolian Islands.

Hz	Q_i^{-1}	Q_s^{-1}	Q_t^{-1}	Q_i	Q_s	Q_t
4	0.015	0.036	0.011	67	28	95
6	0.013	0.025	0.008	80	40	120
8	0.010	0.196	0.007	100	51	152
12	0.007	0.014	0.005	136	70	206
16	0.006	0.011	0.004	170	88	258
20	0.005	0.010	0.003	211	107	319

4.1 Average Values

Since our approach provides single Q_t, Q_s, and Q_i values for each shot-station pair, lapse time, and frequency band, it is possible to obtain average values for the region. It should be noted that in the study of seismic attenuation there is an indistinguishable, but sometimes confusing, use of the terms Q and Q^{-1}. Here, seismic attenuation refers directly to the term Q^{-1}, since the attenuation is directly proportional to Q^{-1}. The parameter Q represents the socalled quality factor; that is, it is the ratio of total energy to energy loss, which is inversely proportional to attenuation. When we refer to numerical seismic attenuation values, it is common to speak in terms of Q values, since Q takes positive values greater than 1. In general, highly attenuating structures are reflected by

low Q values and vice versa. We obtained the average values for Q_i^{-1}, Q_s^{-1}, Q_t^{-1}, Q_i, Q_s, and Q_t for lapse times of 20 and 30 s (Tables 1, 2, respectively).

We found that scattering dominates over intrinsic attenuation for all frequencies. As such, seismograms reflect geological heterogeneities at shallow depth. Using local and regional earthquakes with a source-receiver distance of 5–70 km, Del Pezzo et al. (2019) analysed intrinsic and scattering attenuation for a region that included our study area using the Multiple Lapse Time Window Analysis (MLTWA) method (Hoshiba, 1991; Akinci et al., 1995). They also found that scattering dominates over intrinsic absorption in the Aeolian Islands region. However, while we observed this for all frequency bands, they found that at higher frequencies intrinsic attenuation was stronger than scattering. These differences reflect differences in the depths of seismic sources. In this study, seismograms were generated at the surface (air-gun shots) and provide data pertinent to the uppermost crust (i.e., the first few kilometres). In Del Pezzo et al. (2019), earthquakes were deeper (~10 km) and could be recorded at distances of up to 100 km, and thus provided data to resolve deeper structures. These differences confirm that the Q factor increases with depth (Ibáñez et al., 1990; Badi et al., 2009).

Figure 6 compares Q_i and Q_s values obtained for different volcanic areas in studies performed by our research group. We compared results using similar time lapses; the shortest (15 s) was used for Deception and Stromboli islands and the largest (30 s) was used for the Long Valley case. For the remaining areas, a 20 s lapse time was used. We observe that Q_s is always significantly lower than Q_i, implying that scattering attenuation is stronger that intrinsic attenuation for all compared areas. Unsurprisingly, results derived using the MLTWA method (using earthquakes of different depths; Del Pezzo et al., 2019) show much higher Q (i.e., lower seismic attenuation) values (for both scattering and intrinsic attenuation). However, when comparing only those values obtained using the same method and data type, we generally observe the following results:

1) Q_s values for the Aeolian Islands exceed those of other volcanic regions. We suggest that this difference reflects subsurface structural characteristics. Although the region is obviously volcanic, the results are also influenced by the attenuation of oceanic crust, which has lower apparent scattering.

97

2) In terms of intrinsic attenuation, for a small lapse time (20 s), Qi for the Aeolian Islands region is among the lowest of the studied regions (i.e., it exhibits greater intrinsic attenuation). However, for a longer lapse time (30 s), the intrinsic attenuation is the lowest (i.e., the highest Q_i). These differences reflect a number of different factors. For a small lapse time, the areas sampled by seismic waves are very shallow and the contribution to attenuation includes volcanic structures and marine sediments. These sediments make a lower contribution to the scattering effect, but have a greater impact on intrinsic attenuation. For longer lapse times, seismic waves sample to greater depths, and thus there is a contribution from oceanic crust, which is less attenuating than any volcanic structure.

These results justify the need to obtain maps of the spatial distributions of both scattering and intrinsic attenuation in order to determine how volcanic structures affect these values.

TABLE 2 | Average values of Q_i^{-1}, Q_s^{-1}, Q_t^{-1}, Q_i, Q_s, and Q_t for a lapse time of 30 s for the Aeolian Islands.

Hz	Q_i^{-1}	Q_s^{-1}	Q_t^{-1}	Q_i	Q_s	Q_t
4	0.006	0.016	0.004	181	64	245
6	0.005	0.010	0.003	207	98	305
8	0.004	0.008	0.003	257	123	380
12	0.003	0.006	0.002	344	164	508
16	0.002	0.005	0.002	430	197	627
20	0.002	0.004	0.001	523	229	752

4.2 Spatial Distribution of Attenuation Values

Spatial representation of attenuation was performed by plotting the distribution of Q^{-1} values (directly proportional to the attenuation) rather than by plotting the absolute values. The Q^{-1} values were calculated as the difference in percentage from the average value, with a maximum of up to ±120%. We use a rainbow colour scale, where the average value of the seismic attenuation is represented in green, areas of low attenuation

are represented by cold colours (tending towards blue), and areas of high attenuation are represented by warm colours (tending towards red). With the exception of some peripheral areas, the study region is well-resolved.
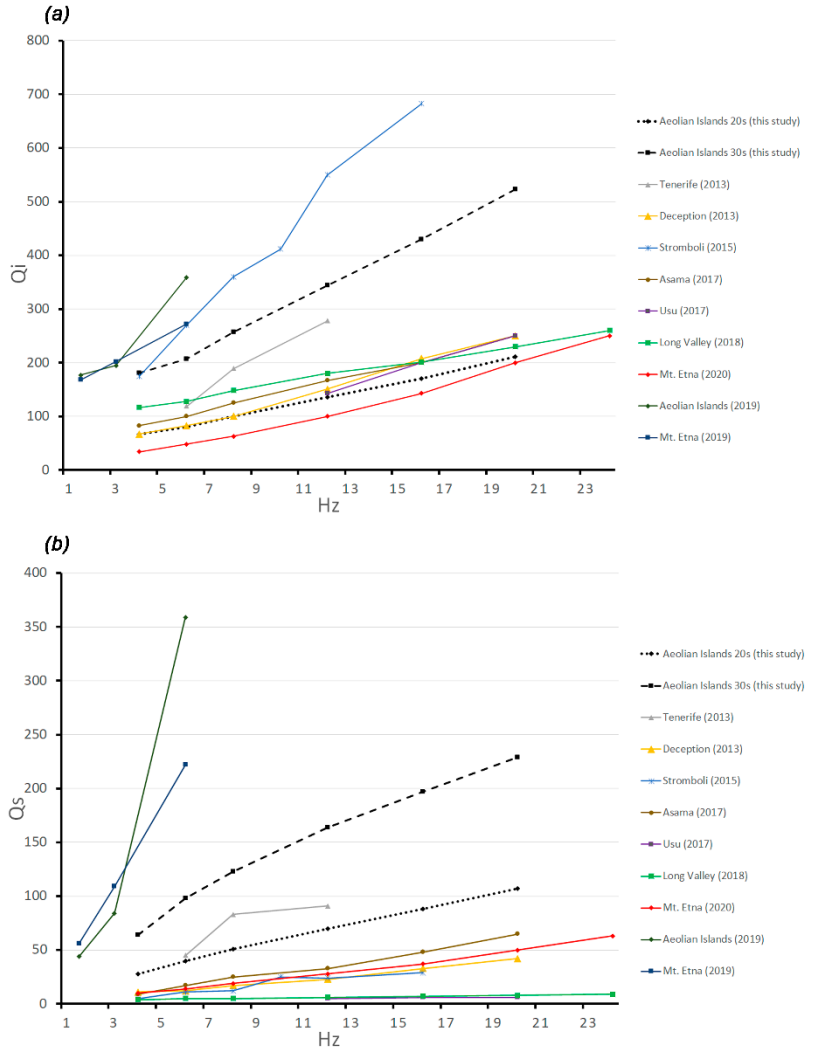
FIGURE 6 | Seismic attenuation for different volcanic regions. Comparisons of (A) Q^i and (B) Q^s for different regions using similar methodologies. The different results were obtained from the following references: Tenerife (2013) from Prudencio et al. (2013a); Deception (2013) from Prudencio et al. (2013b); Stromboli (2015) from Prudencio et al. (2015c); Asama (2017) from Prudencio et al. (2017a); Usu (2017) from Prudencio et al. (2017b); Long Valley (2018) from Prudencio et al. (2018); Mt. Etna (2019) and Aeolian Islands (2019) from Del Pezzo et al. (2019); Mt. Etna (2020) from Ibáñez et al. (2020).

As previously mentioned, the mean attenuation by scattering dominates over the intrinsic attenuation. We investigated whether this trend is general for the entire region under study or if there are structural elements for which the opposite occurs. Figure 7 shows anomaly maps for intrinsic, scattering, and total attenuation (represented by Q^{-1}) for the 4 Hz frequency of the two lapse times analysed (20 and 30 s, as shown in Figures 7A,B, respectively). In these maps we have used the same colour scale for all values, for Q_T, Q_S, and Q_i. On this scale, the lowest Q values are represented in red and the highest in blue. In this way, areas with the greatest attenuation are dominated by red hues, and those with the lowest attenuation by blue hues.

In general, scattering attenuation dominates over intrinsic attenuation throughout the region. To better illustrate this observation, Figure 8 shows the Q_S/Q_i ratios for the 20 s time lapse and the frequencies of 4, 6, 8, and 12 Hz. As observed for the entire region, this ratio is less than 1, which confirms that attenuation by scattering clearly dominates over intrinsic attenuation. We must emphasize that around the islands of Stromboli, Lipari, and Vulcano, this scattering effect is an order of magnitude greater than that of areas located further to the west, where marine deposits predominate and where there is a certain similarity between the two attenuation mechanisms.

We made maps of the spatial distributions of intrinsic (Figure 9) and scattering attenuation (Figure 10), from which we identified a set of attenuation anomalies. We interpret as anomalies those zones that differ significantly from the mean value of the region (represented by green hues). From the intrinsic attenuation maps, we identified at least seven regions (labelled as I1 to I7) and from the scattering maps another four anomalous areas (labelled as S1 to S4).

Table 3 shows the average size of the main identified attenuation anomalies, both for intrinsic and scattering attenuation. This sizes vary between a minimum area of ~400 km2 to some of more than 2,400 km2. As the total size of the studied region is 16,800 km2, these represent proportionally small-scale attenuation anomalies.
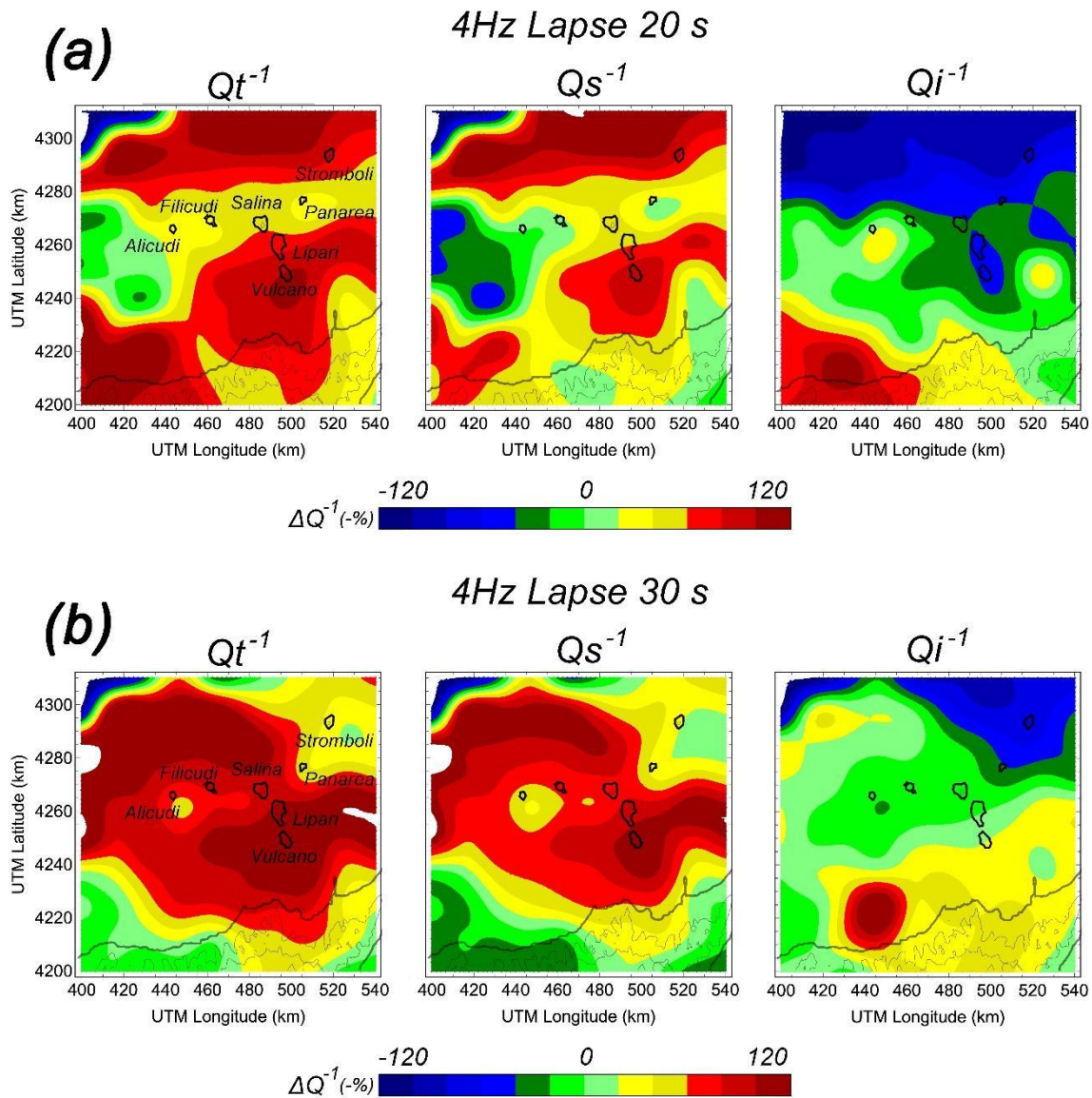
FIGURE 7 | Attenuation anomaly maps of intrinsic, scattering, and total attenuation (represented by Q^{-1}) for a frequency of 4 Hz. Maps are given for two lapse times: (A) 20 s and (B) 30 s.

At this time, we do not have an explanation for all of these regions; however, for the others we are able to offer some interpretation.

In reference to the spatial distribution of the intrinsic attenuation (Figure 9), we offer the following observations:

(1) From Tables 1, 2, there is not a strong dependency on frequency. In areas of high intrinsic attenuation, the dependence on frequency is even lower.

(2) Two regions, I1 and I2, show relatively elevated intrinsic attenuation. Neither appears to be directly associated with volcanic phenomena, but rather with attenuating effects of the oceanic crust. However, for the lapse time of 30 s and at higher frequencies, I1 and I2 tend to unify and may be associated with volcanic structures of the islands of Vulcano and Lipari.

As discussed, this high intrinsic attenuation likely reflects sedimentary deposits on the seabed, which in this region are enhanced by the additional presence of volcanoclastic deposits (e.g., Romagnoli et al., 2013). According to De Ritis et al. (2010), these areas are also characterised by negative density and magnetization contrasts owing to the thick sedimentary cover.

In reference to the spatial distribution of the scattering attenuation (Figure 10), we make the following observations:

(1) Attenuation by scattering is more dependent on frequency than intrinsic attenuation. In this way, an evident shift from high attenuation anomalies at low frequencies to low attenuation anomalies at high frequencies is observed.

(2) We identified two areas, S1 and S2, associated with Volcanic structural elements, where attenuation by scattering is much more intense than in the rest of the region.

Lapse time 20 s
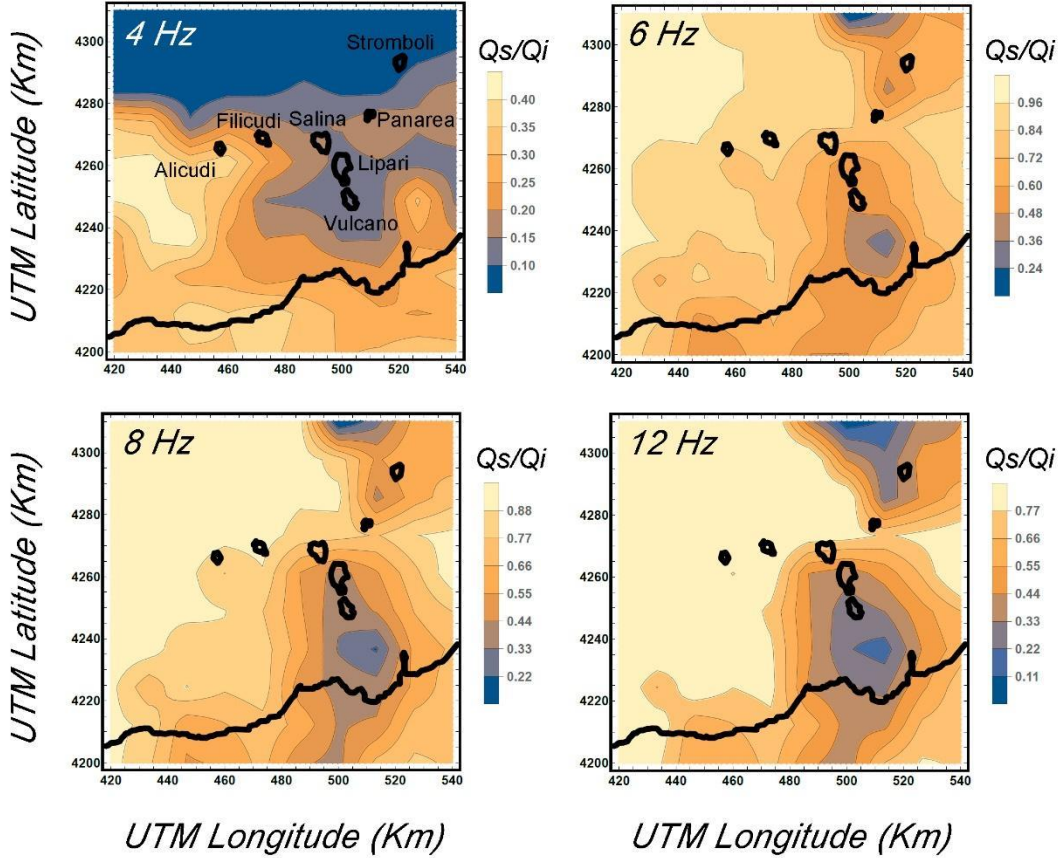
FIGURE 8 | Maps of Q_s/Q_i ratios for frequencies of 4, 6, 8, and 12 Hz with a lapse time of 20 s.

It is possible to explain these two observations based on the volcanic nature of the region; that is, on the presence of volcanic islands, where the dependence on frequency is obvious. As discussed, the islands are small in size, and scattering depends on the relationship between the dimensions of the heterogeneity and the wavelength of the incident wave. The fact that scattering attenuation tends to disappear at high frequencies (i.e., at shorter wavelengths) shows that it is the volcanic structures of the islands as a whole that most influence this type of seismic attenuation. For this reason, scattering attenuation is more relevant than intrinsic attenuation. Finally, the two regions marked as S1 and S2 are generally associated with volcanic structures and if these results are compared to the velocity tomography of Díaz-Moreno et al. (2018) there is a high

concordance between high seismic attenuation by scattering and low velocity of propagation. In other words, structures of magmatic origin produce greater scattering of seismic waves. It is interesting to highlight that these two areas of high attenuation by scattering were also identified in a pioneering study of attenuation carried out by Del Pezzo et al. (1979).

On the other hand, at the time lapse of 20 s (Figure 10) there is a small region located to the west (marked as S4) where there is a low scattering effect and medium or low intrinsic attenuation. As this region is outside of the volcanic zones and is only observable for a 20 s time lapse (i.e., for the most superficial areas) we interpret this as attenuation due to the presence of marine sediments in the oceanic crust. This area belongs to the Cefalù Basin, a structural depression filled by a sedimentary cover formed by Tortonian to recent deposits (Pepe et al., 2004). The thickness of the Cefalù Basin cover is variable and can reach 1.5–2.0 km (Pepe et al., 2004; Milia et al., 2018), and gives rise to negative gravimetric and magnetic anomalies (De Ritis et al., 2010). According to Milia et al. (2018), the sedimentary cover of the Cefalù basin is made of deep-water turbidite deposits.
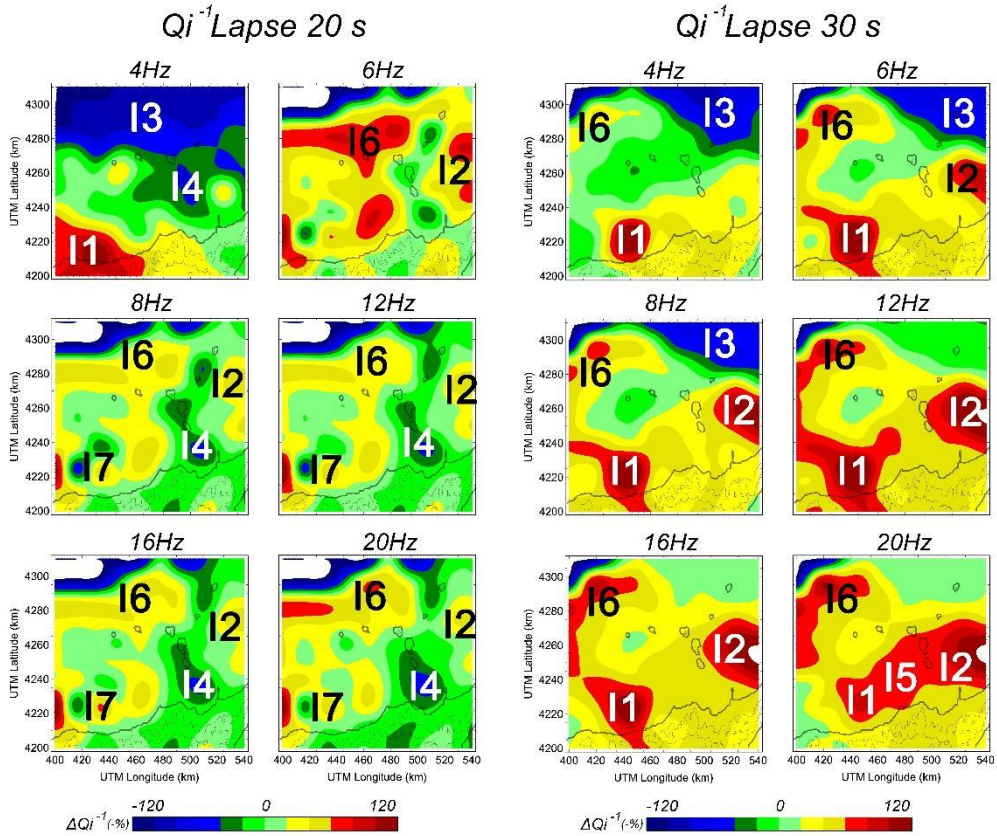
FIGURE 9 | Maps of intrinsic attenuation (represented by Q_i^{-1}) for all analysed frequency bands. Maps are given for two lapse times: (A) 20 s and (B) 30 s.

In summary, our results show that this area is not a large volcanic structural complex such as that of nearby Mt. Etna volcano, but rather it contains multiple dimensionally smaller volcanic structures.

It is also worth noting that the S1 feature spatially coincides with the northernmost part of the so-called Aeolian–Tindari–Letojanni fault system (e.g., Ghisetti, 1979; Lanzafame and Bousquet, 1997; Palano et al., 2012; Barreca et al., 2014). This system extends from the central sector of the Aeolian Archipelago to the Ionian coast and is characterized by right-lateral kinematics (Alparone et al., 1998; Ventura et al., 1999; De Astis et al., 2003; Ventura, 2013). Moreover, the unusual NNW–SSE orientation of the islands composing the central sector of the Aeolian archipelago (Salina, Lipari, and Vulcano), in contrast to the general geometry of the arc, is considered to be the expression of such a major regional tectonic structure, whose interpretation is still open to debate

(Barreca et al., 2014 and references therein). It is not surprising that a rock volume affected by a fault system is characterised by high seismic attenuation by scattering. Based on a 3-D distribution of scatterers in central California, Nishigami (2000) found that the scatterer distribution was roughly correlated with the surface trace of the San Andreas fault system. High attenuation and high-scattering anomalies were also reported by De Siena et al. (2014) for fractured volumes of the Mt. St. Helens Seismic Zone.
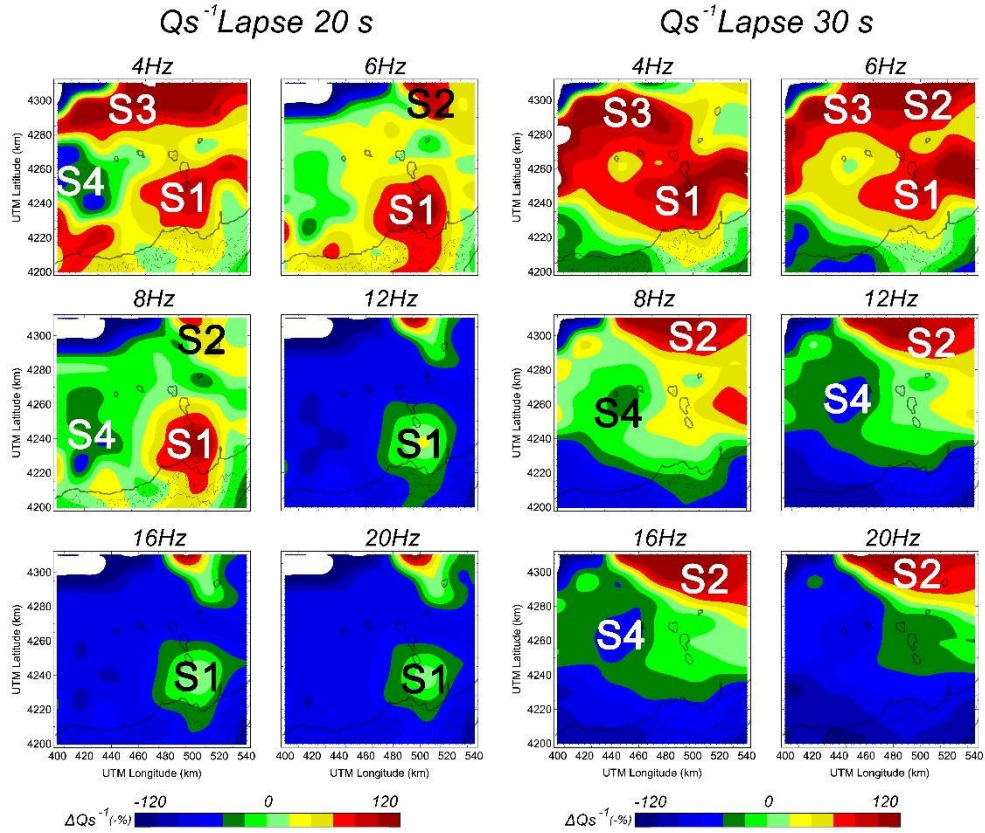
FIGURE 10 | Maps of scattering attenuation (represented by Q_s^{-1}) for all analysed frequency bands. Maps are given for two lapse times: (A) 20 s and (B) 30 s.

In the present work we have demonstrated that kernel-based, separated intrinsic- and scattering-attenuation imaging allows the detection of local lateral contrasts in attenuation even for small lateral contrasts. This technique offers new opportunities study complex regions, including volcanic regions dominated by small islands or several

isolated volcanic complexes, in order to better constrain their structures and improve understanding of their dynamics.

TABLE 3 | Average sizes of identified anomalies in the Aeolian Islands region (total area = 16,800 km2).

Q_i	Size (km^2)	Q_s	Size (km^2)
I1	1,225	S1	1,800
I2	600	S2	1,050
I3	2,000	S3	2,400
I4	728	S4	400
I5	1,225		
I6	900		
I7	400		

5. CONCLUSIONS

We have presented the first seismic attenuation maps for the volcanic archipelago of the Aeolian Islands. The special geographic distribution of the region, along with the limited data and seismic station coverage, limits the resolution of our images; however, we have been able to separate the contributions of intrinsic and scattering seismic attenuation and to represent them spatially. The mean attenuation values reflect that, as expected, the region is highly attenuating. In general, its physical behaviour from the point of view of attenuation processes is similar to that of other volcanic regions previously studied. As it has been observed, scattering phenomena are more important than dissipative phenomena when they are attenuating the elastic energy of seismic waves. This region contains small volcanic islands, and we observed that scattering is strongly associated with the volcanic complexes represented by the islands. For this reason, for high frequencies, where the morphology of the islands is less constrained, there is a strong change in the attenuative behaviour (i.e., the scattering process is less relevant). It is well known that scattering phenomena are associated with the size of the heterogeneities. When incident wavelengths are similar to these heterogeneities, the scattering phenomena of seismic waves are more intense. In our case, as we increased the

frequency of the waves, their wavelengths decreased, and the island structures producing scattering became less efficient. For this reason, we observed that there is a greater contribution of scattering at low frequencies compared with high frequencies. A particularly interesting observation is the influence of marine sediments on seismic attenuation. In areas where the influence of volcanic structures is less significant, intrinsic attenuation is more relevant than scattering attenuation. Although this observation is common to many studies, we have observed this change in behaviour over a relatively small region and over short distances. Our results show that this area is not a large volcanic structural complex such as that of nearby Mt. Etna volcano, but rather it contains multiple dimensionally smaller and isolated volcanic structures with no apparent physical connection, at least in the subsurface portion (Ruch et al., 2016 postulate that Lipari and Vulcano belong to the same magmatic system). This confirms that the model used for the determination and separation of attenuation types is a very powerful tool for structural characterization based on the physical properties of the Earth's crust. For seismic attenuation studies of small-dimension volcanic arcs, like the Aeolian Island, the detection of lateral small-scale attenuation contrasts improves geological interpretation, allowing us to separate consolidated marine structures from independent volcanic bodies. We believe that our findings will open up new research avenues for similar regions around the world.

DATA AVAILABILITY STATEMENT

Publicly available datasets were analyzed in this study. This data can be found here: https://geofon.gfz-potsdam.de/doi/network/1T/2014.

AUTHOR CONTRIBUTIONS

IC-M: Data analysis. This work forms a part of his PhD research. JP: Experimental planning and data analysis, and manuscript preparation. PhD co-advisor. AC: Revision of the manuscript and interpretation of the results. EP: Data analysis and quality checking of the results. JI: Coordinator of the research team, experimental planning, and manuscript preparation. PhD co-advisor.

REFERENCES

Aki, K. (1980). Scattering and Attenuation of Shear Waves in the Lithosphere. *J. Geophys. Res. 85*(B11), 6496–6504. doi:10.1029/jb085ib11p06496

Akinci, A., Pezzo, E., and Ibáñez, J. M. (1995). Separation of Scattering and Intrinsic Attenuation in Southern Spain and Western Anatolia (Turkey). *Geophys. J. Int. 121*(2), 337–353. doi:10.1111/j.1365-246x.1995.tb05715.x

Alparone, S., Cardaci, C., Privitera, E., and Spampinato, S. (1998). Stress Tensor Computation at the Aeolian Islands Based on Earthquake Fault-Plane Solutions. *Proc. Earthq. Fault Plane Solution*, 92–95. Database. Derived Parameter. Geodyn. Inf.

Badi, G., Del Pezzo, E., Ibanez, J. M., Bianco, F., Sabbione, N., and Araujo, M. (2009). Depth Dependent Seismic Scattering Attenuation in the Nuevo Cuyo Region (Southern central Andes). *Geophys. Res. Lett*. *36*(24), 1–5. doi:10.1029/2009gl041081

Barreca, G., Bruno, V., Cultrera, F., Mattia, M., Monaco, C., and Scarfì, L. (2014). New Insights in the Geodynamics of the Lipari-Vulcano Area (Aeolian Archipelago, Southern Italy) from Geological, Geodetic and Seismological Data. *J. Geodynamics 82*, 150–167. doi:10.1016/j.jog.2014.07.003

Bueno, A., Benitez, C., De Angelis, S., Moreno, A. D., and Ibanez, J. M. (2019). Volcano-seismic Transfer Learning and Uncertainty Quantification with Bayesian Neural

Networks. *IEEE Trans. Geosci. Remote Sens* *58*(2), 892–902. doi:10.1109/tgrs.2019.2941494

Bueno, A., Benítez, C., Zuccarello, L., De Angelis, S., and Ibáñez, J. M. (2021). End to End Bayesian Monitoring of Seismo Volcanic Dynamics. *IEEE Trans. Geosci. Remote Sens.* doi:10.1109/TGRS.2021.3076012

Carmona, E., Almendros, J., Alguacil, G., Soto, J. I., Luzón, F., and Ibáñez, J. M. (2015). Identification of T-Waves in the Alboran Sea. *Pure Appl. Geophys. 172*(11), 3179–3188. doi:10.1007/s00024-014-1018-1

Castellano, M., Augusti, V., De Cesare, W., Favali, P., Frugoni, F., Montuori, C., et al. (2008). Seismic Tomography experiment at Italy's Stromboli Volcano. *Eos Trans. AGU 89*(30), 269–270. doi:10.1029/2008eo300001

Castro-Melgar, I., Prudencio, J., Del Pezzo, E., Giampoccolo, E., and Ibáñez, J. M. (2021). Shallow Magma Storage beneath Mt. Etna: Evidences from New Attenuation Tomography and Existing Velocity Models. *J. Geophy. Res. 126*(7), 1–18. doi:10.1029/2021JB022094

Chiarabba, C., De Gori, P., and Speranza, F. (2008). The Southern Tyrrhenian Subduction Zone: Deep Geometry, Magmatism and Plio-Pleistocene Evolution. *Earth Planet. Sci. Lett. 268*(3–4), 408–423. doi:10.1016/j.epsl.2008.01.036

Chouet, B., De Luca, G., Milana, G., Dawson, P., Martini, M., and Scarpa, R. (1998). Shallow Velocity Structure of Stromboli Volcano, Italy, Derived from Small-Aperture Array Measurements of Strombolian Tremor. *Bull. Seismol. Soc. Am. 88*(3), 653–666.

Coltelli, M., Cavallaro, D., Firetto Carlino, M., Cocchi, L., Muccini, F., D'Aessandro, A., et al. (2016). The marine Activities Performed within the TOMO-ETNA experiment. *Ann. Geophys. 59*(4), 1–23. doi:10.4401/ag-7081

De Astis, G., Ventura,G., andVilardo,G. (2003).Geodynamic Significance of theAeolian Volcanism (Southern Tyrrhenian Sea, Italy) in Light of Structural, Seismological, and Geochemical Data. *Tectonics 22*(4), 1–17. doi:10.1029/2003tc001506

De Luca, G., Filippi, L., Caccamo, D., Neri, G., and Scarpa, R. (1997). Crustal Structure and Seismicity of Southern Tyrrhenian basin. *Phys. Earth Planet. Int 103*(1–2), 117–133. doi:10.1016/s0031-9201(97)00026-5

De Ritis, R., Ventura, G., Chiappini, M., Carluccio, R., and Von Frese, R. (2010). Regional Magnetic and Gravity Anomaly Correlations of the Southern Tyrrhenian Sea. *Phys. Earth Planet. Int 181*(1–2), 27–41. doi:10.1016/j.pepi.2010.04.003

De Siena, L., Chiodini, G., Vilardo, G., Del Pezzo, E., Castellano, M., Colombelli, S., et al. (2017). Source and Dynamics of a Volcanic Caldera Unrest: Campi Flegrei, 1983-84. *Sci. Rep. 7*(1), 8099–8113. doi:10.1038/s41598-017-08192-7

De Siena, L., Thomas, C., Waite, G. P., Moran, S. C., and Klemme, S. (2014). Attenuation and Scattering Tomography of the Deep Plumbing System of Mount St. Helens. *J. Geophys. Res. Solid Earth 119*(11), 8223–8238. doi:10.1002/2014jb011372

Del Pezzo, E., De La Torre, A., Bianco, F., Ibáñez, J., Gabrielli, S., and De Siena, L. (2018). Numerically Calculated 3D Space-Weighting Functions to Image Crustal Volcanic Structures Using Diffuse Coda Waves. *Geosciences 8*(5), 175. doi:10.3390/geosciences8050175

Del Pezzo, E., Ferulano, F., Giarrusso, A., and Martini, M. (1983). Seismic Coda Q and Scaling Law of the Source Spectra at the Aeolian Islands, Southern Italy. *Bull. Seismol. Soc. Am. 73*(1), 97–108. doi:10.1785/bssa0730010097

Del Pezzo, E., Giampiccolo, E., Tuvè, T., Di Grazia, G., Gresta, S., and Ibàñez, J. M. (2019). Study of the Regional Pattern of Intrinsic and Scattering Seismic Attenuation in Eastern Sicily (Italy) from Local Earthquakes. *Geophys. J. Int. 218*(2), 1456–1468. doi:10.1093/gji/ggz208

Del Pezzo, E., and Ibáñez, J. M. (2020). Seismic Coda-Waves Imaging Based on Sensitivity Kernels Calculated Using an Heuristic Approach. *Geosciences 10*(8), 304. doi:10.3390/geosciences10080304

Del Pezzo, E., Ibáñez, J., Prudencio, J., Bianco, F., and De Siena, L. (2016). Absorption and Scattering 2-D Volcano Images from Numerically Calculated Space-Weighting Functions. *Geophys. J. Int. 206*(2), 742–756. doi:10.1093/gji/ggw171

Del Pezzo, E., Luongo, G., and Scarpa, R. (1979). Seismic Wave Transmission in Southern Tyrrhenian Sea. *Boll. Geofis. Teor. Appl. 21*(81), 53–66.

Díaz-Moreno, A., Barberi, G., Cocina, O., Koulakov, I., Scarfì, L., Zuccarello, L., et al. (2018). New Insights on Mt. Etna's Crust and Relationship with the Regional Tectonic

Framework from Joint Active and Passive P-Wave Seismic Tomography. *Surv. Geophys.* *39*(1), 57–97. doi:10.1007/s10712-017-9425-3

Gabrielli, S., De Siena, L., Napolitano, F., and Del Pezzo, E. (2020). Understanding Seismic Path Biases and Magmatic Activity at Mount St Helens Volcano before its 2004 Eruption. *Geophys. J. Int*. *222*(1), 169–188. doi:10.1093/gji/ggaa154

Ganci, G., Cappello, A., Bilotta, G., and Del Negro, C. (2020). How the Variety of Satellite Remote Sensing Data over Volcanoes Can Assist hazard Monitoring Efforts: The 2011 Eruption of Nabro Volcano. *Remote Sensing Environ*. *236*, 111426. doi:10.1016/j.rse.2019.111426

García, L., Álvarez, I., Benítez, C., Titos, M., Bueno, Á., Mota, S., et al. (2016). Advances on the Automatic Estimation of the P-Wave Onset Time. *Ann. Geophys*. *59*(4), 0434. doi:10.4401/ag-7087

García-Yeguas, A., Ibáñez, J. M., Koulakov, I., Jakovlev, A., Romero-Ruiz, M. C., and Prudencio, J. (2014). Seismic Tomography Model Reveals Mantle Magma Sources of Recent Volcanic Activity at El Hierro Island (Canary Islands, Spain). *Geophys. J. Int*. *199*(3), 1739–1750. doi:10.1093/gji/ggu339

García-Yeguas, A., Koulakov, I., Ibáñez, J. M., and Rietbrock, A. (2012). High Resolution 3D P Wave Velocity Structure beneath Tenerife Island (Canary Islands, Spain) Based on Tomographic Inversion of Active-Source Data. *J. Geophys. Res. Solid Earth 117*(B9), 1–20. doi:10.1029/2011jb008970

Ghisetti, F. (1979). Relazioni tra strutture e fasi trascorrenti e distensive lungo i sistemi Messina-Fiumefreddo, Tindari-Letojanni e Alia-Malvagna (Sicilia nordorientale): uno studio microtettonico. *Geol. Romana 18*, 23–58.

Giampiccolo, E., Del Pezzo, E., Tuvé, T., Grazia, Di., and Ibáñez, G. J. M. (2021). 3-D Q-Coda Attenuation Structure at Mt. Etna (Italy). *Geophys. J. Int*. *227*(1), 544–558. doi:10.1093/gji/ggab235

Giordano, G., and De Astis, G. (2021). The Summer 2019 Basaltic Vulcanian Eruptions (Paroxysms) of Stromboli. *Bull. Volcanol 83*(1), 1–27. doi:10.1007/s00445-020-01423-2

Giudicepietro, F., López, C., Macedonio, G., Alparone, S., Bianco, F., Calvari, S., et al. (2020). Geophysical Precursors of the July-August 2019 Paroxysmal Eruptive Phase and

Their Implications for Stromboli Volcano (Italy) Monitoring. *Sci. Rep.* *10*(1), 10296–10316. doi:10.1038/s41598-020-67220-1

Gvirtzman, Z., and Nur, A. (2001). Residual Topography, Lithospheric Structure and Sunken Slabs in the central Mediterranean. *Earth Planet. Sci. Lett*. *187*(1–2), 117–130. doi:10.1016/s0012-821x(01)00272-2

Havskov, J., Peña, J. A., Ibáñez, J. M., Ottemöller, L., and Martínez-Arévalo, C. (2003). Magnitude Scales for Very Local Earthquakes. Application for Deception Island Volcano (Antarctica). *J. Volcanol. Geotherm. Res*. *128*(1–3), 115–133. doi:10.1016/s0377-0273(03)00250-6

Hoshiba, M. (1991). Simulation of Multiple-Scattered Coda Wave Excitation Based on the Energy Conservation Law, *Phys. Earth Planet. Int*. *67*(1–2), 123–136. doi:10.1016/0031-9201(91)90066-q

Ibáñez, J. M., Castro-Melgar, I., Cocina, O., Zuccarello, L., Branca, S., Del Pezzo, E., et al. (2020). First 2-D Intrinsic and Scattering Attenuation Images of Mt Etna Volcano and Surrounding Region from Active Seismic Data. *Geophys. J. Int*. *220*(1), 267–277. doi:10.1093/gji/ggz450

Ibáñez, J. M., Del Pezzo, E., De Miguel, F., Herraiz, M., Alguacil, G., and Morales, J. (1990). Depth-dependent Seismic Attenuation in the Granada Zone (Southern Spain). *Bull. Seismol. Soc. Am*. *80*(5), 1232–1244.

Ibáñez, J. M., Díaz-Moreno, A., Prudencio, J., Patené, D., Zuccarello, L., Cocina, O., et al. (2016b). TOMO-ETNA experiment at Etna Volcano: Activities on Land. *Ann. Geophys. 59*(4), 1–23. doi:10.4401/ag-7080

Ibáñez, J. M., Lühr, B., and Dahm, T. (2014). TOMO-ETNA. GFZ *Data Services*. Other/Seismic Network. doi:10.14470/6G7569676919

Ibáñez, J. M., Prudencio, J., Díaz-Moreno, A., Patanè, D., Puglisi, G., Lühr, B. G., et al. (2016a). The TOMO-ETNA experiment: an Imaging Active Campaign at Mt. Etna Volcano. Context, Main Objectives, Working-Plans and Involved Research Projects. *Ann. Geophys*. *59*(4), 0426. doi:10.4401/ag-7079

Koulakov, I., and Shapiro, N. (2015). "Seismic Tomography of Volcanoes," in *Encyclopedia of Earthquake Engineering*. Editors M. Beer, I.A. Kougioumtzoglou, E.

Patelli, and S.K. Au (Heidelberg: Springer-Verlag Berlin), 51–1. doi:10.1007/978-3-642-36197-5

La Rocca, M., Petrosino, S., Saccorotti, G., Simini, M., Ibanez, J. M., Almendros, J., et al. (2000). Location of the Source and Shallow Velocity Model Deduced from the Explosion Quakes Recorded by Two Seismic Antennas at Stromboli Volcano. *Phys. Chem. Earth A. Solid Earth Geod 25*(9–11), 731–735. doi:10.1016/s1464-1895(00)00113-7

Lanzafame, G., and Bousquet, J. C. (1997). The Maltese Escarpment and its Extension from Mt. Etna to Aeolian Islands (Sicily): Importance and Evolution of a Lithosphere Discontinuity. *Acta Vulcanol 9*, 113–120.

Linde, N., Baron, L., Ricci, T., Finizola, A., Revil, A., Muccini, F., et al. (2014). 3-D Density Structure and Geological Evolution of Stromboli Volcano (Aeolian Islands, Italy) Inferred from Land-Based and Sea-Surface Gravity Data. *J. Volcanology Geothermal Res. 273*, 58–69. doi:10.1016/j.jvolgeores.2014.01.006

Lucchi, F., Peccerillo, A., Keller, J., Tranne, C. A., and Rossi, P. L. (2013). The Aeolian Islands Volcanoes. London: Geological Society of London.

Martínez, V. L., Titos, M., Benítez, C., Badi, G.,Casas, J.A.,Craig, V.H.O., et al. (2021). Advanced Signal Recognition Methods Applied to Seismo-Volcanic Events from Planchon Peteroa Volcanic Complex: Deep Neural Network Classifier. *J. South Am. Earth Sci. 107*, 103115. doi:10.1016/j.jsames.2020.103115

Milia, A., Iannace, P., Tesauro, M., and Torrente, M. M. (2018). Marsili and Cefalù Basins: The Evolution of a Rift System in the Southern Tyrrhenian Sea (Central Mediterranean). *Glob. Planet. Change 171*, 225–237. doi:10.1016/j.gloplacha.2017.12.003

Nishigami, K. y. (2000). Deep Crustal Heterogeneity along and Around the San Andreas Fault System in central California and its Relation to the Segmentation. *J. Geophys. Res. 105*(B4), 7983–7998. doi:10.1029/1999jb900381

Palano, M., Ferranti, L., Monaco, C., Mattia, M., Aloisi, M., Bruno, V., et al. (2012). GPS Velocity and Strain fields in Sicily and Southern Calabria, Italy: Updated Geodetic Constraints on Tectonic Block Interaction in the central Mediterranean. *J. Geophys. Res. Solid Earth 117*(B7). doi:10.1029/2012jb009254

Patanè, D., Barberi, G., De Gori, P., Cocina, O., Zuccarello, L., Garcia-Yeguas, A., et al. (2017). The Shallow Magma Chamber of Stromboli Volcano (Italy). *Geophys. Res. Lett.* *44*(13), 6589–6596. doi:10.1002/2017gl073008

Pepe, F., Bertotti, G., Cella, F., and Marsella, E. (2000). Rifted Margin Formation in the South Tyrrhenian Sea: A High-Resolution Seismic Profile across the north Sicily Passive continental Margin. *Tectonics 19*(2), 241–257. doi:10.1029/1999tc900067

Pepe, F., Bertotti, G., and Cloetingh, S. (2004). Tectono-stratigraphic Modelling of the North Sicily continental Margin (Southern Tyrrhenian Sea). *Tectonophysics 384*(1–4), 257–273. doi:10.1016/j.tecto.2004.04.002

Petrosino, S., Cusano, P., Saccorotti, G., and Del Pezzo, E. (2002). Seismic Attenuation and Shallow Velocity Structures at Stromboli Volcano, Italy. *Bull. Seismological Soc. America 92*(3), 1102–1116. doi:10.1785/0120010147

Petrosino, S., La Rocca, M., and Del Pezzo, E. (1999). Shallow Velocity Model of the Northern Flank of Stromboli Volcano, Deduced by High Frequency Surface Wave Dispersion. *J. Seismol 3*(1), 83–94. doi:10.1023/a:1009716203083

Pezzo, E. D. (2008). "Chapter 13 Seismic Wave Scattering in Volcanoes. "Seismic Wave Scattering in Volcanoes"," in *Earth Heterogeneity and Scattering Effects on Seismic Waves*. Editor R. Dmowska (Elsevier), *50*, 353–371. doi:10.1016/S0065-2687(08)00013-7

Pontevivo, A., and Panza, G. F. (2006). The Lithosphere-Asthenosphere System in the Calabrian Arc and Surrounding Seas - Southern Italy. *Pure Appl. Geophys. 163*(8), 1617–1659. doi:10.1007/s00024-006-0093-3

Prudencio, J., Aoki, Y., Takeo, M., Ibáñez, J. M., Del Pezzo, E., and Song, W. (2017a). Separation of Scattering and Intrinsic Attenuation at Asama Volcano (Japan): Evidence of High Volcanic Structural Contrasts. *J. Volcanology Geothermal Res*. 333-334, 96–103. doi:10.1016/j.jvolgeores.2017.01.014

Prudencio, J., De Siena, L., Ibáñez, J. M., Del Pezzo, E., García-Yeguas, A., and Díaz-Moreno, A. (2015a). The 3D Attenuation Structure of Deception Island (Antarctica). *Surv. Geophys. 36*(3), 371–390. doi:10.1007/s10712-015-9322-6

Prudencio, J., Del Pezzo, E., García-Yeguas, A., and Ibáñez, J. M. (2013a). Spatial Distribution of Intrinsic and Scattering Seismic Attenuation in Active Volcanic Islands - I: Model and the Case of Tenerife Island. *Geophys. J. Int*. *195*(3), 1942–1956. doi:10.1093/gji/ggt361

Prudencio, J., Del Pezzo, E., Ibáñez, J. M., Giampiccolo, E., and Patané, D. (2015c). Two-dimensional Seismic Attenuation Images of Stromboli Island Using Active Data. *Geophys. Res. Lett*. *42*(6), 1717–1724. doi:10.1002/2015gl063293

Prudencio, J., Ibáñez, J.M., Del Pezzo, E., Martí, J., García-Yeguas, A., and De Siena, L. (2015b). 3D Attenuation Tomography of the Volcanic Island of Tenerife (Canary Islands). *Surv. Geophys*. *36*(5), 693–716. doi:10.1007/s10712-015-9333-3

Prudencio, J., Ibáñez, J. M., García-Yeguas, A., Del Pezzo, E., and Posadas, A. M. (2013b). Spatial Distribution of Intrinsic and Scattering Seismic Attenuation in Active Volcanic Islands - II: Deception Island Images. *Geophys. J. Int*. *195*(3), 1957–1969. doi:10.1093/gji/ggt360

Prudencio, J., and Manga, M. (2020). 3-D Seismic Attenuation Structure of Long Valley Caldera: Looking for Melt Bodies in the Shallow Crust. *Geophys. J. Int*. *220*(3), 1677–1686. doi:10.1093/gji/ggz543

Prudencio, J., Manga, M., and Taira, T. (2018). Subsurface Structure of Long Valley Caldera Imaged with Seismic Scattering and Intrinsic Attenuation. *J. Geophys. Res. Solid Earth 123*(7), 5987–5999. doi:10.1029/2017jb014986

Prudencio, J., Taira, T., Aoki, Y., Aoyama, H., and Onizawa, S. (2017b). Intrinsic and Scattering Attenuation Images of Usu Volcano, Japan. *Bull. Volcanol 79*(4), 29. doi:10.1007/s00445-017-1117-9

Rawlinson, N., Pozgay, S., and Fishwick, S. (2010). Seismic Tomography: a Window into Deep Earth. *Phys. Earth Planet. Int 178*(3–4), 101–135. doi:10.1016/j.pepi.2009.10.002

Romagnoli, C., Casalbore, D., Bortoluzzi, G., Bosman, A., Chiocci, F. L., D'Oriano, F., et al. (2013). Chapter 4 Bathy-Morphological Setting of the Aeolian Islands. *Geol. Soc. Lond. Mem*. *37*(1), 27–36. doi:10.1144/m37.4

Rosi, M., Pistolesi, M., Bertagnini, A., Landi, P., Pompilio, M., and Di Roberto, A. (2013). Chapter 14 Stromboli Volcano, Aeolian Islands (Italy): Present Eruptive Activity and Hazards. *Geol. Soc. Lond. Mem.* *37*(1), 473–490. doi:10.1144/m37.14

Ruch, J., Vezzoli, L., De Rosa, R., Di Lorenzo, R., and Acocella, V. (2016). Magmatic Control along a Strike-Slip Volcanic Arc: The central Aeolian Arc (Italy). *Tectonics 35*(2), 407–424. doi:10.1002/2015tc004060

Saccorotti, G., and Lokmer, I. (2021). A Review of Seismic Methods for Monitoring and Understanding Active Volcanoes. *Forecast. Plan. Volcanic Hazard. Risks Disaster*, 25–73. doi:10.1016/b978-0-12-818082-2.00002-0

Sanborn, C. J., and Cormier, V. F. (2018). Modelling the Blockage of Lg Waves from Three-Dimensional Variations in Crustal Structure. *Geophys. J. Int.* *214*(20), 1426–1440. doi:10.1093/gji/ggy206

Sato, H., Fehler, M., and Maeda, T. (2012). *Seismic Wave Propagation and Scattering in Heterogeneous Earth*. 2nd edn. Springer.

Selva, J., Bonadonna, C., Branca, S., De Astis, G., Gambino, S., Paonita, A., et al. (2020). *Multiple Hazards and Paths to Eruptions: A Review of the Volcanic System of Volcano*. Aeolian Islands, Italy: Earth Sci. Rev, 103186.

Selvaggi, G., and Chiarabba, C. (1995). Seismicity and P-Wave Velocity Image of the Southern Tyrrhenian Subduction Zone. *Geophys. J. Int.* *121*(3), 818–826. doi:10.1111/j.1365-246x.1995.tb06441.x

Shalev, E., Kenedi, C. L., Malin, P., Voight, V., Miller, V., Hidayat, D., et al. (2010). Threedimensional Seismic Velocity Tomography of Montserrat from the SEA-CALIPSO Offshore/onshore experiment. *Geophys. Res. Lett.* *37*(19), 1–6. doi:10.1029/2010gl042498

Tarquini, S., Isola, I., Favalli, M., and Battistini, A. (2007). *TINITALY, a Digital Elevation Model of Italy with a 10 M-Cell Size*. Version 1.0. Rome: Istituto Nazionale di Geofisica e Vulcanologia (INGV). Data set. doi:10.13127/TINITALY/1.0

Titos, M., Bueno, A., García, L., Benítez, M. C., and Ibañez, J. (2018). Detection and Classification of Continuous Volcano-Seismic Signals with Recurrent Neural Networks. *IEEE Trans. Geosci. Remote Sens 57*(4), 1936–1948. doi:10.1109/tgrs.2018.2870202

Ventura, G. (2013). Chapter 2 Kinematics of the Aeolian Volcanism (Southern Tyrrhenian Sea) from Geophysical and Geological Data. *Geol. Soc. Lond. Mem.* *37*(1), 3–11. doi:10.1144/m37.2

Ventura, G., Vilardo, G., Milano, G., and Pino, N. A. (1999). Relationships Among Crustal Structure, Volcanism and Strike–Slip Tectonics in the Lipari–Vulcano Volcanic Complex (Aeolian Islands, Southern Tyrrhenian Sea, Italy). *Phys. Earth Planet. Int* *116*(1–4), 31–52. doi:10.1016/s0031-9201(99)00117-x

Viccaro, M., Cannata, A., Cannavò, F., De Rosa, R., Giuffrida, M., Nicotra, E., et al. (2021). Shallow Conduit Dynamics Fuel the Unexpected Paroxysms of Stromboli Volcano during the Summer 2019. *Sci. Rep.* *11*(1), 266–315. doi:10.1038/s41598-020-79558-7

Voight, B., Sparks, R. S. J., Shalev, E., Minshull, T., Paulatto, M., Annen, C., et al. (2014). Chapter 15 the SEA-CALIPSO Volcano Imaging experiment at Montserrat: Plans, Campaigns at Sea and on Land, Scientific Results, and Lessons Learned. *Geol. Soc. Lond. Mem.* *39*(1), 253–289. doi:10.1144/m39.15

Wegler, U., and Lühr, B.-G. (2001). Scattering Behaviour at Merapi Volcano (Java) Revealed from an Active Seismic experiment. *Geophys. J. Int.* *145*(3), 579–592. doi:10.1046/j.1365-246x.2001.01390.x

Wu, R. (1985). Multiple Scattering and Energy Transfer of Seismic Waves—Separation of Scattering Effect from Intrinsic Attenuation—I. TheoreticalModelling. *Geophys. J. R. Astr. Sci.* *82*(1), 57–80. doi:10.1111/j.1365-246X.1985.tb05128.x

Yoshimoto, K. (2000). Monte Carlo Simulation of Seismogram Envelopes in Scattering media. *J. Geophys. Res.* *105*(B3), 6153–6161. doi:10.1029/1999jb900437

Zandomeneghi, D., Almendros, J., Ibáñez, J. M., and Saccorotti, G. (2008). Seismic Tomography of Central São Miguel, Azores. *Phys. Earth Planet. Int* *167*(1–2), 8–18. doi:10.1016/j.pepi.2008.02.005

Zandomeneghi, D., Barclay, A., Almendros, J., Ibañez, J. M., Wilcock, W. S., and Ben-Zvi, T. (2009). Crustal Structure of Deception Island Volcano from P Wave Seismic Tomography: Tectonic and Volcanic Implications. *J. Geophys. Res. Solid Earth* *114*(B6), 1–16. doi:10.1029/2008jb006119

Zulfakriza, Z., Nugraha, A. D., Widiyantoro, S., Cummins, P. R., Sahara, D. P., Rosalia, S., et al. (2020). Tomographic Imaging of the Agung-Batur Volcano Complex, Bali, Indonesia, from the Ambient Seismic Noise Field. *Front. Earth Sci*. *8*, 43. doi:10.3389/feart.2020.00043

II. PUBLICACIONES: MONTE ETNA

i. FIRST 2-D INTRINSIC AND SCATTERING ATTENUATION IMAGES OF MT ETNA VOLCANO AND SURROUNDING REGION FROM ACTIVE SEISMIC DATA

Ibáñez, J.M., Castro-Melgar, I., Cocina, O., Zuccarello, Z., Branca, S., Del Pezzo, E. and Prudencio, J. (2020). First 2-D intrinsic and scattering attenuation images of Mt Etna volcano and surrounding region from active seismic data, *Geophysical Journal International*, Volume 220, Issue 1, Pages 267–277, https://doi.org/10.1093/gji/ggz450

FIRST 2-D INTRINSIC AND SCATTERING ATTENUATION IMAGES OF MT ETNA VOLCANO AND SURROUNDING REGION FROM ACTIVE SEISMIC DATA

Jesús M. Ibáñez[1,2,3], Ignacio Castro-Melgar[3], Ornella Cocina[2], Luciano Zuccarello[1,3], Stefano Branca[2], Edoardo Del Pezzo[1,4] and Janire Prudencio[1,3]

[1]*Andalusian Institute of Geophysics, University of Granada, Profesor Clavera 12, 18071 Granada, Spain. E-mail:* jibanez@ugr.es

[2]*Istituto Nazionale di Geofisica e Vulcanologia, Osservatorio Etneo, 95125 Catania, Italy*

[3]*Department of Theoretical Physics and Cosmos, Faculty of Science, University of Granada, 18071 Granada, Spain*

[4]*Istiuto Nazionale di Geofisica e Vulcanologia, Osservatorio Vesuviano, 80124 Naples, Italy*

Summary

We present 2-D attenuation images of the Mt Etna volcanic region on the basis of separation of intrinsic and scattering effects. The analysis presented here exploits a large active seismic database that fully covers the area under study. We observe that scattering effects dominate over intrinsic attenuation, suggesting that the region is very heterogeneous. Comparison with analyses conducted at other volcanoes reveals that the Mt Etna region is characterized by high intrinsic attenuation, resulting from the presence of large volcanoclastic deposits at shallow depth. The 2-D distributions of intrinsic and scattering anomalies show the presence of regions characterized by high and low attenuation effects, corresponding to several tectonic and volcanic features. In particular, we identify a high attenuation region in the SW sector of the Mt Etna volcanic complex, which is correlated with high seismicity rates and volcanism. This work supports the hypothesis of a link between the dynamics of the SW flank and the recharge of the volcano in the last decades, occurring under the summit crater and, secondarily, the upper South rift zone.

1 INTRODUCTION

Knowledge of the subsurface structure of volcanoes is crucial to successfully model the dynamics of volcanic unrest, and to inform eruption early-warning. Traditionally, the internal structure of volcanic systems is investigated using seismic imaging methods such as 3-D seismic velocity tomography (e.g. Koulakov et al. 2016). Recently, seismic attenuation imaging focused on small-scale highly heterogeneous geological structures (Prudencio et al. 2015a, b; De Siena et al. 2016, 2017) has been extensively applied to provide information on important physical properties of the subsurface that are not characterized by ordinary seismic velocity tomography. The attenuation of seismic waves is mainly affected by inelastic absorption and scattering effects. Both can be associated with different structural properties, including the number and extent of fractures, the structural complexity or presence of heterogeneities (e.g. small and abrupt density and/or velocity changes that influence scattering phenomena), and rheological properties (e.g. thermal states of rocks and the rate of consolidation, which contribute to inelastic absorption). However, it is important to separate the relative influence of both factors in order to correctly interpret heterogeneities in the medium and identify the physical mechanisms producing seismic attenuation.

At present, the most accurate technique for discerning the contributions of scattering versus intrinsic attenuation is based on the Energy Transport Model (classical Boltzmann Integral Equation), or its two asymptotic approximations: (i) the so called Single Scattering Model (Aki and Chouet 1975), which is suitable for almost uniform media and (ii) the Diffusion Model (Wu 1985), used when heterogeneity is high, as in the case of volcanoes (e.g. Wegler and Lühr 2001; Del Pezzo 2008). Dainty and Toksöz (1981) first formulated a technique to fit the Energy Seismogram envelope to the Diffusion Model. Modifications of this technique by Wegler and Lühr (2001) and Wegler (2003) can be used to retrieve nearly unbiased estimates of both intrinsic and scattering attenuation coefficients from a single path seismogram, and hence can be used for imaging purposes. This technique has been applied in a number of studies (e.g. Prudencio

et al. 2013a; Del Pezzo et al. 2016) to obtain separate 2D attenuation images of volcanoes using data from shallow artificial sources whose coda is confined in the first 2–3 km of the crust. Coupled with the use of 2-D Gaussian Space Sensitivity Kernels, Prudencio et al. (2013a) used this approach to generate robust and stable images of both intrinsic and scattering attenuation beneath the island of Tenerife. Prudencio et al. (2013b) proposed a direct relationship between strong scattering effects and the presence of a potential partial melting body near the surface at Deception Island (Antarctica), and simultaneously, low intrinsic attenuation effects associated with the contact of a consolidate crystalline basement with the volcanic structure. At Stromboli volcano (Italy), Prudencio et al. (2015c) identified two main high attenuation zones, the first corresponding to the centre of the island, where volcanic activity takes place, and the second associated with an area where the ancient volcanic edifice is located. At Mt Asama volcano, Prudencio et al. (2017a) identified a zone where both scattering and intrinsic attenuation are present, corresponding to a strong structural contrast associated with the presence of a shallow magma intrusion. At Usu volcano, Japan, a gradient of scattering attenuation is associated with deepening of the basement, while intrinsic attenuation indicates areas of debris avalanche deposits (Prudencio et al. 2017b). This method can also be applied using passive data generated in the first few kilometers of the crust as Del Pezzo et al. (2016, 2018) or De Siena et al. (2017) demonstrated. An example of this shallow seismicity application is the study performed at Long Valley Caldera, USA (Prudencio et al. 2018). These authors highlighted the hydrothermal system and recent eruptive areas based on high attenuation (both intrinsic and scattering) values.

In this paper, we provide, for the first time, two separate images of intrinsic and scattering attenuation parameters within the upper 2–3 km of crust in the Mt. Etna volcanic region using the data set produced by the TOMO-ETNA seismic experiment (Coltelli et al. 2016; Ibañez et al. 2016a; Ibañez et al. 2016b); in this experiment, air-gun shots were recorded by a very dense temporary seismic network operating over this volcanic area.

The Mt Etna region is a dynamic environment in which continuous structural changes associated with different volcanic stages are observed (Patanè et al. 2006). One of the advantages of the present study is that the seismic data used were recorded over a very short-time period (less than 1 month), providing a snapshot of the volcanic structure in the first 2–3 km below the crust. Our results complement a 3-D seismic tomography

study performed by Diaz-Moreno et al. (2018) using the same data set. Mt Etna is one of the best studied volcanic regions worldwide. Ibáñez et al. 2016a and references therein provided a review of the most recent geophysical studies. Del Pezzo et al. 2019 and references therein offered a review of its tectonic and seismic framework. Chiarabba et al. (2004), De Gori et al. (2005), Martinez-Arevalo et al. (2005) and Alparone et al. (2012) give descriptions and interpretations of tomography images. However, uncertainties remain regarding the nature of several structures of the volcano at all depths.

2 METHOD: ASSUMING A DIFFUSIVE REGIME

Volcanoes are frequently characterized by very heterogeneous geological structures, which are well represented in seismology by diffusive random media (e.g. Wu 1985; Wegler and Lühr 2001; Del Pezzo 2008).

The diffusion approximation of the solution of the Energy Transport Equation is valid when

$$\lambda < lg \ll la, \tag{1}$$

where lambda is the dominant wavelength, and *la* and *lg* are the intrinsic and scattering mean free paths, respectively. In turn, *la* and *lg* can be written as

$$l = \frac{vQs}{2\pi f}; la = \frac{vQi}{2\pi f}, \tag{2}$$

where *f* is the dominant frequency, *v* is the wave velocity and *Qi* and *Qs* are the intrinsic and scattering quality factors, respectively. For lambda of ~0.3 km, corresponding to a dominant frequency of 6 Hz with *v* = 2.6 km s–1 (value of the theoretical *S*-waves velocity derived from the results of the tomography of Díaz-Moreno et al. 2018 using the same set of data in where *Vp* was of 4.4 km s–1 and the derived

124

Vp/Vs ratio was of 1.7), *lg*, as Del Pezzo (2008) indicates, should be greater than 0.3 and much less than 30 km, or, in the same range of frequency and wave speed, *Qs* should be approximately in the range between 30 and 100.

This condition is fulfilled at Mt Etna (e.g. Del Pezzo et al. 2019) and, therefore, the diffusion model is an appropriate approximation for the data used in the present study. We thus applied the transport equation in its asymptotic approximation (diffusion model) to separately estimate scattering and intrinsic attenuation coefficients (Sato et al. 2012). We followed the fitting procedure described by Wegler and Lühr (2001).

The seismogram energy envelope is described by the diffusion model ($E[r, t]$) as a function of source–receiver distance, *r* and lapse time, *t*, through the equation

$$E[r,t] = E_0(4\pi dt)^{-p/2} \, exp \, exp \left[-\frac{r^2}{4dt} - bt\right], \qquad (3)$$

where E_0 is the energy at the source, *d* is the diffusivity, *b* is the intrinsic attenuation coefficient and *p* is a dimensional factor related to the geometrical spreading term as it is described by Dainty and Toksöz (1981) and used by Wegler and Lühr (2001) or Wegler (2003). Coefficients *d* and *b* are directly related to *Qi* and *Qs*, respectively, through the equations

$$Q_i = \frac{2\pi f}{b} \qquad (4)$$

$$Q_s = \frac{2\pi f p d}{v^2} \qquad (5)$$

where *f* is the central frequency of filtered seismograms and *v* is the half-space velocity.

From the above definitions of the intrinsic and scattering mean free path,

$$la = \frac{v}{b} \; and \; lg \; lg \; = \frac{pd}{v}$$

(6)

Finally, the total *Q* can be defined by

$$Q_t^{-1} = Q_i^{-1} + Q_s^{-1}$$

(7)

3 SEISMIC DATA, DATA ANALYSIS AND DATA MAPPING

3.1 Seismic data

The data analysed in this study is a subset of data from the TOMOETNA active seismic experiment, which was performed between June and December 2014 (Ibáñez et al. 2016a,b). Here, we preliminary selected 9705 air-gun shots fired by the Spanish oceanographic vessel 'Sarmiento de Gamboa' in the Ionian Sea and recorded by 120 inland seismic stations on and around Mt Etna volcano (Fig. 1).

3.2 Data analysis

For each seismogram, intrinsic and scattering coefficients were estimated following the procedure of Prudencio et al. (2013a, b, 2015c)

Map of the region
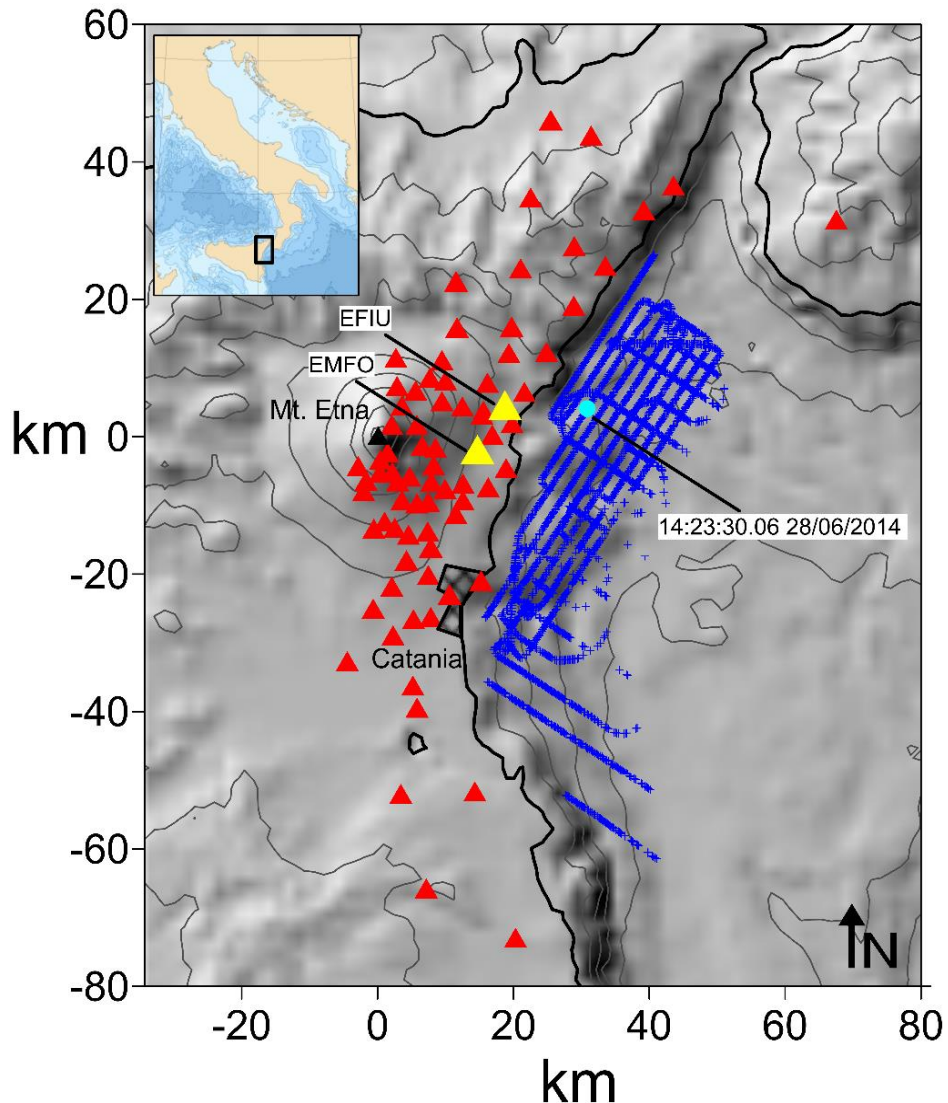
Figure 1. Map of the study region. Red triangles represent the positions of seismic stations used in this study. Blue dots are the locations of the airgun shots generated during the TOMO-ETNA experiment. The highlighted stations (yellow triangles) and shot (light blue dot) are the stations and shot used as examples in Figs 2 and 3.

in where similar marine data sources were used. The most important steps of the procedure include filtering, signal extraction, water wave extraction, signal envelope and parameter extraction.

3.2.1 *Filtering*

We first analysed the spectra of a selected sample of seismograms to identify the frequency range in which the signal-to-noise ratio is suitable for further analysis. Based on this analysis, seismic signals were filtered at frequency bands centred at 4, 6, 8, 12, 16, 20 and 24 Hz with a bandwidth of $fc \pm 0.6fc$, using a Butterworth bandpass filter with eight poles. The signal-to-noise ratio was measured in each seismogram, and all waveforms showing values of less than 2 at the end of the seismogram coda were rejected. The final data set analysed and used to performour images consisted of 15 961 vertical waveforms for the lowest frequency (4 Hz) and 13 932 vertical waveforms for the highest frequency (24 Hz). The distance range of the selected signals range between 3.8 and 25.9 km. Fig. 2 shows an example filtered seismogram and the corresponding spectrum of the unfiltered signal.

3.2.2 *Signal extraction*

We extracted the portion of the filtered seismograms from the theoretical *S*-wave onset and to a lapse time of 20 s, measured from the origin time. Hence, $t$min was equal to the theoretically calculated *S*-wave arrival time and $t$max corresponded to the time interval, which was always 20 s long. Fig. 3 shows the selected signal analysis window. The active seismic source is a pure pressure *P*-wave generated on the surface of the sea, and propagated towards the sea bottom. Therefore, it is expected that after to impact the sea bottom only *P* waves should be propagated to the received. However, as Yamamoto andSato (2010) demonstrated, with the exception of a very small portion of the first seismic package, the main part of the seismogram is composed by converted *P* to *S* waves.
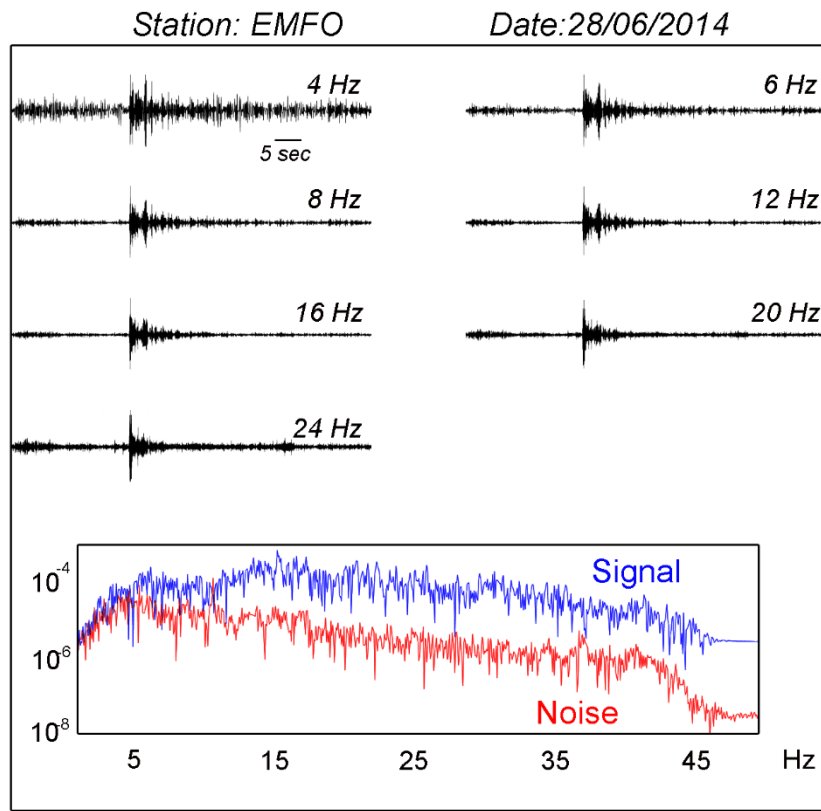
Figure 2. (a) Example seismic records filtered at different frequency bands. (b) Comparison of noise and signal spectra of the same signal; note that the signal-to-noise ratio is high up to 24 Hz. The seismic station and shot are identified in Fig. 1.
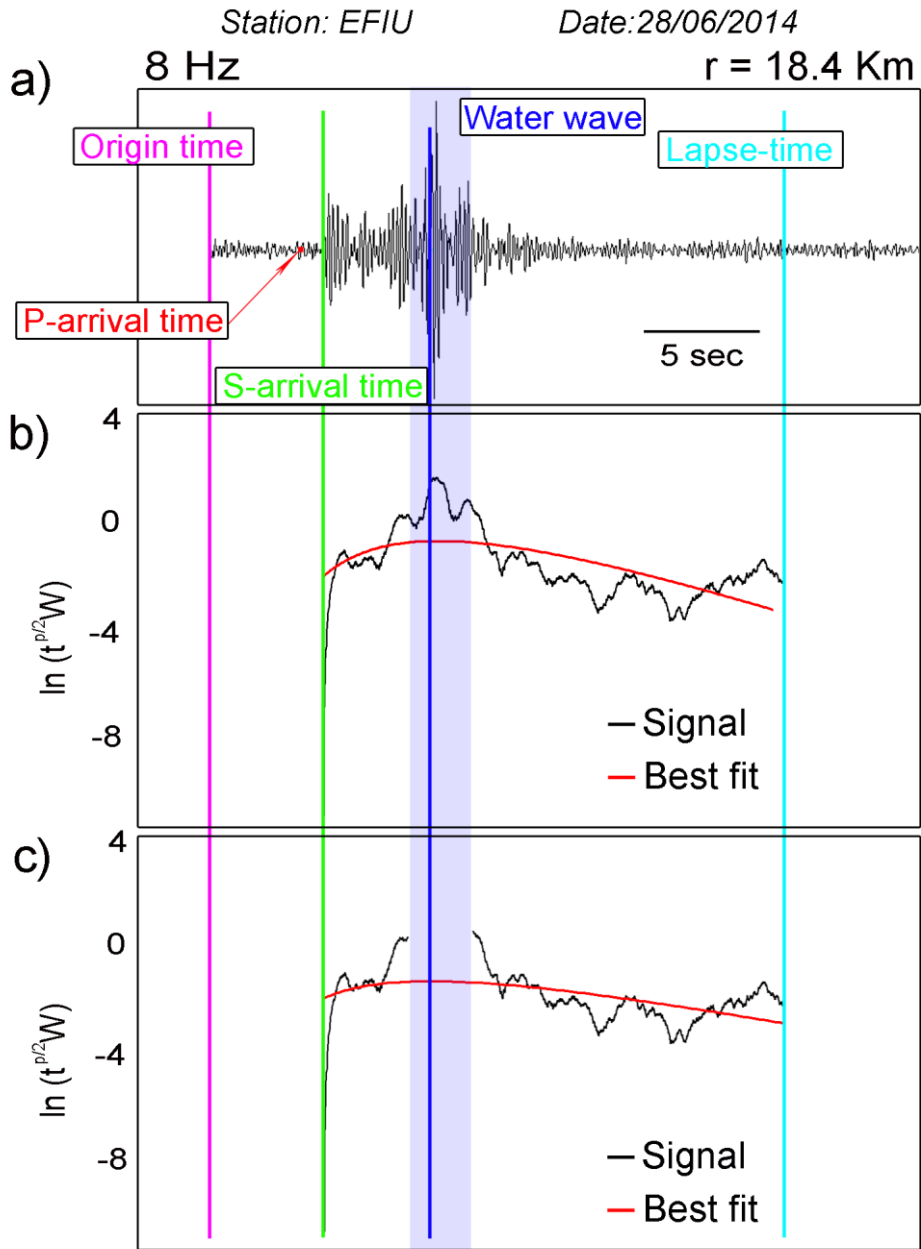
Figure 3. (a) Seismogram of a shot with the water-wave highlighted (dark blue line). The pink line denotes the origin time of the shot; the red arrow indicates the real *P*-wave onset; the green line denotes the theoretically calculated *S*-waves arrival; and the light blue line marks the end of the analysis window. (a) and (b) Comparisons of best fit between the data and model (b) with and (c) without the water-wave energy package.

3.2.3 Water wave extraction

The seismic sources were air-gun shots generated on the surface of the sea. This type of signal produces secondary waves that travel directly from the source to the station through the water volume. Previous analysis of similar experiments (Zandomeneghi et al. 2009; García-Yeguas et al. 2012) has shown that this type of wave has a known propagation velocity and high energy, and is therefore easily identifiable on seismograms. Recently Carmona et al. (2015) identified these types of T waves in the Mediterranean basin for shallow earthquakes.

The sound speed profile in the Mediterranean area differs from that in open oceans (in the temperate zone), especially for the minimum shape under the thermocline, and the absence of the deep SOFAR channel (Munk et al. 1995). As mentioned by Flattè et al. (1979) and by Northup and Colborn (1974), the presence of the SOFAR channel, in the ocean environmental, is generally located between 800 and 1200 m. Instead, the location of this propagation channel in the Mediterranean Sea is affected by a surface thermocline and warm deep waters, due to the thermal vertical structure.

The sound speed in the Mediterranean basins is characterized by a seasonal variability with two extremes in February and August (Taburni 2011). During the summer period (August), the water column is characterized by a velocity profile divided into three different layers, from top to bottom: (i) a surface layer with marked decreasing values, heavily influenced by the rapid decrease of temperature; (ii) a minimum velocity value located at the base of the seasonal thermocline and (iii) a slow but steady increase due to the effect of pressure under the thermocline layer (Salon et al. 2003). In terms of the propagation of sound waves, this produces a channeled propagation that is constrained below the thermocline. The velocity profile in winter (February) in the northwestern Mediterranean is characterized by a steady increase with depth, due to the homogeneous vertical distribution of water masses, and therefore it is highly influenced by the effect of pressure. Under 600 m, the vertical velocity gradient is almost constant (about 1 ms–1 every 60 m of depth, in agreement with the value of 0.0167 s–1 calculated by Jensen et al. (1994) for an average of Mediterranean profile), due to the main role of the pressure, the temperature and salinity constant values.

We have performed local velocity measurements, related to summer period (the same period in which the TOMO-ETNA experiment was carried out), using the model proposed by Medwin (1975), limited to a 1000 m depth:

$$c = 1449.2 + 4.6T - 0.055T2 + 0.00029T3 + (1.34 - 0.01T)(S - 35) + \qquad (8)$$
$$0.016Z$$

where c is the sound speed (ms^{-1}), T is the temperature (◦C), Z is the depth (m) and S is the salinity (p.s.u.). Due to the lack of any CTD casts database from TOMO-ETNA experiment, we have used the temperature, salinity and pressure data provided by NOAA (National Oceanic and Atmospheric Administration) through the World Ocean Database (http://www.nodc.noaa.gov/OC5/SELECT/dbsearch/dbsearch.html). We have selected the parametric profiles measured in the Aeolian archipelago in the months of July and August in order to maintain the same parametric conditions of the TOMO-ETNA experiment time period providing an average sound speed value of 1509 ms^{-1}.

The water waves should be cut off before applying the fitting procedure to retrieve the attenuation parameters. Here, we directly removed them instead of using any kind of filtering since their frequency content was the same as that of the signal under study.

We removed the intervals 0.5 s before and 2.5 s after the theoretically estimated first onset of water waves; Fig. 3 illustrates an example of this procedure, which was applied to all seismograms. In Fig. 3(a), a seismogram filtered at 8 Hz clearly shows the water wave (notice its high amplitude with respect to the rest of the seismogram); in Fig. 3(b), we show the bias corresponding to the fit of the observed Energy Envelope to the theoretical Energy Envelope (including the water wave). Finally, Fig. 3(c) shows the fit to the signal modified by removing the water wave interval.

3.2.4 Parameter estimation

Seismogram Energy Envelopes were calculated by applying a Hilbert transform to 0.7-s time windows sliding with an overlap of 50 per cent for each frequency band. We fit energy envelopes to eq. (3) by using a least square method to obtain the b and d parameters and, consequently, Qi and Qs. The first term of eq. (3), the trade-off between the b and d parameters were obtained following Mayeda et al. (1992) and Akinci et al. (1995) using the F distribution at a 70 per cent level of confidence to estimate the

uncertainty intervals in parameters. The average measured uncertainty intervals were of 8 and 6 per cent for b and d, respectively. The lack of a severe trade-off between b and d allowed attenuation effects to be estimated independently. We assumed $p = 3$ as the dimension term for body waves (Wegler and Lühr 2001; Wegler 2003) and discarded data with a correlation coefficient between the theoretical model and experimental data of $R < 0.7$. Finally, we used b and d to obtain Qi and Qs using eqs (4) and (5), respectively. Given b and d, the scattering mean free path ($lg = 3d/v$) and the absorption mean free path ($li = v/b$) could also be calculated. The v (S-wave velocity) was set at 2.6 km s^{-1}, as derived from a velocity model calculated for the Etna region by Diaz-Moreno et al. (2018), after averaging Vp in the first 3 km and successively dividing for the Vp/Vs ratio, set at 1.7. Fig. 3 shows an example of the data fit.

4 MAPPING PROCEDURE AND RESOLUTION TESTS

4.1 Mapping procedure

The 2-D spatial images were calculated through space-weighting functions describing the spatial sensitivity of observable data to scattering and intrinsic anomalies. A detailed description of the applied methodology is available in Del Pezzo et al. (2016); a recent application to Long Valley Caldera can be found in Prudencio et al. (2018). Here we give only a brief summary of the procedure.

Functions were estimated using a heuristic approach based on Monte Carlo numerical solutions of the energy transport equation. The weighting functions numerically calculated for each source–receiver couple result were well approximated by

$$w\,[x, y, x_r, y_r, x_s, y_s] \tag{9}$$

$$= \frac{1}{4\pi\delta_\chi D^2 \delta_y} Exp\left[-\frac{\left(x - \frac{x_r + x_s}{2}\right)^2}{2(\delta_x D)^2} + \frac{\left(y - \frac{y_r + y_s}{2}\right)^2}{0.5(\delta_y D)^2}\right]$$

$$+ \frac{1}{2\pi\delta_\chi D^2 \delta_y} Exp\left[-\frac{(x - x_s)^2}{2(\delta_x D)^2} + \frac{(y - y_s)^2}{2(\delta_y D)^2}\right]$$

$$+ \frac{1}{2\pi\delta_\chi D^2 \delta_y} Exp\left[-\frac{(x - x_r)^2}{2(\delta_x D)^2} + \frac{(y - y_r)^2}{2(\delta_y D)^2}\right],$$
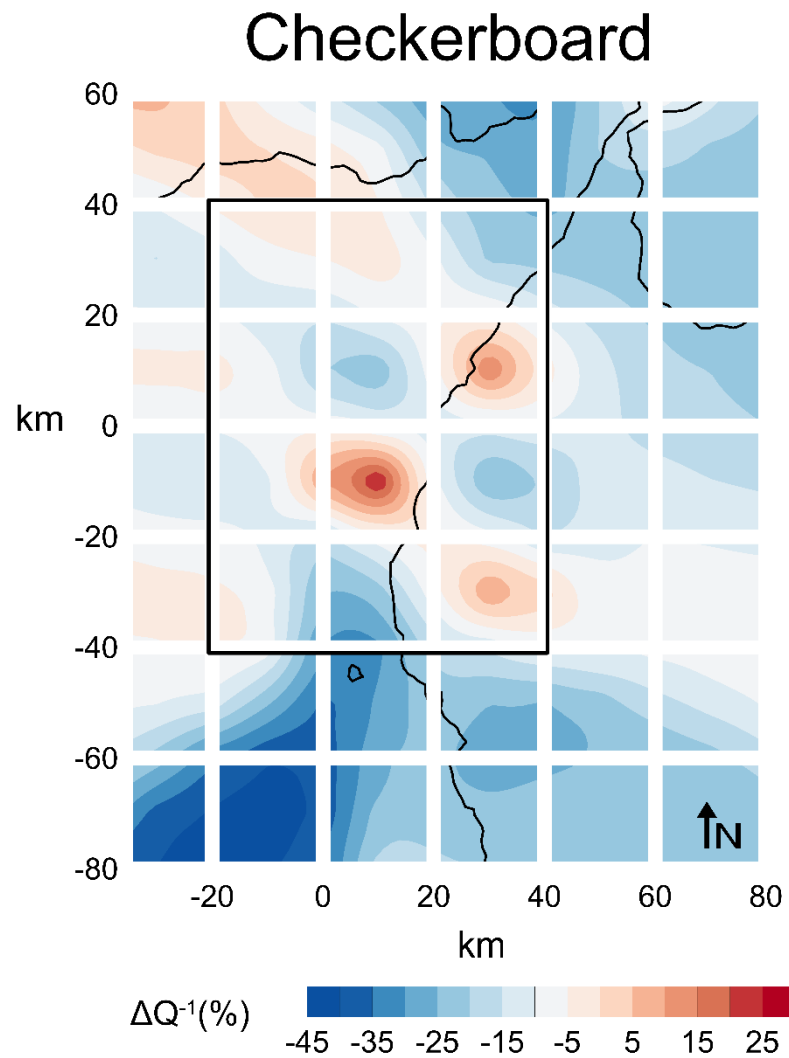
Figure 4. Checkerboard test with 20×20 km2 cell size. We assigned $b = 0.75$ ($Qi = 50$) and $d = 0.21$ ($Qs = 3$) for the high intrinsic and scattering anomalies and $b = 0.4$ ($Qi =$

100) and $d = 23$ ($Qs = 333$) for the low intrinsic and scattering anomalies. The best resolved area is marked by the black contour.

where $w[x, y, xr, yr, xs, ys]$ fits reasonably well to numerical weighting functions with $\delta x = \delta y = 0.2$; δx and δy represent the spatial aperture of the weighting function in 2-D; and $w[x, y, x0, y0, xr, yr]$ is proportional to the probability that, for a source–receiver couple with coordinates at xs,ys and xr,yr, the estimated parameter couple (Qi^{-1}, Qs^{-1}) is effectively the true value at the space point with coordinates x and y. In other words, the value of the attenuation parameter couple Qi^{-1} and Qs^{-1} estimated for a single source–receiver is assigned to the whole space volume, weighted by the $w[x,y,xs,ys,xryr]$ associated with the same source–receiver couple. Discretizing the study area or volume in cells, for each cell a number, N, of weighted measures will thus be available, where N is the number of source–receiver couples. However, for many cells, the value of the space weighting functions (SWF) will be extremely small. Finally, the best estimator for the value of $\{Qi^{-1}, Qs^{-1}\}$ is calculated under the assumption of Gaussian statistics (the weighted arithmetical average) through the equation

$$Q^{-1}[x, y] = \frac{\sum_{k=1}^{N} w[x, y, x_{rk}, y_{rk}, x_{sk}, y_{sk}]Q_k^{-1}}{\sum_{k=1}^{N} w[x, y, x_{rk}, y_{rk}, x_{sk}, y_{sk}]} \qquad (10)$$

where $Q^{-1}[x,y]$ is the estimate in the space point $\{x,y\}$ (centre cell), k is the source–receiver index spanning from 1 to N, Qk^{-1} is the kth measurement, and $\{xrk, yrk\}$ and $\{xsk, ysk\}$ are the coordinates of the receiver and source for the kth source–receiver couple, respectively.

4.2 Sensitivity tests

To check resolution and accuracy of the imaging method, sensitivity tests were performed (see Del Pezzo et al. 2016 and references therein for details) using the following approach:

(1) An a priory checkerboard-like 2-D structure (otherwise called an input test) was numerically generated and Q^{-1} values were assigned to checkerboard cells such that the contrasts between
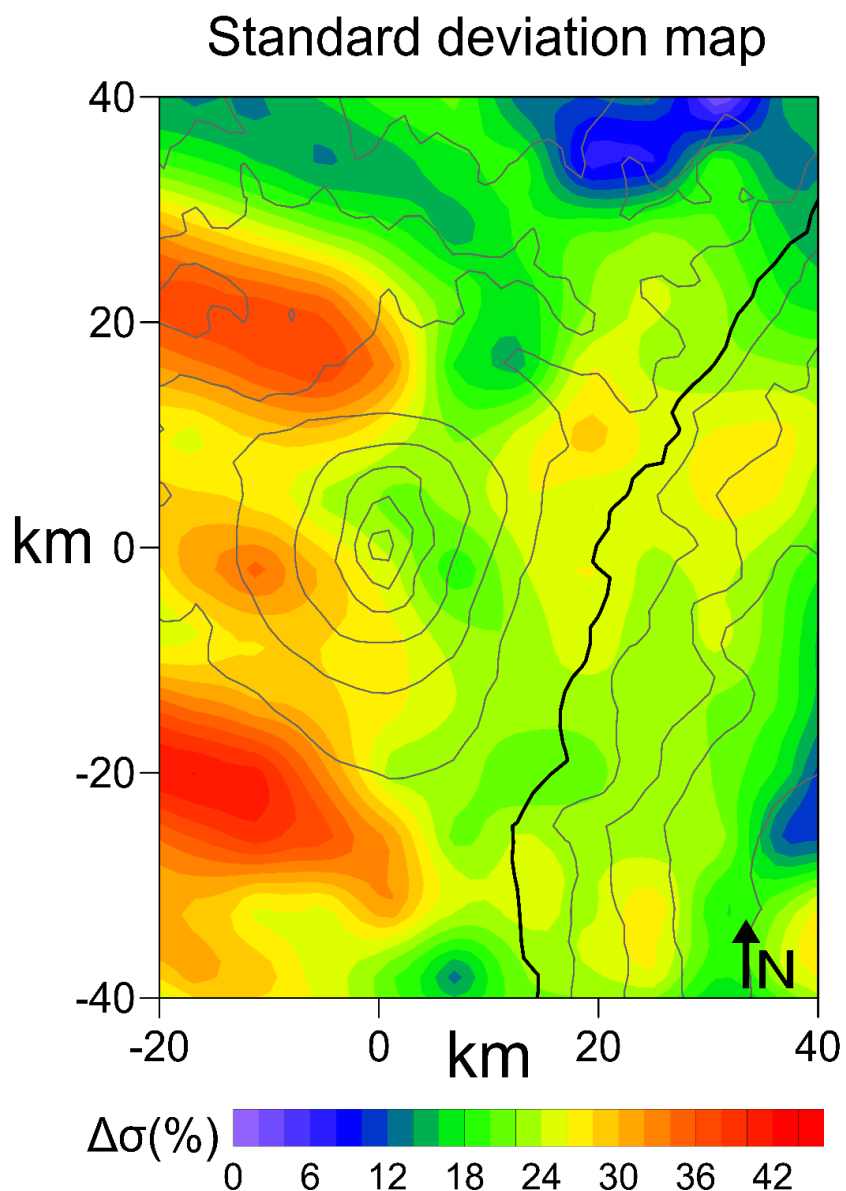
Figure 5. Spatial distribution of calculated standard deviation as a representative quality check of the validity of the obtained images.

checkerboard cells were well outside the average per cent uncertainty in the parameter estimation.

(2) For each source–receiver couple of real data, a space weighting-average of the checkerboard structure was calculated, using eq. (8) as the weighting function. It is worth noting that the weighting functions for Qi^{-1} and Qs^{-1} are the same.

(3) The same imaging method used with real data was applied to the above synthetic data set and the results were compared with the input test. Fig. 4 shows an example checkerboard test.

(4) The resolution function (see Appendix A) was calculated. Fig. 5 shows the pattern of the resolution function calculated for the present data set.

5 RESULTS AND DISCUSSION

We interpreted the results by excluding topographic effects, depth dependence and Energy leakage from the upper layers to the deepest structures of the volcano as recently Sanborn and Cormier (2018) confirmed. The reasons for these exclusions are discussed in detail in Prudencio et al. (2017a) and Del Pezzo et al. (2018). For example, topography is one of the main potential sources of surface wave scattering, being thus potentially a source of bias. As Prudencio et al. (2017a) observed, these effects are of aminor order in our approach, and it is even lower when the attenuation is mapped as perturbation. On the other hand, Del Pezzo et al. (2018) demonstrated that when shallow active sources are used, 3-D images strongly resemble 2-D images, making this 3-D extension redundant.

5.1 Average intrinsic and scattering attenuation values

Table 1 summarizes average values of Qi, Qs, Qt, lg and li for each central frequency estimated by fitting the diffusion model to the energy envelopes. It is clearly observed that scattering dominates over

Table 1. Average values of b, d, Qi, Qs, Qt, Qi^{-1}, Qs^{-1}, Qt^{-1}, ltr and li for the Mt Etna volcanic region.

	b ± error	d ± error	Qi	Qs	Qt	Qi⁻¹	Qs⁻¹	Qt⁻¹	Ltr (m)	Li (Km)
4 Hz	0.719 ± 0.084	1.437 ±0.085	63	16	80	0.029	0.105	0.134	980	6.1
6 Hz	0.782 ± 0.085	1.383 ± 0.080	80	23	104	0.021	0.073	0.094	943	5.6
8 Hz	0.780 ± 0.084	1.311 ± 0.079	103	30	133	0.016	0.054	0.070	894	5.6
12 Hz	0.775 ± 0.083	1.277 ± 0.079	153	43	196	0.010	0.036	0.047	871	5.7
16 Hz	0.752 ± 0.083	1.238 ± 0.080	205	56	261	0.007	0.027	0.034	844	5.8
20 Hz	0.689 ± 0.079	1.211 ± 0.084	276	68	344	0.005	0.020	0.026	826	6.4
24 Hz	0.637 ± 0.078	1.188 ± 0.089	349	80	429	0.004	0.016	0.021	810	6.9

B: intrinsic attenuation coefficient.

d: diffusivity.

Qi: intrinsic Q value, where Qi^{-1} is the inverse Q value.

Qs: scattering Q value, where Qs^{-1} is the inverse Q value.

Qt: total attenuation Q value, where Qt^{-1} is the inverse Q value.

ltr: transport mean free path measured in metres.

li: absorption length measured in kilometres.

intrinsic attenuation at all frequencies. Seismograms are thus controlled by the presence of geological heterogeneities at the surface. Recently, Del Pezzo et al. (2019) analysed regional patterns of intrinsic and scattering attenuation for a region that includes our study

area using the Multiple Lapse Time Window Analysis (MLTWA) method (Hoshiba 1991; Akinci et al. 1995) with local and regional earthquakes and a source–receiver distance range of between 5 and 70 km. As in the present work, they observed that scattering effects dominate over intrinsic absorption in the Etna region, while their absolute Q-values (see table 1 of their paper) were much larger than those presented here. These differences are explained by the greater depth of the seismic sources analysed. In the present study, seismograms were generated at the surface (air-gun shots) and recorded at epicentral distances between 3 and 25 km; the data provide information on the uppermost part of the crust (i.e. the first few kilometers). In the work of Del Pezzo et al. (2019), earthquakes had crustal depths ($\sim$10 km) and were recorded at distances of up to 100 km, providing information on deeper structures. This result implicitly confirms that the Q factor increases with depth in the crust (Ibáñez et al. 1991).

The attenuation parameters estimated for the Mt Etna volcanic region are in agreement with values obtained for other volcanic areas where scattering phenomena dominate over intrinsic dissipation (Zieger et al. 2016; Prudencio et al. 2018, and references therein). Scattering Q values obtained for Mt Etna are almost the same as those obtained for Deception Island (Prudencio et al. 2013b) and Mt Asama volcano (Prudencio et al. 2017a), but higher than those measured at Stromboli (Prudencio et al. 2015c) and Mt Usu (Prudencio et al. 2017b). The fact that scattering effects nearly always dominate over intrinsic attenuation provides additional confirmation that volcanoes are heterogeneous geological objects with multiple fracture systems (e.g. Martínez-Arévalo et al. 2003) the co-occurrence of molten and rigid structures (e.g. Prudencio et al. 2013b; De Siena et al. 2014), feeding systems such as dikes and sills (e.g. De Siena et al. 2017) and embedded layers of ash and lava flows (e.g. De Siena et al. 2016), all alter the geometry of wave fronts producing secondary waves with high intensity. We observe the similar patterns at the Mt Etna, Deception Island, and Mt Asama volcanoes, where evidence for shallow molten material combined with hydrothermal interaction can explain the scattering Q values observed. Nevertheless, Mt Etna shows intrinsic Q values that are smaller than those at other volcanoes analysed using the present technique. This can be explained by the large size of shallow volcanoclastic deposits as De Siena et al. (2016) or Wegler (2003) observed in other volcanoes.

Mt Etna volcano covers a region of approximately 1200 km2 and has a total volume of approximately 530 km3 (Branca and Ferrara 2013; Barreca et al. 2018); the

edifice consists of a complex volcanic succession made up of massive and scoriaceous lava flows overlying interbedded unwelded and lithified volcanoclastic deposits that rest on the sedimentary and metamorphic rocks that control the rigidity of the shallow regional structure.

5.2 Attenuation image anomalies

The spatial distribution of intrinsic and scattering attenuation estimated with respect to the average values reported in Table 1 are presented in Fig. 5. Intrinsic attenuation is at least 1 order of magnitude lower than scattering attenuation; therefore, total attenuation images are very similar to scattering attenuation images and are not shown. To interpret the images from a geo-volcanological point of view, it is necessary to take into account that the attenuation images are 2-D, thus they represent an average over the first 2–3 km below the surface. The estimated depths for scattered waves inferred by 3-D numerically simulated weighting functions (Del Pezzo et al. 2018) are concentrated in the first few kilometres of the crust when the source and receiver are both located at the surface and at a distance comparable with the average distances of the present data set. Moreover, ray tracing performed for velocity tomography shows ray coverage with the highest density in the first 2–3 km below the surface (see D´ıaz-Moreno et al. 2018).

According to previous studies carried out using the present technique and already mentioned above, it is more explanatory to consider the distribution of attenuation anomalies than it is to consider the absolute values; however, geological structures that are smaller than the cell dimension (5 km × 5 km) are invisible to our data set. To eliminate potential boundary distortions, after to perform the checkerboard test and identify the best resolved region, that is the area in which the method successfully retrieves the anomalies (see Fig. 4), we interpreted the data for an extracted smaller subregion.

5.2.1 Intrinsic attenuation anomalies

Fig. 6(a) shows the distribution of intrinsic attenuation anomalies in the Mt Etna region. As discussed, space averaged intrinsic Q values are low compared with most other

140

volcanic regions; the areas characterized by strong intrinsic attenuation show changes of almost ±50 per cent with respect to the average. In this study, high contrast regions were labelled as I1–I4, while I1–I3 represent high attenuation anomalies, and I4 is characterized by low attenuation values.
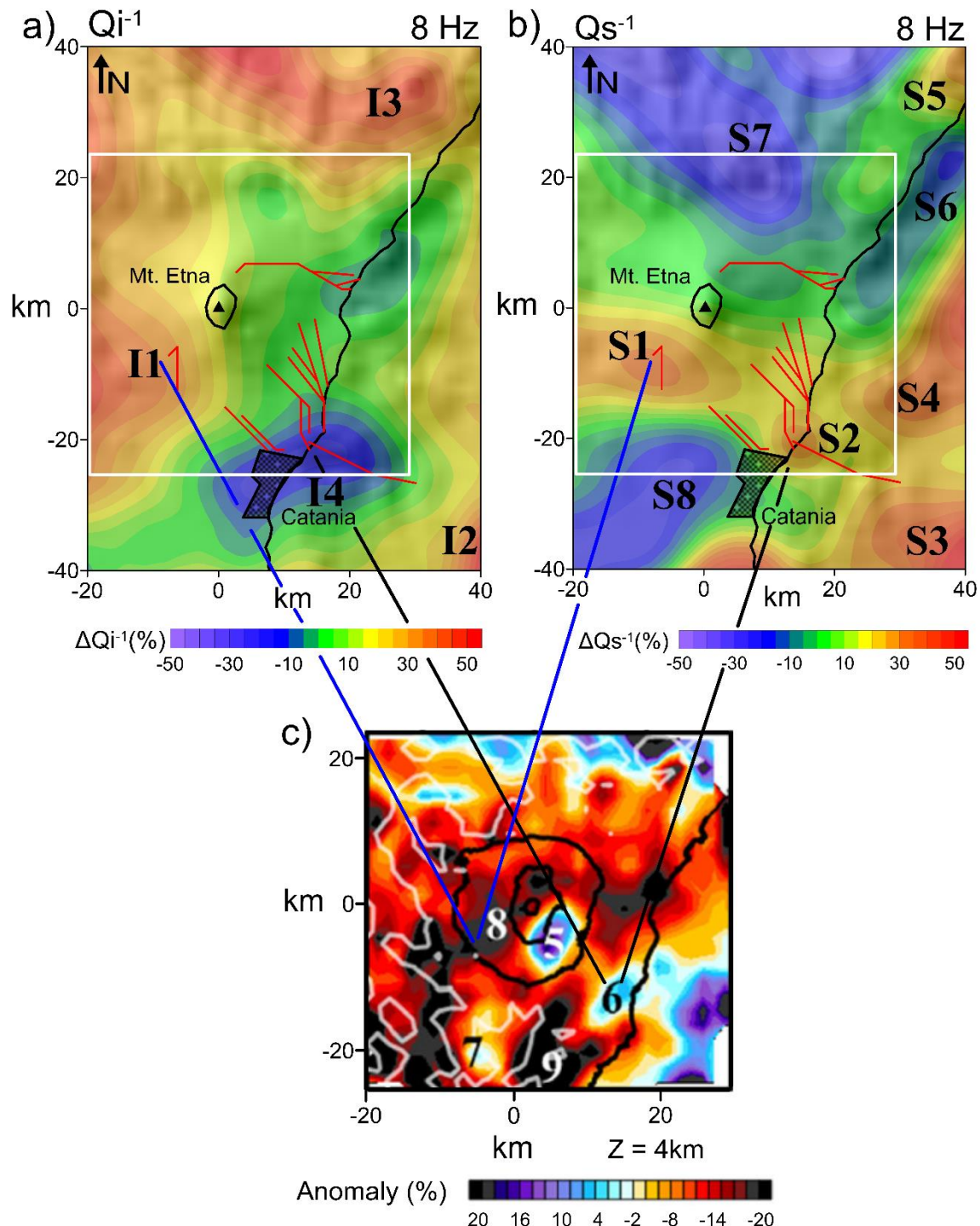
Figure 6. (a) Qi^{-1} and (b) Qs^{-1} anomaly maps obtained at 8 Hz for the best resolved region. The I and S labels correspond to the anomaly regions discussed in the text. Important fault systems are marked in red. (c) Modified map derived from Díaz-Moreno et al. (2018) for comparison of velocity and Attenuation characteristics.

A high attenuation anomaly observed to the south west of Mt Etna (I1) is associated with the tectonic units of the Apenninic–Maghrebian chain, which are mainly formed by varicoloured clays and terrigenous turbiditic successions (Branca et al. 2011; Branca and Ferrara 2013). The high attenuation structure I2 is located in the southeastern part of the region and can be interpreted as the northern segments of the Alfeo-Etna Fault System (Polonia et al. 2017).

High attenuation area I3, located in the northern part of the volcanic edifice, reflects a high level of fracturing belonging to the Apenninic Maghrebian Chain and could represent prolongation of I1 towards the north (Cristofolini et al. 1979; Bianchi et al. 1987; Branca et al. 2011). The high attenuation values can be interpreted as the effects of a shallow fracture system associated with regional structural dynamics at the roof of this thrust system. Evidence for high levels of fracturing in this area is also presented in other studies (e.g. Barreca et al. 2018, and references therein). This region represents the Nebrodi-Peloritani Transition Zone, extending from the Aeolian Islands to the Ionian Sea. The area is characterized by complex fault systems in which NNW–SSE and WNW–ESE oriented fault segments (Lentini et al. 1995; Finetti et al. 1996) are overlapped by second-order N–S and NE–SW-striking faults (Giampiccolo and Tuvè 2018).

The most significant high-Q anomaly (I4; Fig. 6c) is located near of the city of Catania and correlates with a high velocity volume observed by Diaz Moreno et al. (2018). Owing to the relatively low attenuation value, it may correspond to a highly consolidated body. Intrinsic attenuation is a reliable indicator of magmatic intrusions (e.g. De Siena et al. 2017) and therefore I4 is likely also associated to potential shallow magmatic bodies and submarine volcanism. These magmatic anomalies could be related to the earliest phase of volcanism and intruded into the Pleistocene marly clay succession of the Gela-Catania foredeep (Fig. 6a), as recently revealed in this sector by magnetic anomalies (Nicolosi et al. 2018).

142

5.2.2 Scattering attenuation anomalies

The scattering attenuation pattern is more heterogeneous than the intrinsic attenuation one (Figs 6a and b). We identified at least eight areas, denoted S1–S5 (high attenuation structures) and S6–S8 (low scattering attenuation).

A high scattering attenuation anomaly (S1) is located in the south west region of Mt Etna. In the last decades, several seismological studies linked the seismic activity occurring in this sector of the volcano to its recharging phases, leading to eruptive activity. In particular, the analysis of the seismicity occurred in this area before the 2001, 2002–2003 and 2008 lateral eruptions have been considered the fragile response of the Etna crust to magmatic intrusions mainly in the summit area and secondary in the upper South Rift zone (Bonaccorso et al. 2006; Sicali et al. 2015). In this area, the high degree of heterogeneity implied by the high scattering attenuation is confirmed by the presence of the shallow (up to 5 km bsl) Ragalna Fault System and South Volcanic Rift Zone (Azzaro et al. 2012). Moreover, from September 2017, this sector of the volcano was characterized by shallow seismicity that pre-dated and accompanied the December 2018 eruption (Gruppo Analisi Dati Sismici 2019). The S1 anomaly is located just to the south of the area in which Dʹıaz-Moreno et al. (2018) and Aloisi et al. (2002) identified a shallow low-velocity anomaly region. It is suggested that this anomaly represents a magma storage volume on the basis of anomalous *b* values (Murru et al. 1999) and ground deformation inversions (Nunnari and Puglisi 1994; Bonaccorso et al. 1996).

Another high scattering anomaly is located north of Catania (S2). This anomaly could be associated with the Fiadanca, Santa Tecla and Timple faults (Azzaro *et al.* 2012), which are linked to the lithospheric dextral transtensional North Alfeo fault system (Gutscher et al. 2016, 2017; Polonia et al. 2017) dissecting the lower SE flank of the volcano.

In the southeastern area, at the same location as the I2 anomaly, a high scattering anomaly is also observed (S3). Following Polonia et al. (2017), we interpret this anomaly as a segment of the Alfeo-Etna fault system. The S4 high scattering anomaly is located east of Mt Etna, offshore and beneath the Ionian Sea. This anomaly can be interpreted as a highly fractured region where the Ionian Fault and Alfeo-Etna fault system converge (Polonia et al. 2017). Near I3, a high scattering attenuation anomaly is also observed (S5).

143

As such, this area is characterized by both high intrinsic and scattering attenuation values and can be interpreted as a volume with a very high level of fracturing. The S6 anomaly is located northeast of Mt Etna, and partly extends offshore. This region could be connected to the large low scattering anomaly of S7, and both can be related to shallow (1–2 km bsl) carbonate units of the external thrust system (Branca et al. 2011). Finally, the S8 anomaly is located to the west of Catania. Owing to its scattering behaviour it can be interpreted as a homogeneous body; this interpretation is consistent with the results of Branca et al. (2011), who identified compact carbonates of the Hyblean Plateau covered by the Catania-Gela foredeep sediments at a depth of approximately 1 km bsl (Torelli et al. 1998).

6 CONCLUSIONS

This work provides new evidence of the structural complexity of the Mt Etna volcanic area. The data set used comprised waveforms recorded during the TOMO-ETNA experiment, with nearly uniform and homogeneous ray coverage. The methodology used in this study, which had not been applied to this area before, allowed us to characterize intrinsic and scattering attenuation in the region, which in turn supports an improved geological interpretation. Mt Etna appears as a single domain, for which the shallowest rocks (2–3 km bsl) have the highest intrinsic and scattering attenuation. However, attenuation beneath the Mt Etna area is dominated by scattering effects, which are strong enough to fully justify the use of diffusion approximation for the energy transport equation.

From the scattering attenuation anomaly map, it is possible to infer that Mt Etna volcano is situated between two large tectonic regions that dynamically stress and fracture the area. Good correlations between attenuation and velocity anomalies confirm that the method is a suitable complement to ordinary seismic velocity tomography.

The most prominent result is a strong correlation among the occurrence of seismicity, volcanic activity, and high attenuation effects in the southwestern area of Mt Etna (named S1). In conclusion, this work supports the hypothesis that the SW flank dynamics, including the summit area and upper South Rift Zone, are linked to magma recharge during recent decades.

ACKNOWLEDGEMENTS

REFERENCES

Alparone, S., Barberi, G., Cocina, O., Giampiccolo, E., Musumeci, C. and Patanè, D., 2012. Intrusive mechanism of the 2008–2009 Mt. Etna eruption: constraints by tomographic images and stress tensor analysis, *J. Volc. Geotherm. Res., 229*, 50–63.

Aki, K. and Chouet, B., 1975. Origin of coda waves: source, attenuation, and scattering effects, *J. Geophys. Res.,* **80**(23), doi:10.1029/JB080i023p03322.

Akinci, A., Del Pezzo, E. and Ibanez, J.M., 1995. Separation of scattering and intrinsic attenuation in southern Spain and western Anatolia (Turkey), *Geophys. J. Int., 121*(2), 337–353.

Aloisi, M., Cocina, O., Neri, G., Orecchio, B. and Privitera, E., 2002. Seismic tomography of the crust underneath the Etna volcano, Sicily, *Phys. Earth planet. Inter., 134*, 139–155.

Azzaro, R., Branca, S., Gwinner, K. and Coltelli, M., 2012. The volcano-tectonic map of Etna volcano, 1: 100.000 scale: an integrated approach based on a morphotectonic

analysis from high-resolution DEM constrained by geologic, active faulting and seismotectonic data, *Ital. J. Geosci., 131*(1), 153–170.

Barreca, G., Branca, S. and Monaco, C., 2018. Three-dimensional modeling of mount etna volcano: volume assessment, trend of eruption rates, and geodynamic significance, *Tectonics,* **37**(3), 842–857.

Bianchi, F., Carbone, S., Grasso, M., Invernizzi, G., Lentini, F., Longaretti, G., Merlini, S. and Mostardini, F., 1987. Sicilia orientale: profile geologico Nebrodi-Iblei, *Mem. Soc. Geol. It., 38***,** 429–458.

Bonaccorso, A., Ferucci, F., Patanè, D. and Villari, L., 1996. Fast deformation processes and eruptive activity at Mr. Etna (Italy), *J. Geophys. Res., 101***,** 17 467–17 480.

Bonaccorso, A., Bonforte, A., Guglielmino, F., Palano, M. and Puglisi, G., 2006. Composite ground deformation pattern forerunning the 2004–2005 Mount Etna eruption, *J. Geophys. Res., 111***,** B12, doi:10.1029/2005JB004206.

Branca, S. and Ferrara, V., 2013. The morphostructural setting of Mount Etna sedimentary basement (Italy): implications for the geometry and volume of the volcano and its flank instability, *Tectonophysics, 586*(26), 46–64.

Branca, S., Coltelli, M., Groppelli, G. and Lentini, F., 2011. Geological map of Etna volcano, 1: 50,000 scale, *Ital. J. Geosci., 130*(3), 265–291.

Carmona, E., Almendros, J., Alguacil, G., Soto, J. I., Luzón, F. and Ibáñez, J. M., 2015. Identification of T-Waves in the Alboran Sea, *Pure appl. Geophys., 172*(11), 3179–3188.

Chiarabba, C., De Gori, P. and Patanè, D., 2004. The Mt. Etna plumbing system: the contribution of seismic tomography, *Washington DC American Geophysical Union Geophysical Monograph Series, 143***,** 191–204.

Coltelli, M., Cavallaro, D., Firetto Carlino, M., Cocchi, L., Muccini, F., D'Aessandro, A. and Patanè, D., 2016. The marine activities performed within the TOMO-ETNA experiment, *Ann. Geophys., 59*(4), doi:10.4401%2Fag-7081.

Cristofolini, R., Lentini, F., Patanè, G. and Rasè, R., 1979. Integrazione di dati geologici, geofisici e petrologici per la stesura di un profilo crostale in corrispondenza dell'Etna, *Boll. Soc. Geol. It., 98*(2), 239–247.

Dainty, A.M. and Toksöz, M.N., 1981. Seismic codas on the Earth and the Moon: a comparison, *Phys. Earth planet. Int., 26*(4), 250–260.

De Gori, P., Chiarabba, C. and Patanè, D., 2005. Qp structure of Mount Etna: constraints for the physics of the plumbing system, *J. Geophys. Res., 110*(B5), doi:10.1029/2003JB002875.

De Siena, L., Thomas, C., Waite, G.P., Moran, S.C. and Klemme, S., 2014. Attenuation and scattering tomography of the deep plumbing system of Mount St. Helens, *J. Geophys. Res., 119*(11), 8223–8238.

De Siena, L., Calvet, M., Watson, K.J., Jonkers, A.R.T. and Thomas, C., 2016. Seismic scattering and absorption mapping of debris flows, feeding paths, and tectonic units at Mount St. Helens volcano, *Earth planet. Sci. Lett., 442*, 21–31.

De Siena, L., Amoruso, A., Del Pezzo, E., Wakeford, Z., Castellano, M. and Crescentini, L., 2017. Space-weighted seismic attenuation mapping of the aseismic source of Campi Flegrei 1983–1984 unrest, *Geophys. Res. Lett., 44*(4), 1740–1748.

Del Pezzo, E., 2008. Chapter 13 Seismic Wave Scattering in Volcanoes, in *Earth Heterogeneity and Scattering Effects on Seismic Waves,* Vol. *50*, 353–371, ed. Dmowska, R, Elsevier, doi:10.1016/S0065-2687(08)000 13-7.

Del Pezzo, E., Ibanez, J., Prudencio, J., Bianco, F. and De Siena, L., 2016. Absorption and scattering 2-D volcano images from numerically calculated space-weighting functions, *Geophys. J. Int., 206*(2), 742–756.

Del Pezzo, E., De La Torre, A., Bianco, F., Ibanez, J., Gabrielli, S. and De Siena, L., 2018. Numerically calculated 3D space-weighting functions to image crustal volcanic structures using diffuse coda waves, *Geoscience, 8*(5), 175, doi:10.3390/geosciences8050175.

Del Pezzo, E., Giampiccolo, E., Tuvè, T., Di Grazia, G., Gresta, S. and Ibanez, J., 2019. Study of the regional pattern of intrinsic and scattering seismic attenuation in Eastern Sicily (Italy) from local earthquakes, *Geophys. J. Int., 218*, 2, 1456–1468.

Díaz-Moreno, A., Barberi, G., Cocina, O., Koulakov, I., Scarfì, L., Zuccarello, L. and Ibáñez, J.M., 2018. New insights on Mt. Etna's crust and relationship with the regional

tectonic framework from joint active and passive P-wave seismic tomography, *Surev. Geophys., 39*(1), 57–97.

Finetti, I., Lentini, F., Carbone, S. and Catalano, S., 1996. Il sistema Apennino Meridionale-Arco Calabro-Sicilia nel Mediterraneo Centrale: studio geologico-geofisico, *Boll. Soc. Geol. It., 115*, 529–559.

Flatté, S.M., Dashen, R., Munk, W., Watson, K. and Zachariasen, F., 1979. *Sound Transmission Through a Fluctuating Ocean,* Cambridge Univ. Press.

García-Yeguas, A., Koulakov, I., Ibáñez, J.M. and Rietbrock, A., 2012. High resolution 3D P wave velocity structure beneath Tenerife Island (Canary Islands, Spain) based on tomographic inversion of active-source data, *J. Geophys. Res., 117*(B9), doi:10.1029/2011JB008970.

Giampiccolo, E. and Tuvè, T., 2018. Regionalization and dependence of coda Q on frequency and lapse time in the seismically active Peloritani region (northeastern Sicily, Italy), *J. Seismol., 22*(4), 1059–1074.

Gruppo Analisi Dati Sismici, 2019. *Catalogo dei terremoti della Sicilia Orienta–e - Calabria Meridionale (1999–2019),* INGV, Catania, http: //www.ct.ingv.it/ufs/analisti/catalogolist.php.

Gutscher, M.A., Dominguez, S., de Lepinay, B.M., Pinheiro, L., Gallais, F., Babonneau, N. and Rovere, M., 2016. Tectonic expression of an active slab tear from high-resolution seismic and bathymetric data offshore Sicily (Ionian Sea), *Tectonics, 35*(1), 39–54.

Gutscher, M.A., Kopp, H., Krastel, S., Bohrmann, G., Garlan, T., Zaragosi, S. and San Pedro, L., 2017. Active tectonics of the Calabrian subduction revealed by new multi-beam bathymetric data and high-resolution seismic profiles in the Ionian Sea (Central Mediterranean), *Earth planet. Sci. Lett., 461*, 61–72.

Hoshiba, M., 1991. Simulation of multiple-scattered coda wave excitation based on the energy conservation law, *Phys. Earth planet. Int., 67*(1–2), 123–136.

Ibáñez, J.M., Morales, J., De Miguel, F., Vidal, F., Alguacil, G. and Posadas, A.M., 1991. Effect of a sedimentary basin on estimations of Qc and QLg, *Phys. Earth planet. Int., 66*(3–4), 244–252.

Ibáñez, J.M., Prudencio, J., Díaz-Moreno, A., Patanè, D., Puglisi, G., Lühr, B.G. and Del Pezzo, E., 2016a. The TOMO-ETNA experiment: an imaging active campaign at Mt. Etna volcano. Context, main objectives, working-plans and involved research projects, *Ann. Geophys., 59*(4), 0426, doi:10.4401/ag-7079.

Ibáñez, J.M., Díaz-Moreno, A., Prudencio, J., Patanè, D., Zuccarello, L., Cocina, O. and Bianco, F., 2016b. TOMO-ETNA experiment at Etna volcano: activities on land, *Ann. Geophys., 59*(4), doi:10.4401/ag-7080.

Jensen, F.B., Kuperman, W.A., Porter, M.B. and Schmidt, H., 1994. Computational Ocean Acoustics. AIP Series in Modern Acoustics and Signal Processing.

Koulakov, I., Maksotova, G., Jaxybulatov, K., Kasatkina, E., Shapiro, N.M., Luehr, B.G. and Al-Arifi, N., 2016. Structure of magma reservoirs beneath Merapi and surrounding volcanic centers of Central Java modeled from ambient noise tomography, *Geochem. Geophys. Geosyst., 17*(10), 4195–4211.

Lentini, F., Carbone, S., Catalano, S., Di Stefano, A., Gargano, C., Romeo, M. and Vinci, G., 1995. Sedimentary evolution of basins in mobile belts: examples from the Tertiary terrigenous sequences of the Peloritani Mountains (NE Sicily), *Terra Nova,* **7**(2), 161–170.

Martínez-Arévalo, C., Bianco, F., Ibáñez, J. M. and Del Pezzo, E. 2003. Shallow seismic attenuation and shear-wave splitting in the short period range of Deception Island volcano (Antarctica), *J. Volc. Geotherm. Res., 128*(1-3), 89–113.

Martínez-Arévalo, C., Patanè, D., Rietbrock, A. and Ibáñez, J.M., 2005. The intrusive process leading to the Mt. Etna 2001 flank eruption: constraints from 3-D attenuation tomography, *Geophys. Res. Lett., 32*(21), doi:10.1029/2005GL023736.

Mayeda, K., Koyanagi, S., Hoshiba, M., Aki, K. and Zheng, Y., 1992. A comparative study of scattering, intrinsic, and coda Q^{-1} for Hawaii, Long Valley and Central California between 1.5 and 15 Hz. *J. Geophys. Res., 97***,** 6643–6659. https://doi.org/10.1029/91JB03094

Medwin, H., 1975. Speed of sound in water: a simple equation for realistic parameters, *J. Acoust. Soc. Am., 58*(6), 1318–1319.

Munk, W., Worcester, P. and Wunsch, C., 1995. *Ocean Acoustic Tomography.* Cambridge Univ. Press.

Murru, M., Montuori, C., Wyss, M. and Privitera, E., 1999. The locations of magma chambers at Mt. Etna, Italy, mapped by b-values, *Geophys. Res. Lett., 26*(16), doi:10.1029/1999GL900568.

Nicolosi, I., D'Ajello Caracciolo, F., Branca, S., Speranza, F. and Chiappini, M., 2018. Unravelling Mount Etna's early eruptive history by three-dimensional magnetic modeling, *Bull. geol. Soc. Am., 130*, 9–10, 1664–1674.

Northrup, J. and Colborn, J. G., 1974. Sofar channel axial sound speed and depth in the Atlantic Ocean, *J. Geophys. Res., 79*, 5633–5641.

Nunnari, G. and Puglisi, G., 1994. The global positioning system as a useful technique for measuring ground deformations in volcanic areas, *J. Volc. Geotherm. Res., 61*(3/4), 267–280.

Patanè, D., Barberi, G., Cocina, O., De Gori, P. and Chiarabba, C., 2006. Time-resolved seismic tomography detects magma intrusions at Mount Etna, *Science, 313*(5788), 821–823.

Polonia, A., Torelli, L., Gasperini, L., Cocchi, L., Muccini, F., Bonatti, E. and Carlini, M., 2017. Lower plate serpentinite diapirism in the Calabrian Arc subduction complex, *Nat. Commun., 8*(1), 2172, doi:10.1038/s41467-017-02273-x.

Prudencio, J., Del Pezzo, E., García-Yeguas, A. and Ibáñez, J.M., 2013a. Spatial distribution of intrinsic and scattering seismic attenuation in active volcanic islands–I: model and the case of Tenerife Island, *Geophys. J. Int., 195*(3), 1942–1956.

Prudencio, J., Ibáñez, J.M., García-Yeguas, A., Del Pezzo, E. and Posadas, A.M., 2013b. Spatial distribution of intrinsic and scattering seismic attenuation in active volcanic islands–II: deception Island images, *Geophys. J. Int., 195*(3), 1957–1969.

Prudencio, J., De Siena, L., Ibáñez, J.M., Del Pezzo, E., Garcia-Yeguas, A. and Diaz-Moreno, A., 2015a. The 3D attenuation structure of deception Island (Antarctica), *Surv. Geophys., 36*(3), 371–390.

Prudencio, J., Ibáñez, J.M., Del Pezzo, E., Martí, J., García-Yeguas, A. and De Siena, L., 2015b. 3D attenuation tomography of the volcanic island of Tenerife (Canary Islands), *Surv. Geophys., 36*(5), 693–716.

Prudencio, J., Del Pezzo, E., Ibáñez, J.M., Giampiccolo, E. and Patané, D., 2015c. Two-dimensional seismic attenuation images of Stromboli Island using active data, *Geophys. Res. Lett., 42*(6), 1717–1724.

Prudencio, J., Aoki, Y., Takeo, M., Ibáñez, J.M., Del Pezzo, E. and Song, W., 2017a. Separation of scattering and intrinsic attenuation at Asama volcano (Japan): Evidence of high volcanic structural contrasts, *J. Volc. Geotherm. Res., 333*, 96–103.

Prudencio, J., Taira, T., Aoki, Y., Aoyama, H. and Onizawa, S., 2017b. Intrinsic and scattering attenuation images of Usu volcano, Japan, *B. Volcanol., 79*(4), 29, doi:10.1007/s00445-017-1117-9.

Prudencio, J., Manga, M. and Taira, T., 2018. Subsurface Structure of Long Valley Caldera Imaged with Seismic Scattering and Intrinsic Attenuation, *J. Geophys. Res., 123*(7), 5987–5999.

Salon, S., Crise, A., Picco, P., De Marinis, E. and Gasparini, O., 2003. Sound speed in the Mediterranean Sea: an analysis from a climatological data set, *Ann. Geophys., 21*, 833–846.

Sanborn, Christopher J. and Cormier, Vernon F. 2018. Modelling the blockage of Lg waves from three-dimensional variations in crustal structure, *Geophys. J. Int. 214*(20), 1426–1440.

Sato, H., Fehler, M.C. and Maeda, T., 2012. *Seismic Wave Propagation and Scattering in the Heterogeneous Earth,* Vol. *496*, Springer.

Sicali, S., Barberi, G., Cocina, O., Musumeci, C. and Patanè, D., 2015. Volcanic unrest leading to the July-August 2001 lateral eruption at Mt. Etna: seismological constraints, *J. Volc. Geotherm. Res., 304*, 11–23.

Taburni, D., 2011. Elaborazione e sperimentazione di un modello matemático di propagazione dell'inquinamento acustico subacqueo, nell'ambito del progetto GIONHA "Governance and Integrated Observation of marine Natural Habitat", Technical Report CNR-IDASC, http://www.gionha.it/risorse/pubblicazioni/report/.

Torelli, L., Grasso, M., Mazzoldi, G. and Peis, D., 1998. Plio–Quaternary tectonic evolution and structure of the Catania foredeep, the northern Hyblean Plateau and the Ionian shelf (SE Sicily), *Tectonophysics, 298*, 209–221.

Wegler, U., 2003. Analysis of multiple scattering at Vesuvius volcano, Italy, using data of the TomoVes active seismic experiment, *J. Volc. Geotherm. Res., 128*(1–3), 45–63.

Wegler, U. and Lühr, B.G., 2001. Scattering behaviour at Merapi volcano (Java) revealed from an active seismic experiment, *Geophys. J. Int., 145*(3), 579–592, doi:10.1046/j.1365-246x.2001.01390.x.

Wu, R., 1985. Multiple scattering and energy transfer of seismic waves—separation of scattering effect from intrinsic attenuation — I. Theoretical modelling, *Geophys. J. R. Astr. Sci., 82*(1), doi:10.1111/j.1365-246X.1985.tb05128.x.

Yamamoto, M. and Sato, H., 2010. Multiple scattering and mode conversion revealed by an active seismic experiment at Asama volcano, Japan, *J. Geophys. Res.: Solid Earth, 115* (B7).

Zandomeneghi, D., Barclay, A., Almendros, J., Ibañez Godoy, J.M., Wilcock, W.S. and Ben-Zvi, T., 2009. Crustal structure of Deception Island volcano from P wave seismic tomography: tectonic and volcanic implications, *J. Geophys. Res. 114*(B6), doi:10.1029/2008JB006119.

Zieger, T., Sens-Schönfelder, C., Ritter, J.R., Lühr, B.G. and Dahm, T., 2016. P-wave scattering and the distribution of heterogeneity around Etna volcano, *Ann. Geophys., 59*(4), 0432.

APPENDIX A: RESOLUTION FUNCTION

To simplify the mathematical notation, we removed the dependence of function *w* (eq. 1) on space, source, and receiver coordinates, and denoted the weighting functions (each normalized for their maximum) by w_{ij}, where i is the event–source index and j represents the jth pixel of coordinates *x,y*; i spans from 1 to N, where N is the number of source–receiver couples in the data set; and j spans from 1 to M, where M is the number of pixels (square regions or cells in which the input image is divided).

We further denote with q_i the Q-value (or its inverse) measured for the ith source–receiver couple, and with q_j the output of the mapping method for the jth pixel. In this simplified notation, the mapping method (eq. 9) yields

$$q_j = \frac{\sum_i q_i w_{ij}}{\sum_i w_{ij}} \qquad (A1)$$

Assuming that the standard deviation, σ, is the same for all measures of q_i and by applying the error propagation equation to eq. (A1) we obtain

$$\sigma_{qj}^2 = \frac{\sigma^2 \sum w_{ij}^2}{(\sum w_{ij})^2} \qquad (A2)$$

Finally, we can reasonably assume that the quantity $\frac{\sigma 2}{\sigma_{qj}}$ represents an estimate of the resolution of the method. In other words, pixels showing smaller resolution should be associated with higher error and vice versa. Resolution at the ith pixel is thus given by

$$R_j = \left(\frac{(\sum w_{ij})^2}{\sum w_{ij}^2} \right)^{\frac{1}{2}} \qquad (A3)$$

where R_j represents all pixels in Fig. 5.

Q_i^{-1} and Q_s^{-1} anomaly maps for 4-24Hz are represented in Fig. B1.
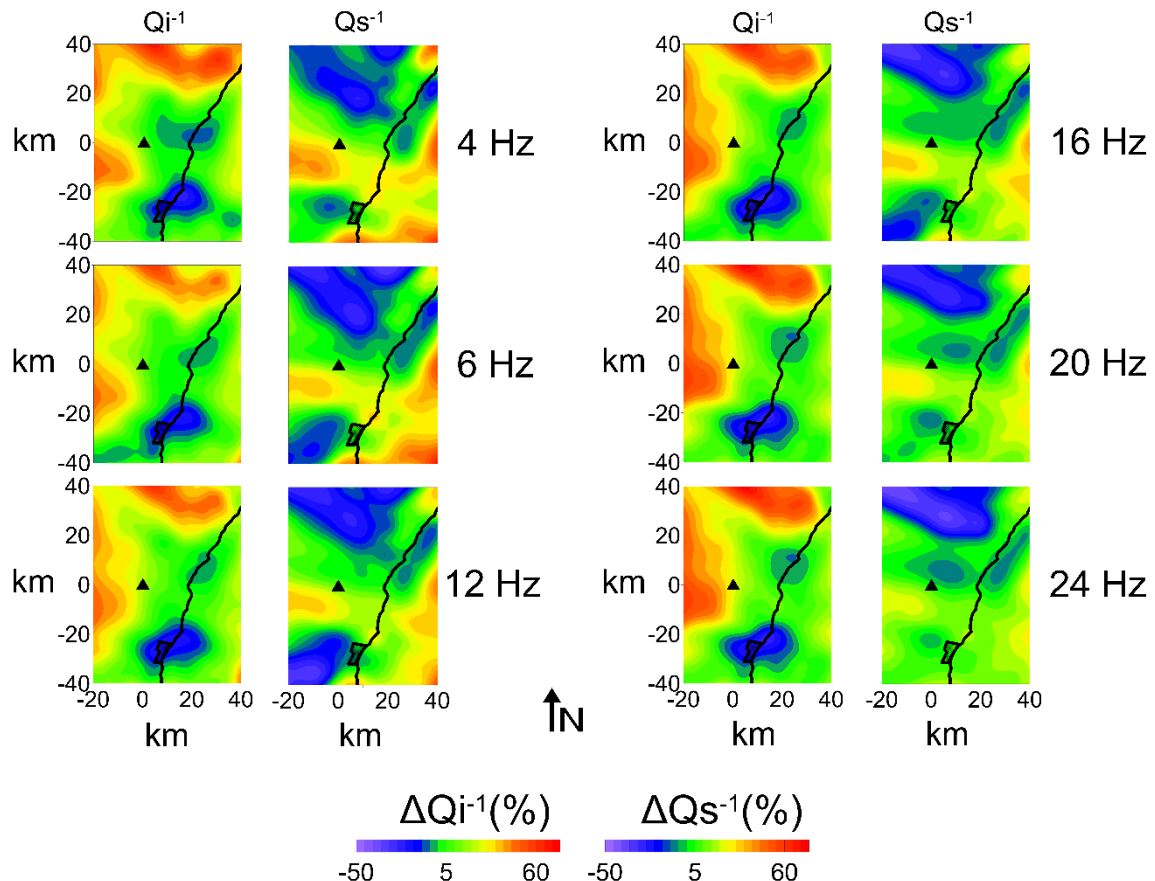
Figure B1. *Qi*-1 and *Qs*-1 anomaly maps for all analysed frequency bands.

ii. SHALLOW MAGMA STORAGE BENEATH MT. ETNA: EVIDENCE FROM NEW ATTENUATION TOMOGRAPHY AND EXISTING VELOCITY MODELS

Castro-Melgar, I., Prudencio, J., Del Pezzo, E., Giampiccolo, E., and Ibáñez, J. M. (2021). Shallow magma storage beneath Mt. Etna: Evidence from new attenuation tomography and existing velocity models. *Journal of Geophysical Research: Solid Earth*, 126 (7), e2021JB022094. https://doi.org/10.1029/2021JB022094

SHALLOW MAGMA STORAGE BENEATH MT. ETNA: EVIDENCE FROM NEW ATTENUATION TOMOGRAPHY AND EXISTING VELOCITY MODELS

Ignacio Castro-Melgar[1], Janire Prudencio[1,2], Edoardo Del Pezzo[2,3], Elisabetta Giampiccolo[4] and Jesús M. Ibáñez[1,2,4]

[1]*Department of Theoretical Physics and Cosmos, University of Granada, Granada, Spain*

[2]*Andalusian Institute of Geophysics, University of Granada, Granada, Spain*

[3]*Istituto Nazionale di Geofisica e Vulcanologia, Osservatorio Vesuviano, Napoli, Italy*

[4]*Istituto Nazionale di Geofisica e Vulcanologia, Osservatorio Etneo, Catania, Italy*

Abstract

We present a new three-dimensional (3D) image of attenuation beneath Mt. Etna volcano based on the coda normalization method. Mt. Etna is an ideal natural laboratory for the application of new or unconventional tomography techniques owing to high levels of seismicity spanning a wide range of epicentral distances and depths. We retrieved seismic waveforms from the database generated in the 2014 TOMO-ETNA seismic experiment and performed a joint interpretation of tomographic and geophysical inversion models to better constrain interpretations of the volcanic structure. We compared the attenuation tomography results with seismic inversion models (two *P* wave seismic models and a 3D coda wave seismic attenuation model) and the literature to highlight and interpret structural elements and their impact on the volcano dynamics. We created a new image of the inner structure of Mt. Etna that will help to constrain present and future volcanic behavior. In particular, we focused on magma storage below the summit area and identified a large high-attenuation volume that is characterized by physical properties compatible with the presence of magma and other fluids. The existence of such a large volume of magma in the shallow crust below Mt. Etna has implications for the eruptive potential of the volcano.

Plain Language Summary

Mount Etna, Italy, is one of the world's most active volcanoes and presents an almost constant state of activity. To correctly interpretate potential volcanic hazards, there is a need to better understand the complex inner structure of the volcano. To this end, Mt. Etna is an ideal natural laboratory for the application of new or unconventional tomography techniques. We analyzed seismic attenuation, which measures the loss of energy of the seismic waves, to obtain a three-dimensional attenuation model of Mt. Etna. We compared our attenuation tomography results with other geophysical data in order to interpret key structural elements and their impact on volcano dynamics. We identified a large volume below the summit area that is compatible with the presence of magma and other volcanic fluids, highlighting the continued eruptive potential of the volcano.

1. INTRODUCTION

Determining the location and size of potential magma reservoirs is crucial to constrain the size of future eruptions or eruptive frequency. Magma accumulation and melt migration have been the focus of extensive research at Mt. Etna volcano. Recent geophysical imaging of Mt. Etna has shown the growing importance of several geological bodies in explaining the migration of eruptive materials inside the volcano. One such body, known as the High Velocity Body (HVB), is a highly consolidated structure located below the central-southern part of the volcano. The HVB has been observed in several tomography studies (Giampiccolo et al., 2020 and references therein) and is interpreted as a massive accumulation of intrusions within the sedimentary basement. In addition, new structural elements have been identified tomographically to the west and southwest of the main volcanic edifice (e.g., Diaz-Moreno et al., 2018 and references therein). Despite not being widely discussed and interpreted in studies based on travel time tomography, these bodies have been well resolved using other techniques. In addition, recent studies (Alparone et al., 2015; Barberi et al., 2016) have found a strong association between deep seismicity beneath Mt. Etna and these geological objects, indicating the need for further study. Apparent contradictions between older and newer tomographic images possibly reflect the increased sensitivity of new tomography techniques to rock heterogeneity associated with the presence of dykes and fractures permeated by volcanic fluids. Moreover, volcanoes are dynamic systems, where fluid movements accompany the temporal evolution of the structural elements that comprise the bulk of the volcano;

157

this is reflected in variation between tomographic images. Detecting these changes is crucial for improving early-warning protocols.

From a geological perspective, time-dependent three-dimensional (3D) tomography models—4D models—allow us to study the temporal evolution of volcanic structures and the fluids within them in order to understand the pre-eruptive behavior of the system. Passive 4D tomographic models of active volcanoes (e.g., De Gori et al., 2011; Giampiccolo et al., 2020; Koulakov and Vargas, 2018; Koulakov et al., 2018; Patanè et al., 2006) rely on strict hypotheses for seismic datasets; for example, assuming the same source-station configuration for different time periods, which is uncommon. They are also affected by large uncertainties in source locations for different time periods. An alternative approach is to perform active seismic experiments, which provide an instantaneous snapshot of the volcanic system (e.g., Ben-Zvi et al., 2009; García-Yeguas et al., 2012; Ibanez, Diaz-Moreno, et al., 2016; Ibanez, Prudencio, et al., 2016; Ibanez et al., 2008; Shalev et al., 2010; Voight et al., 2014; Zandomeneghi et al., 2009). There are obvious limitations to this procedure, including the logistical complexity, high economic cost, and resolution limits associated with the distribution of the active seismic sources. However, once these data are available, new methodologies that allow modeling and inverting for different seismic attributes can better inform on the structure and dynamics of the volcanic system (Prudencio, Ibáñez, et al., 2013; Prudencio, Ibáñez, et al., 2015; Prudencio, Del Pezzo, et al., 2013; Prudencio, De Siena, et al., 2015).

Mt. Etna is an ideal natural laboratory for the application of new or unconventional tomography techniques owing to high levels of seismicity spanning a wide range of epicentral distances and depths, and because of the extended network of its monitoring institution (the Istituto Nazionale di Geofisica e Vulcanologia, Osservatorio Etneo, INGV-OE). It is therefore unsurprising that so many tomographic works have used Mt. Etna as a template for exporting new methodologies to other volcanoes. Geographical, morphological, geological, volcanological, and geophysical descriptions of Mt. Etna volcano are widely available in the literature, and highlight the importance of this volcanic system (e.g., Aloisi et al., 2020; Azzaro et al., 2012; Barreca et al., 2018, 2020; Branca and Ferrara, 2013; De Guidi et al., 2015; Neri et al., 2009; Presti et al., 2020). Studies focused on geophysical and tomographic models of the volcano are also abundant (i.e., Bonforte et al., 2008; Chiarabba et al., 2004; De Gori et al., 2011; Díaz-Moreno et al., 2018; Giampiccolo et al., 2020; Guardo and De Siena, 2017; Guardo et al.,

158

2020; Ibáñez et al., 2020; Laiolo et al., 2019; Martínez-Arévalo et al., 2005; Patanè et al., 2002).

In this work, we present a new 3D model of Mt. Etna volcano based on seismic attenuation techniques. The coda normalization method (Aki, 1980; Del Pezzo et al., 2006; De Siena, Thomas, and Aster, 2014; De Siena, Thomas, Waite, et al., 2014; De Siena et al., 2017; Matsumoto et al., 2009; Prudencio, Ibáñez, et al., 2015; Prudencio, De Siena, et al., 2015; Prudencio and Manga, 2020; Nazemi et al., 2017; Sketsiou et al., 2021), was used for the first time in this setting to study *P* wave attenuation. We retrieved seismic waveforms from the database generated in the 2014 TOMO-ETNA seismic experiment (Ibáñez, Díaz-Moreno, et al., 2016; Ibáñez, Prudencio, et al., 2016). The travel-time and coda-wave measurements from this data set have been used to perform direct *P* wave velocity tomography (Díaz-Moreno et al., 2018), and to separate the effects of intrinsic and scattering attenuation (Ibáñez et al., 2020), among others. This database corresponds to an active seismic experiment using air guns and a large number of temporary and permanent seismic stations. The high number of receiver-source couples available provides homogeneous spatial coverage that increases the quality of the obtained images. These images were generated over a short time interval and reflect a snapshot of the structure of Mt. Etna at the time of their realization. During the investigated period, Mt. Etna was characterized by several episodes of Strombolian activity and lava emissions from the main upper craters (i.e., Viccaro et al., 2016 and references therein).

Volcanoes are complex structures that respond differently to different geodynamic conditions. This complexity is reflected in the difficulty of interpreting structures from single geophysical observations and/or tomographic models. Joint interpretation of tomographic and geophysical models can better constrain interpretations of a volcanic structure. In recent works (e.g., Basant et al., 2021; Cordell et al., 2020; De Siena et al., 2017; García-Yeguas et al., 2017), the integration of different geophysical models has highlighted important structures for different volcanic scenarios. Here, we compared our attenuation tomography results with geophysical models—two *P* wave seismic tomographies (Díaz-Moreno et al., 2018; Giampiccolo et al., 2020) and a 3D coda waves seismic attenuation model (Giampiccolo et al., 2021)—and the literature to highlight and interpret structural elements and their role in volcano dynamics at Mt. Etna. In particular, we focused on magma storage below the summit, where high-attenuation

159

volumes mark the presence of an extended molten body. This body is the likely cause of the continuous volcanic activity, including the highly energetic eruption underway at the time of writing (June 2021).

2. Methods and Seismic Data

2.1 Coda Normalization Method

Coda normalization (CN) was based on the approach developed Del Pezzo et al. (2006); this method provides a measure of the single-path attenuation coefficient using the phenomenological coda wave properties. Aki (1980) first proposed this method to calculate space-averaged *S* wave attenuation in Japan. By normalizing the direct S wave spectrum and using a late "lapse time" (tc, the time spanned from the origin time along the coda), it was demonstrated that the source intensity, the site transfer functions, and the instrument transfer functions disappear in the ratio. The method is applied to obtain single station estimates of the total inverse *P* wave quality factor (*Q*) along the seismic path. Here, we briefly review the method; for more detailed descriptions, please see Del Pezzo et al. (2006), De Siena, Thomas, and Aster (2014), De Siena, Thomas, Waite, et al. (2014), and/or Prudencio, Ibáñez, et al. (2015), Prudencio, De Siena, et al. (2015).

The average total attenuation coefficient, QT^{-1}, measures the average loss suffered by seismic energy body waves owing to heterogeneous attenuation (and thus excluding geometrical spreading). In the spectral domain and for a single source (*i*)–station (*j*) observation:

$$E_{ij}(f,r) = s_i(f)\theta_{ij}(\sigma,\varphi)I_j(f)T_j(f)G_{ij}(r)x\ exp\ exp\ (-2\pi f\ \frac{t_{ij(r)}}{Q_T^{ij}(r)}) \qquad (1)$$

in which *E(f,r)* is the energy density spectrum, where *f* is the frequency of the *S* wave radiation emitted by source *i* at distance *r* along the source-station raypath; *Si(f)* is the source energy spectrum, modulated by the radiation pattern $\theta(\upsilon,\phi)$; *Ij* is the instrument transfer function; *Tj* is the site transfer function; *G* is the geometrical spreading; *tij* is the travel time along the ray; and *QT ij* is the total quality factor calculated along the raypath,

which defines the fractional energy lost per cycle (ΔE) according to the equation $Q_T^{ij} = -2\pi E_{ij}/\Delta E_{ij}$. To avoid the effects of diffraction, waveguides, and surface waves in given frequency bands, G and $QT^{-1}$are preliminarily inverted and then kept constant, inverting only for spatial variations of quality factors (De Siena, Thomas, Waite, et al., 2014).

Yoshimoto et al. (1993) proved that the CN method can be applied to measure average P wave attenuation (P wave quality factor, Q_p) by using the S wave coda to normalize observations, and remove source, site, and instrumental effects.

In this study, we used active sources that only produce P waves; as such, we could neglect radiation pattern effects. Ibáñez et al. (2020) showed that pure compressional signals convert to shear after a few mean free paths from the signal origin. However, the first arrivals remain purely compressional (Díaz-Moreno et al., 2016, 2018; García et al., 2016). Using a 1 s window guarantied that we obtained pure direct P waves.

The seismic attenuation coefficient at each node of the inversion grid (Qb) was obtained using the following equation (Del Pezzo et al., 2006):

$$R_{ij} = K(f) - \pi f \sum_{b=1}^{B} l_{ijb} s_b Q_b^{-1}, \qquad (2)$$

where Rij is the spectral ratio between the direct P wave energy ($E_{ij}{}^P$) and the coda energy at a given lapse ($E_{ij}{}^C$ (fc, tc)), pre-multiplied by r; index b indicates the bth block and B represents the total number of blocks; sb represents the slowness; l_{ijb} is the length of the ray-segment crossing the bth block for each ij source-station couple; and $K(f)$ is a constant depending on the phenomenological coda attenuation. This equation can be linearly inverted for $Q_b{}^{-1}$.

2.2 Seismic Data

The TOMO-ETNA experiment was designed to perform detailed structural imaging of the crust beneath Mt. Etna volcano and north-eastern Sicily up to the Aeolian

Islands (Ibáñez, Díaz-Moreno, et al., 2016; Ibáñez, Prudencio, et al., 2016). As detailed in Coltelli et al. (2016), the survey was conducted from aboard the "Sarmiento de Gamboa" Spanish oceanographic vessel in June 2014. Approximately 9700 air-gun shots were generated in the Ionian and Tyrrhenian Seas, and the data were used in perform high-resolution seismic tomography using the wide-angle seismic refraction method (Díaz-Moreno et al. 2016, 2018). The vessel-mounted air-gun array shoots with a power capacity of up to 5,200 cubic inches. Active seismic data were recorded at 90 campaign short-period three-component seismic stations, 17 campaign broadband seismometers, and 133 permanent seismic stations belonging to Italy's Istituto Nazionale di Geofisica e Vulcanologia (INGV). The area covered by the experiment (see Figure 2 of Díaz-Moreno et al., 2018) was >300 × 300 km. Following a magnitude duration scale (MD) calibrated for volcanic regions (Havskov et al., 2003), and by measuring the average duration of each record (between 25 and 30 s), the equivalent magnitude of these events varied between MD 1.2 and 1.4. The focus of this study was Mt. Etna; however, given the large distances between the shots fired in the Tyrrhenian Sea and Mt. Etna volcano, these signals were not recorded at all of the seismic stations within the study region; those that were recorded had very low signal-to-noise ratios. For direct wave tomography, large distances are not an issue for the 3D velocity model because of the use of advanced first arrival detection techniques (García et al., 2016). However, they cannot be used for attenuation tomography, in which wave packets with a good signal-to-noise ratio are critical. Therefore, we selected a subset of 145 seismic stations and 850 seismic sources for use in this study; this allowed us to analyze a total of 1,380,473 seismograms. The selection of seismograms was made according to different quality criteria relative to the seismic attributes analyzed (direct wave amplitudes and coda intensity). The coda normalization method requires both clear, energetic P wave packet and coda amplitudes with a high signal-to-noise ratio. Figure 1 shows a map of the region and an example signal filtered in different frequency bands.

2.3 Quality Control for Seismic Signals and Data Selection

The coda normalization method, and its application through the MURAT code, can be applied to different frequency bands. Therefore, analyses can be carried out for different frequency bands depending on the spectral content of the signal and on the quality based on the signal-to-noise ratio. According to the dominant source frequency of

the active seismic signals (Coltelli et al., 2016), the spectral content is theoretically very low (from <4 up to 16 Hz). To select the best frequency bands for attenuation analysis, a set of signals were pre-processed by filtering at different frequency bands and studying their signal-to-noise ratios. We selected a subset of waveforms representing all source-station distances and seismic stations. For this subset, the signals were filtered in seven frequency bands (centered at 4, 6, 8, 12, 20, and 24 Hz, with a bandwidth of ±2 Hz) using a Butterworth band-pass filter with eight poles as in Ibáñez et al. (2020); an example is shown in Figure 1b. Based on the signal-to-noise ratio, we decided to estimate the attenuation values, and therefore the attenuation images of Mt. Etna volcano and surrounding regions, in the frequency band of 8 Hz (i.e., using signals filtered between 6 and 10 Hz). All signals were checked using quality control based on the signal-to-noise ratio. The P/noise, Coda/noise, and P/Coda ratios were calculated, and any signal for which any of these ratios was <2 was eliminated. Figure 2 shows examples of these window analyses for events characterized by small and large epicentral distances.

As discussed in previous works (e.g., Ibáñez et al., 2020), seismic signals generated with air guns over the sea produce so-called water-waves, whose energy content can alter the seismogram. Since both the propagation speed of this wave packet and the time window of the coda are known, it is possible to theoretically determine which source-station pairs will have the arrival of these waves in the reference coda window. In this way, all data pairs that could have been contaminated by the arrival of the water-wave package in the coda window were eliminated.

In summary, the time windows selected for this study included a *P* wave window with a duration of 1 s from the arrival of the *P* wave, a coda window beginning 11 s after the arrival of the *P* wave and with a duration of 2 s, and a window located 5 s before the origin time and with a duration of 5 s, which was used for noise estimation. After all quality checks, 31,482 traces were retained for the final inversion.
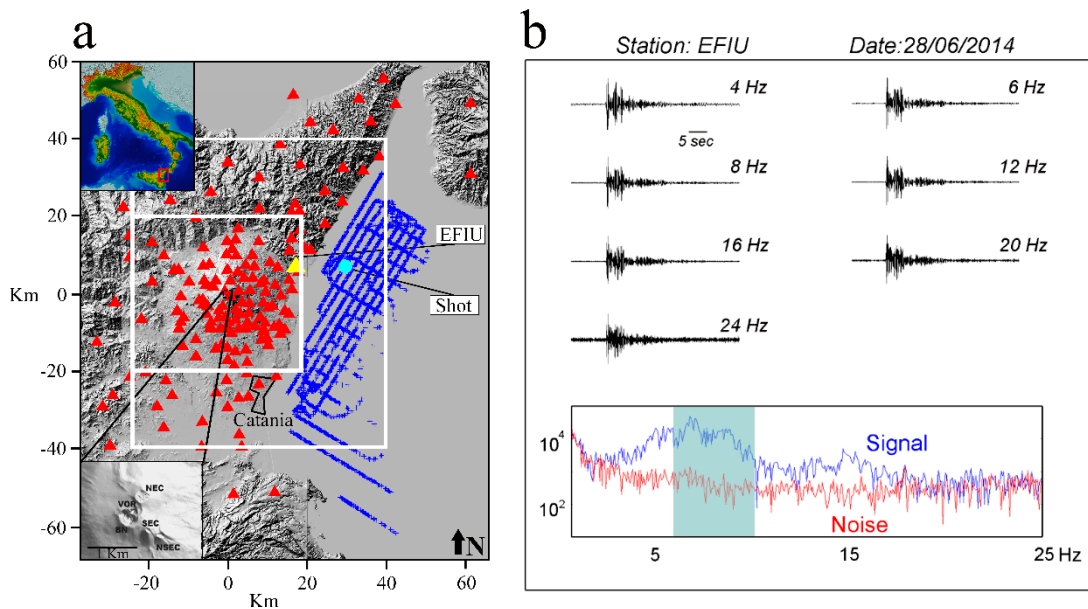
Figure 1. Study region location and an example signal filtered at multiple frequencies. (a) Map of the study region, with seismic stations represented by red triangles and explosions or air gun shots represented by blue pluses; inset maps show the regional location of Mt. Etna (upper left-hand side) and the active craters of Mt. Etna (lower left-hand side; BN, Bocca Nuova; VOR, Voragine; NEC, North East crater; SEC, South East crater; NSEC, New South East Crater). (b) Example signal filtered at multiple frequencies; this signal was generated by an explosion (light blue dot in part "a") and recorded at a station near Mt. Etna (yellow triangle in part "a"). The seismic signal is filtered every 4 Hz, from 4 to 24 Hz. The lower plot compares the spectrum of the signal with that of the prevent noise. The 8 Hz frequency band (shown in light blue) was selected for this study because it presents the best signal-to-noise ratio.

3. P WAVE ATTENUATION TOMOGRAPHY

For the inversion of P-to-coda energy ratios we used the MuRAT1.0 Code (De Siena, Thomas, and Aster, 2014). MuRAT is a Matlab©-based tomographic code that measures and inverts the average *P* and/or *S* wave quality factors using the method described in the previous section. The most recent release adds tools to invert for the 3D

scattering and absorption structure of the area. This code allows testing of the recovered patterns with checkerboard and synthetic anomaly tests. To obtain our 3D attenuation images, we devised a multi-resolution approach. Tomography was performed on a regional image (lateral extension of 80×60 km) with resolution cells of 12×12 km, and on a local image centered on the summit zone of Mt. Etna (40×40 km with a cell resolution of 6×6 km).

3.1 Velocity Model and Ray Tracing

For this inversion, we used a 3D velocity model obtained using joint active-passive seismic tomography by Díaz-Moreno et al. (2018) with spacing of 2 km in both the horizontal and vertical axes. This model takes vertical and lateral heterogeneities into account, giving velocity values for each cell of a defined 3D grid.

The model was used to trace the source-receiver ray-paths obtained using a Thurber-modified ray-bending approach developed by Block (1991). This approach has been applied by De Siena et al. (2010) in Campi Flegrei and Prudencio and Manga (2020) in the Long Valley Caldera, confirming its applicability in volcanic areas despite their high heterogeneity. Figure 3 shows seismic ray density maps in which the number of rays per cell always exceeds five (i.e., the number of rays per cell exceeds the minimum quality standard). In areas of higher density, the number of rays exceeds 1,000. For the volcanic area of Mt. Etna, there are between 200 and 300 rays per resolution cell.
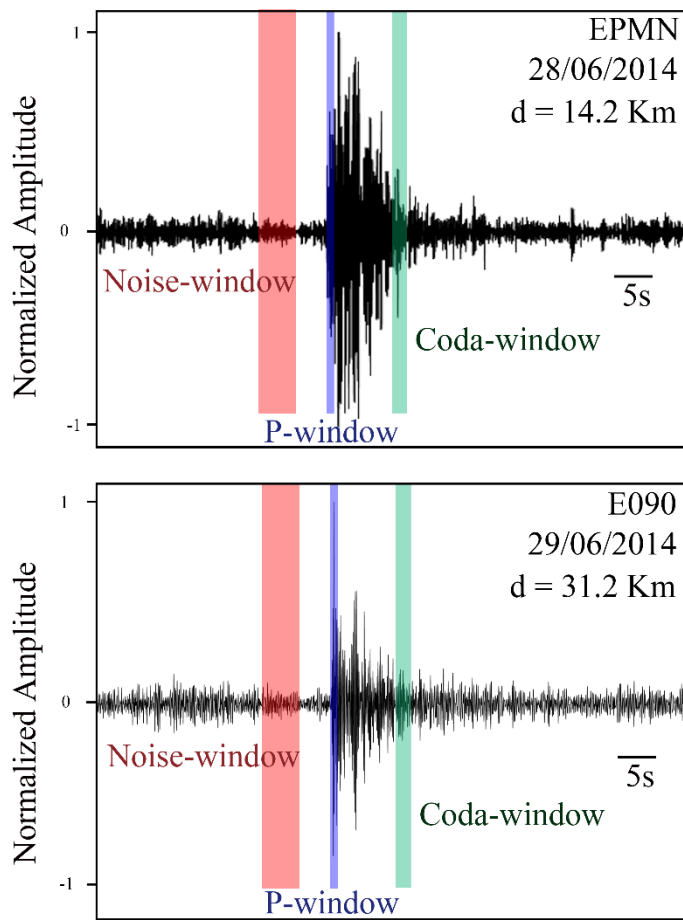
Figure 2. Two examples of vertical seismograms used for this study showing the window used for noise, *P*-wave and reference coda waves for the normalization analysis.

3.2 Geometrical Spreading

Before solving for the total attenuation variation, it is necessary to set the average geometrical spreading and Q_p^{-1} values. In highly heterogeneous volcanic regions, the geometrical spreading factor (*n*) takes a higher value than the theoretical one (2 for 3D media), as shown by Ibanez et al. (1993) and Akinci, Del Pezzo, and Ibáñez (1995), Akinci, Ibáñez, et al. (1995). As *n* and Q_p are coupled, and based on previous studies, the value of geometrical spreading was fixed at *n* = 2.1.

3.3 Picard Condition and l-curve

The MuRAT code from De Siena, Thomas, and Aster (2014) performs a stability test of the Picard condition by comparing singular values with the dot product of the columns of the matrix spanning the data space and the data vector. When the dot products decay to zero more quickly than the singular values, the Picard condition is satisfied. Figure 4a shows the Picard condition for the Mt. Etna data. The dot products (blue line) decay faster than the singular values (red line); therefore, instabilities due to small singular values are unlikely. Figure 4b shows the L-curve used to estimate the damping parameter (α).

3.4 Resolution Test

Two types of tests were performed in order to assess (1) the spatial resolution of our data over the entire area (checkerboard test) and (2) to study the capability our data to resolve specific contrasts in attenuation (synthetic anomaly test). For the checkerboard test, we followed a multi-scale procedure developed for a similar active database (Prudencio, De Siena, et al., 2015). We solved the inversions for regions of different extensions and node spacings, and added Gaussian random noise (10%) to the synthetic energy ratios calculated from a checkerboard synthetic structure. The attenuation contrasts in the synthetic anomaly tests were placed according to the results obtained in the velocity and attenuation tomography studies (Díaz-Moreno et al., 2018; Giampiccolo et al., 2020). This allowed us to interpret the details we recovered on these structures.

As indicated above, we divided the study area in two regions—a large region including Mt. Etna and its surroundings (Figure 5) and a smaller area centered on the volcano (Figure 6). For the large region, the data have excellent resolution over an area extending 60 km in an E–W direction and 80 km in a N–S direction; this is consistent with the ray density maps (Figure 3). For the small region, the data have excellent resolution over an area of 40×40 km; this coincides with the region of highest ray densities (i.e., >500 rays per cell; Figure 3).

The resolution tests confirmed that our data for both the larger and smaller regions are very well resolved. Therefore, geological interpretations based on our inversion of the QP values can be considered robust. The final resolution of our results is the combination of all of the tests performed. A single test can be good or bad, but using a set of multiple tests allows one to comprehensively demonstrate the goodness of the model. In our case,

we performed three independent tests. (1) For the ray density, we ensured that all cells in our representation volume were covered by an adequate minimum number of rays to guarantee stable results. (2) For the checkerboard tests, the choice of attenuation contrast was important. For Q_p^{-1}, we introduced a contrast value of ±0.01 (i.e., only 2× the estimated error). Using this very low contrast allowed us to show that the attenuation anomalies in our final model are real. However, low contrast also makes it more difficult to obtain good test results, and some portions of some cells do not correctly return the starting model. (3) Finally, for the isolated synthetic anomaly tests, we also used a low contrast attenuation value. The test
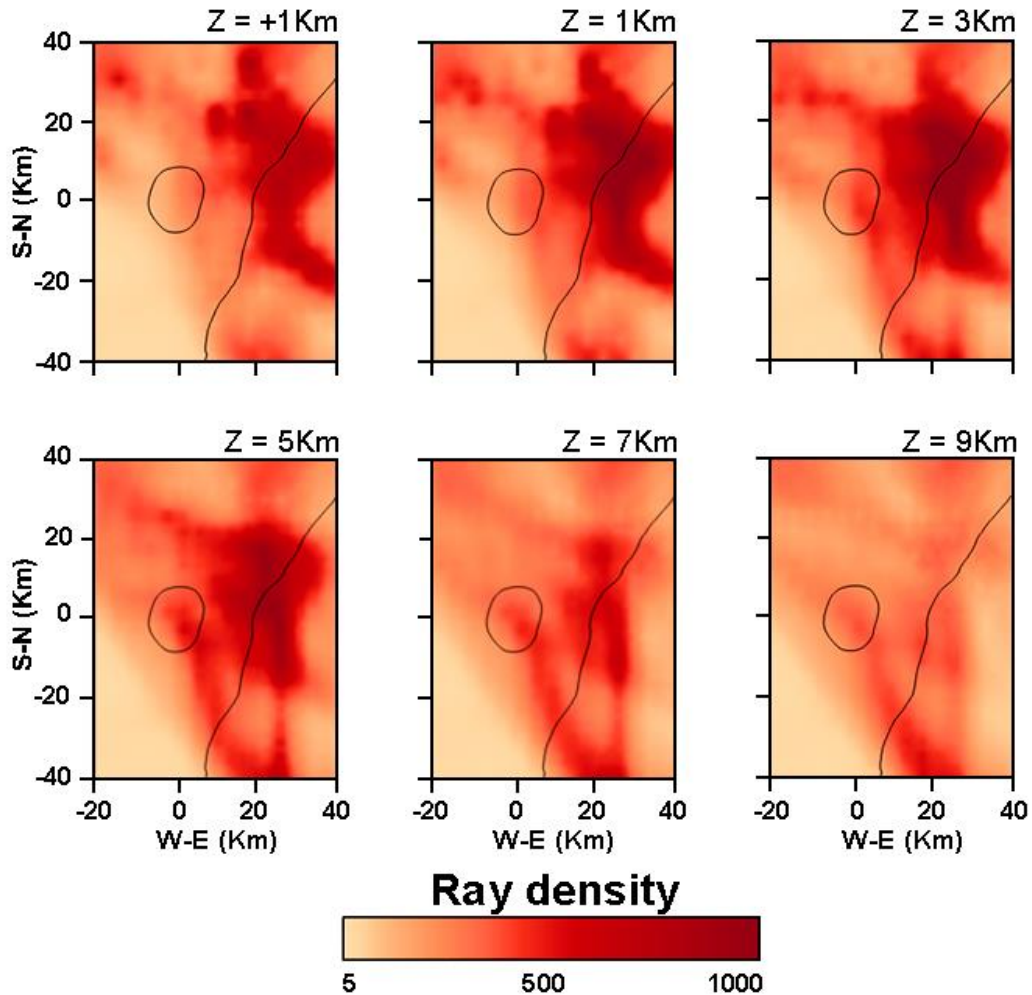

Figure 3. Seismic ray density maps of Mt. Etna at different depths. Densities are represented as a function of the sampled depth, and the number of rays per cell always exceeds five.

168

results for these anomalies have high reliability. In the final results, darker shading highlights regions with lower resolution.

4. RESULTS AND DISCUSSION

4.1 Attenuation Model Results

The average $Q_p{}^{-1}$ value of all the energy ratios obtained using a least squares inversion of the coda-normalized energy versus travel time (Figure 7) is 0.027. Although the inversion algorithm provides a final attenuation model based on $Q_p{}^{-1}$, our discussion of the results is made using Q_p values, since integer numbers are easier to be compared and understand. In this sense the studied region has an average Q_p value of 37. This is lower than the values obtained in some other volcanic regions—Prudencio and Manga (2020) obtained a value of 250 for the Long Valley Caldera, and Prudencio, Ibanez, et al. (2015) obtained a value of 125 for the island of Tenerife—but is comparable with those determined by Prudencio, De Siena, et al. (2015) for Deception Island (29). At Mt. Etna, Martínez-Arévalo et al. (2005) derived a value of 75; the difference between the present study and that of Martínez-Arévalo et al. (2005) reflects the deeper volumes sampled in the earthquake data set. Regardless, this value reflects a highly attenuative region, consistent with a heterogeneous area subject to continuous volcanic activity.

Figures 8 and 9 show horizontal projections for the larger and smaller areas of interest, respectively, from 1 km above sea level (a.s.l.; i.e., within the edifice) to 9 km below sea level (b.s.l.). Figures 10 and 11 show two vertical sections (N–S and W–E) passing through the summit zone of Mt. Etna volcano.

In summary, we obtained two 3D models of Mt. Etna. We emphasize that even in the smaller-scale model, we sampled a very large volume compared with previous studies. This was thanks to the high quality of the data set used, the density of the stations, and the versatility of the method. Even so, the images cannot fully reflect small-scale variation in seismic attenuation; as such, the results are dominated by large structural contrasts. According to the starting Q_P value used for the inversion procedure ($Q_P = 37$) at 8 Hz, we found that the study area is dominated by very high attenuation, as observed in previous attenuation studies (e.g., Del Pezzo et al., 2019 and references therein).
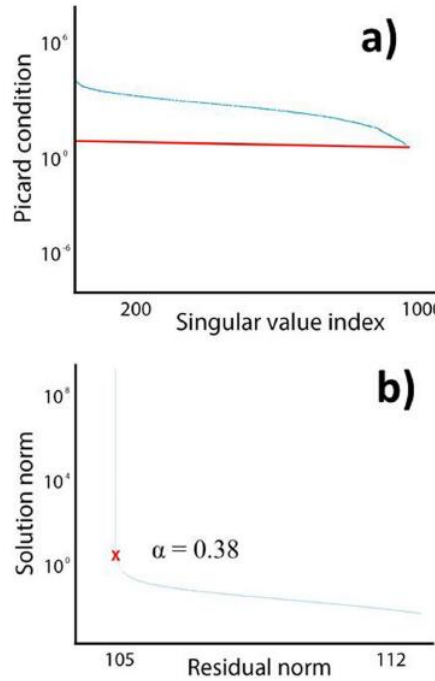
Figure 4. Picard condition and L-curve of the Mt. Etna data. (a) Picard condition plot, in which dot products (blue curve) decay to zero more quickly than the singular values (red curve) and the Picard condition is satisfied. (b) L-curve used to estimate the damping parameter (α) for the inversion.

4.2 Large Scale Attenuation Model

In our regional model, there is no clear evidence for shallow magma storage beneath Mt. Etna (i.e., there is no apparent contrast with the region surrounding the volcano; see Figure 8 [horizontal layers] and Figure 10 [vertical cross sections]). However, the model does show regional structural difference, including two zones with opposite attenuation characteristics. There is a low seismic attenuation body (high QP value) located 10 km east of the Mt. Etna crater appears out at almost every depth. Although this body reaches the limits of our graphical representation, it is not affected by edge distortion effects and according to the resolution tests it is well resolved. This volume corresponds to the inferred location of a volcanic shield complex formed before Mt. Etna volcano. This body would be highly consolidated compared with its

170

surroundings, which would explain its low seismic attenuation characteristics. In the same area, Díaz-Moreno et al. (2018) highlighted a high-velocity anomaly, located to the southeast of Mt. Etna, compatible with the plumbing system feeding an ancient shield volcano located offshore of the Timpe area (Chiocci et al., 2011; Corsaro et al., 2002). This complex has been hypothesized as the cause of a wide and intense positive magnetic anomaly (>700 nT) related to deep sources (Cavallaro et al., 2016), as evidenced by a magnetic survey carried out during the TOMO-ETNA experiment; a probable connection between this high-velocity anomaly and the HVB was hypothesized.

A second high Q_P region is located on the north-western edge of study area. Features in this area need to be interpreted with caution owing to partial distortion of the solution. However, previous studies have also shown a high-velocity contrast (Díaz-Moreno, 2016; Díaz-Moreno et al., 2018) area related to different attenuation mechanisms (e.g., low scattering and high intrinsic attenuation; Ibáñez et al., 2020). The strong attenuation contrast (from high-to-low Q_P values), which strikes approximately NE–SW, is consistent with regional tectonic processes acting on the northwestern sector of the volcano. This sector is buttressed against a pre-existing unit, developed in the metamorphic and sedimentary rocks of the Apennine Maghrebian Chain. Therefore, extensive fracturing and seismicity associated with the compressive regime could be responsible for the low-Q_P volume, which correlates well with a low V_p and high V_p/V_s volume observed by Giampiccolo et al. (2020).

4.3 Small Scale Attenuation Model

The most significant result from the second inversion, performed on a smaller volume but with higher resolution, is the presence of a high-attenuation area below the volcano summit. While high attenuation is expected below erupting volcanos, neither a low-velocity nor a high-attenuation volume of this form and dimension have been observed in previous tomographic models of Mt. Etna (e.g., Aloisi et al., 2002; Giampiccolo et al., 2021; Patanè et al., 2006). We believe that this reflects the limitations of regional-scale sampling; even in this study, the larger-scale model failed to identify an anomalous zone below the volcano. To adequately resolve high resolution contrasts, a tomographic inversion must use the most precise starting model available. As shown here,

a regional scale active survey provides the necessary attenuation characteristics to highlight fluid- and melt-filled structures.
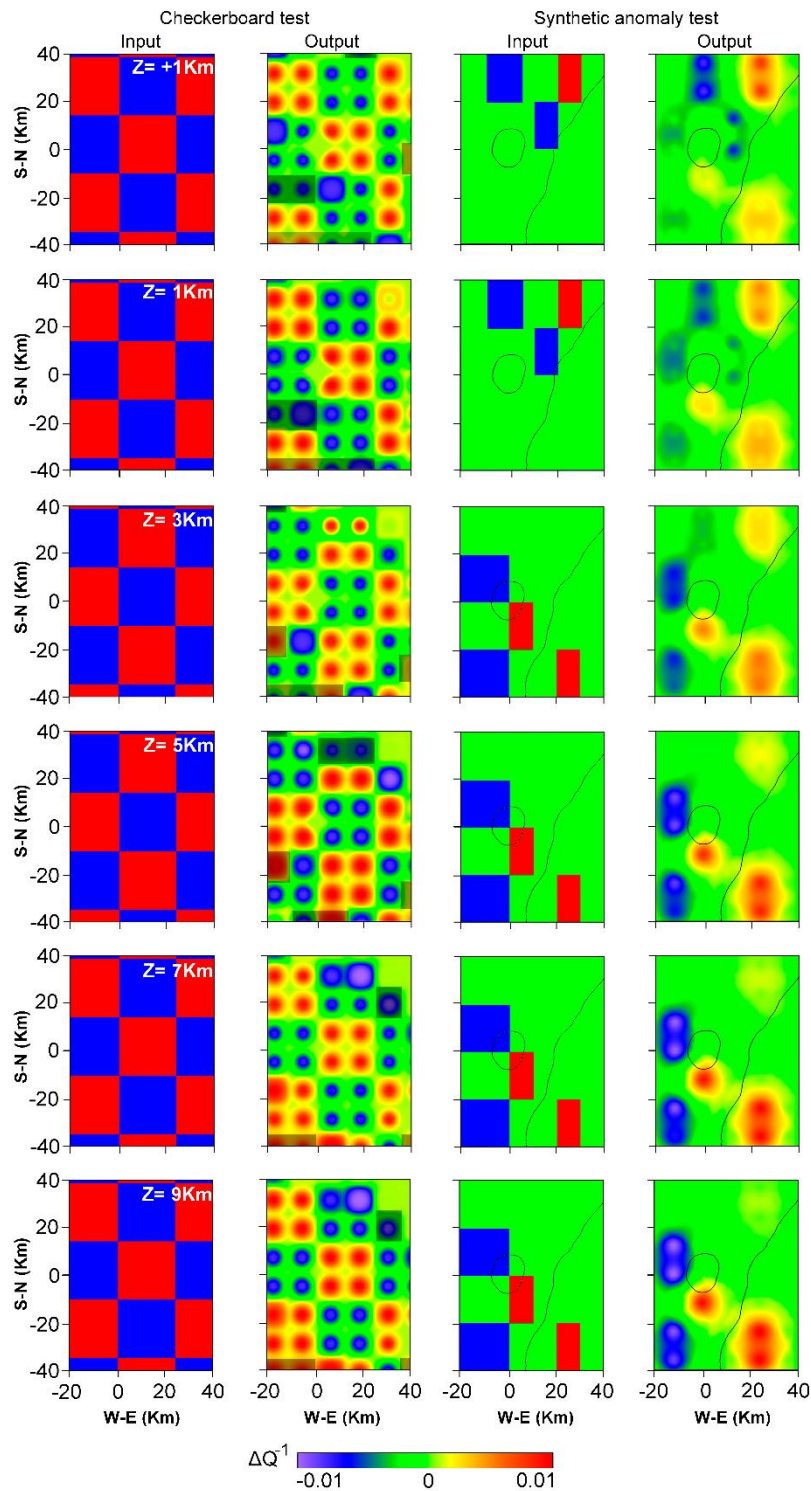
Figure 5. Results of checkerboard and localized synthetic anomaly resolution tests carried out to determine the resolution and sensitivity of our tomographic study. Checkerboard and localized synthetic anomaly resolution test results for a large region that comprises Mt. Etna and the surrounding area using cells of 12×12 km. In the central column we present the input model for the localized synthetic anomaly resolution test. In the first image of the checkerboard test we remarked in black the lines of the input model. For $Q_p{}^{-1}$, we introduced a contrast value of ± 0.01.
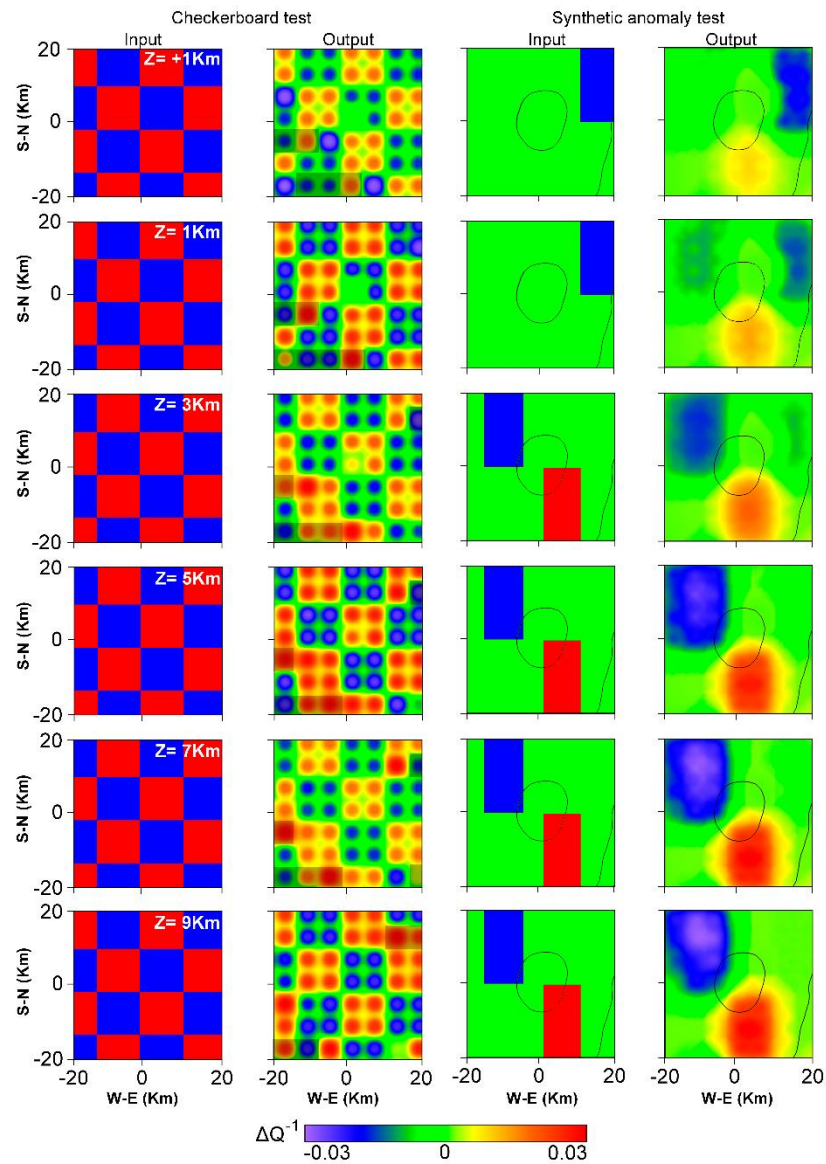

Figure 6. Results of checkerboard and localized synthetic anomaly resolution tests carried out to determine the resolution and sensitivity of our tomographic study. Checkerboard and localized synthetic anomaly resolution test results for a small region

173

centered over Mt. Etna (cells of 6×6 km). In the central column we present the input model for the localized synthetic anomaly resolution test. In the first image of the checkerboard test we remarked in black the lines of the input model. For Q_p^{-1}, we introduced a contrast value of ±0.01.

The morphology of the high-attenuation volume under the volcano is a two-lobed system that moves from E to W when ascending from depth to the surface. The volume develops from ~1 km a.s.l. (i.e., within the edifice) down to ~8 km b.s.l.; the region of maximum attenuation occurs at ~5 km depth. Melts and fluids are associated with abrupt drops in shear wave velocity, and are generally inferred from high V_p/V_s anomalies. However, Giampiccolo et al. (2020) did not observe distinct low V_P and high V_p/V_s anomalies in the upper crust beneath the summit craters. Instead, the shallow portion of the volcano is characterized by broad low V_p/V_s anomalies; when associated with low Q anomalies, these can be interpreted as gas-filled volumes (i.e., Giampiccolo et al., 2020).
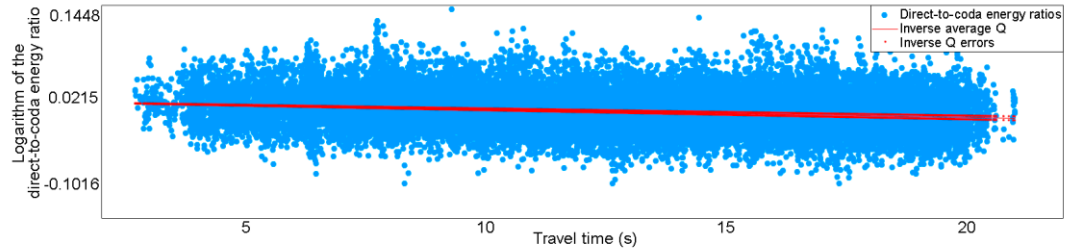
Figure 7. Fit of coda-normalized energy ratios versus travel time. The red line is the best mean square fit, from which we obtained the average Q-value for the Mt. Etna region.

In addition to this large volume of high attenuation material, we identified three low-attenuation structures, two in the western sector that, as previously discussed, correlate well with high V_p/V_s volumes reported by Giampiccolo et al. (2020), and one south of the summit craters extending from ~6 km b.s.l. to greater depths. The latter may be compatible with the HVB observed in many tomographic models. In our model, this feature does not appear exactly where many other authors represent it, but the location becomes more compatible with depth. Giampiccolo et al. (2020) found that the upper part

of the HVB has persistent low V_p/V_s anomalies which, together with high the V_p and low Q_P, suggest the presence of broad gas-dominated volumes within the upper portion of the body.

Finally, we identified small volumes with high Q_P values in the western sector of the volcano; these were also observed in the regional model, albeit less intense (Figures 8 and 10). In this sector of the volcano, volumes with high Q-coda values have been observed in other studies (Giampiccolo et al., 2021) and were associated with seismically active fault structures. However, comparing our results with those of previous studies (Díaz-Moreno et al., 2018; Giampiccolo et al., 2020 and references therein; Ibáñez et al., 2020), this area contains different volumes with low and high anomalies in terms of both velocity and attenuation. Since each previous model analyses a different type of wave and/or propagation processes, the directions of the anomalies also differ. However, the widespread consensus that different seismic and volcanic processes are occurring in this area is consistent with our observations. In particular, one of the most accepted explanations is the presence of over-pressurized regions resulting from aquifers embedded in the system and affected by volcanic heat flow (i.e., Giampiccolo et al., 2020). This could explain observations of multiple volumes with low seismic velocities (Aloisi et al., 2002; Díaz-Moreno, 2016; Díaz-Moreno et al., 2018; Giampiccolo et al., 2020), high scattering attenuation (Ibáñez et al., 2020), but low attenuation of P waves.

Figure 12 shows a 3D representation of the shallowest of these attenuation bodies. The position and shape are compatible with the presence of molten or partially molten material (magma) that feeds the eruptive processes observed at Mt. Etna volcano.

4.4 Joint Interpretation

Figure 13 shows the joint interpretation of four different tomographic models of the Mt. Etna area, including two velocity tomography models (Díaz-Moreno, 2016; Díaz-Moreno et al., 2018; Giampiccolo et al., 2020) and two attenuation models, one using coda waves (Giampiccolo et al., 2021) and one presented in this study. Several studies have made an association between the values of attenuation and velocity of seismic waves and other physical properties of the medium, as summarized in table 1 of Prudencio, Ibáñez, et al. (2015). De Siena, Thomas, Waite, et al. (2014) made these associations in their joint interpretation of Mt. St Helen velocity and attenuation images. Sato et al.

(2012) describe a theoretical foundation for many of these associations. Based on these results, we performed a joint interpretation.
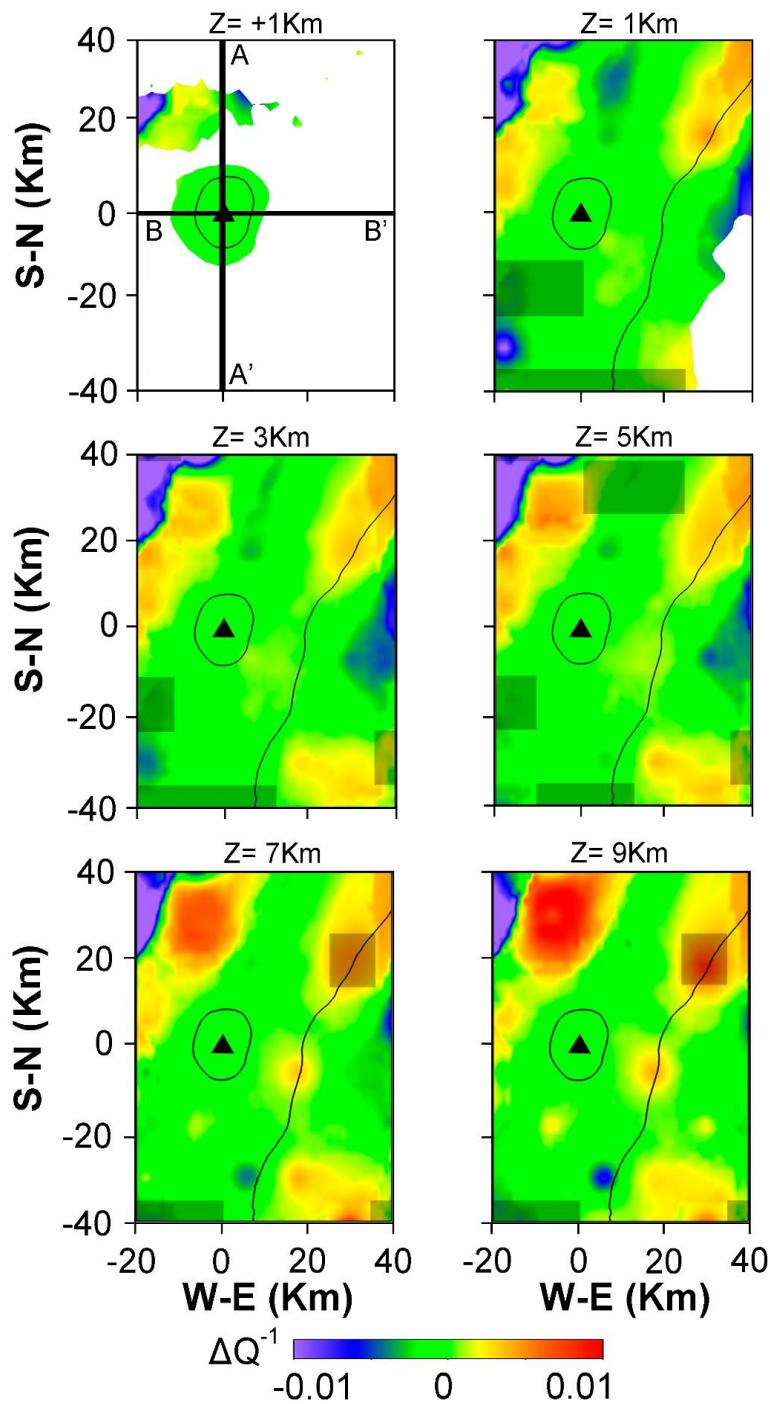
Figure 8. Tomographic images of the region around Mt. Etna volcano in different horizontal layers, from 1 km above sea level (i.e., within the edifice) to 9 km below sea level (the resolution limit). Darker shading highlights regions with lower resolution.
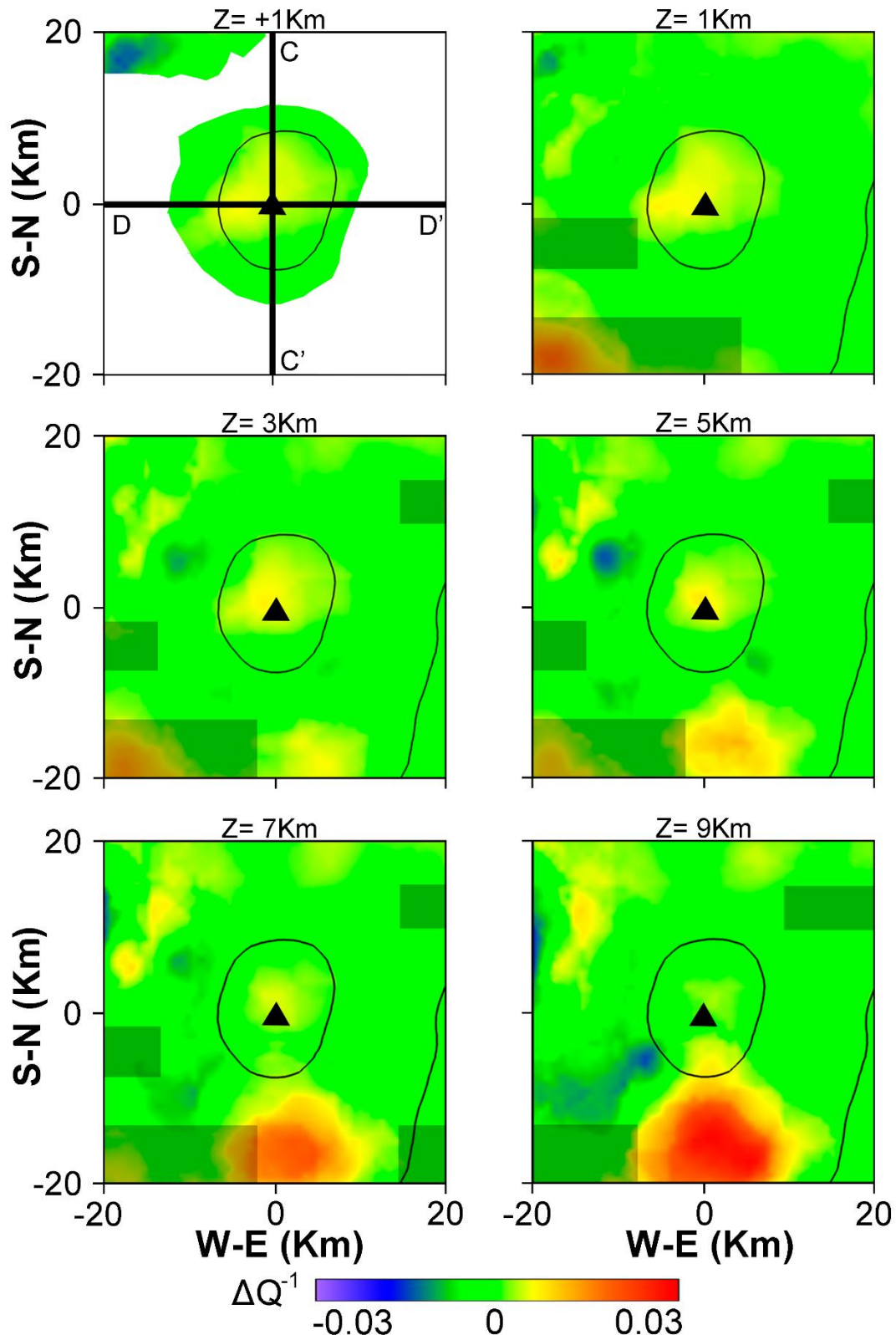
Figure 9. Tomographic images of Mt. Etna volcano in different horizontal layers, from 1 km above sea level (i.e., within the edifice) to 9 km below sea level (the resolution limit). Darker shading highlights regions with lower resolution.

Six main structures are depicted in Figure 13.

1. High V_p, high V_p/V_s ratios, average to high Q_p and Q_c (depicted in blue): This feature is consistent with highly consolidated material interpreted as the remnants of old intrusions (that fed past activity at the volcano) pervading the sedimentary basement (i.e., Branca and Ferrara, 2013). In the southeastern sector of the volcano, the highly consolidated volume correlates well with the position of the HVB observed in the literature (i.e., Giampiccolo et al., 2020 and references therein).

2. Low V_p, low V_p/V_s ratios, low Q_p (depicted in red): This feature is consistent with the presence of fluids; given the nature of this volcanic environment, we interpret this to be a region of magma storage in the shallow crust below Mt. Etna. The structure has a large volume (at least 450 km3), revealing a large eruptive potential. At the time of writing (June 2021), Mt. Etna volcano is undergoing a new and very energetic eruptive process.

178
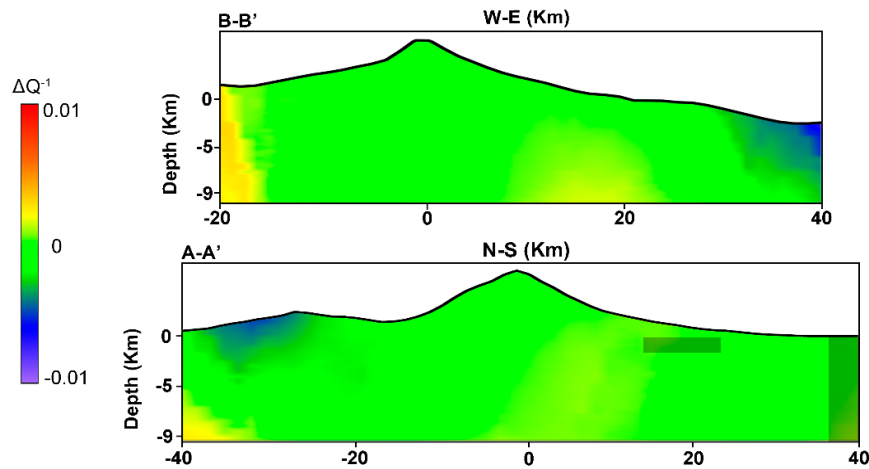
Figure 10. North–south (A–A') and east–west (B–B') vertical sections across the Mt. Etna region. The locations of A–A' and B–B' are shown in Figure 7. Darker shading highlights regions with lower resolution.

3. High V_p, high V_p/V_s ratios, low Q_p (depicted in deep purple): This feature can be interpreted as a transition zone because it is located in an intermediate region between the highly consolidated volume and a region containing partially molten material, and could represent high temperature rock (with altered physical properties) adjacent to the magma storage region. This is supported by the high attenuation, reflecting the higher sensitivity of seismic attenuation to small temperature variations as compared with seismic velocity.

4. Deep low V_p, high V_p/V_s ratios, average to low Q_p and Q_c values (depicted in pink): The high V_p/V_s ratios are indicative of fluid-filled pressurized rock (Dvorkin et al., 1999; Giampiccolo et al., 2020).

5. High V_p, low V_p/V_s ratios, average to low Q_p (depicted in turquoise): We have no interpretation for this volume, but it is consistent with a consolidated material with plastic properties.

6. Shallow low V_p, high V_p/V_s ratios, average to low Q_p and Q_c values (depicted in orange): These zones are consistent with volcanoclastic materials and/or sedimentary units around the volcano (i.e., Branca et al., 2007). This is confirmed by previous shallow velocity models of Mt. Etna performed based on correlations of ambient seismic noise using a dense seismic array and a borehole (Zuccarello et al., 2016). This type of analysis is common in volcanic areas where the use of seismic arrays is available (e.g., Luzon et al., 2011).
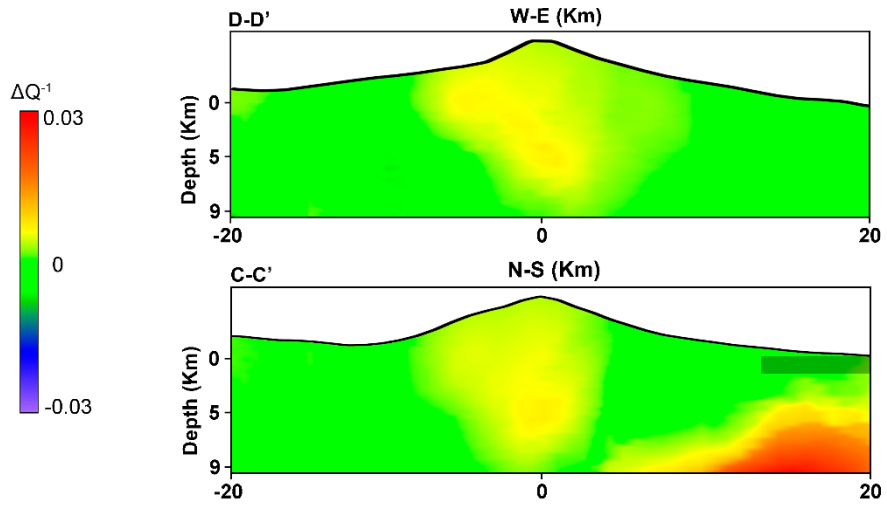
Figure 11. North–south (C–C') and east–west (D–D') vertical sections across Mt. Etna volcano. The locations of C–C 'and D–D' are shown in Figure 8. Darker shading highlights regions with lower resolution.

Our results confirm the remarkable complexity of the geological structure beneath Mt. Etna. It is likely that this complexity is common to other stratovolcanoes; however, without the abundance of data from multiple studies that contribute to Mt. Etna as a laboratory volcano, such observations and interpretations would not be possible. Further insight in this high structural complexity will require new advances in data and methods, which in turn will improve our understanding of volcano structures and help us to better constrain their behavior.
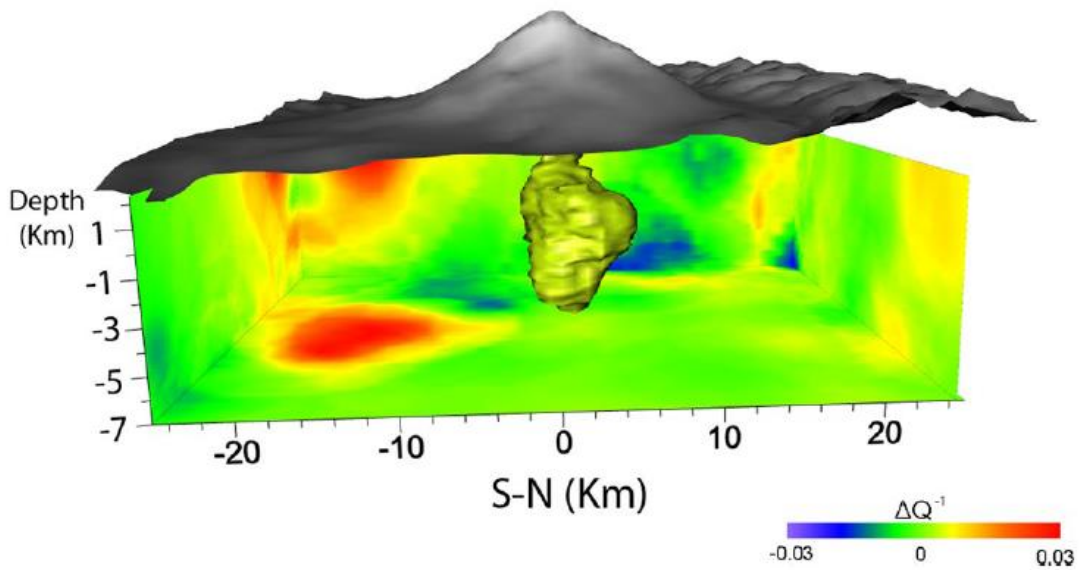
Figure 12. Three-dimensional (3D) attenuation model of the shallowest attenuation body identified beneath Mt. Etna volcano.

5. CONCLUSIONS

Volcanoes are highly heterogeneous structures; at present, tomographic images based on velocity and attenuation are some of the most powerful tools available for investigating their complex structures and behaviors. Several techniques can be used to obtain these images, with each revealing different physical properties of the medium and each having different resolution limits. Although these models aim to associate physical properties with geological structures, in most cases individual images can only partially reveal the sub-surface volcanic system. This limits interpretations and introduces uncertainties.

Here, we have presented a new attenuation-based tomographic model derived using *P* waves from an active seismic experiment; this method has not previously been applied at Mt. Etna. We used a sufficiently large data volume to cover the Mt. Etna region to a depth of 8 km. These new images reveal a large volume of partially molten material in the very shallow crust beneath Mt. Etna. During the investigated period, Mt. Etna was characterized by several episodes of Strombolian activity and lava emissions from the

181

main upper craters (i.e., Viccaro et al., 2016 and references therein). Our results provide a visualization of the magmatic source feeding these eruptive episodes. Integrated analysis of geodetic, seismic, and petrological data suggests that magma stored at ~4 km b.s.l. drove the eruptive activity of July–August 2014; this body of melt was fed by a batch of magma that started ascending from >8 km depth in late 2013 (Viccaro et al., 2016). This magmatic reservoir is considered as the region of neutral buoyancy at Mt. Etna (Corsaro and Pompilio, 2004).
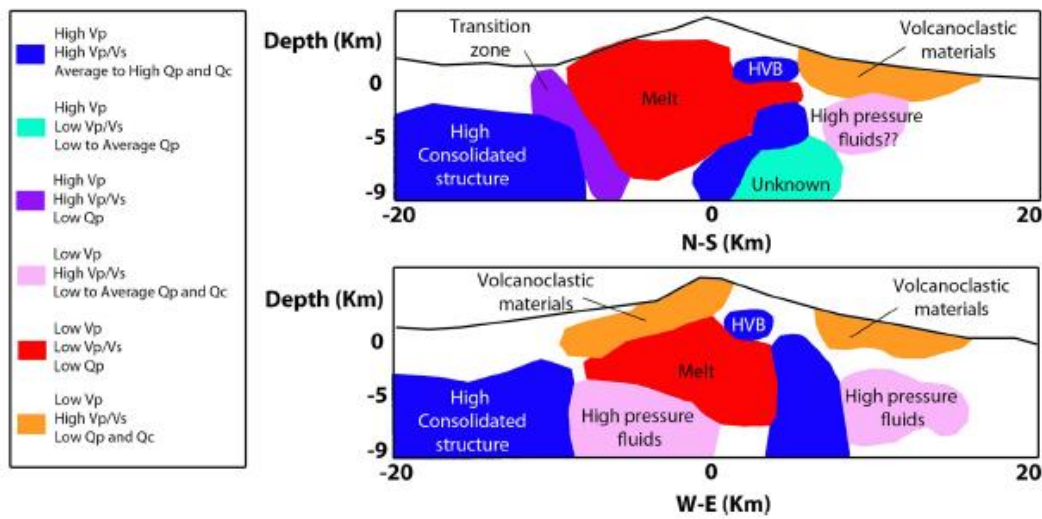
Figure 13. Schematic view of the structure beneath Mt. Etna volcano based on the joint interpretation of four different tomographic models of attenuation and velocity. HVB, High Velocity Body.

To better constrain the main geological framework of this volcano, we performed a joint interpretation of recent velocity and attenuation tomographies performed by our research team. The results confirm the presence of several different geological bodies, and provide a new and more complete picture of the inner structure of Mt. Etna volcano. In particular, we identified a large shallow region below the summit area that is consistent with the presence of fluids. We interpret this to represent a large area of shallow magma storage. This finding confirms the significant eruptive potential of Mt. Etna volcano. Our results provide new insights into the volcanic system at Mt. Etna, and have the potential

to inform on present and future eruptive behavior. Moreover, we have confirmed that the joint interpretation of different models provides a useful tool for the study of volcanic systems.

Our findings, on both attenuation- and velocity-based tomography, highlight the structural complexity of the interior of Mt. Etna volcano. Volcanic edifices are not comprised of well-defined units with distinct physical properties; rather, they represent complex and dynamic structural units that evolve along with magmatic dynamics. Being able to delimit these heterogeneities is essential to understanding the future kinematics and dynamics of volcanic scenarios. For example, we can now explain the migration of the eruptive locus at Mt. Etna as a function of multiple internal systems that favor the ascent of magma through different pathways. These observations also have relevance to other volcanoes; although an eruptive system may seem predictable in space and time, in reality the internal structural complexity is subject to sudden change, impacting both the mechanism and location of subsequent eruptions. As such, volcanic hazard models and management plans must also be reviewed regularly to ensure that they evolve with changes in eruptive phenomena.

DATA AVAILABILITY STATEMENT

ACKNOWLEDGMENTS

REFERENCES

Aki, K. (1980). Scattering and attenuation of shear waves in the lithosphere. *Journal of Geophysical Research*, *85*(B11), 6496–6504. https://doi.org/10.1029/jb085ib11p06496

Akinci, A., Del Pezzo, E., and Ibáñez, J. M. (1995). Separation of scattering and intrinsic attenuation in southern Spain and western Anatolia (Turkey). *Geophysical Journal International*, *121*(2), 337–353. https://doi.org/10.1111/j.1365-246x.1995.tb05715.x

Akinci, A., Ibáñez, J. M., Del Pezzo, E., and Morales, J. (1995). Geometrical spreading and attenuation of Lg waves: A comparison between western Anatolia (Turkey) and southern Spain. *Tectonophysics*, *250*(1–3), 47–60. https://doi.org/10.1016/0040-1951(95)00046-1

Aloisi, M., Bonaccorso, A., Cannavo, F., Currenti, G., and Gambino, S. (2020). The 24 December 2018 eruptive intrusion at Etna volcano as revealed by multidisciplinary continuous deformation networks (CGPS, Borehole Strainmeters and Tiltmeters). *Journal of Geophysical Research: Solid Earth*, *125*, e2019JB019117. https://doi.org/10.1029/2019jb019117

Aloisi, M., Cocina, O., Neri, G., Orecchio, B., and Privitera, E. (2002). Seismic tomography of the crust underneath the Etna volcano, Sicily. *Physics of the Earth and Planetary Interiors*, *134*(3–4), 139–155. https://doi.org/10.1016/s0031-9201(02)00153-x

Alparone, S., Maiolino, V., Mostaccio, A., Scaltrito, A., Ursino, A., Barberi, G., et al. (2015). Instrumental seismic catalogue of Mt. Etna earthquakes (Sicily, Italy): Ten years (2000–2010) of instrumental recordings. *Annals of Geophysics*, *58*(4), 0435.

Azzaro, R., Branca, S., Gwinner, K., and Coltelli, M. (2012). The volcano-tectonic map of Etna volcano, 1: 100.000 scale: An integrated approach based on a morphotectonic analysis from high-resolution DEM constrained by geologic, active faulting and seismotectonic data. *Italian Journal of Geosciences*, *131*(1), 153–170.

Barberi, G., Giampiccolo, E., Musumeci, C., Scarfi, L., Bruno, V., Cocina, O., et al. (2016). Seismic and volcanic activity during 2014 in the region involved by TOMO-ETNA seismic active experiment. *Annals of Geophysics*, *59*. https://doi.org/10.4401/ag-7082

Barreca, G., Branca, S., Corsaro, R. A., Scarfi, L., Cannavo, F., Aloisi, M., et al. (2020). Slab detachment, mantle flow, and crustal collision in eastern Sicily (southern Italy): Implications on Mount Etna volcanism. *Tectonics*, *39*(9), e2020TC006188. https://doi.org/10.1029/2020tc006188

Barreca, G., Branca, S., and Monaco, C. (2018). Three-dimensional modeling of mount etna volcano: Volume assessment, trend of eruption rates, and geodynamic significance. *Tectonics*, *37*(3), 842–857. https://doi.org/10.1002/2017tc004851

Basant, R. A., Ryan, G. A., Peacock, J. R., Camacho, A. G., Blake, O. O., Hautmann, S., and Lynne, B. Y. (2021). Multi-geophysical parameter classification of the Montserrat geothermal system. *Geothermics*, *90*, 102006. https://doi.org/10.1016/j.geothermics.2020.102006

Ben-Zvi, T., Wilcock, W. S., Barclay, A. H., Zandomeneghi, D., Ibáñez, J. M., and Almendros, J. (2009). The P-wave velocity structure of Deception Island, Antarctica, from two-dimensional seismic tomography. *Journal of Volcanology and Geothermal Research*, *180*(1), 67–80. https://doi.org/10.1016/j.jvolgeores.2008.11.020

Block, L. V. (1991). *Joint hypocenter-velocity inversion of local earthquakes arrival time data in two geothermal regions*, (Doctoral thesis). Cambridge. Massachusetts Institute of Technology.

Bonforte, A., Bonaccorso, A., Guglielmino, F., Palano, M., and Puglisi, G. (2008). Feeding system and magma storage beneath Mt. Etna as revealed by recent inflation/deflation cycles. *Journal of Geophysical Research*, *113*, B05406. https://doi.org/10.1029/2007JB005334

Branca, S., Coltelli, M., De Beni, E., and Wijbrans, J. (2007). Geological evolution of Mount Etna volcano (Italy) from earliest products until the first central volcanism (between 500 and 100 ka ago) inferred from geochronological and stratigraphic data. *International Journal of Earth Sciences*, *97*, 135, 152. https://doi.org/10.1007/s00531-006-0152-0

Branca, S., and Ferrara, V. (2013). The morphostructural setting of Mount Etna sedimentary basement (Italy): Implications for the geometry and volume of the volcano and its flank instability. *Tectonophysics*, *586*, 46–64. https://doi.org/10.1016/j.tecto.2012.11.011

Cavallaro, D., Cocchi, L., Coltelli, M., Muccini, F., Carmisciano, C., Firetto Carlino, M., et al. (2016). Acquisition procedures, processing methodologies and preliminary results of magnetic and ROV data collected during the TOMO-ETNA experiment. *Annals of Geophysics*, *59*(4). https://doi.org/10.4401/ag-7084

Chiarabba, C., De Gori, P., and Patanè, D. (2004). The Mt. Etna plumbing system: The contribution of seismic tomography. In A. Bonaccorso,

S. Calvari, M. Coltelli, C. DelNegro, S. Falsaperla (Eds.), *Etna volcano laboratory, Geophysical Monograph Series* (pp. 191–204). Washington, DC. American Geophysical Union. https://doi.org/10.1029/143gm12

Chiocci, F. L., Coltelli, M., Bosman, A., and Cavallaro, D. (2011). Continental margin large-scale instability controlling the flank sliding of Etna volcano. *Earth and Planetary Science Letters*, *305*(1–2), 57–64. https://doi.org/10.1016/j.epsl.2011.02.040

Coltelli, M., Cavallaro, D., Firetto Carlino, M., Cocchi, L., Muccini, F., D'Aessandro, A., et al. (2016). The marine activities performed within the TOMO-ETNA experiment. *Annals of Geophysics*, *59*(4). https://doi.org/10.4401/ag-7081

Cordell, D., Unsworth, M. J., Lee, B, Diaz, D., Bennington, N. L., and Thurber, C. H. (2020). Integrating magnetotelluric and seismic images of silicic magma systems: A case study from the Laguna del Maule Volcanic Field, central Chile. *Journal of Geophysical Research: Solid Earth*, *125*, e2020JB020459. https://doi.org/10.1029/2020jb020459

Corsaro, R. A., Neri, M., and Pompilio, M. (2002). Paleo-environmental and volcano-tectonic evolution of the southeastern flank of Mt. Etna during the last 225 ka inferred from the volcanic succession of the 'Timpe', Acireale, Sicily. *Journal of Volcanology and Geothermal Research*, *113*(1–2), 289–306. https://doi.org/10.1016/s0377-0273(01)00262-1

Corsaro, R. A., and Pompilio, M. (2004). Buoyancy-controlled eruption of magmas at Mt Etna. *Terra Nova*, *16*(1), 16–22. https://doi.org/10.1046/j.1365-3121.2003.00520.x

De Gori, P., Chiarabba, C., Giampiccolo, E., Martínez–Arévalo, C., and Patanè, D. (2011). Body wave attenuation heralds incoming eruptions at Mount Etna. *Geology*, *39*(5), 503–506. https://doi.org/10.1130/g31993.1

De Guidi, G., Barberi, G., Barreca, G., Bruno, V., Cultrera, F., Grassi, S., et al. (2015). Geological, seismological and geodetic evidence of active thrusting and folding south of Mt. Etna (eastern Sicily): Revaluation of "seismic efficiency" of the Sicilian Basal Thrust. *Journal of Geodynamics*, *90*, 32–41. https://doi.org/10.1016/j.jog.2015.06.001

De Siena, L., Amoruso, A., Del Pezzo, E., Wakeford, Z., Castellano, M., and Crescentini, L. (2017). Space-weighted seismic attenuation mapping of the aseismic source of Campi Flegrei 1983–1984 unrest. *Geophysical Research Letters*, *44*(4), 1740–1748.

De Siena, L., Del Pezzo, E., and Bianco, F. (2010). Seismic attenuation imaging of Campi Flegrei: Evidence of gas reservoirs, hydrothermal basins, and feeding systems. *Journal of Geophysical Research*, *115*, B09312. https://doi.org/10.1029/2009jb006938

De Siena, L., Thomas, C., and Aster, R. (2014). Multi-scale reasonable attenuation tomography analysis (MuRAT): An imaging algorithm designed for volcanic regions. *Journal of Volcanology and Geothermal Research*, *277*, 22–35. https://doi.org/10.1016/j.jvolgeores.2014.03.009

De Siena, L., Thomas, C., Waite, G. P., Moran, S. C., and Klemme, S. (2014). Attenuation and scattering tomography of the deep plumbing system of Mount St. Helens. *Journal of Geophysical Research: Solid Earth*, *119*, 8223–8238. https://doi.org/10.1002/2014JB011372

Del Pezzo, E., Bianco, F., De Siena, L., and Zollo, A. (2006). Small scale shallow attenuation structure at Mt. Vesuvius, Italy. *Physics of the Earth and Planetary Interiors*, *157*(3–4), 257–268. https://doi.org/10.1016/j.pepi.2006.04.009

Del Pezzo, E., Giampiccolo, E., Tuve, T., Di Grazia, G., Gresta, S., and Ibáñez, J. M. (2019). Study of the regional pattern of intrinsic and scattering seismic attenuation in Eastern Sicily (Italy) from local earthquakes. *Geophysical Journal International*, *218*(2), 1456–1468.

Díaz-Moreno, A. (2016). *Joint active and passive seismic tomography in active volcanoes: The case of study of Mt. Etna, and further implications in active volcanic regions (Doctoral dissertation)*, Universidad de Granada. Retrieved from https://dialnet.unirioja.es/servlet/tesis?codigo=61163

Díaz-Moreno, A., Barberi, G., Cocina, O., Koulakov, I., Scarfi, L., Zuccarello, L., et al. (2018). New insights on Mt. Etna's crust and relationship with the regional tectonic

framework from joint active and passive P-wave seismic tomography. *Surveys in Geophysics*, *39*(1), 57–97. https://doi.org/10.1007/s10712-017-9425-3

Díaz-Moreno, A., Koulakov, I., García-Yeguas, A., Jakovlev, A., Barberi, G., Cocina, O., et al. (2016). PARTOS-Passive and Active Ray TOmography Software: Description and preliminary analysis using TOMO-ETNA experiment's dataset. *Annals of Geophysics*, *59*(4). https://doi.org/10.4401/ag-7088

Dvorkin, J., Prasad, M., Sakai, A., and Lavoie, D. (1999). Elasticity of marine sediments: Rock physics modeling. *Geophysical Research Letters*, *26*(12), 1781–1784. https://doi.org/10.1029/1999gl900332

García, L., Álvarez, I., Benítez, C., Titos, M., Bueno, A., Mota, S., et al. (2016). Advances on the automatic estimation of the P-wave onset time. *Annals of Geophysics*, *59*(4).

García-Yeguas, A., Koulakov, I., Ibáñez, J. M., and Rietbrock, A. (2012). High resolution 3D P wave velocity structure beneath Tenerife Island (Canary Islands, Spain) based on tomographic inversion of active-source data. *Journal of Geophysical Research*, *117*, B09309. https://doi.org/10.1029/2011JB008970

García-Yeguas, A., Ledo, J., Pina-Varas, P., Prudencio, J., Queralt, P., Marcuello, A., et al. (2017). A 3D joint interpretation of magnetotelluric and seismic tomographic models: The case of the volcanic island of Tenerife. *Computers and Geosciences*, *109*, 95–105. https://doi.org/10.1016/j.cageo.2017.08.003

Giampiccolo, E., Cocina, O., De Gori, P., and Chiarabba, C. (2020). Dyke intrusion and stress-induced collapse of volcano flanks: The example of the 2018 event at Mt. Etna (Sicily, Italy). *Scientific Reports*, *10*(1), 6373. https://doi.org/10.1038/s41598-020-63371-3

Giampiccolo, E., Del Pezzo, E., Tuvé, T., Di Grazia, S., and Ibáñez, J. M. (2021). 3-D Q-coda attenuation structure at Mt. Etna. *Geophysical Journal International*. https://doi.org/10.1093/gji/ggab235

Guardo, R., and De Siena, L. (2017). Integrating ambient noise with GIS for a new perspective on volcano imaging and monitoring: The case study of Mt. Etna. *Journal of Volcanology and Geothermal Research*, *347*, 397–407. https://doi.org/10.1016/j.jvolgeores.2017.10.007

Guardo, R., De Siena, L., and Dreidemie, C. (2020). Mt. Etna feeding system and sliding flank: A New 3D image from earthquakes distribution in a customisable GIS. *Frontiers in Earth Sciences*, *8*, 1–12. https://doi.org/10.3389/feart.2020.589925

Havskov, J., Pena, J. A., Ibáñez, J. M., Ottemoller, L., and Martínez-Arevalo, C. (2003). Magnitude scales for very local earthquakes. Application for Deception Island Volcano (Antarctica). *Journal of Volcanology and Geothermal Research*, *128*(1–3), 115–133. https://doi.org/10.1016/s0377-0273(03)00250-6

Ibáñez, J. M., Castro-Melgar, I., Cocina, O., Zuccarello, L., Branca, S., Del Pezzo, E., and Prudencio, J. (2020). First 2-D intrinsic and scattering attenuation images of Mt Etna volcano and surrounding region from active seismic data. *Geophysical Journal International*, *220*(1), 267–277. https://doi.org/10.1093/gji/ggz450

Ibáñez, J. M., Del Pezzo, E., Alguacil, G., De Miguel, F., Morales, J., De Martino, S., et al. (1993). Geometrical spreading function for short-period S and coda waves recorded in southern Spain. *Physics of the Earth and Planetary Interiors*, *80*(1–2), 25–36. https://doi.org/10.1016/0031-9201(93)90070-p

Ibáñez, J. M., Díaz-Moreno, A., Prudencio, J., Patanè, D., Zuccarello, L., Cocina, O., et al. (2016). TOMO-ETNA experiment at Etna volcano: Activities on land. *Annals of Geophysics*, *59*(4). https://doi.org/10.4401/ag-7080

Ibáñez, J. M., Lühr, B., and Dahm, T. (2014). *TOMO-ETNA. GFZ Data Services*. Other/Seismic Network. https://doi.org/10.14470/6G7569676919

Ibáñez, J. M., Prudencio, J., Díaz-Moreno, A., Patanè, D., Puglisi, G., Lühr, B. G., et al. (2016). The TOMO-ETNA experiment: An imaging active campaign at Mt. Etna volcano. Context, main objectives, working-plans and involved research projects. *Annals of Geophysics*, *59*(4), 0426.

Ibáñez, J. M., Rietbock, A., and García-Yeguas, A. (2008). Imaging an active volcano edifice at Tenerife Island, Spain. *Eos Transactions*, *89*(32), 289–290. https://doi.org/10.1029/2008eo320001

Koulakov, I., Smirnov, S. Z., Gladkov, V., Kasatkina, E., West, M., El Khrepy, S., and Al-Arifi, N. (2018). Causes of volcanic unrest at Mt. Spurr in 2004–2005 inferred from repeated tomography. *Scientific Reports*, *8*(1), 1–7. https://doi.org/10.1038/s41598-018-35453-w

Koulakov, I., and Vargas, C. A. (2018). Evolution of the magma conduit beneath the Galeras volcano inferred from repeated seismic tomography. *Geophysical Research Letters*, *45*, 7514–7522. https://doi.org/10.1029/2018gl078850

Laiolo, M., Ripepe, M., Cigolini, C., Coppola, D., Della Schiava, M., Genco, R., et al. (2019). Space-and ground-based geophysical data tracking of magma migration in shallow feeding system of Mount Etna volcano. *Remote Sensing*, *11*(10), 1182. https://doi.org/10.3390/rs11101182

Luzon, F., Almendros, J., and García-Jerez, A. (2011). Shallow structure of Deception Island, Antarctica, from correlations of ambient seismic noise on a set of dense seismic arrays. *Geophysical Journal International*, *185*(2), 737–748. https://doi.org/10.1111/j.1365-246x.2011.04962.x

Martínez-Arévalo, C., Patanè, D., Rietbrock, A. and Ibáñez, J. (2005). The intrusive process leading to the Mt. Etna 2001 flank eruption: Constraints from 3D attenuation tomography. *Geophysical Research Letters*, *32*, L21309. https://doi.org/10.1029/2005GL023736

Matsumoto, S., Uehira, K., Watanabe, A., Goto, K., Iio, Y., Hirata, N., and Kanazawa, T. (2009). High resolution Q^{-1} estimation based on extension of coda normalization method and its application to P-wave attenuation structure in the aftershock area of the 2005 West Off Fukuoka Prefecture Earthquake (M 7.0). *Geophysical Journal International*, *179*(2), 1039–1054. https://doi.org/10.1111/j.1365-246x.2009.04313.x

Nazemi, N., Pezeshk, S., and Sedaghati, F. (2017). Attenuation of Lg waves in the New Madrid seismic zone of the central United States using the coda normalization method. *Tectonophysics*, *712*, 623–633. https://doi.org/10.1016/j.tecto.2017.06.026

Neri, M., Casu, F., Acocella, V., Solaro, G., Pepe, S., Berardino, P., et al. (2009). Deformation and eruptions at Mt. Etna (Italy): A lesson from 15 years of observations. *Geophysical Research Letters*, *36*. 10.1029/2008GL036151

Patanè, D., Barberi, G., Cocina, O., De Gori, P., and Chiarabba, C. (2006). Time-resolved seismic tomography detects magma intrusions at Mount Etna. *Science*, *313*(5788), 821–823. https://doi.org/10.1126/science.1127724

Patanè, D., Chiarabba, C., Cocina, O., De Gori, P., Moretti, M., and Boschi, E. (2002). Tomographic images and 3D earthquake locations of the seismic swarm preceding the

2001 Mt. Etna eruption: Evidence for a dyke intrusion. *Geophysical Research Letters*, *29*, 135-1-135-4. https://doi.org/10.1029/2001GL014391

Presti, D. L., Riggi, F., Ferlito, C., Bonanno, D. L., Bonanno, G., Gallo, G., et al. (2020). Muographic monitoring of the volcano-tectonic evolution of Mount Etna. *Scientific Reports*, *10*(1), 1–11. https://doi.org/10.1038/s41598-020-68435-y

Prudencio, J., De Siena, L., Ibáñez, J. M., Del Pezzo, E., García-Yeguas, A., and Díaz-Moreno, A. (2015). The 3D attenuation structure of Deception Island (Antarctica). *Surveys in Geophysics*, *36*(3), 371–390. https://doi.org/10.1007/s10712-015-9322-6

Prudencio, J., Del Pezzo, E., García-Yeguas, A., and Ibáñez, J. M. (2013). Spatial distribution of intrinsic and scattering seismic attenuation in active volcanic islands–I: Model and the case of Tenerife Island. *Geophysical Journal International*, *195*(3), 1942–1956. https://doi.org/10.1093/gji/ggt361

Prudencio, J., Ibáñez, J. M., Del Pezzo, E., Martí, J., García-Yeguas, A., and De Siena, L. (2015). 3D attenuation tomography of the volcanic island of Tenerife (Canary Islands). *Surveys in Geophysics*, *36*(5), 693–716. https://doi.org/10.1007/s10712-015-9333-3

Prudencio, J., Ibáñez, J. M., García-Yeguas, A., Del Pezzo, E., and Posadas, A. M. (2013). Spatial distribution of intrinsic and scattering seismic attenuation in active volcanic islands–II: Deception Island images. *Geophysical Journal International*, *195*(3), 1957–1969. https://doi.org/10.1093/gji/ggt360

Prudencio, J., and Manga, M. (2020). 3-D seismic attenuation structure of Long Valley caldera: Looking for melt bodies in the shallow crust. *Geophysical Journal International*, *220*(3), 1677–1686. https://doi.org/10.1093/gji/ggz543

Sato, H., Fehler, M. C., and Maeda, T. (2012). *Seismic wave propagation and scattering in the heterogeneous Earth*. Berlin. Springer.

Shalev, E., Kenedi, C. L., Malin, P., Voight, V., Miller, V., Hidayat, D., et al. (2010). Three-dimensional seismic velocity tomography of Montserrat from the SEA-CALIPSO offshore/onshore experiment. *Geophysical Research Letters*, *37*, L00E17. https://doi.org/10.1029/2010gl042498

Sketsiou, P., De Siena, L., Gabrielli, S., and Napolitano, F. (2021). 3-D attenuation image of fluid storage and tectonic interactions across the Pollino fault network. *Geophysical Journal International*, *226*(1), 536–547. https://doi.org/10.1093/gji/ggab109

Viccaro, M., Barca, D., Bohrson, W. A., D'Oriano, C., Giuffrida, M., Nicotra, E., and Pitcher, B. W. (2016). Crystal residence times from trace element zoning in plagioclase reveal changes in magma transfer dynamics at Mt. Etna during the last 400 years. *Lithos*, *248*, 309–323. https://doi.org/10.1016/j.lithos.2016.02.004

Voight, B., Sparks, R. S. J., Shalev, E., Minshull, T., Paulatto, M., Annen, C., et al. (2014). The SEA-CALIPSO volcano imaging experiment at Montserrat: Plans, campaigns at sea and on land, scientific results, and lessons learned. *Geological Society, London, Memoirs*, *39*(1), 253–289. https://doi.org/10.1144/m39.15

Yoshimoto, K., Sato, H., and Ohtake, M. (1993). Frequency-dependent attenuation of P and S waves in the Kanto area, Japan, based on the coda-normalization method. *Geophysics Journal International*, *114*, 165–174. https://doi.org/10.1111/j.1365-246x.1993.tb01476.x

Zandomeneghi, D., Barclay, A., Almendros, J., Ibáñez, J. M., Wilcock, W. S., and Ben-Zvi, T. (2009). Crustal structure of Deception Island volcano from P wave seismic tomography: Tectonic and volcanic implications. *Journal of Geophysical Research*, *114*. https://doi.org/10.1029/2008jb006119

Zuccarello, L., Paratore, M., La Rocca, M., Ferrari, F., Messina, A., Branca, S., et al. (2016). Shallow velocity model in the area of Pozzo Pitarrone, Mt. Etna, from single station, array methods and borehole data. *Annals of Geophysics*, *59*. https://doi.org/10.4401/ag-7086

TERCERA PARTE

CONCLUSIONES Y LÍNEAS FUTURAS

Conclusiones

Como se ha podido comprobar, el producto final de esta tesis doctoral ha sido la elaboración de tres artículos de investigación que se centran en la obtención de la estructura de atenuación de dos regiones volcánicas: las islas Eolias y el Mt. Etna. Mediante la aplicación del modelo de difusión y el método de normalización de la coda, se han obtenido estructuras bidimensionales de Q_i y Q_s y tridimensional de Q_c, respectivamente. Entre las conclusiones más destacadas podemos enumerar las siguientes:

i)   Para la región la región de las Islas Eolias se han obtenido los primeros mapas bidimensionales de las contribuciones de atenuación intrínseca y de *scattering*.

Tanto los mapas como los valores medios de atenuación intrínseca y *scattering* nos indican que es una región fuertemente atenuada, como es de esperar, ya que los valores obtenidos son similares al de otras áreas volcánicas. Los valores de atenuación por *scattering* son más importantes que los de atenuación intrínseca, indicando que la atenuación por *scattering* prevalece, al menos en un orden de magnitud, a la atenuación intrínseca. Este hecho también se ha observado en otras regiones volcánicas debido al carácter altamente heterogéneo de las regiones volcánicas.

Los resultados también muestran diferencias en el comportamiento en el fenómeno atenuativo con respecto a las frecuencias analizadas, de este modo, para las frecuencias altas la presencia de atenuación por *scattering* decae. Esto es debido a que este tipo de atenuación depende del tamaño de la heterogeneidad, por lo tanto, cuando la longitud de la onda incipiente es similar a la presencia de la heterogeneidad existe una mayor atenuación por *scattering* y esto ocurre, para nuestra región, en longitudes de onda más pequeñas.

El fuerte *scattering* observado en la zona más septentrional se asocia al sistema de fallas Eolias-Tindari-Letojanni. En áreas donde la influencia de las estructuras

volcánicas es menos significativa, la atenuación intrínseca es más relevante que la atenuación por *scattering*. Si bien esto era esperable según trabajos previos, se ha podido corroborar este hecho en una región que es de un tamaño reducido y en distancias cortas. Se interpreta este cambio en el comportamiento atenuante como un reflejo del gran volumen de material sedimentario depositado en el lecho marino. Debido a su naturaleza poco consolidada, los sedimentos facilitan la atenuación intrínseca por disipación de energía, pero en general presentan una alta homogeneidad estructural que se refleja en bajos niveles de *scattering*.

Otro de los hitos que muestra esta investigación es que el archipiélago de las Eolias no es un gran complejo volcánico como por ejemplo el Monte Etna, sino que son pequeñas y múltiples estructuras volcánicas aisladas entre sí. Este hecho demuestra la robustez y la potencia que el modelo de difusión tiene para la caracterización de la estructura interna en función de las propiedades físicas de la corteza.

ii) En el Monte Etna se han obtenido modelos tanto bidimensionales como tridimensionales que proporcionan nuevas evidencias de la complejidad estructural del área. Las metodologías utilizadas han sido pioneras para esta región y han permitido una mejor interpretación geológica. Además, la realización de una interpretación conjunta de diferentes tomografías sísmicas de velocidad y de atenuación, incluida la obtenida en esta tesis, ha posibilitado superar las limitaciones que cada una de las técnicas tiene por separado, ya que cada una revela diferentes propiedades físicas del medio.

a. Conclusiones metodológicas

El método de difusión y el método de normalización de la coda se han demostrado como métodos muy eficaces en su aplicación en la región, al correlacionar de manera muy efectiva con tomografías sísmicas de velocidad hechas previamente.

b. Conclusiones estructura bidimensional

El volcán Etna es una estructura única que en los primeros 2-3 kilómetros de profundidad tiene una fuerte atenuación tanto intrínseca como de *scattering*; aunque domina el fenómeno de *scattering,* como se ha observado en otras regiones volcánicas, lo que sugiere que la región es muy heterogénea. Además, la comparación con los análisis realizados en otros volcanes revela que la región del Monte Etna se caracteriza por una alta atenuación intrínseca, como resultado de la presencia de grandes depósitos volcanoclásticos a poca profundidad. Se puede deducir, a partir de los mapas de atenuación, que el Monte Etna se sitúa entre dos regiones tectónicas que tensionan y fracturan el área. Se ha podido identificar una región de alta atenuación en el flanco SO que se correlaciona con altas tasas de sismicidad y actividad eruptiva, apoyando la hipótesis de un vínculo entre la dinámica del flanco SO y la recarga del volcán en las últimas décadas, ocurriendo bajo el cráter y, secundariamente, en la zona superior del rift sur.

c. Conclusiones estructura tridimensional

Mediante la aplicación del método de normalización de la coda, se ha conseguido obtener imágenes hasta una profundidad de 8 kilómetros que revelan un gran cuerpo de material parcialmente fundido en la corteza. Este reservorio de magma es el que ha nutrido los episodios eruptivos que tuvieron lugar durante el periodo de investigación, entre julio y agosto de 2014. La actividad eruptiva durante este periodo consistió en actividad estromboliana y emisiones de lava en la zona de cráteres principales del volcán. El hallazgo de esta gran región que se ha interpretado como el área de almacenamiento del volcán, muestra el importante potencial eruptivo que tiene el Monte Etna.

Al realizar la interpretación conjunta de las tomografías sísmicas en velocidad y atenuación se ha conseguido alcanzar una confirmación de distintos cuerpos geológicos que mejoran el conocimiento presente de la estructura interna del Monte Etna y muestran su gran complejidad estructural altamente dinámica, puesto que los volcanes tienen estructuras complejas que evolucionan rápidamente junto a la dinámica eruptiva del volcán. Conocer las heterogeneidades que forman el edificio volcánico permite conocer la cinemática y los futuros escenarios hacia los que el volcán evolucionará. Como se ha visto en

el Monte Etna, la dinámica volcánica actual del volcán se caracteriza por la migración del lugar eruptivo mediante una sucesión de numerosos sistemas de alimentación internos que favorecen el ascenso del magma.

Tras los grandes resultados alcanzados, los estudios con interpretación conjunta de tomografías sísmicas en velocidad y atenuación se muestran como una de las herramientas más útiles y potentes para estudiar los complejos volcánicos. Algunas de las consideraciones alcanzadas para el Monte Etna también pueden ser extrapoladas a otros volcanes, dado que la complejidad estructural de los sistemas eruptivos está sometida a dinámicas muy cambiantes. Los modelos de riesgo volcánico y los planes de gestión de erupciones volcánicas han de ser continuamente revisados para evolucionar junto a la dinámica estructural del volcán.

Líneas futuras

Esta tesis se cierra con esta memoria, pero no así la investigación iniciada. Animados por los resultados del trabajo, comprobada la validez del método y su gran precisión, se ha continuado por esta línea de investigación y se ha aplicado la metodología presente en este trabajo en otras regiones para la obtención de tomografías de atenuación sísmica tanto bidimensionales como tridimensionales. Por un lado, se ha obtenido la estructura tridimensional del volcán Soufrière Hills, en la isla de Montserrat (Reino Unido) mediante el análisis de señales provenientes de un experimento de sísmica activa. El volcán Soufrière Hills, el más activo del Caribe, se caracteriza por episodios de gran explosividad, debido al crecimiento y posterior colapso del domo volcánico que, incluso, se ha tenido que establecer una zona de exclusión en la zona centro-sur de la isla. Por otro lado, y por primera vez, se ha estudiado una región geotermal con estas técnicas: "The Geysers" en California (EUA). Si bien no es una región volcánica, las regiones geotermales se caracterizan por la presencia de fluidos y anomalías de temperatura, lo que se traduce en regiones altamente atenuativas. Los resultados obtenidos en estos trabajos han sido de gran interés, avanzando en el conocimiento de las regiones y se enviarán para su publicación en revistas de alto impacto en los próximos meses.

Debido al potencial que tienen los estudios de atenuación sísmica, y especialmente la interpretación conjunta de diferentes modelos tomográficos tanto en velocidad como en atenuación, uno de los objetivos futuros a corto plazo es poder realizar interpretaciones conjuntas en diferentes regiones volcánicas. Una de las regiones más inmediatas a estudiar es la isla de El Hierro, donde ya se realizó una tomografía en velocidad. La obtención de una tomografía de atenuación tridimensional proporcionaría nueva información estructural de la isla y la interpretación conjunta de ambas permitirá avanzar en el conocimiento de la dinámica eruptiva de El Hierro, que podrá ser extrapolada a otras islas.

CONCLUSIONS AND FUTURE WORK

Conclusions

It can be verified that the final product of this thesis has been three research articles that focus on obtaining the attenuation structure of two volcanic regions: the Aeolian Islands and Mt. Etna. The application of the diffusion model and the coda normalization method have been used, obtaining two-dimensional structures of Q_i and Q_s, and three-dimensional structure of Q_c, respectively. The most outstanding conclusions are the following:

i) For the region of the Aeolian Islands, the first two-dimensional maps of the contributions of intrinsic attenuation and scattering have been obtained.

The maps and the mean values of intrinsic attenuation and scattering indicate that it is a strongly attenuated region, as expected, since the values obtained are similar to those of other volcanic areas. The scattering attenuation values are more important than the intrinsic attenuation, indicating that the scattering attenuation prevails, at least by an order of magnitude, over the intrinsic attenuation. This fact has also been observed in other volcanic regions due to the highly heterogeneous character of the volcanic regions.

The results also show differences in the behavior of the attenuation phenomenon with respect to the analyzed frequencies, thus, for high frequencies the presence of scattering attenuation decreases. This is because this type of attenuation depends on the size of the heterogeneity, therefore, when the incipient wavelength is similar to the presence of heterogeneity, there is greater attenuation due to scattering and this occurs, for our region, in smaller wavelengths.

The strong scattering observed in the northernmost area is associated with the Aeolian-Tindari-Letojanni fault system. In areas where the influence of volcanic structures is less significant, intrinsic attenuation is more relevant than scattering attenuation. This was expected according to previous works, it has been possible to corroborate this fact in a region that is small in size and over short distances. This change in attenuating behavior is interpreted as a reflection of the large volume of sedimentary material deposited on the seabed. Due to their unconsolidated nature, sediments facilitate intrinsic attenuation due to energy dissipation, but in general they present a high structural homogeneity that is reflected in low levels of scattering.

Another result shown by this research is that the Aeolian archipelago is not a large volcanic complex like Mount Etna, but small and multiple volcanic structures isolated from each other. This fact demonstrates the robustness and power that the diffusion model has for the characterization of the internal structure as a function of the physical properties of the crust.

ii) In Mount Etna, two-dimensional and three-dimensional models have been obtained that provide new evidence of the structural complexity of the area. The methodologies used have been pioneers for this region and have allowed a better geological interpretation. In addition, the joint interpretation of different velocity and attenuation seismic tomographies, including the one obtained in this thesis, has made it possible to overcome the limitations that each of the techniques has separately, since each one reveals different physical properties of the medium.

a. Methodological conclusions

It has been proven that the diffusion method and the coda normalization method are very effective in their application to the region, since they correlate very effectively with previously made seismic velocity tomographies.

b. Conclusions two-dimensional structure

The Etna volcano is a unique structure where in the first 2-3 kilometers of depth it has a strong intrinsic and scattering attenuation; scattering dominates as has been observed in other volcanic regions, suggesting that the region is highly heterogeneous. Furthermore, comparison with analyzes performed on other volcanoes reveals that the Mount Etna region is characterized by high intrinsic attenuation, as a result of the presence of large volcanoclastic deposits at shallow depths. It can be deduced from the attenuation maps that Mount Etna is located between two tectonic regions that stress and fracture the area. It has been possible to identify a region of high attenuation on the SW flank that correlates with high rates of seismicity and eruptive activity, supporting the hypothesis of a link between the dynamics of the SW flank and the recharge of the volcano in recent decades, occurring under the crater and, secondarily, the upper southern rift zone.

c. Conclusions three-dimensional structure

Images to a depth of 8 km revealing a large body of partially molten material in the crust have been successfully obtained by applying the coda normalization method. This magma reservoir is what has fed the eruptive episodes that took place during the research period between July and August 2014. The eruptive activity during this period consisted of Strombolian activity and lava emissions in the area of the main craters of the volcano. The discovery of this large region, which has been interpreted as the volcano's magma storage area, shows the significant eruptive potential of Mount Etna.

The joint interpretation of the seismic tomographies in velocity and attenuation has made it possible to reach a confirmation of different geological bodies that improve the present knowledge of the internal structure of Mount Etna and show its great highly dynamic structural complexity, since volcanoes have complex structures that evolve quickly along with the eruptive dynamics of the volcano. Knowing the heterogeneities that form the volcanic edifice allows us to know the kinematics and the future scenarios in which the volcano will evolve. The current volcanic dynamics of the volcano is characterized by the migration of the eruptive site through a succession of numerous internal feeding systems that favor the rise of magma as seen on Mount Etna.

After the great results achieved, studies with the joint interpretation of seismic tomography in velocity and attenuation are shown to be one of the most useful and powerful tools for studying volcanic complexes. Some of the considerations reached for Mount Etna can also be extrapolated to other volcanoes, since the structural complexity of eruptive systems is subject to highly changing dynamics. Volcanic hazard models and volcanic eruption management plans need to be continually revised to evolve along with the structural dynamics of the volcano.

Future Work

The research of this thesis continues with the investigation started. Encouraged by the results of the work, verifying the validity of the method and its great precision, this line of research has been continued and the methodology present in this work has been applied in other regions to obtain both two-dimensional and three-dimensional seismic attenuation tomography. On the one hand, the three-dimensional structure of the Soufrière Hills volcano on the island of Montserrat (United Kingdom) has been obtained by analyzing signals from an active seismic experiment. The Soufrière Hills volcano, the most active in the Caribbean, is characterized by highly explosive episodes due to the growth and subsequent collapse of the volcanic dome, which has even led to the establishment of an exclusion zone in the center-south of the island. On the other hand, and for the first time, a geothermal region has been studied with these techniques: "The Geysers" in California (USA). Although not a volcanic region, geothermal regions are characterized by the presence of fluids and temperature anomalies, resulting in highly attenuating regions. The results obtained in these works have been of great interest, advancing in the knowledge of the regions and will be sent for publication in high-impact journals in the coming months.

Due to the potential of seismic attenuation studies, and especially the joint interpretation of different tomographic models both in velocity and in attenuation, one of the short-term future objectives is to be able to carry out joint interpretations in different volcanic regions. One of the most immediate regions to study is the island of El Hierro, where a velocity tomography has already been carried out. Obtaining a three-dimensional attenuation tomography would provide new structural information on the island and the joint interpretation of both will allow progress in understanding the eruptive dynamics of El Hierro that can be extrapolated to other islands.

BIBLIOGRAFÍA

Aki, K., Christoffersson, A., Husebye, E. S. and Powell, C. (1974). Three-dimensional seismic velocity anomalies in the crust and upper-mantle under the USGS, California seismic array. *Eos Transactions. American Geophysical Union*, *56*, 1145.

Aki, K. and Chouet, B. (1975). Origin of coda waves: source, attenuation, and scattering effects, *Journal of Geophysical Research,* *80*(23), https://doi.org/10.1029/JB080i023p03322

Aki, K. and Richards, P.G. (1980). Quantitative seismology. Theory and methods. *W.H. Freeman, San Francisco*.

Aki, K. (1980). Attenuation of shear-waves in the lithosphere for frequencies from 0.05 to 25 Hz. *Physics of the Earth and Planetary Interiors*, *21*(1), 50-60. https://doi.org/10.1016/0031-9201(80)90019-9

Aki, K. (1980). Scattering and Attenuation of Shear Waves in the Lithosphere. *Journal of Geophysiscal Research,* *85*(B11), 6496–6504. https://doi.org/10.1029/jb085ib11p06496

Aki, K. (1982). Scattering and attenuation. *Bulletin of the Seismological Society of America*, *72*(6B), 319-330, https://doi.org/10.1785/BSSA07206B0319

Akinci, A., Del Pezzo, E. and Ibañez, J. (1995). Separation of scattering and intrinsic Attenuation in southern Spain and western Anatolia (Turkey). *Geophysical Journal International*, *121*(2), 337-353. https://doi.org/10.1111/j.1365-246X.1995.tb05715.x

Akinci, A., Ibanez, J. M., Del Pezzo, E., and Morales, J. (1995). Geometrical spreading and attenuation of Lg waves: a comparison between western Anatolia (Turkey) and southern Spain. *Tectonophysics*, *250*(1-3), 47-60. https://doi.org/10.1016/0040-1951(95)00046-1

Aloisi, M., Cocina, O., Neri, G., Orecchio, B. and Privitera, E. (2002). Seismic tomography of the crust underneath the Etna volcano, Sicily. *Physics of the Earth and Planetary Interiors*, *134*, 139-155. https://doi.org/10.1016/S0031-9201(02)00153-X

Aloisi, M., Bonaccorso, A., Cannavò, F., Currenti, G., and Gambino, S. (2020). The 24 December 2018 eruptive intrusion at Etna volcano as revealed by multidisciplinary continuous deformation networks (CGPS, borehole strainmeters and tiltmeters). *Journal of Geophysical Research: Solid Earth*, *125*(8), e2019JB019117. https://doi.org/10.1029/2019JB019117

Alparone, S., Cardaci, C., Privitera, E., and Spampinato, S. (1998). Stress Tensor Computation at the Aeolian Islands Based on Earthquake Fault-Plane Solutions. *Proceedings Earthquake Fault Plane Solutions: Databases, Derived Parameters, Geodynamic Inferences*, 92–95.

Alparone, S., Barberi, G., Cocina, O., Giampiccolo, E., Musumeci, C. and Patanè, D. (2012). Intrusive mechanism of the 2008–2009 Mt. Etna eruption: Constraints by tomographic images and stress tensor analysis. *Journal of volcanology and geothermal research*, *229*, 50-63. https://doi.org/10.1016/j.jvolgeores.2012.04.001

Alparone, S., Maiolino, V., Mostaccio, A., Scaltrito, A., Ursino, A., Barberi, G., D'Amico, S., Di Grazia, G., Giampiccolo, E., Musumeci, C., Scarfi, L. and Zuccarello, L. (2015). Instrumental seismic catalogue of Mt. Etna earthquakes (Sicily, Italy): ten years (2000-2010) of instrumental recordings. *Annals of Geophysics*. https://doi.org/10.4401/ag-6591

Ambrose, S. H. (1998). Late Pleistocene human population bottlenecks, volcanic winter, and differentiation of modern humans. *Journal of human evolution*, *34*(6), 623-651. https://doi.org/10.1006/jhev.1998.0219

Anderson, D.L. and Archambeau, C.B. (1964). The anaelasticity of the Earth. *Journal of Geophysical Research*, *69*(10), 2071-2084. https://doi.org/10.1029/JZ069i010p02071

Azzaro, R., Branca, S., Gwinner, K., and Coltelli, M. (2012). The volcano-tectonic map of Etna volcano, 1: 100.000 scale: an integrated approach based on a morphotectonic analysis from high-resolution DEM constrained by geologic, active faulting and seismotectonic data. *Italian journal of geosciences*, *131*(1), 153-170. https://doi.org/10.3301/IJG.2011.29

Badi, G., Del Pezzo, E., Ibanez, J. M., Bianco, F., Sabbione, N., and Araujo, M. (2009). Depth dependent seismic scattering attenuation in the Nuevo Cuyo region (southern

central Andes). *Geophysical research letters*, *36*(24). https://doi.org/10.1029/2009GL041081

Banda, E., Deichmann, N., Braile, L.W. and Ansorge, J. (1982). Amplitude study of the Pg phase. *Journal of Geophysics*, *51*, 153-154.

Barberi, F., Gasparini, P., Innocenti, F. and Villari, L. (1973). Volcanism of the southern Tyrrhenian Sea and its geodynamic implications. *Journal of Geophysical Research*, *78*(23), 5221-5232. https://doi.org/10.1029/JB078i023p05221

Barberi, G., Giampiccolo, E., Musumeci, C., Scarfì, L., Bruno, V., Cocina, O., Diaz-Moreno, A., Sicali, S., Tusa, G., Tuvè, T., Zuccarello, L., Ibanez, J. M. and Patanè, D. (2016). Seismic and volcanic activity during 2014 in the region involved by TOMO-ETNA seismic active experiment. *Annals of Geophysics*. https://doi.org/10.4401/ag-7082

Barreca, G., Bruno, V., Cultrera, F., Mattia, M., Monaco, C., and Scarfì, L. (2014). New insights in the geodynamics of the Lipari–Vulcano area (Aeolian Archipelago, southern Italy) from geological, geodetic and seismological data. *Journal of Geodynamics*, *82*, 150-167. https://doi.org/10.1016/j.jog.2014.07.003

Barreca, G., Branca, S., and Monaco, C. (2018). Three-Dimensional Modeling of Mount Etna Volcano: Volume Assessment, Trend of Eruption Rates, and Geodynamic Significance. *Tectonics*, *37*(3), 842-857. https://doi.org/10.1002/2017TC004851

Barreca, G., Branca, S., Corsaro, R. A., Scarfì, L., Cannavò, F., Aloisi, M., Monaco, C. and Faccenna, C. (2020). Slab detachment, mantle flow, and crustal collision in eastern Sicily (southern Italy): Implications on Mount Etna volcanism. *Tectonics*, *39*(9), e2020TC006188. https://doi.org/10.1029/2020TC006188

Basant, R. A., Ryan, G. A., Peacock, J. R., Camacho, A. G., Blake, O. O., Hautmann, S., and Lynne, B. Y. (2021). Multi-geophysical parameter classification of the Montserrat geothermal system. *Geothermics*, *90*, 102006. https://doi.org/10.1016/j.geothermics.2020.102006

Battaglia, M., Gottsmann, J., Carbone, D. and Fernández, J. (2008). 4D volcano gravimetry. *Geophysics*, *73*(6), WA3-WA18. https://doi.org/10.1190/1.2977792

Beccaluva, L., Gabbianelli, G., Lucchini, F., Rossi, P. L. and Savelli, C. (1985). Petrology and K/Ar ages of volcanics dredged from the Eolian seamounts: implications for

geodynamic evolution of the southern Tyrrhenian basin. *Earth and Planetary Science Letters*, *74*(2-3), 187-208. https://doi.org/10.1016/0012-821X(85)90021-4

Behncke, B., and Neri, M. (2003). The July–August 2001 eruption of Mt. Etna (Sicily). *Bulletin of Volcanology*, *65*(7), 461-476. https://doi.org/10.1007/s00445-003-0274-1

Ben-Zvi, T., Wilcock, W. S., Barclay, A. H., Zandomeneghi, D., Ibáñez, J. M., and Almendros, J. (2009). The P-wave velocity structure of Deception Island, Antarctica, from two-dimensional seismic tomography. *Journal of Volcanology and Geothermal Research*, *180*(1), 67–80. https://doi.org/10.1016/j.jvolgeores.2008.11.020

Bianchi, F., Carbone, S., Grasso, M., Invernizzi, G., Lentini, F., and Longaretti, G. (1987). Sicilia orientale. Profilo geologico Nebrodi-Iblei. *Memorie della Società Geologica Italiana*, *38*, 429-458.

Bianco, F., Castellano, M., Del Pezzo, E. and Ibáñez, J.M. (1999). Attenuation of short-period seismic waves at Mt. Vesuvius, Italy. *Geophysical Journal International*. *138*(1), 67-76. https://doi.org/10.1046/j.1365-246x.1999.00868.x

Block, L. V. (1991). *Joint hypocenter-velocity inversion of local earthquakes arrival time data in two geothermal regions*, (Doctoral thesis). Cambridge. Massachusetts Institute of Technology.

Bonaccorso, A., Ferrucci, F., Patanè, D., and Villari, L. (1996). Fast deformation processes and eruptive activity at Mount Etna (Italy). *Journal of Geophysical Research: Solid Earth*, *101*(B8), 17467-17480. https://doi.org/10.1029/96JB01151

Bonaccorso, A., Calvari, S., Coltelli, M., Del Negro, C., and Falsaperla, S. (2004). Mt. Etna: volcano laboratory. *Washington DC American Geophysical Union Geophysical Monograph Series*, *143*.

Bonaccorso, A., Bonforte, A., Guglielmino, F., Palano, M., and Puglisi, G. (2006). Composite ground deformation pattern forerunning the 2004–2005 Mount Etna eruption. *Journal of Geophysical Research: Solid Earth*, *111*(B12). https://doi.org/10.1029/2005JB004206

Bonforte, A., Bonaccorso, A., Guglielmino, F., Palano, M., and Puglisi, G. (2008). Feeding system and magma storage beneath Mt. Etna as revealed by recent

inflation/deflation cycles. *Journal of Geophysical Research*, *113*, B05406. https://doi.org/10.1029/2007JB005334

Bousquet, J. C. and Lanzafame, G. (2001). Nouvelle interpretation des fractures des eruptions laterales de l'Etna; consequences pour son cadre tectonique. *Bulletin de la Société Géologique de France*, *172*(4), 455-467. https://doi.org/10.2113/172.4.455

Branca, S., Coltelli, M., De Beni, E., and Wijbrans, J. (2007). Geological evolution of Mount Etna volcano (Italy) from earliest products until the first central volcanism (between 500 and 100 ka ago) inferred from geochronological and stratigraphic data. *International Journal of Earth Sciences*, *97*, 135, 152. https://doi.org/10.1007/s00531-006-0152-0

Branca, S., Coltelli, M., De Beni, E. and Wijbrans, J. (2008). Geological evolution of Mount Etna volcano (Italy) from earliest products until the first central volcanism (between 500 and 100 ka ago) inferred from geochronological and stratigraphic data. *International Journal of Earth Sciences*, *97*(1), 135-152. https://doi.org/10.1007/s00531-006-0152-0

Branca, S., Coltelli, M., Groppelli, G., and Lentini, F. (2011). Geological map of Etna volcano, 1: 50,000 scale. *Italian Journal of Geosciences*, *130*(3), 265-291. https://doi.org/10.3301/IJG.2011.15

Branca, S., and Ferrara, V. (2013). The morphostructural setting of Mount Etna sedimentary basement (Italy): Implications for the geometry and volume of the volcano and its flank instability. *Tectonophysics*, *586*, 46-64. https://doi.org/10.1016/j.tecto.2012.11.011

Briffa, K., Jones, P., Schweingruber, F.H. and Osborn, T.J. (1998) Influence of volcanic eruptions on Northern Hemisphere summer temperature over the past 600 years. *Nature, 393*, 450–455 https://doi.org/10.1038/30943

Bueno, A., Benitez, C., De Angelis, S., Moreno, A. D., and Ibáñez, J. M. (2019). Volcano-seismic transfer learning and uncertainty quantification with Bayesian neural networks. *IEEE Transactions on Geoscience and Remote Sensing*, *58*(2), 892-902. https://doi.org/10.1109/TGRS.2019.2941494

Bueno, A., Benítez, C., Zuccarello, L., De Angelis, S. and Ibáñez, J. M. (2021). End to End Bayesian Monitoring of Seismo Volcanic Dynamics. *IEEE Transactions on Geoscience and Remote Sensing*. https://doi.org/10.1109/TGRS.2021.3076012

Canas, J. A., Pujades, L. G., Blanco, M. J., Soler, V., and Carracedo, J. C. (1995). Coda-Q distribution in the Canary Islands. *Tectonophysics*, *246*(4), 245-261. https://doi.org/10.1016/0040-1951(94)00258-B

Carcolé, E. and Sato, H. (2010). Spatial distribution of scattering loss and intrinsic absorption of short-period S waves in the lithosphere of Japan on the basis of the Multiple Lapse Time Window Analysis of Hi-net data. *Geophysical Journal International*, *180*(1), 268-290. https://doi.org/10.1111/j.1365-246X.2009.04394.x

Cardaci, C., Coviello, M., Lombardo, G., Patanè, G. and Scarpa, R. (1993). Seismic tomography of Etna volcano. *Journal of volcanology and geothermal research*, *56*(4), 357-368. https://doi.org/10.1016/0377-0273(93)90002-9

Carmona, E., Almendros, J., Alguacil, G., Soto, J. I., Luzón, F., and Ibáñez, J. M. (2015). Identification of T-waves in the Alboran Sea. *Pure and Applied Geophysics*, *172*(11), 3179-3188. https://doi.org/10.1007/s00024-014-1018-1

Cassinis, R., Finetti, I., Giese, P., Morelli, C., Steinmetz, L. and Vecchia, O. (1969). Deep seismic refraction research on Sicily. *Bolletino di Geofisica Teorica ed Applicata*, *11*(43/44), 140-160.

Castellano, M., Augusti, V., De Cesare, W., Favali, P., Frugoni, F., Montuori, C., Sgroi, T., De Gori, P., Govoni, A., Moretti, M., Patanè, D., Cocina, O., Zuccarello, L., Marsella, E., Aiello, G., Di Fiore, V., Ligi, M., Bortoluzzi, G., Ferrante, V., Marchetti, E., Lacanna, G. and Ulivieri, G. (2008). Seismic tomography experiment at Italy's Stromboli Volcano. *Eos, Transactions American Geophysical Union*, *89*(30), 269-270. https://doi.org/10.1029/2008EO300001

Castro-Melgar, I., Prudencio, J., Cannata, A., Del Pezzo, E. and Ibanez, J.M. (2021). Small-scale volcanic structures of the Aeolian volcanic arc revealed by seismic Attenuation. *Frontiers in Earth Science*. 9:725402. https://doi.org/10.3389/feart.2021.725402

Castro-Melgar, I., Prudencio, J., Del Pezzo, E., Giampiccolo, E. and Ibanez, J.M. (2021). Shallow magma storage beneath Mt. Etna: Evidence from new Attenuation tomography

and existing velocity models. *Journal of Geophysical Research: Solid Earth*, *126*(7), e2021JB022094. https://doi.org/10.1029/2021JB022094

Catalano, R., Doglioni, C., and Merlini, S. (2001). On the mesozoic Ionian basin. *Geophysical Journal International*, *144*(1), 49-64. https://doi.org/10.1046/j.0956-540X.2000.01287.x

Cavallaro, D., Cocchi, L., Coltelli, M., Muccini, F., Carmisciano, C., Firetto Carlino, M., Ibáñez, J., Patanè, D., Filippone, M. and Buttaro, E. (2016). Acquisition procedures, processing methodologies and preliminary results of magnetic and ROV data collected during the TOMO-ETNA experiment. *Annals of Geophysics*, *59*(4). https://doi.org/10.4401/ag-7084

Chester, D. K. (1985). *Mount Etna: the anatomy of a volcano.* Stanford University Press.

Chiarabba, C., Pino, N. A., Ventura, G. and Vilardo, G. (2004). Structural features of the shallow plumbing system of Vulcano Island Italy. *Bulletin of volcanology*, *66*(6), 477-484. https://doi.org/10.1007/s00445-003-0331-9

Chiarabba, C., De Gori, P., and Patanè, D. (2004). The Mt. Etna plumbing system: the contribution of seismic tomography. *Washington DC American Geophysical Union Geophysical Monograph Series*, *143*, 191-204.

Chiarabba, C., De Gori, P. and Speranza, F. (2008). The southern Tyrrhenian subduction zone: deep geometry, magmatism and Plio-Pleistocene evolution. *Earth and Planetary Science Letters*, *268*(3-4), 408-423. https://doi.org/10.1016/j.epsl.2008.01.036

Chiocci, F. L., Coltelli, M., Bosman, A., and Cavallaro, D. (2011). Continental margin large-scale instability controlling the flank sliding of Etna volcano. *Earth and Planetary Science Letters*, *305*(1-2), 57-64. https://doi.org/10.1016/j.epsl.2011.02.040

Chouet, B., De Luca, G., Milana, G., Dawson, P., Martini, M. and Scarpa, R. (1998). Shallow velocity structure of Stromboli Volcano, Italy, derived from small-aperture array measurements of Strombolian tremor. *Bulletin of the Seismological Society of America*, *88*(3), 653-666. https://doi.org/10.1785/BSSA0880030653

Colombi, B., Guerra, I., Luongo, G. and Scarascia, S. (1979). Profilo sismico a rifrazione Acireale-Termini Imerese. *Contributti preliminar allá sorveglianza e rischio vulcanico (Etna-Eolie)*, 155-170.

Coltelli, M., Cavallaro, D., Firetto Carlino, M., Cocchi, L., Muccini, F., D'Aessandro, A., Claude, M. E., Monaco, C., Ibáñez, J., Zgur, F., Patanè, D., Carmisciano, C., D'Anna, G., Gonzales, M. T. P., Teixido, T., D'Anna, R., Fertitta, G., Passafiume, G., Speciale, S., Grassa, F., Karageorgis, A., Sormani, L., Facchin, L., Visnovic, G., Cotterle, D., Blanos, R., Mansutti, P., Sulli, A., Cultrera, F., Carrion, F. and Rapisarda, S. (2016). The marine activities performed within the TOMO-ETNA experiment. *Annals of Geophysics*. https://doi.org/10.4401/ag-7081

Cordell, D., Unsworth, M. J., Lee, B, Diaz, D., Bennington, N. L., and Thurber, C. H. (2020). Integrating magnetotelluric and seismic images of silicic magma systems: A case study from the Laguna del Maule Volcanic Field, central Chile. *Journal of Geophysical Research: Solid Earth*, *125*, e2020JB020459. https://doi.org/10.1029/2020jb020459

Corsaro, R. A., Neri, M., and Pompilio, M. (2002). Paleo-environmental and volcano-tectonic evolution of the southeastern flank of Mt. Etna during the last 225 ka inferred from the volcanic succession of the 'Timpe', Acireale, Sicily. *Journal of Volcanology and Geothermal Research*, *113*(1–2), 289–306. https://doi.org/10.1016/s0377-0273(01)00262-1

Corsaro, R. A., and Pompilio, M. (2004). Buoyancy-controlled eruption of magmas at Mt Etna. *Terra Nova*, *16*(1), 16–22. https://doi.org/10.1046/j.1365-3121.2003.00520.x

Cristofolini, R., Lentini, F., Patanè, G., and Rasà, R. (1979). Intergrazione di dati geologici, geofisici e petrologici per la stesura di un profilo crostale in corrispondenza dell'Etna. *Bollettino della Società Geologica Italiana*, *98*(2), 239-247.

Cristofolini, R., Gresta, S., Imposa, S. and Patanè, G. (1988). Feeding mechanism of eruptive activity at Mt. Etna based on seismological and petrological data. In *Modeling of Volcanic Processes,* Vieweg+Teubner Verlag, Wiesbaden, 73-93. https://doi.org/10.1007/978-3-322-89414-4_3

Dainty, A.M. and Toksöz, M.N. (1981). Seismic codas on the Earth and the Moon: a comparison. *Physics of the Earth and Planetary Interiors*, *26*(4), 250-260. https://doi.org/10.1016/0031-9201(81)90029-7

De Astis, G., Ventura, G., and Vilardo, G. (2003). Geodynamic significance of the Aeolian volcanism (Southern Tyrrhenian Sea, Italy) in light of structural, seismological, and geochemical data. *Tectonics*, *22*(4). https://doi.org/10.1029/2003TC001506

De Gori, P., Chiarabba, C. and Patanè, D. (2005). Qp structure of Mount Etna: Constraints for the physics of the plumbing system. *Journal of Geophysical Research: Solid Earth*, *110*(B5). https://doi.org/10.1029/2003JB002875

De Gori, P., Chiarabba, C., Giampiccolo, E., Martinez–Arèvalo, C. and Patanè, D. (2011). Body wave attenuation heralds incoming eruptions at Mount Etna. *Geology*, *39*(5), 503-506. https://doi.org/10.1130/G31993.1

De Guidi, G., Barberi, G., Barreca, G., Bruno, V., Cultrera, F., Grassi, S., et al. (2015). Geological, seismological and geodetic evidence of active thrusting and folding south of Mt. Etna (eastern Sicily): Revaluation of "seismic efficiency" of the Sicilian Basal Thrust. *Journal of Geodynamics*, *90*, 32–41. https://doi.org/10.1016/j.jog.2015.06.001

De Luca, G., Filippi, L., Patanè, G., Scarpa, R. and Vinciguerra, S. (1997). Three-dimensional velocity structure and seismicity of Mt. Etna volcano, Italy. *Journal of volcanology and geothermal research*, *79*(1-2), 123-138. https://doi.org/10.1016/S0377-0273(97)00026-7

De Luca, G., Filippi, L., Caccamo, D., Neri, G., and Scarpa, R. (1997). Crustal structure and seismicity of Southern Tyrrhenian basin. *Physics of the earth and planetary interiors*, *103*(1-2), 117-133. https://doi.org/10.1016/S0031-9201(97)00026-5

De Ritis, R., Ventura, G., Chiappini, M., Carluccio, R., and Von Frese, R. (2010). Regional magnetic and gravity anomaly correlations of the Southern Tyrrhenian Sea. *Physics of the Earth and Planetary Interiors*, *181*(1-2), 27-41. https://doi.org/10.1016/j.pepi.2010.04.003

De Siena, L., Del Pezzo, E., Bianco, F. and Tramelli, A. (2009). Multiple resolution seismic attenuation imaging at Mt. Vesuvius. *Physics of the Earth and Planetary Interiors*, *173*(1-2), 17-32. https://doi.org/10.1016/j.pepi.2008.10.015

De Siena, L., Del Pezzo, E., and Bianco, F. (2010). Seismic attenuation imaging of Campi Flegrei: Evidence of gas reservoirs, hydrothermal basins, and feeding systems. *Journal of Geophysical Research*, *115*, B09312. https://doi.org/10.1029/2009jb006938

De Siena, L., Thomas, C., and Aster, R. (2014). Multi-scale reasonable attenuation tomography analysis (MuRAT): An imaging algorithm designed for volcanic regions. *Journal of Volcanology and Geothermal Research*, *277*, 22–35. https://doi.org/10.1016/j.jvolgeores.2014.03.009

De Siena, L., Thomas, C., Waite, G. P., Moran, S. C., and Klemme, S. (2014). Attenuation and scattering tomography of the deep plumbing system of Mount St. Helens. *Journal of Geophysical Research: Solid Earth*, *119*(11), 8223-8238. https://doi.org/10.1002/2014JB011372

De Siena, L., Calvet, M., Watson, K. J., Jonkers, A. R. T., and Thomas, C. (2016). Seismic scattering and absorption mapping of debris flows, feeding paths, and tectonic units at Mount St. Helens volcano. *Earth and Planetary Science Letters*, *442*, 21-31. https://doi.org/10.1016/j.epsl.2016.02.026

De Siena, L., Chiodini, G., Vilardo, G., Del Pezzo, E., Castellano, M., Colombelli, S., Tisato, N. and Ventura, G. (2017). Source and dynamics of a volcanic caldera unrest: Campi Flegrei, 1983–84. *Scientific reports*, *7*(1), 1-13. https://doi.org/10.1038/s41598-017-08192-7

De Siena, L., Amoruso, A., Pezzo, E. D., Wakeford, Z., Castellano, M., and Crescentini, L. (2017). Space-weighted seismic attenuation mapping of the aseismic source of Campi Flegrei 1983–1984 unrest. *Geophysical Research Letters*, *44*(4), 1740-1748. https://doi.org/10.1002/2017GL072507

Del Pezo, E. (2008) Chapter 13 Seismic Wave Scattering in Volcanoes, *Earth Heterogeneity and Scattering Effects on Seismic Waves, 50,* 353-371, ed. Dmowska, R, Elsevier. https://doi.org/10.1016/S0065-2687(08)00013-7

Del Pezzo, E., Luongo, G. and Scarpa, R. (1979). Seismic Wave Transmission in Southern Tyrrhenian Sea. *Bollettino di Geofisica Teorica ed Applicata. 21(81), 53-66.*

Del Pezzo, E., Ferulano, F., Giarrusso, A., and Martini, M. (1983). Seismic coda Q and scaling law of the source spectra at the Aeolian Islands, southern Italy. *Bulletin of the Seismological Society of America*, *73*(1), 97-108. https://doi.org/10.1785/BSSA0730010097

Del Pezzo, E., Ibáñez, J., Morales, J., Akinci, A. and Maresca, R. (1995). Measurements of intrinsic and scattering seismic attenuation in the crust. *Bulletin of Seismological Society of America*, *85*(5), 1373-1385. https://doi.org/10.1785/BSSA0850051373

Del Pezzo, E., Bianco, F. and Saccorotti, G. (2001). Separation of intrinsic and scattering Q for volcanic tremor: an application to Etna and Masaya Volcanoes. *Geophysical Research Letters*, *28*(16), 3083-3086. https://doi.org/10.1029/2001GL013372

Del Pezzo, E., Bianco, F., De Siena, L. and Zollo, A. (2006). Small scale shallow Attenuation structure at Mt. Vesuvius, Italy. *Physics of the Earth and Planetary Interiors, 157*(3-4), 257-268. https://doi.org/10.1016/j.pepi.2006.04.009

Del Pezzo, E., Ibanez, J., Prudencio, J., Bianco, F., and De Siena, L. (2016). Absorption and scattering 2-D volcano images from numerically calculated space-weighting functions. *Geophysical Journal International*, *206*(2), 742-756. https://doi.org/10.1093/gji/ggw171

Del Pezzo, E., De La Torre, A., Bianco, F., Ibanez, J., Gabrielli, S., and De Siena, L. (2018). Numerically calculated 3D space-weighting functions to image crustal volcanic structures using diffuse coda waves. *Geosciences*, *8*(5), 175. https://doi.org/10.3390/geosciences8050175

Del Pezzo, E., Giampiccolo, E., Tuvè, T., Di Grazia, G., Gresta, S., and Ibàñez, J. M. (2019). Study of the regional pattern of intrinsic and scattering seismic attenuation in Eastern Sicily (Italy) from local earthquakes. *Geophysical Journal International*, *218*(2), 1456-1468. https://doi.org/10.1093/gji/ggz208

Del Pezzo, E., and Ibáñez, J. M. (2020). Seismic coda-waves imaging based on sensitivity kernels calculated using a heuristic approach. *Geosciences*, *10*(8), 304. https://doi.org/10.3390/geosciences10080304

Díaz-Moreno, A. (2016). Joint active and passive seismic Tomography in active volcanoes: The case of study of Mt. Etna, and further implications in active volcanic regions. *PhD thesis, Universidad de Granada, Spain.*

Díaz-Moreno, A., Koulakov, I., García-Yeguas, A., Jakovlev, A., Barberi, G., Cocina, O., et al. (2016). PARTOS-Passive and Active Ray TOmography Software: Description and preliminary analysis using TOMO-ETNA experiment's dataset. *Annals of Geophysics*, *59*(4). https://doi.org/10.4401/ag-7088

Díaz-Moreno, A., Barberi, G., Cocina, O., Koulakov, I., Scarfì, L., Zuccarello, L., Prudencio, J., García-Yeguas, A., Álvarez, I., García, L. and Ibáñez, J.M. (2018). New insights on Mt. Etna's crust and relationship with the regional tectonic framework from joint active and passive p-wave seismic tomography. *Surveys in Geophysics*, *39*, 57-97. https://doi.org/10.1007/s10712-017-9425-3

Doglioni, C., Innocenti, F., and Mariotti, G. (2001). Why Mt Etna? *Terra Nova*, *13*(1), 25-31. https://doi.org/10.1046/j.1365-3121.2001.00301.x

Dvorkin, J., Prasad, M., Sakai, A., and Lavoie, D. (1999). Elasticity of marine sediments: Rock physics modeling. *Geophysical Research Letters*, *26*(12), 1781–1784. https://doi.org/10.1029/1999gl900332

Ferrari, L. and Manetti, P. (1993). Geodynamic framework of the Tyrrhenian volcanism: a review. *Acta Vulcanol*, *3*, 1-10.

Finetti, I., Lentini, F., Carbone, S., and Catalano, S. (1996). Il sistema Apennino Meridionale-Arco Calabro-Sicilia nel Mediterraneo Centrale: studio geologico-geofisico.

Flatté, S.M., Dashen, R., Munk, W., Watson, K. and Zachariasen, F. (1979). *Sound Transmission Through a Fluctuating Ocean,* Cambridge Univ. Press.

Frankel, A., McGarr, A., Bicknell, J., Mori, J., Seeber, L. and Cranswick, E. (1990). Attenuation of high-frequency shear waves in the crust: Measurements from New York State, South Africa and southern California. *Journal of Geophysical Research*, 95 (B11), 17441-17457. https://doi.org/10.1029/JB095iB11p17441

Gabrielli, S., De Siena, L., Napolitano, F., and Del Pezzo, E. (2020). Understanding seismic path biases and magmatic activity at Mount St Helens volcano before its 2004 eruption. *Geophysical Journal International*, *222*(1), 169-188. https://doi.org/10.1093/gji/ggaa154

Ganci, G., Cappello, A., Bilotta, G., and Del Negro, C. (2020). How the variety of satellite remote sensing data over volcanoes can assist hazard monitoring efforts: The 2011 eruption of Nabro volcano. *Remote Sensing of Environment*, *236*, 111426. https://doi.org/10.1016/j.rse.2019.111426

Gasparini, P. and TomoVes Working Group (1998). Looking inside Mt. Vesuvius. *Eos, Transactions American Geophysical Union*, *79*(19), 229-232. https://doi.org/10.1029/98EO00165

García, L., Álvarez, I., Benítez, C., Titos, M., Bueno, Á., Mota, S., De La Torre, A., Segura, J. C., Aguacil, G., Diaz-Moreno, A., Prudencio, J., Garcia-Yeguas, A., Ibanez, J. M., Zuccarello, L., Cocina, O. and Patanè, D. (2016). Advances on the automatic

estimation of the P-wave onset time. *Annals of Geophysics*. https://doi.org/10.4401/ag-7087

García-Yeguas, A., Koulakov, I., Ibáñez, J. M. and Rietbrock, A. (2012). High resolution 3D P wave velocity structure beneath Tenerife Island (Canary Islands, Spain) based on tomographic inversion of active-source data. *Journal of Geophysical Research: Solid Earth*, *117*(B9). https://doi.org/10.1029/2011JB008970

García-Yeguas, A., Ibánez, J. M., Koulakov, I., Jakovlev, A., Romero-Ruiz, M. C., and Prudencio, J. (2014). Seismic tomography model reveals mantle magma sources of recent volcanic activity at El Hierro Island (Canary Islands, Spain). *Geophysical Journal International*, *199*(3), 1739-1750. https://doi.org/10.1093/gji/ggu339

García-Yeguas, A., Ledo, J., Pina-Varas, P., Prudencio, J., Queralt, P., Marcuello, A., et al. (2017). A 3D joint interpretation of magnetotelluric and seismic tomographic models: The case of the volcanic island of Tenerife. *Computers and Geosciences*, *109*, 95–105. https://doi.org/10.1016/j.cageo.2017.08.003

Ghisetti, F. (1979). Relazioni tra strutture e fasi trascorrenti e distensive lungo i sistemi Messina-Fiumefreddo, Tindari-Letojanni e Alia-Malvagna (Sicilia nordorientale): uno studio microtettonico. *Geoogia. Romana, 18*, 23–58

Giampiccolo, E., Tuvé, T., Gresta, S. and Patane, D. (2006). S-waves attenuation and separation of scattering and intrinsic absorption of seismic energy in southeastern Sicily (Italy). *Geophysical Journal International*, *156*(1), 211-222. https://doi.org/10.1111/j.1365-246X.2006.02881.x

Giampiccolo, E., and Tuvè, T. (2018). Regionalization and dependence of coda Q on frequency and lapse time in the seismically active Peloritani region (northeastern Sicily, Italy). *Journal of Seismology*, *22*(4), 1059-1074. https://doi.org/10.1007/s10950-018-9750-0

Giampiccolo, E., Cocina, O., De Gori, P., and Chiarabba, C. (2020). Dyke intrusion and stress-induced collapse of volcano flanks: The example of the 2018 event at Mt. Etna (Sicily, Italy). *Scientific Reports*, *10*(1), 6373. https://doi.org/10.1038/s41598-020-63371-3

Giampiccolo, E., Del Pezzo, E., Tuvè, T., Di Grazia, G. and Ibanez, J. M. (2021). 3-D Q-coda attenuation structure at Mt Etna (Italy). *Geophysical Journal International*, *227*(1), 544-558. https://doi.org/10.1093/gji/ggab235

Giordano, G., and De Astis, G. (2021). The summer 2019 basaltic Vulcanian eruptions (paroxysms) of Stromboli. *Bulletin of Volcanology*, *83*(1), 1-27. https://doi.org/10.1007/s00445-020-01423-2

Giudicepietro, F., López, C., Macedonio, G., Alparone, S., Bianco, F., Calvari, S., De Cesare, W., Delle Donne, D., Di Lieto, B., Esposito, A. M., Orazi, M., Peluso, R., Privitera, E., Romano, P., Scarpato, G. and Tramelli, A. (2020). Geophysical precursors of the July-August 2019 paroxysmal eruptive phase and their implications for Stromboli volcano (Italy) monitoring. *Scientific reports*, *10*(1), 1-16. https://doi.org/10.1038/s41598-020-67220-1

Gruppo Analisi Dati Sismici, 2019. *Catalogo dei terremoti della Sicilia Orienta–e - Calabria Meridionale (1999–2019),* INGV, Catania, http://www.ct.ingv.it/ufs/analisti/catalogolist.php.

Guardo, R., and De Siena, L. (2017). Integrating ambient noise with GIS for a new perspective on volcano imaging and monitoring: The case study of Mt. Etna. *Journal of Volcanology and Geothermal Research*, *347*, 397–407. https://doi.org/10.1016/j.jvolgeores.2017.10.007

Guardo, R., De Siena, L., and Dreidemie, C. (2020). Mt. Etna feeding system and sliding flank: A New 3D image from earthquakes distribution in a customisable GIS. *Frontiers in Earth Sciences*, *8*, 1–12. https://doi.org/10.3389/feart.2020.589925

Gutscher, M. A., Dominguez, S., de Lepinay, B. M., Pinheiro, L., Gallais, F., Babonneau, N., Cattaneo, A., Le Faou, Y., Barreca, G., Micallef, A. and Rovere, M. (2016). Tectonic expression of an active slab tear from high-resolution seismic and bathymetric data offshore Sicily (Ionian Sea). *Tectonics*, *35*(1), 39-54. https://doi.org/10.1002/2015TC003898

Gutscher, M. A., Kopp, H., Krastel, S., Bohrmann, G., Garlan, T., Zaragosi, S., Klaucke, I., Wintersteller, P., Loubrieu, B., Le Faou, Y., San Pedro, L., Dominguez, S., Rovere, M., Lepinay, B. M., Ranero, C. and Sallares, V. (2017). Active tectonics of the Calabrian subduction revealed by new multi-beam bathymetric data and high-resolution seismic

profiles in the Ionian Sea (Central Mediterranean). *Earth and Planetary Science Letters*, *461*, 61-72. https://doi.org/10.1016/j.epsl.2016.12.020

Gvirtzman, Z., and Nur, A. (1999). The formation of Mount Etna as the consequence of slab rollback. *Nature*, *401*(6755), 782-785. https://doi.org/10.1038/44555

Gvirtzman, Z., and Nur, A. (2001). Residual topography, lithospheric structure and sunken slabs in the central Mediterranean. *Earth and Planetary Science Letters*, *187*(1-2), 117-130. https://doi.org/10.1016/S0012-821X(01)00272-2

Hansen, P. C. (1994). Regularization tools: a Matlab package for analysis and solution of discrete ill-posed problems. *Numerical algorithms*, *6*(1), 1-35. https://doi.org/10.1007/BF02149761

Havskov, J., Peña, J. A., Ibáñez, J. M., Ottemöller, L., and Martínez-Arévalo, C. (2003). Magnitude scales for very local earthquakes. Application for Deception Island Volcano (Antarctica). *Journal of volcanology and geothermal research*, *128*(1-3), 115-133. https://doi.org/10.1016/S0377-0273(03)00250-6

Herraiz, M. and Espinosa, A.F. (1987), Coda waves a review. *Pure and Applied Geophysics*, *125*, 499-577. https://doi.org/10.1007/BF00879572

Hirn, A., Nercessian, A., Sapin, M., Ferrucci, F. and Wittlinger, G. (1991). Seismic heterogeneity of Mt Etna: structure and activity. *Geophysical Journal International*, *105*(1), 139-153. https://doi.org/10.1111/j.1365-246X.1991.tb03450.x

Hirn, A., Nicolich, R., Gallart, J., Laigle, M., Cernobori, L. and ETNASEIS Scientific Group (1997). Roots of Etna volcano in faults of great earthquakes. *Earth and Planetary Science Letters*, *148*(1-2), 171-191. https://doi.org/10.1016/S0012-821X(97)00023-X

Hoshiba, M. (1991). Simulation of multiple-scattered coda wave excitation based on the energy conservation law. *Physics of the Earth and Planetary Interiors*, *67*(1-2), 123-136. https://doi.org/10.1016/0031-9201(91)90066-Q

Hoshiba, M., Rietbrick, A., Scherbaum, F., Nakahara, H. and Haberland, C. (2001). Scattering attenuation and intrinsic absorption using uniform and depth-dependent model application to full seismogram envelope recorded in northern Chile. *Journal of Seismology*, *5*, 157-179. https://doi.org/10.1023/A:1011478202750

Ibanez, J. M., Del Pezzo, E., De Miguel, F., Herraiz, M., Alguacil, G., and Morales, J. (1990). Depth-dependent seismic attenuation in the Granada zone (Southern Spain). *Bulletin of the Seismological Society of America*, *80*(5), 1232-1244. https://doi.org/10.1785/BSSA0800051232

Ibáñez, J. M., Morales, J., De Miguel, F., Vidal, F., Alguacil, G., and Posadas, A. M. (1991). Effect of a sedimentary basin on estimations of Qc and QLg. *Physics of the earth and planetary interiors*, *66*(3-4), 244-252. https://doi.org/10.1016/0031-9201(91)90078-V

Ibañez, J., Del Pezzo, E., Alguacil, G., De Miguel, F., Morales, J., De Martino, S., Sabbarese, C. and Posadas, A.M. (1993). Geometrical spreading function for short-period s and coda waves recorded in southern Spain. *Physics of the Earth and Planetary Interiors*, *80*, 25-36. https://doi.org/10.1016/0031-9201(93)90070-P

Ibáñez, J. M., Rietbock, A. and García-Yeguas, A. (2008). Imaging an active volcano edifice at Tenerife Island, Spain. *Eos, Transactions American Geophysical Union*, *89*(32), 289-290. https://doi.org/10.1029/2008EO320001

Ibáñez, J. M., Lühr, B., and Dahm, T. (2014). *TOMO-ETNA. GFZ Data Services*. Other/Seismic Network. https://doi.org/10.14470/6G7569676919

Ibáñez, J. M., Prudencio, J., Díaz-Moreno, A., Patanè, D., Puglisi, G., Lühr, B. G., Carrión, F., Dañobeitia, J. J., Coltelli, M., Bianco, F., Del Pezzo, E., Dahm, T., Willmott, V. and Mazauric, V. (2016). The TOMO-ETNA experiment: an imaging active campaign at Mt. Etna volcano. Context, main objectives, working-plans and involved research projects. *Annals of Geophysics*, *59*(4), S0426-S0426. https://doi.org/10.4401/ag-7079

Ibáñez, J. M., Díaz-Moreno, A., Prudencio, J., Patené, D., Zuccarello, L., Cocina, O., Lühr, B. G., Carrión, F., Coltelli, M., Bruno, P. P. G., Bianco, F., Hellweg M., Abreu, R., Alguacil, G., Álvarez, I., Aranda, C., Benítez, C., Buontempo L., Feriche, M., García, L., García-Quiroga, D., Martín, J. B. M., Morales, J., Serrano, I., Titos, M., Urbano, L., Aiesi, G., Azzaro, R., Barberi, G., Cantarero, M., Cappuccio, P., Cavallaro, D., Contrafatto, D., Di Prima, S., Falsaperla, S., Carlino, M. F., Giampiccolo, E., Larocca, G., Musumeci, C., Paratore, M., Pellegrino, D., Pulvirenti, N., Rapisarda, S., Sassano, M., Scarfì, L., Scuderi, L., Sicali, A., Tusa, G., Tuvè, T., Del Pezzo, E., Fiore, S., Galluzzo, D., La Rocca, M., Longobardi, M., Nocerino, L., Scognamiglio, S., Bottari, C., Criscuoli, F., De

Gori, P., Giovani, L., Messina, A., Silvestri, M., Salimbeni, S., Dahm, T., García-Yeguas, A., Ontiveros, A., Coello, E., Cordero, M., Guillén, C., Romero, M. C., McCann, H., Bretón, M., Boyd, S., Koulakov, I. and Abramenkov, S. (2016). TOMO-ETNA experiment at Etna volcano: activities on land. *Annals of Geophysics*, *59*(4). https://doi.org/10.4401/ag-7080

Ibáñez, J.M., Castro-Melgar, I., Cocina, O., Zuccarello, L., Branca, S., Del Pezzo, E. and Prudencio, J. (2020). First 2-D intrinsic and scattering Attenuation images of Mt Etna Volcano and surrounding región from active seismic data. *Geophysical Journal International*, *220*(1), 267-277. https://doi.org/10.1093/gji/ggz450

Jensen, F.B., Kuperman, W.A., Porter, M.B. and Schmidt, H., 1994. Computational Ocean Acoustics. AIP Series in Modern Acoustics and Signal Processing.

Jin, A. and Aki, K. (1991). Observational and physical basis for coda precursor. *Evaluation of Proposed Earthquake Precursors (Ed. M. Wyss), AGU, Washington D.C.*

Koulakov, I., and Shapiro, N. (2015). Seismic tomography of volcanoes. *Encyclopedia of earthquake engineering*, *15*(1), 1-18. https://doi.org/10.1007/978-3-642-36197-5_51-1

Koulakov, I., Maksotova, G., Jaxybulatov, K., Kasatkina, E., Shapiro, N. M., Luehr, B. G., El Khrepy, S. and Al-Arifi, N. (2016). Structure of magma reservoirs beneath M erapi and surrounding volcanic centers of C entral J ava modeled from ambient noise tomography. *Geochemistry, Geophysics, Geosystems*, *17*(10), 4195-4211. https://doi.org/10.1002/2016GC006442

Koulakov, I., Smirnov, S. Z., Gladkov, V., Kasatkina, E., West, M., El Khrepy, S., and Al-Arifi, N. (2018). Causes of volcanic unrest at Mt. Spurr in 2004–2005 inferred from repeated tomography. *Scientific Reports*, *8*(1), 1–7. https://doi.org/10.1038/s41598-018-35453-w

Koulakov, I., and Vargas, C. A. (2018). Evolution of the magma conduit beneath the Galeras volcano inferred from repeated seismic tomography. *Geophysical Research Letters*, *45*, 7514–7522. https://doi.org/10.1029/2018gl078850

La Rocca, M., Petrosino, S., Saccorotti, G., Simini, M., Ibanez, J., Almendros, J., and Del Pezzo, E. (2000). Location of the source and shallow velocity model deduced from the explosion quakes recorded by two seismic antennas at Stromboli volcano. *Physics and*

Chemistry of the Earth, Part A: Solid Earth and Geodesy, *25*(9-11), 731-735. https://doi.org/10.1016/S1464-1895(00)00113-7

Laiolo, M., Ripepe, M., Cigolini, C., Coppola, D., Della Schiava, M., Genco, R., et al. (2019). Space-and ground-based geophysical data tracking of magma migration in shallow feeding system of Mount Etna volcano. *Remote Sensing*, *11*(10), 1182. https://doi.org/10.3390/rs11101182

Lanzafame, G., and Bousquet, J. C. (1997). The Maltese escarpment and its extension from Mt. Etna to Aeolian Islands (Sicily): importance and evolution of a lithosphere discontinuity. *Acta Vulcanologica*, *9*, 113-120.

Lees, J. M. (2007). Seismic tomography of magmatic systems. *Journal of Volcanology and Geothermal Research*, *167*(1-4), 37-56. https://doi.org/10.1016/j.jvolgeores.2007.06.008

Lekkas, E., Meletlidis, S., Kyriakopoulos, K., Manousaki, M., Mavroulis, S., Kostaki, E., Michailidis, A., Gogou, M., Mavrouli, M., Castro-Melgar, I., Gatsios, T. and Parcharidis, I. (2021). The 2021 Cumbre Vieja volcano eruption in La Palma (Canary Islands). *Newsletter of Environmental, Disaster and Crises Management Strategies*, *26*, ISSN 2653-9454

Lentini, F., Carbone, S., Catalano, S., Di Stefano, A., Gargano, C., Romeo, M., Strazzulla, S. and Vinci, G. (1995). Sedimentary evolution of basins in mobile belts: examples from the Tertiary terrigenous sequences of the Peloritani Mountains (NE Sicily). *Terra Nova*, *7*(2), 161-170. https://doi.org/10.1111/j.1365-3121.1995.tb00685.x

Lentini, F., Carbone, S. and Guarnieri, P. (2006). Collisional and postcollisional tectonics of the Apenninic-Maghrebian orogen (southern Italy). *Geological Society of America Special Papers, 409*, 57-81. https://doi.org/10.1130/2006.2409(04)

Linde, N., Baron, L., Ricci, T., Finizola, A., Revil, A., Muccini, F., Cocchi, L. and Carmisciano, C. (2014). 3-D density structure and geological evolution of Stromboli volcano (Aeolian Islands, Italy) inferred from land-based and sea-surface gravity data. *Journal of volcanology and geothermal research*, *273*, 58-69. https://doi.org/10.1016/j.jvolgeores.2014.01.006

Lucchi, F., Peccerillo, A., Keller, J., Tranne, C. A., and Rossi, P. L. (2013). The Aeolian islands volcanoes. Geological Society of London.

Luzon, F., Almendros, J., and García-Jerez, A. (2011). Shallow structure of Deception Island, Antarctica, from correlations of ambient seismic noise on a set of dense seismic arrays. *Geophysical Journal International*, *185*(2), 737–748. https://doi.org/10.1111/j.1365-246x.2011.04962.x

Malinverno, A. and Ryan, W. B. (1986). Extension in the Tyrrhenian Sea and shortening in the Apennines as result of arc migration driven by sinking of the lithosphere. *Tectonics*, *5*(2), 227-245. https://doi.org/10.1029/TC005i002p00227

Martínez, V. L., Titos, M., Benítez, C., Badi, G., Casas, J. A., Craig, V. H. O. and Ibáñez, J. M. (2021). Advanced signal recognition methods applied to seismo-volcanic events from Planchon Peteroa Volcanic Complex: Deep Neural Network classifier. *Journal of South American Earth Sciences*, *107*, 103115. https://doi.org/10.1016/j.jsames.2020.103115

Martinez-Arevalo, C. (2005). Estructura superficial de atenuación para ondas sísmicas directas, p y s, en ambientes volcánicos. Aplicación al volcán Isla Decepción (Antártida) y al volcán Etna (Italia). *PhD thesis, Universidad de Granada, Spain*.

Martinez-Arevalo, C., Bianco, F., Ibañez, J. and Del Pezzo, E. (2003). Shallow seismic Attenuation and shear-wave splitting in the short-period range of Deception Island volcano (Antarctica). *Journal of Volcanology and Geothermal Research*, *128*(1-3), 89-113. https://doi.org/10.1016/S0377-0273(03)00248-8

Martinez-Arevalo, C., Patane, D., Rietbrock, A. and Ibáñez, J. (2005). The intrusive process leading to the Mt. Etna 2001 flank eruption: Constraints from 3-D attenuation tomography. *Geophysical Research Letters*, *32*(21). https://doi.org/10.1029/2005GL023736

Matsumoto, S., Uehira, K., Watanabe, A., Goto, K., Iio, Y., Hirata, N., and Kanazawa, T. (2009). High resolution Q^{-1} estimation based on extension of coda normalization method and its application to P-wave attenuation structure in the aftershock area of the 2005 West Off Fukuoka Prefecture Earthquake (M 7.0). *Geophysical Journal International*, *179*(2), 1039–1054. https://doi.org/10.1111/j.1365-246x.2009.04313.x

Mayeda, K., Koyanagi, S., Hoshiba, M., Aki, K. and Zeng, Y. (1992). A comparative study of scattering, intrinsic, and coda Q^{-1} for Hawaii, Long Valley, and central California

between 1.5 and 15.0 Hz. *Journal of Geophysical Research*, *97*(B5), 6643-6659. https://doi.org/10.1029/91JB03094

Medwin, H. (1975). Speed of sound in water: A simple equation for realistic parameters. *The Journal of the Acoustical Society of America*, *58*(6), 1318-1319. https://doi.org/10.1121/1.380790

Milia, A., Iannace, P., Tesauro, M., and Torrente, M. M. (2018). Marsili and Cefalù basins: The evolution of a rift system in the southern Tyrrhenian Sea (Central Mediterranean). *Global and Planetary Change*, *171*, 225-237. https://doi.org/10.1016/j.gloplacha.2017.12.003

Monaco, C., Catalano, S., Cocina, O., De Guidi, G., Ferlito, C., Gresta, S., Musumeci, C. and Tortorici, L. (2005). Tectonic control on the eruptive dynamics at Mt. Etna Volcano (Sicily) during the 2001 and 2002–2003 eruptions. *Journal of Volcanology and Geothermal Research*, *144*(1-4), 211-233. https://doi.org/10.1016/j.jvolgeores.2004.11.024

Monteiller, V., Got, J. L., Patanè, D., Barberi, G. and Cocina, O. (2009). Double-difference tomography at Mt Etna volcano: Preliminary results. In *The VOLUME Project–VOLcanoes: Understanding subsurface mass moveMEnt*. ISBN 978-1-905254-39-2

Munk, W., Worcester, P. and Wunsch, C., 1995. *Ocean Acoustic Tomography*. Cambridge Univ. Press.

Murru, M., Montuori, C., Wyss, M., and Privitera, E. (1999). The locations of magma chambers at Mt. Etna, Italy, mapped by b-values. *Geophysical research letters*, *26*(16), 2553-2556. https://doi.org/10.1029/1999GL900568

Nazemi, N., Pezeshk, S., and Sedaghati, F. (2017). Attenuation of Lg waves in the New Madrid seismic zone of the central United States using the coda normalization method. *Tectonophysics*, *712*, 623–633. https://doi.org/10.1016/j.tecto.2017.06.026

Neri, M., Casu, F., Acocella, V., Solaro, G., Pepe, S., Berardino, P., et al. (2009). Deformation and eruptions at Mt. Etna (Italy): A lesson from 15 years of observations. *Geophysical Research Letters*, *36*. https://doi.org/10.1029/2008GL036151

Nicolich, R., Laigle, M., Hirn, A., Cernobori, L. and Gallart, J. (2000). Crustal structure of the Ionian margin of Sicily: Etna volcano in the frame of regional evolution. *Tectonophysics*, *329*(1-4), 121-139. https://doi.org/10.1016/S0040-1951(00)00192-X

Nicolosi, I., D'Ajello Caracciolo, F., Branca, S., Speranza, F., and Chiappini, M. (2018). Unravelling Mount Etna's early eruptive history by three-dimensional magnetic modeling. *Bulletin*, *130*(9-10), 1664-1674. https://doi.org/10.1130/B31793.1

Nishigami, K. Y. (2000). Deep crustal heterogeneity along and around the San Andreas fault system in central California and its relation to the segmentation. *Journal of Geophysical Research: Solid Earth*, *105*(B4), 7983-7998. https://doi.org/10.1029/1999JB900381

Northrop, J., and Colborn, J. G. (1974). Sofar channel axial sound speed and depth in the Atlantic Ocean. *Journal of Geophysical Research*, *79*(36), 5633-5641. https://doi.org/10.1029/JC079i036p05633

Nunnari, G., and Puglisi, G. (1994). The global positioning system as a useful technique for measuring ground deformations in volcanic areas. *Journal of Volcanology and Geothermal Research*, *61*(3-4), 267-280. https://doi.org/10.1016/0377-0273(94)90008-6

Oppenheimer, C. (2003). Climatic, environmental and human consequences of the largest known historic eruption: Tambora volcano (Indonesia) 1815. *Progress in Physical Geography 27*(2), 230-259. https://doi.org/10.1191/0309133303pp379ra

Palano, M., Ferranti, L., Monaco, C., Mattia, M., Aloisi, M., Bruno, V., Cannavò, F. and Siligato, G. (2012). GPS velocity and strain fields in Sicily and southern Calabria, Italy: Updated geodetic constraints on tectonic block interaction in the central Mediterranean. *Journal of Geophysical Research: Solid Earth*, *117*(B7). https://doi.org/10.1029/2012JB009254

Patacca, E., and Scandone, P. (1989). Post-Tortonian mountain building in the Apennines. The role of the passive sinking of a relic lithospheric slab.

Patane, D., Chiarabba, C., Cocina, O., De Gori, P., Moretti, M. and Boschi, E. (2002). Tomographic images and 3D earthquake locations of the seismic swarm preceding the 2001 Mt. Etna eruption: evidence for a dyke intrusion. *Geophysical Research Letters*, *29*(10), 135-1. https://doi.org/10.1029/2001GL014391

Patanè, D., De Gori, P., Chiarabba, C. and Bonaccorso, A. (2003). Magma ascent and the pressurization of Mount Etna's volcanic system. *Science*, *299*(5615), 2061-2063. https://doi.org/10.1126/science.1080653

Patanè, D., Barberi, G., Cocina, O., De Gori, P. and Chiarabba, C. (2006). Time-resolved seismic tomography detects magma intrusions at Mount Etna. *Science*, *313*(5788), 821-823. https://doi.org/10.1126/science.1127724

Patanè, D., Aliotta, M., Cannata, A., Cassisi, C., Coltelli, M., Di Grazia, G., Montalto, P. and Zuccarello, L. (2011). Interplay between Tectonics and Mount Etna's volcanism: insights into the geometry of the plumbing system. In *New frontiers in tectonic research-at the midst of plate convergence*. Edited by Uri Schattner, pp. 73-104, ISBN 978-953-307-594-5

Patanè, D., Barberi, G., De Gori, P., Cocina, O., Zuccarello, L., Garcia-Yeguas, A., Castellano, M., D'Alessandro, A. and Sgroi, T. (2017). The shallow magma chamber of Stromboli Volcano (Italy). *Geophysical Research Letters*, *44*(13), 6589-6596. https://doi.org/10.1002/2017GL073008

Pepe, F., Bertotti, G., Cella, F., and Marsella, E. (2000). Rifted margin formation in the south Tyrrhenian Sea: A high-resolution seismic profile across the north Sicily passive continental margin. *Tectonics*, *19*(2), 241-257. https://doi.org/10.1029/1999TC900067

Pepe, F., Bertotti, G., and Cloetingh, S. (2004). Tectono-stratigraphic modelling of the North Sicily continental margin (southern Tyrrhenian Sea). *Tectonophysics*, *384*(1-4), 257-273. https://doi.org/10.1016/j.tecto.2004.04.002

Petrosino, S., La Rocca, M., and Del Pezzo, E. (1999). Shallow velocity model of the northern flank of Stromboli Volcano, deduced by high frequency surface wave dispersion. *Journal of seismology*, *3*(1), 83-94. https://doi.org/10.1023/A:1009716203083

Petrosino, S., Cusano, P., Saccorotti, G., and Del Pezzo, E. (2002). Seismic attenuation and shallow velocity structures at Stromboli Volcano, Italy. *Bulletin of the Seismological Society of America*, *92*(3), 1102-1116. https://doi.org/10.1785/0120010147

Pezzo, E. D. (2008). "Chapter 13 Seismic Wave Scattering in Volcanoes. "Seismic Wave Scattering in Volcanoes"," in *Earth Heterogeneity and Scattering Effects on Seismic*

Waves. Editor R. Dmowska (Elsevier), *50*, 353–371. https://doi.org/10.1016/S0065-2687(08)00013-7

Polonia, A., Torelli, L., Gasperini, L., Cocchi, L., Muccini, F., Bonatti, E., Hensen, C., Schmidt, M., Romano, S., Artoni, A. and Carlini, M. (2017). Lower plate serpentinite diapirism in the Calabrian Arc subduction complex. *Nature communications*, *8*(1), 1-13. https://doi.org/10.1038/s41467-017-02273-x

Pontevivo, A., and Panza, G. F. (2006). The lithosphere-asthenosphere system in the Calabrian Arc and surrounding seas–Southern Italy. *Pure and Applied Geophysics*, *163*(8), 1617-1659. https://doi.org/10.1007/s00024-006-0093-3

Presti, D. L., Riggi, F., Ferlito, C., Bonanno, D. L., Bonanno, G., Gallo, G., et al. (2020). Muographic monitoring of the volcano-tectonic evolution of Mount Etna. *Scientific Reports*, *10*(1), 1–11. https://doi.org/10.1038/s41598-020-68435-y

Prudencio, J. (2013). From 2D to 3D attenuation tomography in volcanoes. The study of Tenerife (Canary Islands) and Deception Island (Antarctica). *PhD thesis, Universidad de Granada, Spain.*

Prudencio, J., Del Pezzo, E., García-Yeguas, A. and Ibáñez, J. (2013). Spatial distribution of intrinsic and scattering seismic attenuation in active volcanic islands, i: model and the case of Tenerife Island. *Geophysical Journal International*, *195*(3), 1942-1956. https://doi.org/10.1093/gji/ggt361

Prudencio, J., Ibáñez, J., García-Yeguas, A., Del Pezzo, E. and Posadas, A. (2013). Spatial distribution of intrinsic and scattering seismic attenuation in active volcanic islands, ii: Deception Island images. *Geophysical Journal International, 195*(3), 1957-1969. https://doi.org/10.1093/gji/ggt360

Prudencio, J., Del Pezzo, E., Ibáñez, J.M., Giampiccolo, E. and Patané, D. (2015). Two-dimensional seismic attenuation images of Stromboli Using active data. *Geophysical Research Letters*, *42*(6), 1717-1724. https://doi.org/10.1002/2015GL063293

Prudencio, J., De Siena, L., Ibáñez, J.M., Del Pezzo, E., García-Yeguas, A. and Díaz-Moreno, A. (2015). The 3D attenuation structure of Deception Island (Antarctica). *Surveys in Geophysics*, *36*, 371-390. https://doi.org/10.1007/s10712-015-9322-6

Prudencio, J., Ibáñez, J. M., Del Pezzo, E., Martí, J., García-Yeguas, A., and De Siena, L. (2015). 3D attenuation tomography of the volcanic island of Tenerife (Canary Islands). *Surveys in Geophysics*, *36*(5), 693-716. https://doi.org/10.1007/s10712-015-9322-6

Prudencio, J., Aoki, Y., Takeo, M., Ibáñez, J.M., Del Pezzo, E. and Song, W. (2017) Separation of scattering and intrinsic attenuation at Asama volcano (Japan): Evidence of high volcanic structural contrasts. *Journal of Volcanology and Geothermal Research, 333*, 96-103. https://doi.org/10.1016/j.jvolgeores.2017.01.014

Prudencio, J., Taira, T., Aoki, Y., Aoyama, H. and Onizawa, S. (2017) Intrinsic and scattering attenuation images of Usu volcano, Japan. *Bulletin of Volcanology*, *79*(4), 1-12. https://doi.org/10.1007/s00445-017-1117-9

Prudencio, J., Manga, M. and Taira, T. (2018). Subsurface structure of Long Valley caldera imaged with seismic scattering and intrinsic attenuation. *Journal of Geophysical Research: Solid Earth*, *123*(7), 5987-5999. https://doi.org/10.1029/2017JB014986

Prudencio, J. and Manga, M. (2020). 3-D seismic attenuation structure of Long Valley caldera: looking for melt bodies in the shallow crust. *Geophysical Journal International*, *220*(3), 1677-1686. https://doi.org/10.1093/gji/ggz543

Pujades, L.G., Canas, J.A., Egozcue, J.J., Puigví, M.A., Gallart, J., Lana, K., Pous, J. and Casas, A. (1990). Coda-Q distribution in the Iberian Peninsula. *Geophysical Journal International*, *100*(2), 285-301. https://doi.org/10.1111/j.1365-246X.1990.tb02486.x

Rawlinson, N., Pozgay, S., and Fishwick, S. (2010). Seismic tomography: a window into deep Earth. *Physics of the Earth and Planetary Interiors*, *178*(3-4), 101-135. https://doi.org/10.1016/j.pepi.2009.10.002

Romagnoli, C., Casalbore, D., Bortoluzzi, G., Bosman, A., Chiocci, F. L., D'oriano, F., Gamberi, F., Ligi, M. and Marani, M. (2013). Bathy-morphological setting of the Aeolian Islands. *Geological Society, London, Memoirs*, *37*(1), 27-36. https://doi.org/10.1144/M37.4

Rosi, M., Pistolesi, M., Bertagnini, A., Landi, P., Pompilio, M. and Di Roberto, A. (2013). Stromboli volcano, Aeolian Islands (Italy): present eruptive activity and hazards. *Geological Society, London, Memoirs*, *37*(1), 473-490. https://doi.org/10.1144/M37.14

Ruch, J., Vezzoli, L., De Rosa, R., Di Lorenzo, R., and Acocella, V. (2016). Magmatic control along a strike-slip volcanic arc: The central Aeolian arc (Italy). *Tectonics*, *35*(2), 407-424. https://doi.org/10.1002/2015TC004060

Saccorotti, G., and Lokmer, I. (2021). A review of seismic methods for monitoring and understanding active volcanoes. *Forecasting and Planning for Volcanic Hazards, Risks, and Disasters*, 25-73. https://doi.org/10.1016/B978-0-12-818082-2.00002-0

Salon, S., Crise, A., Picco, P., De Marinis, E., and Gasparini, O. (2003). Sound speed in the Mediterranean Sea: an analysis from a climatological data set. *Annales Geophysicae, 21*(3), 833-846. https://doi.org/10.5194/angeo-21-833-2003

Sanborn, C. J., and Cormier, V. F. (2018). Modelling the blockage of Lg waves from three-dimensional variations in crustal structure. *Geophysical Journal International*, *214*(2), 1426-1440. https://doi.org/10.1093/gji/ggy206

Sato, H. (1977). Energy propagation including scattering effects sengle isotropic scattering approximation. *Journal of Physics of the Earth*, *25*(1), 27-41. https://doi.org/10.4294/jpe1952.25.27

Sato, H. and Fehler, M., (1998). Seismic wave propagation and scattering in heterogeneous Earth. *1st edition, Springer, New York.*

Sato, H., Fehler, M., and Maeda, T. (2012). *Seismic Wave Propagation and Scattering in Heterogeneous Earth*. 2nd edn. Springer.

Savelli, C. (1988). Late Oligocene to Recent episodes of magmatism in and around the Tyrrhenian Sea: implications for the processes of opening in a young inter-arc basin of intra-orogenic (Mediterranean) type. *Tectonophysics*, *146*(1-4), 163-181. https://doi.org/10.1016/0040-1951(88)90089-3

Scandone, P. (1979). Origin of the Tyrrhenian Sea and Calabrian arc. *Bollettino della Società Geologica Italiana*, *98*(1), 27-34.

Scherbaum, F. (1990). Combined inversion for the three-dimensional Q structure and source parameters using microearthquake spectra. *Journal of Geophysical Research*, 95 (B8), 12423-12438. https://doi.org/10.1029/JB095iB08p12423

Selva, J., Bonadonna, C., Branca, S., De Astis, G., Gambino, S., Paonita, A., Pistolesi, M., Ricci, T., Sulpizio, R., Tibaldi, A. and Ricciardi, A. (2020). *Multiple Hazards and*

Paths to Eruptions: A Review of the Volcanic System of Volcano. Aeolian Islands, Italy: Earth Sci. Rev, 103186. https://doi.org/10.1016/j.earscirev.2020.103186

Selvaggi, G., and Chiarabba, C. (1995). Seismicity and P-wave velocity image of the Southern Tyrrhenian subduction zone. *Geophysical Journal International*, *121*(3), 818-826. https://doi.org/10.1111/j.1365-246X.1995.tb06441.x

Shalev, E., Kenedi, C. L., Malin, P., Voight, V., Miller, V., Hidayat, D., Sparks, R. S. J., Minshull, T., Paulatto, M., Brown, L. and Mattioli, G. (2010). Three-dimensional seismic velocity tomography of Montserrat from the SEA-CALIPSO offshore/onshore experiment. *Geophysical Research Letters*, *37*(19). https://doi.org/10.1029/2010GL042498

Sharp, A. D. L., Davis, P. M. and Gray, F. (1980). A low velocity zone beneath Mount Etna and magma storage. *Nature*, *287*(5783), 587-591. https://doi.org/10.1038/287587a0

Shimizu, H. and Explosion Seismic Research Group of Unzen Volcano (1997). Subsurface structure of Unzen volcano derived from the 1995 explosion experiment. *Proceedings DPRI symposium on Magma Exploration, 9-15*.

Sicali, S., Barberi, G., Cocina, O., Musumeci, C., and Patanè, D. (2015). Volcanic unrest leading to the July–August 2001 lateral eruption at Mt. Etna: seismological constraints. *Journal of volcanology and geothermal research*, *304*, 11-23. https://doi.org/10.1016/j.jvolgeores.2015.08.004

Sketsiou, P., De Siena, L., Gabrielli, S., and Napolitano, F. (2021). 3-D attenuation image of fluid storage and tectonic interactions across the Pollino fault network. *Geophysical Journal International*, *226*(1), 536–547. https://doi.org/10.1093/gji/ggab109

Stacey, F.D., Gladwin, M.T., McKavanagh, B., Linde, A.T. and Hastie, L.M. (1975). Anelastic damping of acoustic and seismic pulses. *Geophysical Surveys*, *2*, 133-151. https://doi.org/10.1007/BF01447906

Taburni, D., 2011. Elaborazione e sperimentazione di un modello matemático di propagazione dell'inquinamento acustico subacqueo, nell'ambito del progetto GIONHA "Governance and Integrated Observation of marine Natural Habitat", Technical Report CNR-IDASC, http://www.gionha.it/risorse/pubblicazioni/report/.

Tarquini, S., Isola, I., Favalli, M., and Battistini, A. (2007). *TINITALY, a Digital Elevation Model of Italy with a 10 M-Cell Size*. Version 1.0. Rome: Istituto Nazionale di Geofisica e Vulcanologia (INGV). Data set. doi:10.13127/TINITALY/1.0

Titos, M., Bueno, A., García, L., Benítez, M. C., and Ibañez, J. (2018). Detection and classification of continuous volcano-seismic signals with recurrent neural networks. *IEEE Transactions on Geoscience and Remote Sensing*, *57*(4), 1936-1948. https://doi.org/10.1109/TGRS.2018.2870202

Tipler, P.A. (1999). Física. *Ed. Reverté.*

Tipler, P. and Mosca, G. (2005). Física para la ciencia y la tecnología. *Ed. Reverté.*

Thurber, C. H. (1984). Seismic detection of the summit magma complex of Kilauea volcano, Hawaii. *Science*, *223*(4632), 165-167. https://doi.org/10.1126/science.223.4632.165

Tomatsu, T., Kumagai, H. and Dawson, P. B. (2001). Tomographic inversion of P-wave velocity and Q structures beneath the Kirishima volcanic complex, southern Japan, based on finite difference calculations of complex traveltimes. *Geophysical Journal International*, *146*(3), 781-794. https://doi.org/10.1046/j.1365-246X.2001.00491.x

Torelli, L., Grasso, M., Mazzoldi, G., and Peis, D. (1998). Plio–Quaternary tectonic evolution and structure of the Catania foredeep, the northern Hyblean Plateau and the Ionian shelf (SE Sicily). *Tectonophysics*, *298*(1-3), 209-221. https://doi.org/10.1016/S0040-1951(98)00185-1

Um, J., and Thurber, C. (1987). A fast algorithm for two-point seismic ray tracing. *Bulletin of the Seismological Society of America*, *77*(3), 972-986. https://doi.org/10.1785/BSSA0770030972

Ventura, G., Vilardo, G., Milano, G., and Pino, N. A. (1999). Relationships among crustal structure, volcanism and strike–slip tectonics in the Lipari–Vulcano volcanic complex (Aeolian Islands, Southern Tyrrhenian Sea, Italy). *Physics of the Earth and Planetary Interiors*, *116*(1-4), 31-52. https://doi.org/10.1016/S0031-9201(99)00117-X

Ventura, G. (2013). Kinematics of the Aeolian volcanism (Southern Tyrrhenian Sea) from geophysical and geological data. *Geological Society, London, Memoirs*, *37*(1), 3-11. https://doi.org/10.1144/M37.2

Viccaro, M., Barca, D., Bohrson, W. A., D'Oriano, C., Giuffrida, M., Nicotra, E., and Pitcher, B. W. (2016). Crystal residence times from trace element zoning in plagioclase reveal changes in magma transfer dynamics at Mt. Etna during the last 400 years. *Lithos*, *248*, 309–323. https://doi.org/10.1016/j.lithos.2016.02.004

Viccaro, M., Cannata, A., Cannavò, F., De Rosa, R., Giuffrida, M., Nicotra, E., ... and Sacco, G. (2021). Shallow conduit dynamics fuel the unexpected paroxysms of Stromboli volcano during the summer 2019. *Scientific Reports*, *11*(1), 1-15. https://doi.org/10.1038/s41598-020-79558-7

Vidale, J. E. (1990). Finite-difference calculation of traveltimes in three dimensions. *Geophysics*, *55*(5), 521-526. https://doi.org/10.1190/1.1442863

Villasenor, A., Benz, H. M., Filippi, L., De Luca, G., Scarpa, R., Patanè, G. and Vinciguerra, S. (1998). Three-dimensional P-wave velocity structure of Mt. Etna, Italy. *Geophysical research letters*, *25*(11), 1975-1978. https://doi.org/10.1029/98GL01240

Voight, B., and Sparks, R. S. J. (2010). Introduction to special section on the eruption of Soufrière Hills Volcano, Montserrat, the CALIPSO Project, and the SEA-CALIPSO arc-crust imaging experiment. *Geophysical Research Letters*, *37*. https://doi.org/10.1029/2010GL044254

Voight, B., Sparks, R. S. J., Shalev, E., Minshull, T., Paulatto, M., Annen, C., Kenedi, C., Hammond, J., Henstock, T. J., Brown, L., Kiddle, E., Malin, P., Mattioli, G., Ammon, C., Arias-Dotson, E., Belousov, A., Byerly, K., Carothers, L., Clarke, A., Dean, S., Ellett, L., Elsworth, D., Hidayat, D., Herd, A., Johnson, M., Lee, A., Miller, V., Murphy, B., Peirce, C., Ryan, G., Saldana, S., Snelson, C., Stewart, R., Syers, R., Taron, J., Trofimovs, J., Widiwijayanti, C., Young, S. R. and Zamora, W. (2014). The SEA-CALIPSO volcano imaging experiment at Montserrat: plans, campaigns at sea and on land, scientific results, and lessons learned. *Geological Society, London, Memoirs*, *39*(1), 253-289. https://doi.org/10.1144/M39.15

Wegler, U. and Lühr, B.G. Scattering behaviour at Merapi volcano (Java) revealed from an active seismic experiment. (2001). *Geophysical Journal International*, *145*(3), 579-592. https://doi.org/10.1046/j.1365-246x.2001.01390.x

Wegler, U. (2003). Analysis of multiple scattering at Vesuvius volcano, Italy, using data of the TomoVes active seismic experiment. *Journal of Volcanology and Geothermal Research*, *128*(1-3), 45-63. https://doi.org/10.1016/S0377-0273(03)00246-4

Wegler, U. (2004). Diffusion of seismic waves in a thick layer: Theory and application to Vesuvius volcano. *Journal of Geophysical Research: Solid Earth*, *109*(B7). https://doi.org/10.1029/2004JB003048

Wu, R. S. (1985). Multiple scattering and energy transfer of seismic waves—separation of scattering effect from intrinsic attenuation—I. Theoretical modelling. *Geophysical Journal International*, *82*(1), 57-80. https://doi.org/10.1111/j.1365-246X.1985.tb05128.x

Wu, H. and Lees, J.M. (1996). Attenuation of coso geothermal area, California, from waves pulse width. *Bulletin of Seismological Society of America*, *86*(5), 1574-1590. https://doi.org/10.1785/BSSA0860051574

Yamamoto, M., and Sato, H. (2010). Multiple scattering and mode conversion revealed by an active seismic experiment at Asama volcano, Japan. *Journal of Geophysical Research: Solid Earth*, *115*(B7). https://doi.org/10.1029/2009JB007109

Yoshimoto, K. (2000). Monte Carlo simulation of seismogram envelopes in scattering media. *Journal of Geophysical Research: Solid Earth*, *105*(B3), 6153-6161. https://doi.org/10.1029/1999JB900437

Yoshimoto, K., Sato, H., and Ohtake, M. (1993). Frequency-dependent attenuation of P and S waves in the Kanto area, Japan, based on the coda-normalization method. *Geophysics Journal International*, *114*, 165–174. https://doi.org/10.1111/j.1365-246x.1993.tb01476.x

Zandomeneghi, D., Almendro, J., Ibáñez, J. and Saccorotti., G. (2008). Seismic tomography of cental Sao Miguel, Azores. *Physics of the Earth and Planetary Interiors*, *167*, 8-18. https://doi.org/10.1016/j.pepi.2008.02.005

Zandomeneghi, D., Barclay, A., Almendros, J., Ibáñez, J. M., Wilcock, W. S., and Ben-Zvi, T. (2009). Crustal structure of Deception Island volcano from P wave seismic tomography: Tectonic and volcanic implications. *Journal of Geophysical Research*, *114*. https://doi.org/10.1029/2008jb006119

Zeng, Y. (1991). Compact solutions for multiple scattered wave energy in time domain. *Bulletin of the Seismological Society of America*, *81*(3), 1022-1029.

Zeng, Y. (1993). Theory of scattered P-and S-wave energy in a random isotropic scattering medium. *Bulletin of the Seismological Society of America*, *83*(4), 1264-1276. https://doi.org/10.1785/BSSA0830041264

Zieger, T., Sens-Schönfelder, C., Ritter, J. R., Lühr, B., and Dahm, T. (2016). P-wave scattering and the distribution of heterogeneity around Etna volcano. *Annals of Geophysics*, *59*(4).

Zollo, A., Gasparini, P., Virieux, J., Biella, G., Boschi, E., Capuano, P., De Franco, R., Dell'Aversana, P., De Matteis, R., De Natale, G., Iannaccone, G., Guerra, I., Le Meura, H. and Mirabile, L. (1998). An image of mt. Vesuvius obtained by 2-d seismic tomography. *Journal of Volcanology and Geothermal Research*, *82*, 161-173. https://doi.org/10.1016/S0377-0273(97)00063-2

Zuccarello, L., Paratore, M., La Rocca, M., Ferrari, F., Messina, A., Branca, S., et al. (2016). Shallow velocity model in the area of Pozzo Pitarrone, Mt. Etna, from single station, array methods and borehole data. *Annals of Geophysics*, *59*. https://doi.org/10.4401/ag-7086

Zulfakriza, Z., Nugraha, A. D., Widiyantoro, S., Cummins, P. R., Sahara, D. P., Rosalia, S., Priyono, A., Kasbani, K., Syahbana, D. K., Priambodo, I. C., Martanto, M., Ardianto, A., Husni, Y. M., Lesmana, A., Kusumawati, D. and Prabowo, B. S. (2020). Tomographic imaging of the Agung-Batur Volcano Complex, Bali, Indonesia, from the ambient seismic noise field. *Frontiers in Earth Science*, *8*, 43. https://doi.org/10.3389/feart.2020.00043

ANEXOS

A. <u>2D and 3D attenuation tomographies at Mt. Etna (Italy)</u>

Geophysical Research Abstracts, Vol. 21, EGU2019-10447, 2019

EGU General Assembly 2019

Cocina, O., Ibanez, J., Zuccarello, L., Del Pezzo, E., **Castro-Melgar, I**. and Prudencio, J. (2019). 2D and 3D attenuation tomographies at Mt. Etna (Italy). *Geophysical Research Abstracts*, 21, EGU21019-1426.

2D and 3D attenuation tomographies at Mt. Etna (Italy)

Ornella Cocina (1), Jesus Ibanez (2), Luciano Zuccarello (2), Edoardo Del Pezzo (3), **Ignacio Castro-Melgar (2)** and Janire Prudencio (2)

(1) Istituto Nazionale di Geofisica e Vulcanologia, Sezione di Catania, Osservatorio Etneo
(2) Departamento Física Teórica y del Cosmos, University of Granada, Granada, Spain
(3) Instituto Andaluz de geofísica, University of Granada, Granada, Spain

2D and 3D attenuation structures of Mt. Etna have been obtained with measurements of diffusion model and coda normalization method, respectively, with the same data-set used to develop the 3D velocity tomography (Diaz-Moreno et al. 2016). We have obtained intrinsic and scattering 2D maps applying the diffusion model which is an approximation of the general energy transport theory developed by Wegler and Lühr (2001) and Wegler (2003). As a result of the theoretical curves with the energy envelopes of the seismograms, we have obtained intrinsic attenuation coefficient and diffusivity coefficient values in the frequency range of 4-24 Hz. Then, we have quantified the contribution of intrinsic and scattering attenuation by inverse quality factor being more representative. Finally, with a new representation method based in numerically estimated space-weighting functions, we have represented the inverse quality factors obtained into 2D contour maps. To obtain 3D attenuation tomography of Mt Etna, we have used more than 60000 waveforms recorded at over 100 on land seismic stations. The rays were traced in a 3D velocity model. We have inverted the spectral ratios obtained with the coda normalization method to obtain total-Q values. We resolve 5 km cubic cells. Both results, 2D maps and 3D attenuation structure, have shown that there is likewise agreement with the velocity tomography: the low velocity zones being consistent with regions featuring high attenuation effects and the high velocity zones with regions featuring low attenuation effects. This new models will be a complement to the better understand previous geophysical models and will allow remove some grades of uncertainty of the other studies.

B. <u>Seismic Attenuation Imaging of The Geysers Geothermal Field, USA</u>

American Geophysical Union, Fall Meeting 2020, abstract #S061-0015

Prudencio, J., **Castro-Melgar, I.**, Taira, T., Gritto, R. and Ibáñez, J.M. (2020). Seismic Attenuation Imaging of The Geysers Geothermal Field, USA. *AGU Fall Meeting Abstracts 2020*, S061-0015

Seismic Attenuation Imaging of The Geysers geothermal Field, USA

Janire Prudencio[1], **Ignacio Castro-Melgar[1]**, Taka'aki Taira[2], Roland Gritto[3] and Jesús M. Ibáñez[4]

    (1) University of Granada, Granada, Spain

    (2) Univ. California Berkeley, Berkeley, CA, United States

    (3) Array Information Technology. Greenbelt, MD, United States

    (4) University of Granada, Instituto Andaluz de Geofísica, Granada, Spain

The Geysers geothermal field is located in northern California and is the world's largest producer of geothermal energy. Previous studies found spatio-temporal variations in seismic velocity that are likely related to fluid injections and distributions within the reservoir. Because seismic attenuation may exhibit more sensitivity to fluid saturation and to the thermal state of the medium, we obtained for the first time 2D intrinsic (Q_i^{-1}) and scattering (Q_s^{-1}) attenuation models and 3D total-Q^{-1} attenuation structure. These models have been obtained by fitting waveform envelopes to diffusion model and coda-normalization method, respectively. 2D intrinsic and scattering models were derived by applying the diffusion model which is an approximation of the general energy transport theory developed by Wegler and Lühr (2001) and Wegler (2003). We use energy envelopes of the seismograms, to obtain intrinsic attenuation coefficient and diffusivity coefficients. In a subsequent step, we applied a new representation method based on numerically estimated space-weighting functions (Del Pezzo et al., 2016), to estimate inverse quality factors. We have used over 35000 waveforms recorded at 34 seismic stations to estimate the 3D attenuation structure of the reservoir. Seismic ray tracing were based on through the 3D velocity model by Gritto et al., 2013. The spectral ratios obtained with the coda normalization method, were subsequently inverted to obtain total-Q^{-1} values with 3-km grid spacing. Both 2D maps and 3D attenuation structure are in good agreement with the velocity model: the low velocity zones being consistent with regions featuring high attenuation effects and the high velocity zones with regions featuring low attenuation effects. Low attenuation and low Vp regions can be interpreted as region with steam concentration, which have been observed in geothermal reservoirs and volcanic regions (De Siena, 2010).

C. <u>The 2021 Cumbre Vieja volcano eruption in La Palma (Canary Islands)</u>

Newsletter of Environmental, Disaster and Crises Management Strategies, 26

Lekkas, E., Meletlidis, S., Kyriakopoulos, K., Manousaki, M., Mavroulis, S., Kostaki, E., Michailidis, A., Gogou, M., Mavrouli, M., **Castro-Melgar, I.**, Gatsios, T. and Parcharidis, I. (2021). The 2021 Cumbre Vieja volcano eruption in La Palma (Canary Islands). *Newsletter of Environmental, Disaster and Crises Management Strategies*, 26, ISSN 2653-9454.

The 2021 Cumbre Vieja volcano eruption in La Palma (Canary Islands)

Efthymis **Lekkas**
Stavros **Meletlidis**
Konstantinos **Kyriakopoulos**
Maria **Manousaki**
Spyridon **Mavroulis**
Eirini **Kostaki**
Alexandros **Michailidis**
Marilia **Gogou**
Maria **Mavrouli**
Ignacio **Castro-Melgar**
Theodoros **Gatsios**
Issaak **Parcharidis**

About

Non-periodic publication of the Post-graduate Studies Program "Environmental Disasters & Crises Management Strategies" of the National & Kapodistrian University of Athens, issued after significant events for the immediate information of the scientific community and the general public. The publication includes also scientific data from various research teams from universities, organizations and research institutes.

Copyrights

Cite as

Scientific Mission

Of the National and Kapodistrian University of Athens, Faculty of Geology and Geoenvironment, Department of Dynamic Tectonic Applied Geology

Contributors

NATIONAL AND KAPODISTRIAN UNIVERSITY OF ATHENS (GREECE)
FACULTY OF GEOLOGY AND GEOENVIRONMENT
Department of Dynamic Tectonic Applied Geology: Prof. Efthymis Lekkas, Dr. Spyridon Mavroulis
Department of Mineralogy and Petrology: Prof. Konstantinos Kyriakopoulos
NATIONAL AND KAPODISTRIAN UNIVERSITY OF ATHENS (GREECE)
MEDICAL SCHOOL
Department of Microbiology: Dr. Maria Mavrouli
HAROKOPIO UNIVERSITY (GREECE)
Department of Geography: Prof. Issaak Parcharidis, Theodoros Gatsios, MSc
UNIVERSITY OF GRANADA (SPAIN) | FACULTY OF SCIENCE
Department of Theoretical Physics and Cosmos: Dr. Ignacio Castro-Melgar
INSTITUTO GEOGRÁFICO NACIONAL (SPAIN)
Grupo De Volcanología: Dr. Stavros Meletlidis
EARTHQUAKE PLANNING AND PROTECTION ORGANIZATION (GREECE)
Maria Manousaki, Geologist, MSc
EUROPEAN PARLIAMENT (BELGIUM)
Eirini Kostaki, Political Adviser - Accredited Parliamentary Assistant
Alexandros Michailidis, Freelance photojournalist (Brussels, Belgium)

D. Operational Monitoring of a Volcano Before Entering In Unrest Phase Using Sentinel 1 DINSAR and MTINSAR: The Case of La Palma Volcanic Island

SafeGreece Conference Proceedings

SafeGreece – 8th International Conference on Civil Protection and New Technologies

Castro-Melgar, I., Prudencio, J., Ibáñez, J., Gatsios, T. and Parcharidis, I. (2021). Operational Monitoring of a Volcano Before Entering in Unrest Phase Using Sentinel 1 DINSAR and MTINSAR: The Case of La Palma Volcanic Islands. *SafeGreece Conference Proceedings 2021,* pp. 117-120, ISSN 2654-1823.

EXTENDED ABSTRACT

Operational Monitoring of a Volcano Before Entering in Unrest Phase Using Sentinel 1 DINSAR and MTINSAR: The Case of La Palma Volcanic Island

Ignacio Castro-Melgar[1,2], Janire Prudencio[1,3], Jesús Ibáñez[1,3], Theodoros Gatsios[2,4] and Issaak Parcharidis[2]

(1) Department of Theoretical Physics and Cosmos, University of Granada (Spain)
(2) Department of Geography, Harokopio University of Athens (Greece)
(3) Andalusian Institute of Geophysics, University of Granada (Spain)
(4) Department of geophysics and Geothermy, National and Kapodistrian University of Athens (Greece)

ABSTRACT

The volcanic complex of Cumbre Vieja on the island of La Palma is in eruption (October 2021) with serious implications for the inhabits of the island. SAR interferometry has been used as an operational tool in order to monitoring active volcanoes. The current study concerns the application of DinSAR and MTInSAR-SBAS in the area using Sentinel 1 SLC images in order to detect potential precursor of uplift in the unrest area. The final task is to confirm that interferometric techniques could act as a warning system before the explosion of a volcano. Results show that starting from last week of August a pattern of uplift is detected which increased few days before the explosion.

Keywords: SAR Interferometry, DinSAR, SBAS, Volcanic hazard, La Palma

1. INTRODUCTION

The Canary archipelago is formed by a chain of seven volcanic islands and four islets located in the eastern Atlantic Ocean. There is an alignment of the islands, islets and seamounts showing age progression from NE to SW [1]. Its two western, youngest, and active islands in the archipelago (La Palma and El Hierro) are host of the highest potential risk due to their active volcanism. The origin of the volcanism in the Canary Archipelago started in Oligocene and continues active [2], the mechanism that originated its volcanism is still under debate by the scientific community. The most accepted models are the

propagation fracture from the Atlas Mountains [3] or the existence of a hotspot or mantle plume [4, 5] among others models.

One of the youngest islands of the archipelago is La Palma, located in the NW area. It is the second island in height and the fifth in size, it has an area of 706 km^2 and its aligned N-S. Volcanic activity in La Palma first originated with the formation of an underwater complex of seamounts and a plutonic complex between 3 and 4 Ma [6]. In terms of its historical eruption records, La Palma is the most active island, at least 7 eruptions have been reported, including 1585, 1646, 1677, 1712, 1949, 1971 volcanic eruptions and the last one that is currently in progress. The last eruption in the other islands of the archipelago happened in 2011, it was an underwater eruption off the coast El Hierro, the neighbouring island in the Southwest of Canarias.

Currently, the volcanic complex of Cumbre Vieja on the island of La Palma is in eruption (October 2021) with serious implications for the inhabits of the island. In the century XXI different volcanic manifestations have been observed in the Canary Islands such as the seismic series of Tenerife in 2004, the reactivations and eruptions of El Hierro between 2011 and 2014 and the seismic series on La Palma in 2017, 2018, 2020 and 2021.

The previous eruption on La Palma of 1971, it is called the Teneguia eruption, the eruption lasted 24 days and began through a 200m eruptive fissure producing pyroclasts and lavas. Later, the behaviour turned more explosive with strombolian activity. The precursor seismicity had the onset 6 days before the eruption [7] This eruption was probably fed by an another magma plumbing/reservoir system with respect to the older Taburiente/Cumbre Nueva volcanic system [8].

2. METHODOLOGY

Synthetic Aperture Radar (SAR) is a powerful remote sensing satellite sensor used for Earth observation [9]. It emits electromagnetic radiation and then coherently records the amplitude and phase of the returned signal to produce images of the ground. It has cloud-penetrating capabilities, as well as day and night operational capabilities. Spaceborne SAR interferometry is a technique that produces 3D topographic data of Earth's surface directly from two SAR images [10]. An extension of the basic technique, called differential SAR interferometry (DInSAR), allows measurements of land deformation

very precisely with millimetre resolution. It has various applications in the fields of volcanology, cartography, crustal dynamics and land subsidence.

By using large stacks of SAR images acquired over the same area, long deformation time series can be analysed using multitemporal differential SAR interferometry techniques. These coherent methods exploit either permanently coherent Persistent Scatterers (PSs) or temporally coherent Distributed Scatterers (DSs). PSs are typically artificial objects that reflect radar energy well such as metal structures and buildings. The PS methods that have been developed include the Persistent Scatterer Interferometry (PSI). PSI provides a parametric estimation of the 3D location and velocity of each PS along the line of sight (LOS) connecting it to the satellite [11,12]. Many such measurements are combined using PSI to produce highly accurate terrain motion maps. In urban areas where there is a prevalence of PSs, PSI allows analysis of even individual structures on the ground. The DS methods include algorithms such as SBAS. A DS object reflects lower radar energy compared to PSs and it usually covers several pixels in high resolution SAR images. These pixels exhibit similar scattering properties and can be used together for deformation estimation. SBAS estimates the deformation time series even in rural areas where the density of PSs is low [13].

3. RESULTS AND DISCUSSION

The aim of the present work is to prove that in this case SAR interferometry is an important tool for detecting and mapping surface deformation, which is a precursor phenomenon which, in combination with other phenomena, can lead a volcano into unrest phase even to explosion. DInSAR and SBAS methods have been applied using Sentinel 1 A and B SLC. For SBAS method 24 SLC images in descending geometry of acquisition (169 relative orbit) covering the period 01/05/2021 - 16/09/2021 were processed with GAMMA/IPTA s/w. For DInSAR method have been used two interferometric pairs from Sentinel 1 SLC specifically (i) 05/08/2021 and 16/09/2021 in descending geometry (169) and (ii) 09/08/2021 and 14/09/2021 in ascending geometry of acquisition (60) both processed with ESA's open SNAP s/w.
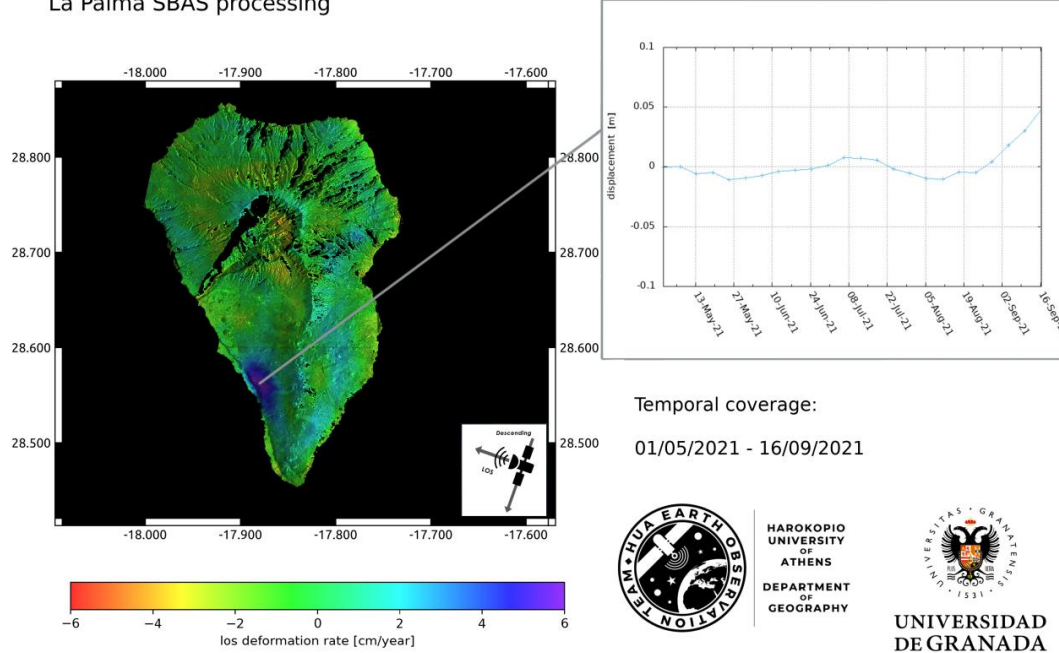
Figure 1. SBAS results (on the left) showing deformation since May of 2021 in cm/y and (on the right) the time series diagram of a scatterer (located in the maximum rate of deformation) showing the trend of deformation during the period 01/05/2021 - 16/09/2021 using Sentinel 1 images of descending orbit.

(a)   (b)
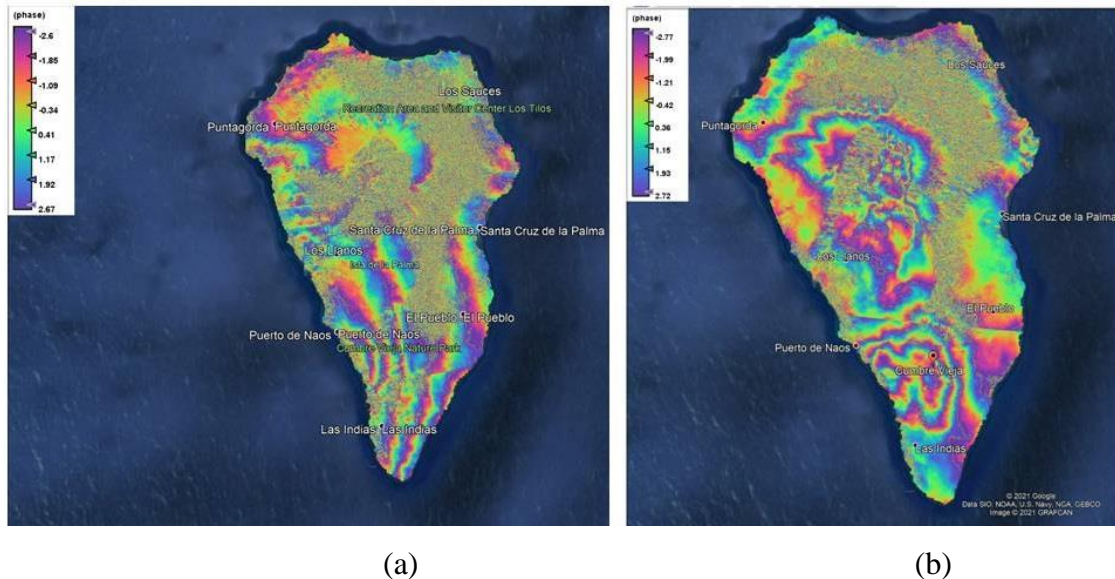
Figure 2. DInSAR results (wrapped interferograms a. Ascending pair and b. Descending pair) it is clear display pattern of fringes in phase showing uplift in the southern part of the island while in the northern part of the island there is "noise" in both images

Our results show that some days before the unrest phase the area of the volcanic complex of Cumbre Vieja was undergone to uplift. Especially in SBAS results with a larger temporal monitoring from time series diagram it is clearly noticed that the after an up-down between May and last week of August there is an abrupt uplift in September until very few days before the explosion.

REFERENCES

1. J. Geldmacher, K. Hoernle, P. Bogaard, S. Duggen, R. Werner (2005). New ^{40}Ar/^{39}Ar age and geochemical data from seamounts in the Canary and Madeira volcanic provinces: support for the mantle plume hypothesis. Earth and Planetary Science Letters, 237(1-2), 85-101. https://doi.org/10.1016/j.epsl.2005.04.037

2. H. Staudigel, H. U. Schmincke (1984). The pliocene seamount series of la palma/canary islands. Journal of Geophysical Research: Solid Earth, 89(B13), 11195-11215. https://doi.org/10.1029/JB089iB13p11195

3. F. Anguita, F. Hernán (1975). A propagating fracture model versus a hot spot origin for the Canary Islands. Earth and Planetary Science Letters, 27(1), 11-19. https://doi.org/10.1016/0012-821X(75)90155-7

4. W. J. Morgan (1983). Hotspot tracks and the early rifting of the Atlantic. In Developments in Geotectonics (Vol. 19, pp. 123-139). Elsevier. https://doi.org/10.1016/B978-0-444-42198-2.50015-8

5. J. C. Carracedo, S. Day, H. Guillou, E. R. Badiola, J. A. Canas, F. P. Torrado (1998). Hotspot volcanism close to a passive continental margin: the Canary Islands. Geological Magazine, 135(5), 591-604. https://doi.org/10.1017/S0016756898001447

6. H. Staudigel, G. Feraud, G. Giannerini (1986). The history of intrusive activity on the island of La Palma (Canary Islands). Journal of Volcanology and Geothermal Research, 27(3-4), 299-322. https://doi.org/10.1016/0377-0273(86)90018-1

7. H. Albert, F. Costa, J. Martí (2016). Years to weeks of seismic unrest and magmatic intrusions precede monogenetic eruptions. Geology, 44(3), 211-214. https://doi.org/10.1130/G37239.1

8. K. Galipp, A. Klügel, T. H. Hansteen (2006). Changing depths of magma fractionation and stagnation during the evolution of an oceanic island volcano: La

Palma (Canary Islands). Journal of Volcanology and Geothermal Research, 155(3-4), 285-306. https://doi.org/10.1016/j.jvolgeores.2006.04.002

9. J. Curlander, R. McDonough (1991). Synthetic aperture radar: Systems and signal processing. John Wiley and Sons. ISBN: 978-0-471-85770-9

10. R. Bamler, P. Hartl (1998). Synthetic aperture radar interferometry. Inverse problems 14, R1-R54, IOP Publishing Limited. https://doi.org/10.1088/0266-5611/14/4/001

11. A. Ferretti, C. Prati, F. Rocca (2000). Nonlinear subsidence rate estimation using permanent scatterers in differential SAR interferometry. IEEE Transactions on Geoscience and Remote Sensing 38 (5), 2202–2212. https://doi.org/10.1109/36.868878

12. A. Ferretti, C. Prati, F. Rocca (2001). Permanent scatterers in SAR interferometry. IEEE Transactions on Geoscience and Remote Sensing 39 (1), 8-20. https://doi.org/10.1109/36.898661

13. P. Berardino, G. Fornaro, R. Lanari, E. Sansosti (2002). A new algorithm for surface deformation monitoring based on small baseline differential SAR interferograms. IEEE Transactions on Geoscience and Remote Sensing 40 (11), 2375-2383. https://doi.org/10.1109/TGRS.2002.803792

E. Operational use of Sentinel 1 data and interferometric methods to detect precursors for volcanic hazard warning system: the case of La Palma volcanic complex last eruption

Living Planet Symposium 2022, ESA

#63321

EXTENDED ABSTRACT

Operational use of Sentinel 1 data and interferometric methods to detect precursors for volcanic hazard warning system: the case of La Palma volcanic complex last eruption.

Ignacio Castro-Melgar[1,2], Theodoros Gatsios[2,4], Janire Prudencio[1,3], Jesús Ibáñez[1,3] and Issaak Parcharidis[2]

(1) Department of Theoretical Physics and Cosmos, University of Granada (Spain)

(2) Department of Geography, Harokopio University of Athens (Greece)

(3) Andalusian Institute of Geophysics, University of Granada (Spain)

(4) Department of Geophysics and Geothermy, National and Kapodistrian University of Athens (Greece)

1. INTRODUCTION

La Palma is the youngest island of the Canary Islands (Spain) and is situated in the NW area. The Canary archipelago is a chain of seven volcanic islands in the Atlantic Ocean off the coast of Africa. This set of islands, islets and seamounts are aligned NE-SW and host a high potential risk due to their active volcanism especially in the western and youngest islands (La Palma and El Hierro). The origin of the volcanism in the Canary Archipelago started in Oligocene and continues active (Staudigel and Schmincke, 1984), the mechanism that originated its volcanism is still under debate by the scientific community. The most accepted models are the propagation fracture from the Atlas Mountains (Anguita and Hernán, 1975) or the existence of a hotspot or mantle plume (Morgan, 1983, Carracedo et al., 1998) among others models. In the last decades different volcanic manifestations occurs in the Canary archipelago such as the seismic series of Tenerife in 2004, the reactivations and eruptions of El Hierro between 2011 and 2014 and the seismic series on La Palma in 2017, 2018, 2020 and 2021.

Volcanic activity in La Palma first originated with the formation of an underwater complex of seamounts and a plutonic complex between 3 and 4 Ma [6]. Is the most volcanic active island in the Canary archipelago in historical times, 7 eruptions have been reported (1585, 1646, 1677, 1712, 1949, 1971 and 2021) The last eruption in the volcanic

complex of Cumbre Vieja, currently in progress (November, 2021), is causing serious implications for the inhabitants of the island with near 3000 buildings destroyed.

2. METHODOLOGY

For this study we use Sentinel 1 A/B TOPSAR (C band), SLC product in both orbits (ascending and descending orbits). Synthetic Aperture Radar (SAR) is a powerful remote sensing satellite sensor used for Earth observation (Curlander and McDonough, 1991). The methodologies used are two, conventional Differential SAR Interferometry (DInSAR) and the MTInSAR of SBAS method. DInSAR allows measurements of land deformation very precisely and It has applications in the field of volcanology.

Long deformation dataset can be analysed using large stacks of SAR images in the same area using multitemporal differential SAR interferometry techniques. These techniques are based in the use of permanently coherent Persistent Scatterers (PSs) and/or temporally coherent Distributed Scatterers (DSs). In urban areas there are a prevalence of PSs allowing an individual analysis of the structures on the ground, meanwhile the DS methods have similar scattering properties and can be used together in order to analyse the deformation even in rural areas where there are low PSs density. Small Baseline Subset (SBAS) method is include in DS methods, SBAS is an of multi-temporal InSAR technique for detecting deformations with millimetre precision using a stack of SAR interferograma (Virk et al., 2018)

For DInSAR technique two different interferometric pairs have been analysed (i) 5/8/2021 and 16/09/2021 in descending orbit and (ii) 09/08/2021 and 14/09/2021 in ascending orbit. The software used for the process was SNAP 8.0 (ESA). In SBAS method two different dataset was analysed (ascending and descending orbit), (a) 24 images of relative orbit 60 Sentinel-1A/B TOPSAR (c-band) between 5 of May 2021 to 14 September 2021 and (b) 23 images of relative orbit 169 Sentinel-1A/B TOPSAR (C-band) between 1st May 2021 to 16 September 2021. The datasets were processed with GAMMA software.

3. RESULTS AND CONCLUSIONS

DInSAR images in wrapped interferograms in ascending and descending orbits show fringes in the southern part of La Palma, these patterns of the fringes are not identical between the because they cover different periods, however, the geographical location of the patterns coincide (Cumbre Vieja volcanic complex in the South of the island).

The SBAS estimated deformation velocities in ascending and descending dataset show an uplift trend up to 5 cm in the southern area, it is possible observe the deformation trend have two different stages, a first period of rest with maximum downlift and uplift of 1 cm and a second period between de last days of August until the end of the studied period (mid of September) when an abrupt uplift started with maximum deformation of 5cm.

In this study it is possible to observe that SAR interferometry (conventional and multi-temporal) allow us to know that eruption of Cumbre Vieja in La Palma was preceded by a prior deformation process that is an obvious symptom of a volcanic unrest and these techniques can be used operationally in early warning system with the aim of taking measures in order to mitigate volcanic risk.

4. REFERENCES

Anguita, F., and Hernán, F. (1975). A propagating fracture model versus a hot spot origin for the Canary Islands. *Earth and Planetary Science Letters*, *27*(1), 11-19. https://doi.org/10.1016/0012-821X(75)90155-7

Carracedo, J. C., Day, S., Guillou, H., Badiola, E. R., Canas, J. A., and Torrado, F. P. (1998). Hotspot volcanism close to a passive continental margin: the Canary Islands. *Geological Magazine*, *135*(5), 591-604. https://doi.org/10.1017/S0016756898001447

Curlander, J., McDonough, R. (1991). Synthetic aperture radar: Systems and signal processing. John Wiley and Sons. ISBN: 978-0-471-85770-9

Morgan, W. J. (1983). Hotspot tracks and the early rifting of the Atlantic. *Tectonophysics, 94,* 123-139. https://doi.org/10.1016/B978-0-444-42198-2.50015-8

Staudigel, H., and Schmincke, H. U. (1984). The pliocene seamount series of la palma/canary islands. *Journal of Geophysical Research: Solid Earth*, *89*(B13), 11195-11215. https://doi.org/10.1029/JB089iB13p11195

Staudigel, H., Feraud, G., and Giannerini, G. (1986). The history of intrusive activity on the island of La Palma (Canary Islands). *Journal of Volcanology and Geothermal Research*, *27*(3-4), 299-322. https://doi.org/10.1016/0377-0273(86)90018-1

Virk, A. S., Singh, A., and Mittal, S. K. (2018). Advanced MT-InSAR landslide monitoring: Methods and trends. *J. Remote Sens. GIS*, *7*, 1-6. https://doi.org/10.4172/2469-4134.1000225

F. INSAR techniques monitoring La Palma island to reveal deformation before unrest period to mitigate impact

Natural Hazards (Under review)

2020 Journal Impact Factor: 3,102; H-INDEX: 105

JCR: Q2 Geosciences, multidisciplinary

SJR: Q1 Earth and Planetary Sciences (miscellaneous)

Castro-Melgar, I., Gatsios, T., Prudencio, J., Ibáñez, J. and Parcharidis, I. (2022). INSAR techniques monitoring La Palma island to reveal deformation before unrest period to mitigate impact, *Natural Hazards (under review)*

InSAR techniques monitoring La Palma island to reveal deformation before unrest period to mitigate impact.

Ignacio Castro-Melgar [1,2] , Theodoros Gatsios[2,3]**,** Janire Prudencio[1,4], Jesús Ibáñez[1, 4] and Issaak Parcharidis[2]. Corresponding autor: icastro@correo.ugr.es

(1) Department of Theoretical Physics and Cosmos, Faculty of Science, University of Granada, 18071, Granada, Spain.

(2) Department of Geography, Harokopio University of Athens, 17671, Athens, Greece

(3) Department of Geophysics and Geothermy, National and Kapodistrian University of Athens, 15784, Athens, Greece

(4) Andalusian Institute of Geophysics, University of Granada, Profesor Clavera 12, 18071 Granada, Spain.

Abstract

In the present work we show how the study of deformation constitutes one of the fundamental parameters in early warning protocols for volcanic eruptions. In this work we have analyzed the deformation prior to the current ongoing eruption of the Island of La Palma (Canary Islands, Spain) which began on September 19, 2021 in the volcanic complex of Cumbre Vieja. We performed a study through the application of the SAR multitemporal interferometry and specifically the SBAS method using Sentinel 1 A & B data in ascending and descending orbits, covering the period from 1/5/2021 to 16/9/2021, prior to the starting of the eruption. In addition, the two passes + DEM conventional interferometry has been used using two interferometric pairs of scenes collected before the eruption in both geometries. SBAS results in both orbits showed that before the volcanic eruption there was a period of about 3 weeks during which there was a continuous ground uplift (maximum deformation of about 5 cm). The same results in terms of pattern of fringes showed on the wrapped interferograms applying the conventional interferometry DInSAR.

Keywords: Remote sensing, SAR Interferometry, DinSAR, SBAS, Volcanic hazard, La Palma